

Canadian Journal of Physics

Editor: H. E. DUCKWORTH

Associate Editors:

L. G. ELLIOTT, *Atomic Energy of Canada, Ltd., Chalk River*
J. S. FOSTER, *McGill University*
G. HERZBERG, *National Research Council of Canada*
L. LEPRINCE-RINGUET, *Ecole Polytechnique, Paris*
B. W. SARGENT, *Queen's University*
G. M. VOLKOFF, *University of British Columbia*
W. H. WATSON, *University of Toronto*
G. A. WOONTON, *McGill University*

Published by THE NATIONAL RESEARCH COUNCIL

OTTAWA

CANADA

CANADIAN JOURNAL OF PHYSICS

(Formerly Section A, Canadian Journal of Research)

Under the authority of the Chairman of the Committee of the Privy Council on Scientific and Industrial Research, the National Research Council issues THE CANADIAN JOURNAL OF PHYSICS and five other journals devoted to the publication, in English or French, of the results of original scientific research. Matters of general policy concerning these journals are the responsibility of a joint Editorial Board consisting of: members representing the National Research Council of Canada; the Editors of the Journals; and members representing the Royal Society of Canada and four other scientific societies.

EDITORIAL BOARD

Representatives of the National Research Council

A. Gauthier, *University of Montreal*
R. B. Miller, *University of Alberta*

H. G. Thode, *McMaster University*
D. L. Thomson, *McGill University*

Editors of the Journals

D. L. Bailey, *University of Toronto*
T. W. M. Cameron, *Macdonald College*
H. E. Duckworth, *McMaster University*

K. A. C. Elliott, *Montreal Neurological Institute*
Léo Marion, *National Research Council*
R. G. E. Murray, *University of Western Ontario*

Representatives of Societies

D. L. Bailey, *University of Toronto*
Royal Society of Canada
T. W. M. Cameron, *Macdonald College*
Royal Society of Canada
H. E. Duckworth, *McMaster University*
Royal Society of Canada
Canadian Association of Physicists

K. A. C. Elliott, *Montreal Neurological Institute*
Canadian Physiological Society
P. R. Gendron, *University of Ottawa*
Chemical Institute of Canada
R. G. E. Murray, *University of Western Ontario*
Canadian Society of Microbiologists
T. Thorvaldson, *University of Saskatchewan*
Royal Society of Canada

Ex officio

Léo Marion (Editor-in-Chief), *National Research Council*
J. B. Marshall (Administration and Awards), *National Research Council*

Manuscripts for publication should be submitted to Dr. H. E. Duckworth, Editor, Canadian Journal of Physics, Hamilton College, McMaster University, Hamilton, Ontario.

(For instructions on preparation of copy, see **Notes to Contributors** (inside back cover).)

Proof, correspondence concerning proof, and orders for reprints should be sent to the Manager, Editorial Office (Research Journals), Division of Administration and Awards, National Research Council, Ottawa 2, Canada.

Subscriptions, renewals, requests for single or back numbers, and all remittances should be sent to Division of Administration and Awards, National Research Council, Ottawa 2, Canada. Remittances should be made payable to the Receiver General of Canada, credit National Research Council.

The journals published, frequency of publication, and prices are:

Canadian Journal of Biochemistry and Physiology	Monthly	\$3.00 a year
Canadian Journal of Botany	Bimonthly	\$4.00 a year
Canadian Journal of Chemistry	Monthly	\$5.00 a year
Canadian Journal of Microbiology	Bimonthly	\$3.00 a year
Canadian Journal of Physics	Monthly	\$4.00 a year
Canadian Journal of Zoology	Bimonthly	\$3.00 a year

The price of regular single numbers of all journals is 75 cents.



Canadian Journal of Physics

Issued by THE NATIONAL RESEARCH COUNCIL OF CANADA

VOLUME 36

JUNE 1958

NUMBER 6

DISPLACEMENTS OF THE RADIANT POINT DURING THE AURORAL DISTURBANCE OF SEPTEMBER 22, 1957¹

W. N. ABBOTT

ABSTRACT

Three detailed photographs of the corona on a well-defined star field taken during the display of September 22, 1957, render possible determination of the position of the radiant point and measurement of its displacements. The photographs cover an interval of 21 minutes and the measured displacement, assumed to be continuous, divided by this interval gives an average rate of motion of about 12 minutes of arc per minute of time. The variation of the magnetic elements in the same interval is such as to indicate displacements of the magnetic zenith which, viewed from ground level, appear unrelated to the displacements of the radiant point.

1. INTRODUCTION

The photographs, *a*, *b*, and *c*, of Fig. 1 were obtained at the Geophysical Institute, College, Alaska, during the great auroral display of September 22, 1957. The camera was equipped with a Voigtlander *f*:3.5 lens of excellent optics and the film used was Tri-X subsequently developed in DK-60-a at 68° F. The duration of the exposures was 8 seconds, and because the sensitivity of the film permitted short exposures for low levels of light intensity, the coronal features are well defined and the stellar background is sharp and untrailed, permitting precise location of the radiant point on the celestial sphere and, by change of coordinates, on the sky. The error in the determination of the radiant point does not exceed 10'. We believe that this precision is rarely attained in this type of measurement since as a rule we do not have faint stars on auroral photographs, and if we do, they are seldom untrailed, the degree of error being thus considerable. The advantage of using good optics (contrary to a current belief which has been launched by the Norwegian observers) and film highly sensitive to low levels of light intensity is that, thanks to short exposures, we obtain clearly defined auroral features and sharp stellar images which are at the same time more densely distributed since they belong to fainter stars. On these photographs the star field is Cepheus and the bright stars marked α and δ are α and δ Cephei, respectively.

A comparison of the motion of the radiant point with the variation of the

¹Manuscript received January 24, 1958.

Contribution from the Geophysical Institute, College, Alaska, and the University of Athens, Athens, Greece.

magnetic elements and the motion of the magnetic zenith derived therefrom is the object of this paper. Magnetic data have been kindly made available by the U.S. Coast and Geodetic Survey Station located in the vicinity of the Geophysical Institute.

2. MOTION OF THE RADIANT POINT

The coordinates of the radiant point on the celestial sphere are obtained from photographs *a*, *b*, and *c* of Fig. 1 by alignment of the coronal features with respect to the faint stars, and the estimated error does not exceed 10'. The celestial and horizontal coordinates are given in Table I. Time is given in Alaska Standard Time (i.e. A.S.T. = U.T. - 10 hours); A.R. and δ are the right ascension and the declination of the radiant point, and *A* and θ are the azimuth (counted west from south) and the true-zenith distance, respectively.

TABLE I

Photograph	A.S.T.	A.R.	δ	<i>A</i>	θ
<i>a</i>	20 ^h 10 ^m	19 ^h 56 ^m	+53.50°	21.27°	11.92
<i>b</i>	21	20 06	52.50	17.3	12.93
<i>c</i>	31	17	51.67	14.10	13.47

Fig. 2 is a vertical projection of the sky on the horizontal; the positions of

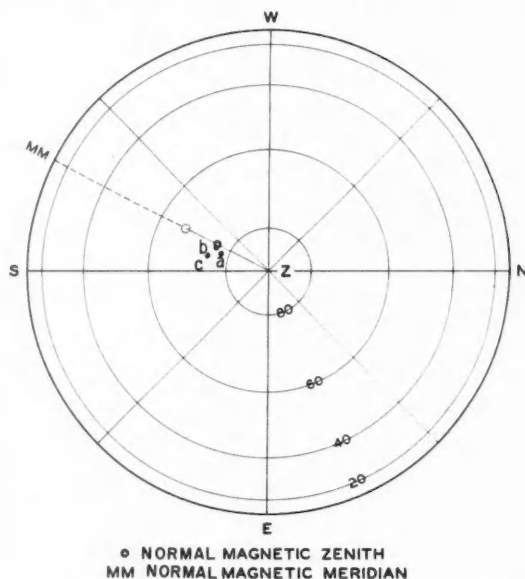


FIG. 2. Changes in the position of the radiant point during the auroral disturbance of September 22, 1957, at College, Alaska. The dots mark the position of the radiant point at times indicated on Fig. 1. The solid circle is the mean, "quiet", magnetic zenith. The dotted circle is the area within which the magnetic zenith was located when photographs *a*, *b*, and *c* of Fig. 1 were taken.

PLATE I

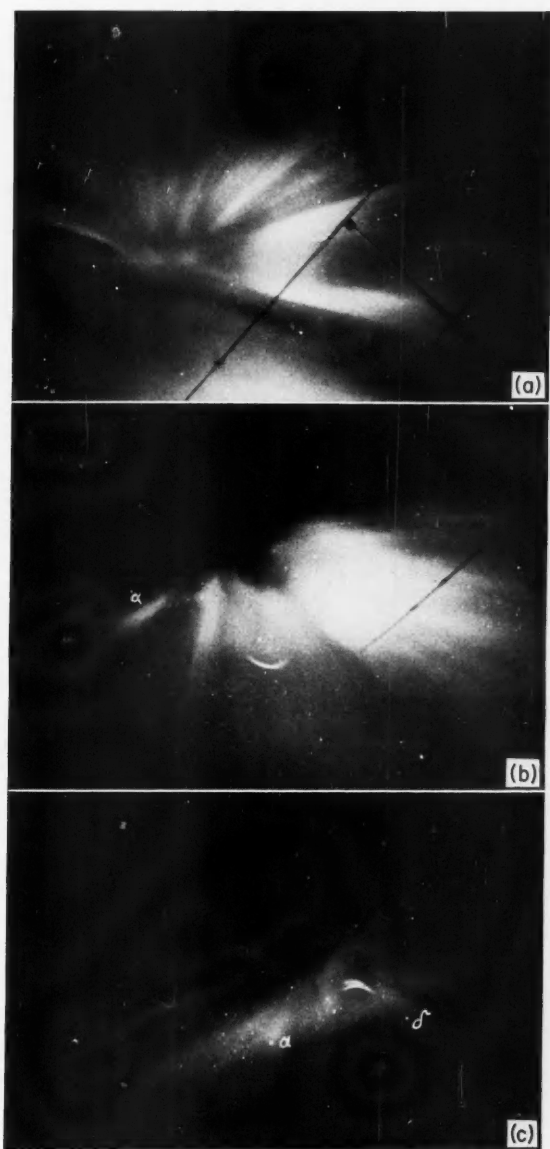
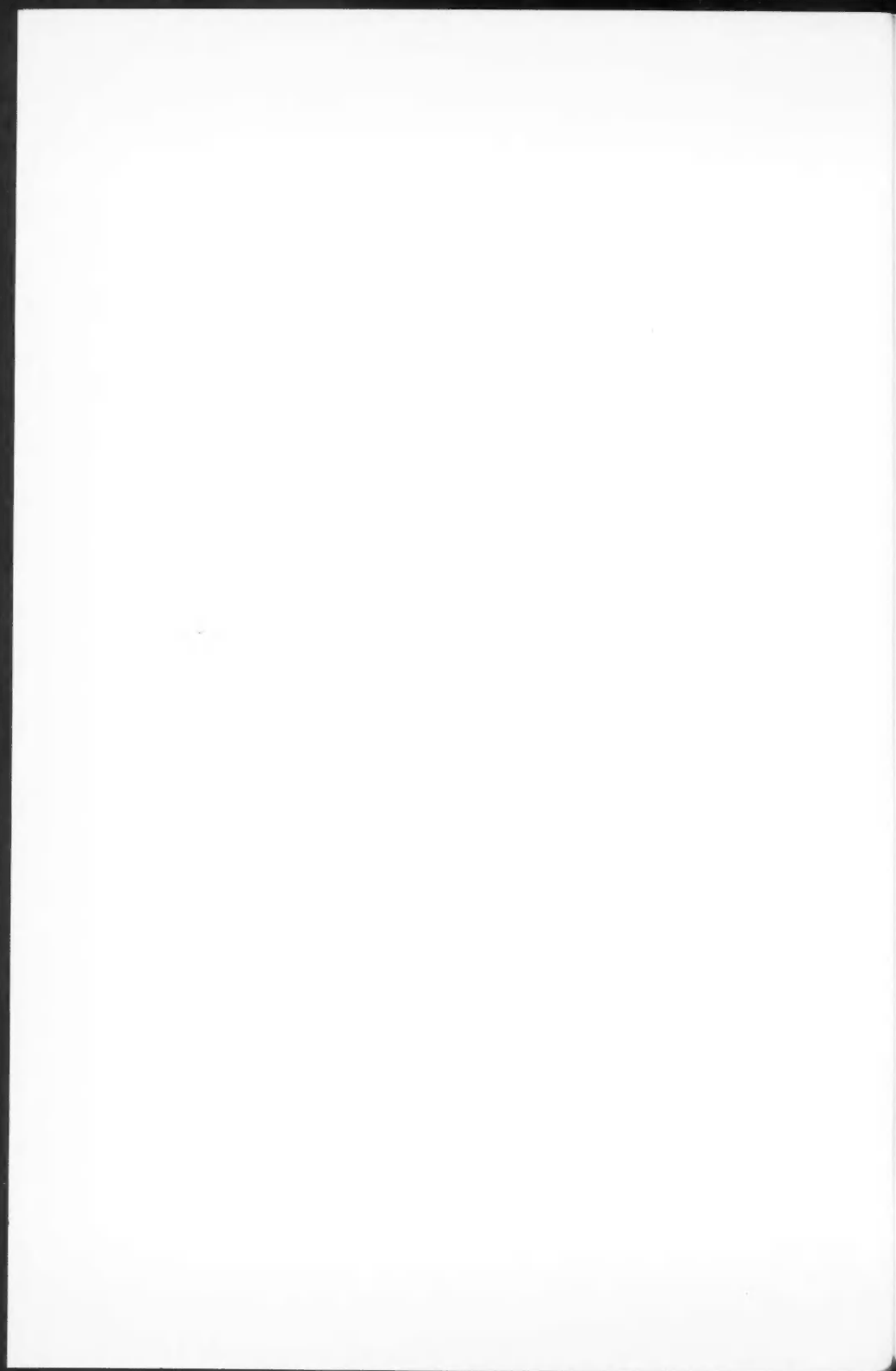


FIG. 1. Photographs of the corona taken during the auroral disturbance of September 22, 1957, at College, Alaska. Star field is in Cepheus and α and δ are α and δ Cephei. (Exposure, 8 seconds; Tri-X film.)

a, taken at 20^h 10^m A.S.T.; *b*, taken at 20^h 20^m A.S.T.; *c*, taken at 20^h 31^m A.S.T.



the radiant point are marked by black dots; the thick circle is the mean, or "quiet", position of the magnetic zenith under undisturbed conditions. The mean, undisturbed, direction of the magnetic meridian is defined by the line MM .

3. GEOMAGNETIC VARIATIONS

An intense magnetic storm accompanied the auroral display, and the variations of the magnetic elements, i.e. the field components H and Z and the declination D , during the display are given in Fig. 3. The azimuth (W. from S.) of the magnetic meridian is equal to D , and the inclination, or true-zenith

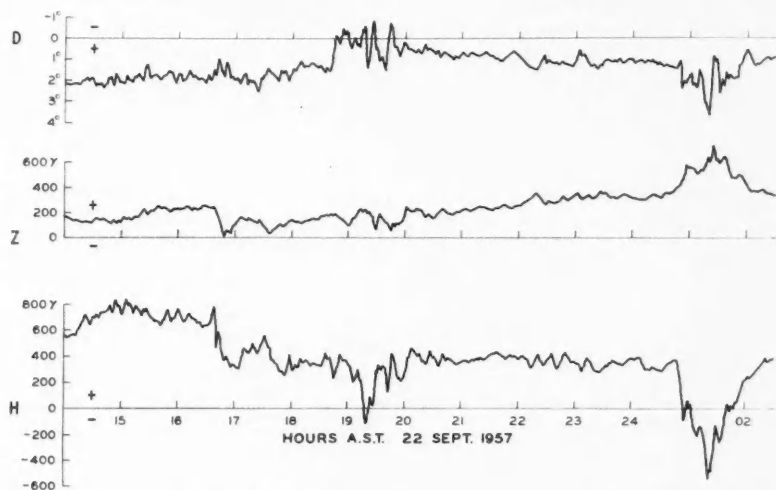


FIG. 3. Variations of the magnetic elements on September 22, 1957, at College, Alaska. The mean, or "quiet", values of H , Z , and D are $H_0 = 1178.7$ gammas, $Z_0 = 5488.3$ gammas, $D_0 = 27^\circ 11.4'$; and $\theta_0 = \arctan H_0/Z_0 = 12^\circ 07.8'$.

(Courtesy of U.S. Coast and Geodetic Survey, College, Alaska.)

distance, θ , has been derived from the relation, $\tan \theta = H/Z$. Values of (a) the azimuth of the magnetic meridian, (b) the true-zenith distance of the magnetic zenith, and (c) the azimuth and zenith distance of the auroral zenith are given in Table II together with the angular distance between magnetic and auroral zeniths. According to the officials of the U.S. Coast and Geodetic Survey Station the response of their variometers may be considered to all practical purposes interesting us, here, as being instantaneous, since their oscillation periods are of the order of 1.5 seconds for D and H , and of the order of 4.5 seconds for Z . On Fig. 2 the dotted circle is the area within which the magnetic zenith was located in the interval from $20^h 10^m$ to $20^h 31^m$.

4. DISCUSSION

From the preceding sections it is obvious that the position and motion of the radiant point are independent of the position and motion of the magnetic

TABLE II

Photograph	A.S.T.	Auroral zenith (radiant point)		Magnetic zenith		Distance between zeniths
		<i>A</i>	θ	<i>A</i>	θ	
<i>a</i>	20 ^h 10 ^m	21.27°	11.92°	27.87°	20.50°	8.8°
<i>b</i>	21	17.3	12.93	27.46	19.20	6.8
<i>c</i>	31	14.10	13.47	27.92	19.73	7.3
Under normal or "quiet" conditions				27.19	12.13	

zenith when seen from the surface of the earth. At 20^h 10^m on September 22, 1957, the azimuth of the radiant point was less than that of the normal or "quiet" magnetic meridian and less than the azimuth of the magnetic zenith at that moment. The azimuth regressed considerably within the next 20 minutes, attaining at 20^h 31^m a value which was almost half the azimuth of the "quiet" magnetic meridian. As for the zenith distance of the radiant point, this steadily increased from 20^h 10^m to 20^h 31^m, and in this interval the radiant point was slowly but steadily swinging downwards; however, the zenith distance did not diverge considerably from that of the normal, or "quiet", magnetic zenith.

On the other hand, the magnetic zenith, the position of which was derived from the well-known relation giving the inclination as a function of the horizontal and vertical components of the field, $\tan \theta = H/Z$, presented an entirely different behavior; the azimuth was slightly larger than normal and fluctuated in this interval of time by about half a degree. As for its true-zenith distance, this was about seven degrees and fluctuated up and down by about half a degree either way as seen on Fig. 4. The dotted circle on Fig. 2 limits the area within which the magnetic zenith was moving from 20^h 10^m to 20^h 31^m.

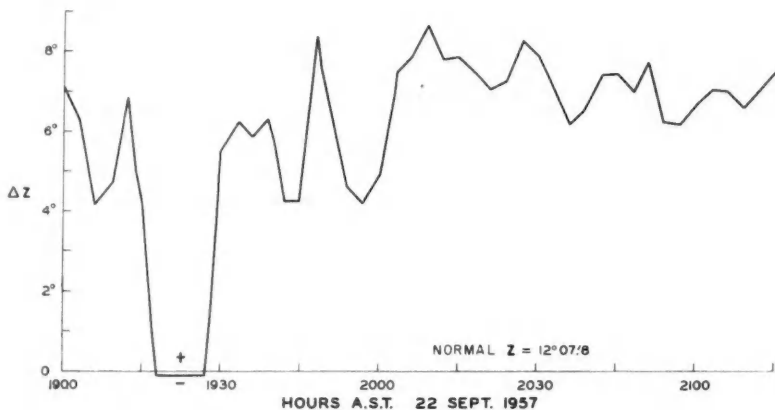


FIG. 4. Variations of true-zenith distance of the magnetic zenith during the auroral disturbance of September 22, 1957, at College, Alaska.
(Courtesy of U.S. Coast and Geodetic Survey, College, Alaska.)

Similar motion of the radiant point of the corona has been observed in the past by Norwegian observers. Their observations were (a) visual and (b) photographic. The visual observations, although quantitatively unreliable, are fairly illustrative of the importance of the motion. Various theodolite pointings of the radiant point made from 1839 to 1914, a summary of which has been published by Vegard and Krogness (1920), present the radiant point as being, in Norway, at a greater true-zenith distance than the magnetic zenith. The use of a theodolite permits the measurement of angles but the use of the telescope of the theodolite introduces a grave source of error, since the radiant point has no objective existence and probably may move even while the instrument is being handled. The conclusion drawn by Fritz (1881) that the radiant point appears to be always at a greater distance from the zenith than the magnetic zenith is based on visual observations—probably the theodolite observations—and appears to be hurried, too general, and anyway limited to Norway's geomagnetic and "auroral" latitudes. The only reliable means of measuring these motions is photography, and it was Størmer (1926, 1938) who initiated these measurements. It is to be regretted that he does not give, with the positions of the radiant point computed from his photographs, the values of the magnetic elements or the positions of the magnetic zenith. Nevertheless, his observations of the displacements of the radiant point during the disturbances of March 22–23, 1920, and of January 25–26, 1938, do give a vivid picture of the mobility of the radiant point itself, a picture which is unfortunately incomplete. As to the older conclusions drawn by Celsius and Hjorter, who mention that the radiant point and the inclination change simultaneously and parallel, these are rough and far too general estimates, possibly not uninfluenced by the philosophy of their century, which had a tendency to find harmony and uniformity in nature.

Reverting to Størmer's measurements, it is interesting to note that he finds displacements which are of the same order as those noted on our photographs during the disturbance of September 22, 1957. Thus, in the table given by Harang (1951) we perceive that between 22^h 11^m and 22^h 41^m of January 25–26, 1938, i.e. in a 20-minute interval, he finds displacements of 1.4°, which are of the order of those measured on our photographs of Fig. 1.

In the light of theory the displacements of the radiant point which present a certain independence of the behavior of the magnetic field, at least at ground level, should be interpreted as being due to the specific geometry and composite dynamics of the lines of force of the magnetic and electric fields during an auroral disturbance. Harang (1951) suggests that the lowering of the radiant point by 0.5–1.0° in relation to the inclination when viewed from ground level indicates that the "direction of the field is slightly changed towards south with increasing heights above the earth's surface". The main criticism to this remark is that it specifically defines the motion as placing the radiant point always at a greater zenith distance than the magnetic zenith, which is entirely inaccurate as a general statement. Vegard and Krogness (1920) consider that the lowering of the magnetic zenith in 200 km. due to the curvature of the line of force is only 0.1°, which is considerably less than what we observe. Our

observations strongly belie the general belief held by the Norwegians that the radiant point is always to be found south of the magnetic zenith, although of course it may occasionally move as far downwards as that. Our observations suggest not only curvature of the lines of force, the convexity being turned to the south, but a possible torque and a variation with time of both curvature and torque, both being related to the motion of the agents occasioning auroral and magnetic disturbances. Apparently the lines of force meet the surface of the earth, or ground level, at angles which are different from the angle of penetration through the 80–120 km. auroral layer, the differences being perhaps greater in Alaska and less in Norway; in terms of the incoming-charged-particle theories, these angles may well be functions of the direction of the stream and of the geomagnetic latitude of the observer, as well as of his "auroral latitude" or his distance from the auroral pole, which would be the pole of the auroral zone. Local differences in the motions would be expected, and there is no doubt that this is a subject which is widely open to investigation.

REFERENCES

- FRITZ, H. 1881. *Das Polarlicht* (Brockhaus, Leipzig).
HARANG, L. 1951. *The aurorae* (John Wiley & Sons, Inc., New York), pp. 40–42.
STØRMER, C. 1926. Résultat des mesures photogrammétriques des aurores boréales observées dans le Norvège méridional de 1911 à 1922, *Geophys. Publ.*, Oslo, **4**, No. 7.
——— 1938a. *Nature*, **141**, 955.
——— 1938b. *Naturwiss.* **26**, 633.
——— 1938c. *Geophys. Publ.*, Oslo, **13**, No. 7, pp. 57–60.
VEGARD, L. and KROGNESS, O. 1920. The position in space of the aurora polaris, *Geophys. Publ.*, Oslo, **1**, No. 1.

THE RANDOM-WALK MODEL WITH AUTOCORRELATION OF FLOW THROUGH POROUS MEDIA¹

A. E. SCHEIDEGGER

ABSTRACT

In pursuit of the idea of applying statistical mechanics to the theory of flow through porous media, this paper reports an investigation of the implications of a random-walk model as opposed to random residence-time models. Although the random-walk model is physically not as satisfactory as other statistical models, it has the advantage of enabling one to introduce and to investigate easily the effect of autocorrelation between subsequent time steps. It is shown that, if autocorrelation exists, the mixing process in porous media is governed by a telegraph equation rather than by a diffusivity equation. Expressions for the constants occurring in the telegraph equation are deduced in terms of other dynamical variables.

1. INTRODUCTION

The introduction of statistical mechanics into the study of flow through porous media has met with considerable success in the investigation of the mutual displacement of miscible phases. Cases where miscible displacement is important include the intrusion of salt water into the fresh-water lens beneath oceanic islands, the displacement of oil by solvents in petroleum reservoirs, and the contamination of ground water resources by the disposal of wastes. Phenomena similar to those mentioned above also occur during the flow in packed towers; the latter have been intensively studied by chemical engineers.

The statistical models that have been used in connection with investigations into the above phenomena are based upon the assumption of a random distribution of velocities in each time step. This automatically leads to a Gaussian distribution for the probability $\psi(x, t)$ for any one particle to arrive at the co-ordinate x at the time t , simply in virtue of the central limit theorem of probability calculus. The Gaussian distribution, in turn, leads to a diffusivity equation for the mixing process within the medium. In a linear-displacement experiment, the solution of the diffusivity equation is an error function.

The displacement mechanism of miscible phases has been discussed in terms of the above theory, for example by Danckwerts (1953), the author (Scheidegger 1954), and Levenspiel and Smith (1957). The general shape of the predicted linear-displacement curve has been experimentally found, for example by Baum (1953) and von Rosenberg (1956). The linear-displacement solution in the form of an error function has theoretically also been obtained starting from different ideas (Taylor 1953; Offeringa and van der Poel 1954), assuming longitudinal diffusion in individual flow channels. However, dynamical conclusions based upon the last model do not seem to be supported by

¹Manuscript received January 10, 1958.

Contribution from the Research Laboratory, Imperial Oil Ltd., Calgary, Alberta. Paper presented orally at the 39th Annual Meeting of the American Geophysical Union in Washington, D.C., May, 1958.

experiments (Morse 1954). The various investigations have been summarized in the writer's book (Scheidegger 1957) to which the reader is referred for further details.

It seems, therefore, that it is well established that statistical methods are useful to describe the displacement mechanism of miscible phases in porous media. The physical process that causes the mixing at the contact front has been termed "dispersion". Although this process is in effect very similar in its manifestations to "diffusion", the name "dispersion" is preferable since it serves to distinguish it from molecular "diffusion" that may or may not occur within each single flow channel. "Dispersion" and "diffusion" are entirely unrelated in their physical causes: the former is a mechanical mixing process due to the geometrical interconnections of the flow channels, the latter depends on the kinetic properties of the fluid molecules.

In pursuit of the statistical treatment of the flow through porous media, we shall investigate in the present study the random-walk model with autocorrelation of flow through porous media.

The random-walk model is, in fact, in its general features somewhat less satisfactory than the assumption of a random distribution of velocities, since it makes specific assumptions requiring equal steps during equal small time intervals. However, it enables one to introduce and then to estimate with ease the effect of autocorrelation between subsequent steps. This has been neglected heretofore. If autocorrelation is taken into account, one ends up with a telegraph equation instead of with a diffusivity equation. In obtaining this equation, the kinematical argument is analogous to that proposed by Goldstein (1951) for turbulent diffusion. However, care should be taken not to draw the analogy between mixing in porous media and mixing in turbulent diffusion in bulk masses of fluid too far: the two processes differ, after all, in some fundamental aspects.

In the final section, an attempt is made to attribute some physical meaning to the constants occurring in the telegraph equation. This is done by discussing the "microdynamics", i.e. the fluid dynamics in each single flow channel. This enables one to make certain predictions with regard to the dependence of the constants of the telegraph equation on other dynamical variables.

2. THE RANDOM-WALK MODEL WITH NO AUTOCORRELATION

The most useful approach to the problem of flow through porous media is by the Lagrangian method. Lagrangian kinematics is characterized by the fact that the instantaneous position of any one particle $\mathbf{x}(t)$ as a function of time is considered as a fundamental variable. We introduce statistics by considering the progress of a particle through a porous medium as a random-walk process.

In what follows, we shall assume that the flow is homogeneous with mean velocity $\bar{\mathbf{v}}$; this is the case, for instance, in a linear flood in a long, packed pipe. Under these circumstances, it is useful to introduce a new co-ordinate system \mathbf{x}' in which the mean flow can be assumed as equal to zero; i.e. we have

$$(2.1) \quad \mathbf{x}' = \mathbf{x} - \bar{\mathbf{v}}t,$$

$$(2.2) \quad \bar{\mathbf{v}}' = 0.$$

Furthermore, all the discussion below will refer only to one co-ordinate x ; the extension to the three-dimensional case is obvious. If there is anisotropy involved, the co-ordinates must be chosen in the principal directions.

Now we assume that the flow of a fluid particle through the porous medium corresponds to a random-walk process. In order to investigate this, we split the time from 0 to t into n equal intervals τ such that

$$(2.3) \quad t = n\tau.$$

During each interval τ , the particle proceeds through the distance $\pm d'$, where the plus and the minus signs are both equally probable and the prime denotes that we are dealing with deviations from the mean flow only. One can now ask for the probability $\psi(n, \nu)$ that the particle reached the position $\nu d'$ after n steps. One has (von Mises 1945, p. 145):

$$(2.4) \quad \psi(n, y) = \binom{n}{y} \left(\frac{1}{2}\right)^n$$

with

$$(2.5) \quad y = \frac{1}{2}(n + \nu),$$

where ν must be an integer number of the series $-n, -n+2, \dots, n-2, n$.

If the number of steps n is very large, this approximates a Gauss distribution:

$$(2.6) \quad \psi(n, \nu) \cong (\frac{1}{2}n\pi)^{-1/2} \exp[-\nu^2/(2n)],$$

where again $\nu = -n, -n+2, -n+4, \dots, n-4, n-2, n$. This means that the intervals for which ψ applies are all of length $2d'$. If one wants to express ψ as a *density*, one must therefore divide by $2d'$, which yields

$$(2.7) \quad \psi(t, x') = (\frac{1}{2}n\pi 4d'^2)^{-1/2} \exp[-\nu^2/(2n)],$$

where $x' = \nu d'$, $t = n\tau$. Hence

$$(2.8) \quad \psi(t, x') = \{2(t/\tau)\pi d'^2\}^{-1/2} \exp\{-x'^2\tau/(2d'^2t)\}.$$

It is customary to introduce a quantity D :

$$(2.9) \quad D = \frac{1}{2}d'^2/\tau;$$

then

$$(2.10) \quad \psi(t, x) = (4Dt\pi)^{-1/2} \exp\{-x'^2/(4Dt)\}.$$

The variance $\overline{x'^2}$ comes out as a linear function of t

$$(2.11) \quad \overline{x'^2} = 2Dt.$$

Furthermore, the Gauss function is an elemental solution of the diffusivity equation

$$(2.12) \quad \partial\psi/\partial t = D \partial^2\psi/\partial x'^2,$$

which describes the progress of the particles through the porous medium. It may be observed that this result is identical with that obtained in other statistical models of flow through porous media.

3. THE LAGRANGIAN CORRELATION FUNCTION

It can be argued that the above theory is somewhat of an oversimplification. It is well known (from the statistical theory of turbulence; cf., e.g., Pai 1957) that statistical Lagrangian kinematics of fluids can be carried well beyond the point attained above. Thus, the random-walk theory can be extended by assuming that there is a correlation between the directions that a particle possesses at time t and at time $t + \tau$.

In order to take care of this case, one introduces the Lagrangian correlation coefficient $R(\tau)$ defined as follows (using again a co-ordinate system where $\bar{v}' = 0$):

$$(3.1) \quad R(\tau) = \overline{v'(t)v'(t+\tau)}/\bar{v'^2}.$$

The average square of the displacement is then

$$(3.2) \quad \left\{ \begin{aligned} \bar{x'^2} &= \overline{\left[\int_0^t v'(\tau) d\tau \right]^2} = \overline{\int_0^t \int_0^t v'(\tau_1) v'(\tau_2) d\tau_1 d\tau_2} \\ &= \bar{v'^2} \int_0^t \int_0^t R(\tau_1 - \tau_2) d\tau_1 d\tau_2. \end{aligned} \right.$$

This can be further simplified to yield

$$(3.3) \quad \bar{x'^2} = 2\bar{v'^2} \int_0^t (t-\tau) R(\tau) d\tau,$$

which is a relation that was first found by Kampé de Fériet (1939) and is very useful in the investigation of limit cases. Introducing the autocorrelation time L_t

$$(3.4) \quad L_t = \int_0^\infty R(\tau) d\tau,$$

one can, for instance, investigate the case

$$(3.5) \quad t \gg L_t.$$

In this case Eq. (3.3) becomes

$$(3.6) \quad \bar{x'^2} = 2\bar{v'^2} L_t t - 2\bar{v'^2} \int_0^\infty \tau R(\tau) d\tau.$$

In this, the last term is a constant which can be neglected for large t ; hence

$$(3.7) \quad \bar{x'^2} = 2\bar{v'^2} L_t t.$$

This is identical to the relation (2.10) with

$$(3.8) \quad D = \bar{v'^2} L_t,$$

which shows that the earlier simple model, in which the autocorrelation was neglected entirely, comes out from the more complete theory for large t .

This, in fact, is how it should be, since the autocorrelation must be insignificant if time intervals that are long compared with it are considered.

In the opposite limit case, viz. when t is very short, one has of course

$$(3.9) \quad \overline{x'^2}(t) = \overline{v'^2} t^2,$$

which simply expresses the fact that, for extremely short time intervals, the autocorrelation has the effect that there is no random process at all, but that every particle progresses for the short time interval considered with the velocity which it possesses. The time limit λ for which (3.9) applies can be obtained by investigating the time interval for which $R(t)$ does not significantly differ from 1. One has

$$(3.10) \quad R(t) = 1 - \frac{\lambda^2}{2} \frac{1}{\overline{v'^2}} \left(\frac{dv'}{dt} \right)^2,$$

which yields the condition

$$(3.11) \quad \frac{\lambda}{2} \frac{1}{\overline{v'^2}} \left(\frac{dv'}{dt} \right)^2 \ll 1,$$

or

$$(3.12) \quad \frac{1}{\lambda^2} \gg \frac{1}{2\overline{v'^2}} \left(\frac{dv'}{dt} \right)^2 = \frac{1}{2} \frac{d^2 R(0)}{dt^2}.$$

In the above analysis, the quantities D , $\overline{v'^2}$, L_t , λ etc. have been taken as constants, which they are indeed in homogeneous flow. However, it must be expected that these quantities depend on the mean flow velocity and thus will change when the pressure drop is changed. The determination of this change is one of the chief problems in trying to elucidate the mechanics of miscible displacement.

One would assume that the correlation function $R(t)$ depends on the pressure gradient, the geometry of the porous medium, etc. In discussing a statistical model, it is preferable to introduce as few parameters as possible, and hence one would assume the following representative correlation function

$$(3.13) \quad R(t) = \exp(-|t|/A).$$

This is of the proper shape ($R = 1$ for $t = 0$, $R = 0$ for $t = \infty$) and introduces only one parameter A . One then obtains

$$(3.14) \quad L_t = A,$$

$$(3.15) \quad \lambda = \sqrt{2}A.$$

4. RANDOM WALK WITH AUTOCORRELATION

In order to proceed from the correlation function to an actual distribution function corresponding to (2.10), one has to make the analogous transition from the random-walk problem to a continuous problem as has been done in connection with Eq. (2.10). This question has been analyzed by Goldstein (1951) in relation to the kinematics of turbulent flow. We shall modify it

here to make it applicable to the flow through porous media and also extend it so that the connection with the Lagrangian correlation function will be shown.

In order to trace the flow of a particle through a porous medium, we follow the treatment of the random walk of "a drunkard with some memory". In order to prevent the argument from becoming too involved, we consider the one-dimensional case and transform into a system (x') where the mean velocity ($\overline{v'}$) is zero. The extension of this to three dimensions is obvious.

We again split the time from 0 to t into small intervals τ such that

$$(4.1) \quad n\tau = t.$$

Since we are considering the case of a drunkard whose absolute velocity $|v'|$ stays constant, he will proceed by the distance $d = \pm v'\tau$ during each time step; the only thing that may change is the sign of the motion. After the elapse of the time $t = 2\tau$ there are four different possibilities: if the drunkard moved to the right (+ direction) he may go on in this direction or reverse it; and similarly, if he moved to the left (- direction) he may go on or turn back. The four probabilities are p_{++} , p_{+-} , p_{-+} , p_{--} . One has:

$$(4.2) \quad p_{++} + p_{+-} = 1, \quad p_{-+} + p_{--} = 1.$$

Furthermore, if the case is isotropic, one has

$$(4.3) \quad p_{++} = p_{--}, \quad p_{+-} = p_{-+}.$$

Because of the "memory", however, one has

$$(4.4) \quad p_{++} - p_{+-} = c > 0,$$

where c is a measure of the correlation. (It is assumed that there is no direct correlation between non-adjointing steps; i.e. the drunkard's memory does not last to the step before the last.)

One can calculate the Lagrangian correlation function for the above case. At time t , assume that the velocity is $+d/\tau$:

$$(4.5) \quad v'(t) = +d/\tau;$$

then at $t+\tau$:

$$(4.6) \quad \overline{v'(t+\tau)} = p_{++}\frac{d}{\tau} - p_{+-}\frac{d}{\tau} = c\frac{d}{\tau}.$$

Similarly:

$$(4.7) \quad \overline{v'(t+2\tau)} = c\frac{d}{\tau}(p_{++} - p_{+-}),$$

and hence

$$(4.8) \quad \overline{v'(t+n\tau)} = c^n \frac{d}{\tau}.$$

Therefore, the correlation function is:

$$(4.9) \quad R(n\tau) = \overline{\{v'(t)v'(t+n\tau)\}}/\overline{v'^2(t)} = c^n.$$

Denoting the probability that the drunkard has arrived at vd after n time steps by $\psi(n\tau, v)$, one has the following continuity conditions:

$$(4.10) \quad \psi([n+1]\tau, v) = \alpha(n+1, v) + \beta(n+1, v),$$

$$(4.11) \quad \psi([n+1]\tau, v) = \alpha(n+2, v+1) + \beta(n+2, v-1),$$

where $\alpha(n, v)$ denotes the probability that the drunkard arrived from the left at position vd at the end of time-step number n . Similarly, β denotes the probability that he arrived from the right. Then, the correlation between subsequent time steps yields:

$$(4.12) \quad \alpha(n+1, v) = p_{++}\alpha(n, v-1) + p_{+-}\beta(n, v-1),$$

$$(4.13) \quad \beta(n+1, v) = p_{--}\beta(n, v+1) + p_{-+}\alpha(n, v+1).$$

From the set of equations (4.10)–(4.13), the α and β can be eliminated, and one ends up with

$$(4.14) \quad \psi([n+1]\tau, v) = p_{++}[\psi(n\tau, v-1) + \psi(n\tau, v+1)] - c\psi([n-1]\tau, v).$$

Taking the limit with $(d/\tau)^2 \rightarrow \bar{v}^2$, $(1-c)/\tau \rightarrow 1/A$, $d \rightarrow 0$, $\tau \rightarrow 0$, $n\tau \rightarrow t$, $n \rightarrow \infty$, one obtains (Goldstein 1951):

$$(4.15) \quad \frac{\partial^2 \psi}{\partial t^2} + \frac{1}{A} \frac{\partial \psi}{\partial t} = \bar{v}^2 \frac{\partial^2 \psi}{\partial x^2}.$$

Again, one can express the quantity A in terms of the Lagrangian correlation function. One has:

$$(4.16) \quad \left\{ \begin{aligned} \frac{1}{A} &= \lim_{\tau \rightarrow 0} \frac{1-c}{\tau} = \lim_{\tau \rightarrow 0} \frac{1-R(n\tau)^{1/n}}{\tau} = \lim_{\tau \rightarrow 0} \frac{1-R(t)^{1/n}}{\tau}, \\ &= \lim_{t/n \rightarrow 0} \frac{1-R(t)^{1/n}}{t/n} = t \lim_{n \rightarrow \infty} n(1-R(t)^{1/n}). \end{aligned} \right.$$

Using a well-known (cf., e.g., Prange 1943, p. 154) relation for the natural logarithm, this yields

$$(4.17) \quad 1/A = -t \log R(t).$$

Hence

$$(4.18) \quad R(t) = \exp(-t/A).$$

This shows that the telegraph equation proposed by Goldstein represents motion through a porous medium if the correlation function has the particular form given above.

5. MICRODYNAMICS

The next step is to investigate the meaning of the constants $D = \bar{A}\bar{v}^2$ and A that have been introduced with the telegraph equation.

We therefore specify the random-walk model (with autocorrelation) of the porous medium somewhat more precisely. The porous medium shall consist of small capillaries of length d (projected onto the x direction).

In the laminar flow domain, the displacement ξ_t during the time step τ is given by (the summation convention being applied)

$$(5.1) \quad \xi_t = \tau \frac{1}{\mu} b_{ik} \frac{\partial p}{\partial x_k}.$$

If we are interested only in one direction (say the x direction) the displacement becomes

$$(5.2) \quad \xi = \tau \frac{1}{\mu} b \cos^2 \theta \text{ grad } p,$$

where the quantity $b \cos^2 \theta$ depends on the flow channel under consideration and $\text{grad } p$ is the one-dimensional pressure gradient. If we are to transform everything into a co-ordinate system where $v' = 0$, we have

$$(5.3) \quad \begin{aligned} \xi' &= \tau \frac{1}{\mu} (b \cos^2 \theta - \overline{b \cos^2 \theta}) \text{ grad } p, \\ &\equiv \tau \frac{1}{\mu} \beta \text{ grad } p. \end{aligned}$$

The quantity β depends only on the geometry of this flow channel:

$$(5.4) \quad \beta = (b \cos^2 \theta - \overline{b \cos^2 \theta}).$$

Since the random-walk model assumes that, during any one time step τ , the motion is $\pm d$, this implies

$$(5.5) \quad \frac{d}{\tau} = \pm \frac{1}{\mu} \beta \text{ grad } p.$$

The random-walk model, thus, is adequate if and only if the last relation is fulfilled.

We have now (from 2.9)

$$(5.6) \quad D = \frac{1}{2} \frac{d^2}{\tau} = \frac{1}{2\mu} \beta d \text{ grad } p,$$

which gives the connection between the macroscopic quantity D and the microscopic quantities d and β .

Similarly, one can calculate the Lagrangian correlation function for the model under consideration. One has obviously

$$(5.7) \quad R(t) = 1 \quad \text{for} \quad t < \frac{d}{(1/\mu)\beta \text{ grad } p},$$

$$(5.8) \quad R(t) = 0 \quad \text{for} \quad t > \frac{d}{(1/\mu)\beta \text{ grad } p}.$$

Hence

$$(5.9) \quad L_t = \int_0^\infty R(t) dt = \frac{d}{(1/\mu)\beta \text{ grad } p}.$$

This yields for A , in virtue of condition (3.14):

$$(5.10) \quad A = \frac{\mu d}{\beta \text{ grad } p}.$$

Since the quantities β and d depend on the porous medium, the random-walk model (with autocorrelation) makes the following measurable predictions:

$$(5.11) \quad D = \text{const.} \frac{1}{\mu} \text{grad } p,$$

$$(5.12) \quad A = \text{const.} \frac{\mu}{\text{grad } p}.$$

6. DISCUSSION

It remains to compare the random-walk model of flow through porous media with other statistical models.

From the outset, it may be said that the random-walk model has basically less appeal than random-velocity models, owing to the specific assumptions that have to be made regarding the dynamic occurrences in each time step. Nevertheless, the random-walk model enables one to estimate easily the effect of autocorrelation, which has been neglected heretofore. Accordingly, it is seen that the mixing process may be governed by a telegraph equation rather than by a diffusivity equation.

The basic weakness of the random-walk model (with autocorrelation) is particularly apparent during the discussion of the "microdynamics" in each flow channel. Here one gets caught in the network of specific assumptions and it is therefore not easy to ascribe a physically evident meaning to the constants occurring in the macroscopic telegraph equation. The expression that was obtained for the factor of dispersion D is less general than that yielded by other statistical theories, viz. no possibility of a "dynamic" dispersivity is obtained; the expression (5.11) corresponds only to the "geometrical" dispersivity (cf. Scheidegger (1957) for definition of these terms). Similarly, the discussion leading to the expression (5.12) for A is very crude, as the shapes of the correlation functions $R(t)$ in (5.7), (5.8), and (4.18) are only slightly similar.

The relation (3.14), leading ultimately to the expression (5.12) for A , is therefore, strictly speaking, not applicable. Nevertheless, confidence may be had in the qualitative content of the final expressions for A and D .

The main result, thus, is that *autocorrelation leads to a telegraph equation rather than to a diffusivity equation*. The final judgment of whether this autocorrelation is really important will eventually have to come from experiments.

ACKNOWLEDGMENT

The writer is indebted to the management of Imperial Oil Limited for permission to publish this paper. The congenial atmosphere of the Technical Service and Research Laboratory under the direction of Mr. J. W. Young has made the completion of this study possible.

REFERENCES

- BAUM, V. A. 1953. Izvest. Akad. Nauk S.S.S.R., Otdel. Tekh. Nauk, No. 9, 1317.
 DANCKWERTS, P. V. 1953. Chem. Eng. Sci. 2, 1.
 GOLDSTEIN, S. 1951. Quart. J. Mech. Appl. Math. 4, 129.
 KAMPÉ DE FÉRIET, J. 1939. Ann. soc. sci. Bruxelles, Sér. 1, 59, 145.

- LEVENSPIEL, O. and SMITH, W. K. 1957. Chem. Eng. Sci. **6**, 227.
- MORSE, R. A. 1954. J. Petrol. Technol. **6**, No. 12, 42.
- OFFERINGA, J. and VAN DER POEL, C. 1954. Trans Am. Inst. Mining Met. Engrs. **201**, 310.
- PAI, S. I. 1957. Viscous flow theory, Vol. II, Turbulent flow (D. van Nostrand Co., Inc., New York).
- PRANGE, G. 1943. Vorlesungen über Integral- und Differentialrechnung (J. Springer, Berlin).
- SCHEIDEGGER, A. E. 1954. J. Appl. Phys. **25**, 994.
- SCHEIDEGGER, A. E. 1957. The physics of flow through porous media (University of Toronto Press, Toronto, and Macmillan Co., New York).
- TAYLOR, G. I. 1953. Proc. Roy. Soc. (London), A, **219**, 186.
- VON MISES, R. 1945. Wahrscheinlichkeitsrechnung (M. S. Rosenberg, New York).
- VON ROSENBERG, D. V. 1956. J. Am. Inst. Chem. Engrs. **2**, 55.

ELECTRON BEAM FLUORESCENCE PROBE FOR MEASURING THE LOCAL GAS DENSITY IN A WIDE FIELD OF OBSERVATION¹

B. W. SCHUMACHER² AND E. O. GADAMER

ABSTRACT

An electron beam was fired across the field of observation of the UTIA low-density wind tunnel. Along its path gaseous fluorescence was excited and visible light emitted. The total light output per unit length of the electron beam can be assumed to be proportional to the density of the gas if suitable spectral lines are selected. A three-dimensional scan of the field would give the local density for each spot. Visual, photographic, and photometric observation is possible. Some photographs are presented along with approximate data for the light output in air. The spatial resolution of the fluorescence probe is also discussed.

1. INTRODUCTION

The problems encountered in aerodynamic measurements at low densities have induced many experimenters to try new techniques. X-ray and ultra-violet absorption were used for measuring densities (Winkler 1951; Evans 1957), but they are restricted to specific gases. The attenuation of electron beam probes was used for the same purpose (Schopper, Schumacher, and Knapp 1950; Schopper and Schumacher 1951; Venable and Kaplan 1955; Markevitch and Hurlbut 1957). Here spatial resolution and sensitivity are conflicting requirements except perhaps for the "high-vacuum" region where the dark-field method can be applied (Marton, Schubert, and Mielczarek 1956; Boersch 1937). Flow visualization was accomplished by afterglow due to "activated" gas atoms either produced by an electric discharge before entering the flow field (Kaplan 1932; Kunkel and Hurlbut 1957) or excited in the flow field itself by electron beams (Grün, Schopper, and Schumacher 1953, 1954; Grün 1954a). The presentation of the flow pattern is excellent; a numerical evaluation, however, is impossible. Electron shadowgraphs were also used for flow visualization (Schumacher 1953a; Grün, Schopper, and Schumacher 1953). In this case the usable depth of the field is very limited.

All the beam attenuation methods give integral values for the density taken over the path length. The differential values can never be regained. In the afterglow methods, the point of emission of the light one sees can never be exactly determined, since each point along a line of sight is emitting light. In addition, the degree of excitation of a volume element of the gas is never known exactly; hence no general relation between luminous intensity and gas density can be expected.

The new method described below was first suggested by Schumacher and Grün (1955) (Schumacher 1955). A specified degree of excitation is produced along the path of a concentrated beam of fast electrons and the light emitted

¹Manuscript received January 3, 1958.

Contribution from the Institute of Aerophysics, University of Toronto, and the Ontario Research Foundation, Toronto, Ontario.

²Senior Research Fellow, Ontario Research Foundation.

spontaneously by the gas molecules from short-lived excitation states is observed. The number of these molecules will depend upon the gas density only, provided energy and current in the electron beam are kept constant.

The results of a preliminary set of experiments are presented in the following paragraphs.

2. EXPERIMENTAL

A high-energy electron beam was generated in a high-vacuum electron gun, comprising a tungsten filament cathode, a negatively charged Wehnelt cylinder, a pointed anode, and a three-ring electrostatic lens. The gun was mounted vertically on top of the UTIA low-density wind tunnel. Its lower end, a tube of 1 in. diameter, 30 in. long, projected into the interior of the tunnel facing the test section. The electron beam was focused by the lens on a small open orifice at the lower end of the gun. Gas entering there was continuously pumped off. With a pressure up to 2 mm. Hg in front of the gun and an opening of 1 mm. diameter, 12 mm. long, the necessary vacuum of 5×10^{-4} mm. Hg in the gun was readily obtained. With modifications of the system a working pressure of several atmospheres could be tolerated. The design of such dynamic pressure stages was described elsewhere (Schumacher 1953*b*).

Below the orifice, the narrow electron beam passed through the low-density air flow of the wind tunnel. On passing through the test section it produced fluorescence of the gas molecules and its path could be seen as a fluorescent line with the naked eye. The light output from small sections of this line may be obtained from photographs. However, we did not calibrate the photographic plates, etc., and our photographs are only qualitative. In another experiment a photomultiplier tube and optical system were used. If arrangements were made for this device to scan over the entire length of the line, the light output at each point of the line could be measured and, since the total light output at a point is related to the air density at that point, a point-to-point measurement of the air density would be possible. So far, only a static calibration curve has been taken.

Fig. 1 shows the test section of the low-density wind tunnel. At the right is a Mach-4 nozzle which produces a horizontal air flow; above and below, respectively, are the lower end of the electron gun and a Faraday cup which receives the electron beam. The latter is connected to a microammeter which measures the beam current; in the middle is a movable flat plate used as an aerodynamic obstacle. It was placed in the central axis of the flow; its supporting rod lay behind that axis. The electron beam intersected the central axis of the flow.

Fig. 2 shows a photograph of the luminescent path of a beam of 60-kev. electrons. The current was $I_e = 200 \mu\text{a.}$, and the exposure 5 seconds at $f:4.5$ on Kodak Royal Ortho Film. The static pressure in the wind tunnel was 40 microns of mercury, the flow a Mach-4 flow of dry air.

The aerodynamic obstacle was placed in the flow somewhat upstream of the beam, giving rise to a detached shock front. In this picture the shock front

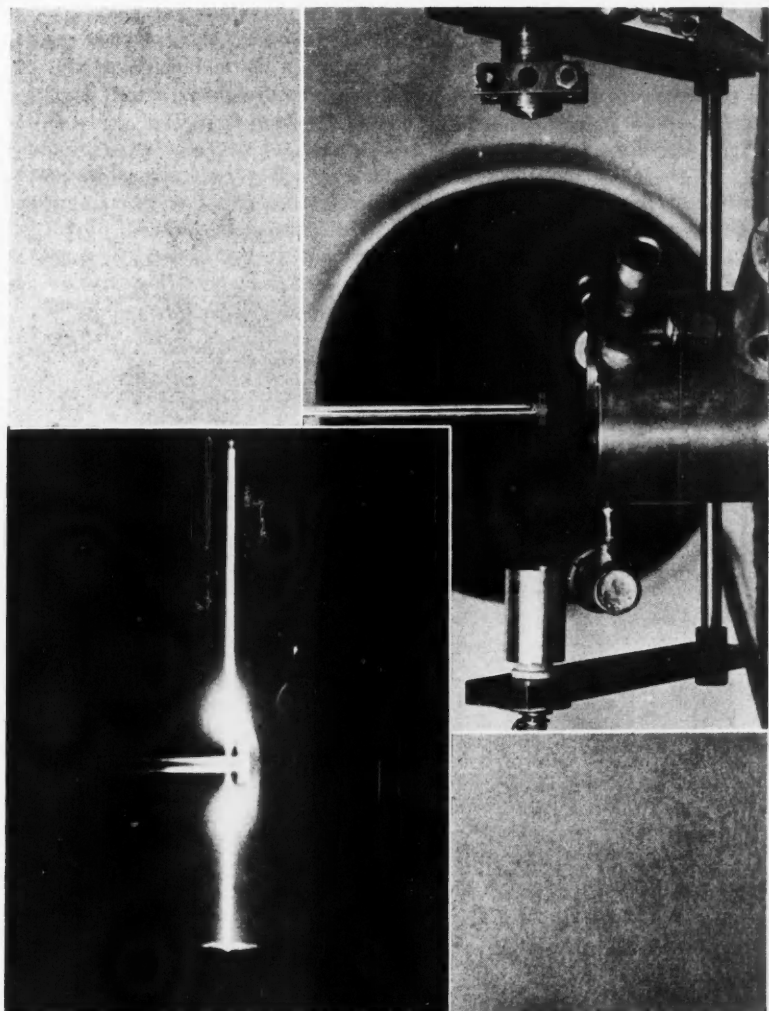


FIG. 1 (Top). Test section of UTIA low-density wind tunnel with Mach-4 nozzle (right), obstacle (flat plate normal to jet), exit end of the electron gun (top), and Faraday cage for the measurement of the beam current (bottom).

FIG. 2 (Bottom). Electron beam passing through the flow; secondary electrons from the Faraday cage are utilized to "illuminate" a larger volume.

is made visible by a discharge of secondary electrons emitted from the Faraday cup when a small negative voltage is applied to it. By this method the position of the electron beam relative to the flow pattern can be seen. From the photo-

graph it is evident that the beam remains *well confined along its path*. Furthermore, at regions of varying air density, the total light output is seen to be *varying as well*. (The variation of the luminescent width of the beam is partly real, but partly due to the photographic process which always shows isophotic lines. This point will be discussed later.)

Fig. 3, upper row, shows a series of similar photographs with the aerodynamic obstacle gradually moved downstream. The lower-row photographs were taken with the same positions of the obstacle except that no discharge from the Faraday cup was present. In Fig. 3*a* and *a'* the electron beam passed between the obstacle and the detached shock front. In Fig. 3*b* and *b'* it passed at a small distance downstream of the obstacle, and in *c* and *d* this distance was gradually increased. The regions of higher and lower air densities are clearly indicated. For instance, in *b*, *c*, and *d*, the low density in the wake of the obstacle

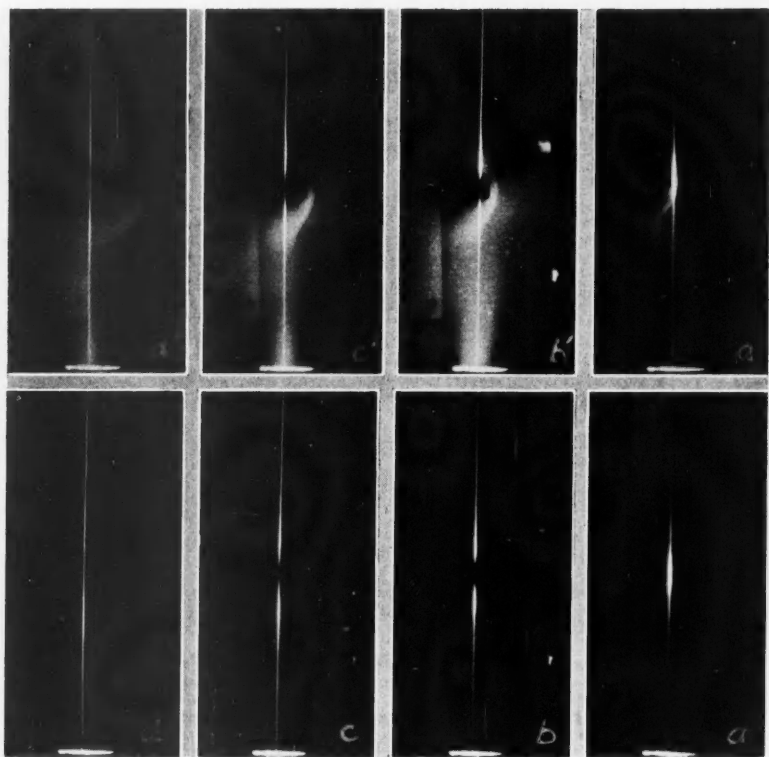


FIG. 3. Electron beam passing vertically (top to bottom) through a Mach-4 air flow with obstacle (flat plate normal to jet) which is shifted relative to the flow.

Top row: Secondary electrons from the Faraday cage are utilized to illuminate the whole flow region.

Bottom row: Same geometry as in top-row picture but no secondary electrons.

is well revealed. Particularly from *b* it is seen that the density immediately behind the obstacle is much smaller than that of the flow in other regions, as one would expect.

Fig. 4 presents a stepwise approach of the electron beam towards the detached shock front from the upstream direction. In Fig. 4*a* the beam passes through the flow about $\frac{1}{2}$ mm. upstream of the shock front without touching it. The higher air density in the free Mach-4 flow is clearly indicated. In *b*, the beam passes 1 mm. behind the apex, and in *d* it passes close to the obstacle. Good spatial resolution is observed. The spatial resolution of this method will be discussed in detail below.

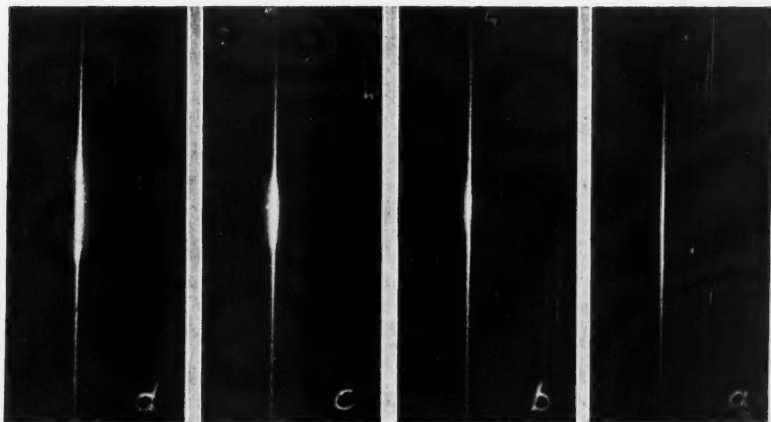


FIG. 4. Electron beam moving into a detached shock; in *a*, beam is 0.5 mm. from the apex of the shock.

In order to get some preliminary quantitative data on the light output as a function of air density and, hence, the sensitivity and limits for the application of the method, the light output from a small section of the beam was focused by an achromatic objective (glass) on a photomultiplier tube, type 1P21, which was cooled with liquid air. The aperture of the system was approximately 1:10. In a no-flow experiment the pressure of the air in the wind tunnel was varied between 15 and 90 microns of mercury, an electron beam of $E_0 = 60$ kev. and $I_e = 70 \mu\text{a.}$ was maintained, and the light of a fixed beam section $S = 7$ mm. long was observed with the photomultiplier. For the photocurrent I_p as a function of the gas density (air) a straight line through zero was obtained, as expected. Its equation was $I_p = 0.8 \times 10^5 \rho I_e$, with an accuracy of about $\pm 5\%$, ρ measured in g./cm.^3 . A more elaborate optical system which will allow scanning of the fluorescent line is under construction.

3. DISCUSSIONS

3.1 Light Output as a Function of Gas Density and Electron Energy in Air

For low gas densities we can assume that the number of interactions between

gas molecules and electrons, which are strictly statistical events, is proportional to the gas density and the number of electrons in the beam, i.e. the electron current.

A fraction of these interactions leads to the excitation of short-lived excitation states of the gas molecules and a subsequent emission of light.

The cross section for this latter process, which may be called fluorescence yield, depends upon the electron energy and the particular gas used. The fluorescence yield and the detection efficiency of the optical system used determine the limits for the application of the method. If we write

$$I_p = \gamma S \rho_{\text{air}} I_e$$

and the energy of the electrons is 60 kev. as above, then we obtain for the factor γ which gives the over-all detection efficiency

$$\gamma = 1.15 \times 10^5 \text{ cm.}^2 \text{g.}^{-1}.$$

The lowest level of air density at which we may perform measurements depends upon the lowest level of I_p at which we can measure, the path length S or resolution which is required, and possible increases in the efficiency factor.

$$\begin{aligned} \text{Let us assume } I_p (\text{min.}) &= 1 \times 10^{-9} \text{ amp.,} \\ I_e &= 200 \text{ } \mu\text{a.,} \\ S (\text{min.}) &= 1 \text{ cm.;} \end{aligned}$$

then our present system (γ as above) could be used up to

$$\rho_{\text{air}} (\text{min.}) = 4.4 \times 10^{-9} \text{ g./cm.}^3,$$

which corresponds to a pressure of 2.7×10^{-3} mm. Hg or, in the free atmosphere, an altitude of approximately 50 miles. Increasing the aperture of the system to $f:4.5$, which would still not obstruct the flow section, will yield a factor of 5 in γ . An optical system with a higher transmission for ultraviolet light may improve γ further.

Increasing the fluorescent yield by reducing the energy of the beam electrons will bring another improvement, as long as we can tolerate the increased spread of the beam due to scattering. This depends, of course, on the required spatial resolution. Unfortunately, the scattering increases more than the fluorescence yield when we lower the electron energies.

For the dependence of the light output on the electron energy we may use the data recently determined in most careful experiments by Grün (1957). The light output is strictly proportional to the specific energy loss per unit length of true path of the electrons. Fig. 5 shows the results obtained by Grün (*loc. cit.*). We see that reducing the electron energy from 60 kev. to 25 kev. will double the specific light output, going to 10 kev. will double it again. This will give another factor of 4 in γ .

The lower level of density up to which one could expect to make measurements with an improved system of $f:4.5$ and using 10 kev. electrons would, thus, be

$$\rho_{\text{air}} = 1.6 \times 10^{-10} \text{ g./cm.}^3$$

This corresponds to a pressure of 10^{-4} mm. Hg or an altitude of about 80 miles in the free atmosphere. The composition of the air at this altitude may, however, be different and another factor for the total fluorescence yield may apply, but perhaps partial densities of one component of the air could be obtained.

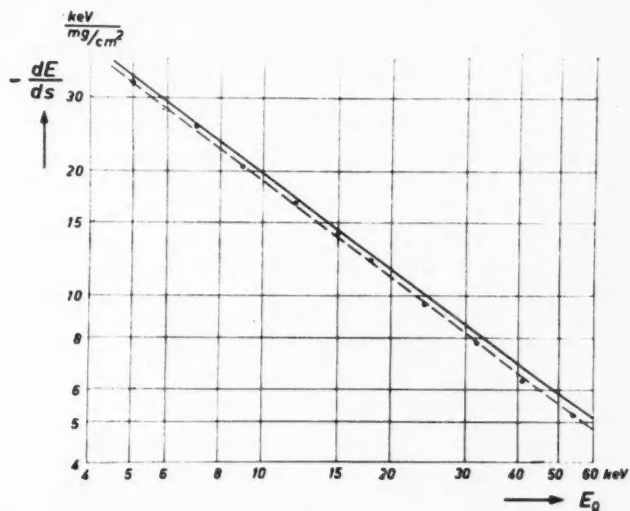


FIG. 5. Specific energy loss dE of electrons along the true path length ds as a function of energy E .

Solid line: Bethe's theory.

Points and dotted line: Grün's measurements of the fluorescence yield in air excited by electrons.

From Fig. 5 we can also get the average energy loss of the electrons in passing the observation field. For a path length of 18 cm. and $\rho = 0.6 \times 10^{-7}$ g./cm.³ (4×10^{-2} mm. Hg) we find $\Delta E_{av} \approx 9$ volts. This loss is negligible compared with the initial energy of 60 keV. Hence, for all practical purposes, the fluorescence yield does not change along the path length of 18 cm.

The beam passes, under the above conditions, through a layer of 3.7×10^{16} molecules/cm.². Since its cross section is only 8×10^{-3} cm.², the beam cylinder contains 3×10^{14} molecules. The charge in the beam of 200 μ a. is 1×10^5 electrons/cm. or 1.8×10^6 electrons in the beam of 18 cm. length. Later experiments must show whether this space charge has any unwanted effects.

3.2 Light Output in Other Gases

The use of the method with other gases than air of normal composition may be of interest.

Data are available from the work of Grün and co-workers (Grün, Schopper, and Schumacher 1954; Grün 1954b). The gross light output in pure nitrogen, and especially in argon-nitrogen mixtures, is much higher than in air. However,

long-lived excitation states are involved and, in a moving gas, part of the excitation energy is carried with the flow and produces an afterglow vane. The lifetime of various excitation states was explored by Grün, Schopper, and Schumacher (1954) by means of so-called spectrochronograms taken on excited-gas jets. Since this is most important in the application of fluorescence probes, we reproduce in Fig. 6 the spectrochronogram for an A/ N_2 mixture. We can see that, for instance, the N_2^+ bands and the A^+ lines are emitted within less than $1 \mu\text{sec.}$ or practically within the range of excitation. Not so the bands of the neutral N_2 , which are excited partly by metastable states of the A and energy transfer. These are emitted with maximum intensity about $0.6 \mu\text{sec.}$ later, and also show a slower decay of the light output. Similarly, Grün found in oxygen the O^+ bands emitted within the range of excitation.

In order to use the electron beam fluorescence probe in a gas showing afterglow we must select proper spectral lines by filters, e.g. the N_2^+ lines or O^+ . For the question of the excitation probabilities see the discussion by Grün and Schopper (Grün 1954b; Grün and Schopper 1954).

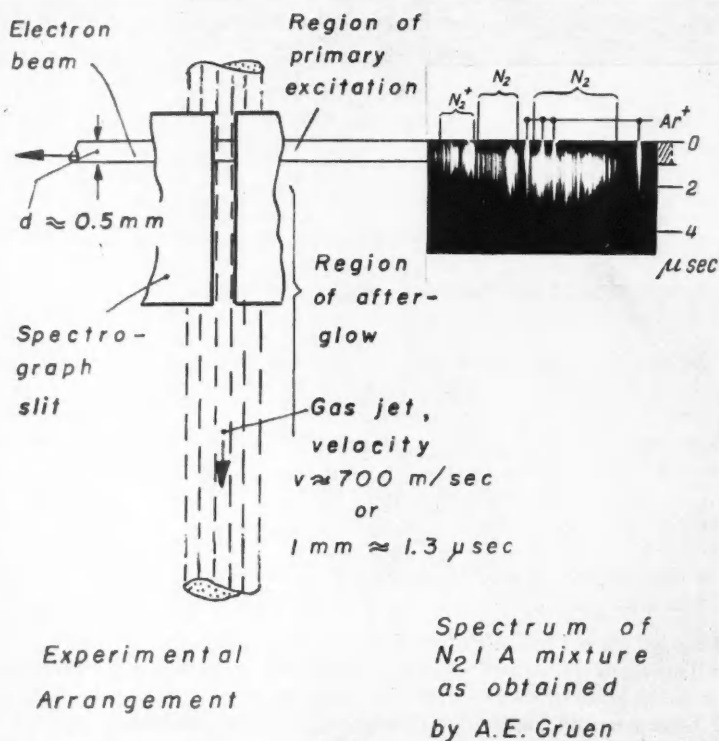


FIG. 6. Selecting short-lived excitation lines by means of a spectrochronogram.

In the case of air, most of the N_2 afterglow is quenched by the O_2 (reducing the gross light output to about 20%) and filters are not necessary.

3.3 The Spatial Resolution of the Fluorescence Probe

3.31 Beam Geometry

The electron beam is produced and focused in the high vacuum, as for example in an electron microscope. Typical beam characteristics for this instrument are (Borries 1948): $E = 60$ kev., $I = 100 \mu a.$, with a current density of 30000 amp./cm.^2 steradian, the diameter of the smallest spot being approximately 0.1 mm. and the aperture of the beam 0.008 radian.

It is of the greatest importance for the electron microscope (Borries 1948), as well as for the fluorescence probes, that a very high energy flux within a small angular aperture can be obtained with an electron beam. For the data given above, the flux amounts to $1.8 \times 10^9 \text{ watt/cm.}^2$ steradian. Thus, even with narrow and slim beams, we get enough energy flux through a volume element of the gas to produce visible fluorescence, in spite of the fact that only a minute fraction of the energy is transferred into light. $9 \text{ v.} \times 2 \times 10^{-4} \text{ amp.} = 1.8 \text{ mw.}$ is the energy absorbed, of which only a fraction is emitted as light. $60 \text{ kv.} \times 2 \times 10^{-4} \text{ amp.} = 12 \text{ w.}$ is the energy flux in the path of the electron beam.

In the first experiments described here, the beam had a diameter of slightly less than 1 mm. when entering the gas. A maximum aperture of 0.01 radian was determined by the geometry of the gun. Hence, over the distance of 180 mm. the beam should not more than triple its width. The pictures do not show any increase in the width of the beam. We do not know whether this is due to gas-focusing or whether the actual beam aperture was lower than the above value.

The diameter of the beam when entering the gas could easily be reduced to, say, 0.01 mm. However, this beam diameter does not determine the resolution of the probe, since the light emitted comes from a cylinder with a diameter larger than that of the beam.

3.32 Fluorescence Halo

In all the pictures presented, the width of the fluorescent line increases with increase in gas density, and this gives actually a first and convenient indication of the gas density. In order to learn more about this fluorescent halo surrounding the beam, we produced a series of isophotic lines of two of the pictures by copying the same negative with different exposure times on ultra-hard paper, Figs. 7 and 8. A quantitative evaluation is not possible since the sensitometric curves of the photographic materials were not determined. We get a good impression, however, of the relative luminous intensity through the region of fluorescence.

We can only attempt a *qualitative* description of the processes in the beam which cause this fluorescence distribution:

(a) The primary electrons (of 60 kev. energy) undergo to a certain extent so-called *inelastic collisions* with some of the gas molecules, which means energy of the electron is transferred to the internal system of the atom. The

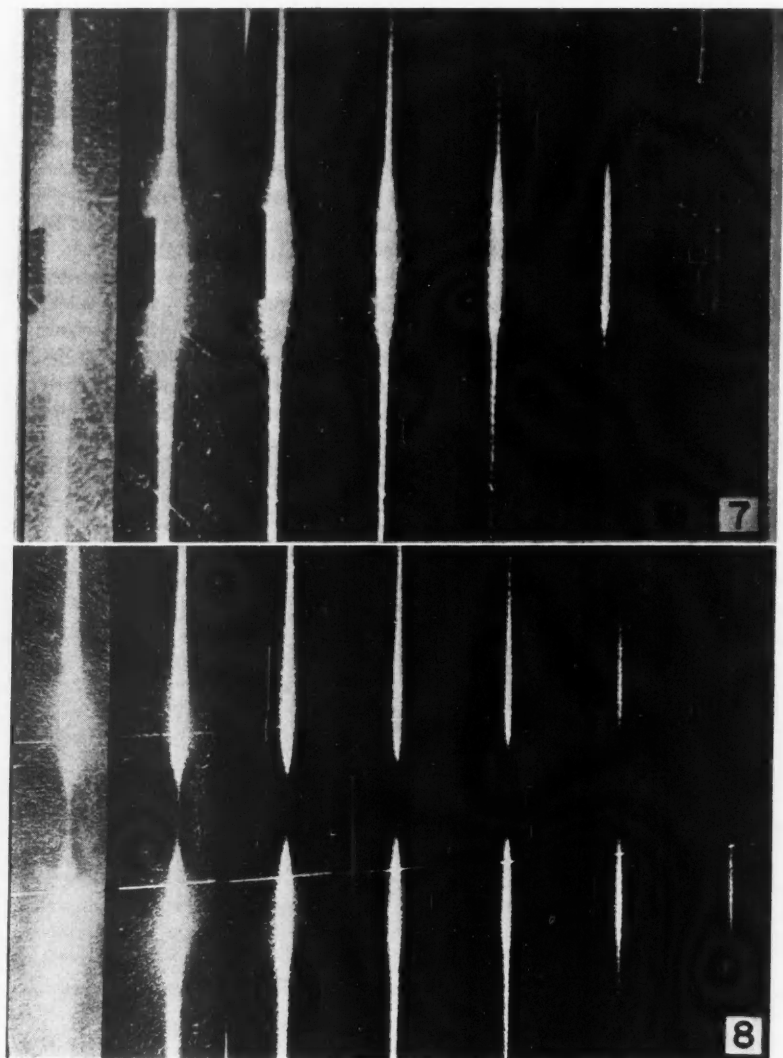


FIG. 7 (Top) and FIG. 8 (Bottom). The halo of the fluorescence at various exposure times; gas flow is from right to left. Electron beam comes from top. Exposure times are: 2.5, 5, 10, 20, 40, 80, 160 seconds.

average energy loss, 9 ev., shows that an electron undergoes hardly more than one such collision in passing the observation field. This keeps the primary beam

of electrons essentially unaltered, which is desired. On the other hand, sufficiently large currents to get enough fluorescent light are required. The deflection of an electron in a single collision is very small. Few quantitative data are available because of the difficulty in measuring the small deflection angles. The energy loss for electrons of 21.5 kev. in aluminum foils of 0.5×10^{-7} g./cm.² and the related scattering angle were measured by Marton (1956); we see from his Fig. 6 that the characteristic energy loss of 15 ev. is seldom associated with a deflection of more than 0.005 radian. That we don't see a beam spread due to scattering confirms this. For single elastic collisions, the deflection angle is similarly small.

The energy loss is quantized. For 35-kev. electrons discrete losses of 13.1 ± 0.3 ev. in nitrogen and 8.0 ± 0.3 ev. and 13.6 ± 0.5 ev. in oxygen were found by Möllenstedt (1952). In air the 13-ev. losses were much more common than the 8-ev. losses. In order to see quantum-mechanical effects on the scattering angle, a resolution below 10^{-3} radian would be necessary. We will not encounter such effects under our experimental conditions. The excitation of the atom is, as such, not essentially different from the excitation by light, since an electron passing the atom at some distance produces, at the atom, an electric field changing its direction 180° within a time dependent upon the speed of the electron (Fermi 1924). This excitation extends a short distance outside the primary beam.

(b) The excited atoms possess their usual *gas kinetic speed* of approximately 400 m./sec. at room temperature. Assuming that there are excitation states with a lifetime of 1 μ sec. present, the thermal movement could spread the fluorescence over a distance of 0.4 mm. This could make the width of the fluorescence region double that of the primary beam, which was 1 mm. However, the halo in the gas jet should be carried with the flow, or at least be off-center, if states of 1 μ sec. are involved. The pictures show no indication of that; hence, spread of the fluorescence due to thermal movement of the atoms is unlikely. Since the mean free path of the gas molecules outside the flow at 4×10^{-2} mm. Hg is approximately 1 mm., the emission of the light has taken place before the excited atom undergoes collisions with its neighbors.

(c) In cases where the excitation leads to ionization there are *secondary electrons* produced. The N_2^+ bands which we observe stem from an ionization process which leaves the ion in an excited state. Not much is known about the energy as a function of the direction for the secondary electrons. Any velocity component perpendicular to the primary beam axis can not be large for general reasons. Secondaries with high energy move under small angles to the beam axis; secondaries with low energy may move perpendicular to the beam axis but their energy is low and, hence, their range is short. They produce, however, fluorescence as well as the primary electrons and the excitation cross section may be much higher.

A change in gas density has two effects as far as the secondary electrons are concerned. First, the number of secondaries increases, and, second, their range is reduced. The first effect undoubtedly increases the intensity of the

halo, the second should increase the specific brightness. We do not know whether the isophotic lines, as shown in Figs. 7 and 8, can be explained on this basis.

It is essential, however, to remember that *as long as we are measuring the total light output we are measuring the gas density, since it simply depends upon the number of primary interactions between beam electrons and gas.* The secondaries transport some of the energy over a certain distance, the latter depending upon the density. This, however, is only of interest in connection with the spatial resolution.

(d) The width of the fluorescence region may increase by *quanta diffusion* or absorption and re-emission of the fluorescence light. Fluorescence may also be spread by X-rays or U.V. light produced in the primary beam. It will be much weaker than the one excited by secondary electrons, but such fluorescence has been observed (James 1955). We do not know whether this effect contributes to the observed width of the fluorescence line.

3.33 Resolution in the Direction of the Beam

The time, or distance, required to establish an equilibrium between the primary beam and its secondaries determines the spatial resolution in the direction of the beam axis. For instance, from a region of higher density an additional number of fast secondaries may enter a following region of lower density. Looking over Figs. 7 and 8, we can only say the resolution is certainly not greatly reduced by this effect. It seems to be in the same order of magnitude as the width of the beam.

From the pictures we can say that a resolution of 2 mm. is easily obtained. A higher resolution, perhaps up to 0.2 mm., may be achieved with smaller probe currents; note in Figs. 7 and 8 the improved resolution in the copy with 160-sec. exposure time. The interplay of sensitivity and resolution is still to be investigated in detail.

4. CONCLUSIONS

The electron beam fluorescence probe for measuring gas densities has been tested in a simple set of experiments. The light output in case of air is high enough to allow measurements under steady state conditions down to very low pressures; the estimated limit being about 1×10^{-4} mm. Hg. In the range of 10^{-2} mm. Hg it is likely applicable to short transients. The spatial resolution proved to be good; perpendicular to the electron beam, as well as in its direction, a resolution of about 2 mm. was obtained, which may still be improved. Hence, the probe can actually be used for scanning a large field of observation, as we had hoped when suggesting the method. It permits the measurement of the local density of the gas at each point of a field regardless of the speed of the flow. The flow is not disturbed by the probe.

ACKNOWLEDGMENTS

The authors are indebted to Dr. H. B. Speakman, Director, Ontario Research Foundation, who permitted the use of the electron gun instrumentation and

the interruption of another research project in favor of these experiments. The kind help and advice of Dr. A. E. R. Westman, Director of Research, Ontario Research Foundation, is also acknowledged.

We are indebted to Dr. G. N. Patterson, Director, Institute of Aerophysics, University of Toronto, for his immediate interest in the suggested new method and his continuous support during the experiments. The costs of the wind tunnel tests were borne by the Defence Research Board of Canada. Our thanks are due to Mr. Leroy Harris for his kind help in running the low-density wind tunnel.

REFERENCES

- BOERSCH, H. 1937. *Z. Physik*, **107**, 493.
BORRIES, B.V. 1948. *Optik*, **3**, 321, 389.
EVANS, R. A. 1957. *J. Appl. Phys.* **28**, 1005.
FERMI, E. 1924. *Z. Physik*, **29**, 315.
GRÜN, A. E. 1954a. *Z. Naturforsch.* **9a**, 833.
——— 1954b. *Z. Naturforsch.* **9a**, 55.
——— 1957. *Z. Naturforsch.* **12a**, 89.
GRÜN, A. E. and SCHOPPER, E. 1954. *Z. Naturforsch.* **9a**, 134.
GRÜN, A. E., SCHOPPER, E., and SCHUMACHER, B. 1953. *J. Appl. Phys.* **24**, 1527.
——— 1954. *Z. angew. Physik*, **6**, 198.
JAMES, J. F. 1955. *In* The airglow and the aurora (Pergamon Press, London and New York).
KAPLAN, J. 1952. *Phys. Rev.* **42**, 807.
KUNKEL, W. B. and HURLBUT, F. C. 1957. *J. Appl. Phys.* **28**, 827.
MARKEVITCH, B. V. and HURLBUT, F. C. 1957 (Feb.). *Inst. of Eng. Research Tech. Rept.* HE-150-142.
MARTON, L. 1956. Review "Experiments on low-energy electron scattering, and energy losses", *Revs. Modern Phys.* **14**, 172.
MARTON, L., SCHUBERT, D. C., and MIELCZAREK, S. R. 1956. *J. Appl. Phys.* **27**, 419.
MÖLLENSTEDT, G. 1952. *Z. Naturforsch.* **7a**, 465.
SCHOPPER, E. and SCHUMACHER, B. 1951. *Z. Naturforsch.* **6a**, 700.
SCHOPPER, E., SCHUMACHER, B., and KNAPP, D. 1950. *Physik. Verhandl.* **6**, 73.
SCHUMACHER, B. 1953a. *Ann. Physik* (6), **13**, 404.
——— 1953b. *Optik*, **10**, 116.
——— 1955. "Technical and research applications of corpuscle-beams", O.R.F. Memorandum, No. 5507 (Dept. of Chemistry) (Sept.).
SCHUMACHER, B. and GRÜN, A. E. 1955 (June). "Apparatur für die Messung der örtlichen Gasdichten innerhalb eines ausgedehnten Beobachtungsraumes", Deutsche Patentanmeldung, Sch. 18144 IX 142-1.
VENABLE, D. and KAPLAN, D. E. 1955. *J. Appl. Phys.* **26**, 539.
WINKLER, E. 1951. *J. Appl. Phys.* **22**, 201.

RADIATION FIELD OF AN ELLIPTIC LOOP ANTENNA WITH A CONSTANT CURRENT¹

S. C. LOH AND J. Y. WONG

ABSTRACT

Expressions for the radiation field are derived for a loop antenna of elliptical shape assuming a uniform current distribution. It is found that the radiation pattern in the plane of the loop depends on both the size and the shape of the antenna. However, for small loops, the radiation pattern is independent of the shape and is essentially circular. Some calculated patterns for loops of different sizes and shapes are presented in order to illustrate the derived results.

INTRODUCTION

The radiation of a circular loop antenna with an assumed uniform current distribution has been treated by Foster (1944). Because of symmetry, he was able to derive the far-field expressions directly from a single spherical component of the vector potential by considering the antenna from the point of view of two diametrically opposed infinitesimal dipoles. The total vector potential is obtained by integrating over the loop.

In this paper, expressions for the radiation field are derived for a loop antenna of elliptical shape. The current distribution on the loop conductor is assumed to be uniform. This assumption is quite valid when the loop is electrically small. However, when the loop becomes comparable in size to the wavelength, it may be necessary to introduce a number of feed points or phase shifters around the loop conductor in order to maintain a uniform current distribution. The vector potential is determined in terms of two rectangular components and by applying the appropriate rectangular-spherical coordinate transformation equations, the field is expressed in terms of a single spherical component. It is found that the radiation pattern in the plane of the loops depends on both the size and the shape of the antenna. However, for small loops, the radiation pattern is independent of the shape of the loop and is essentially circular; that is, the radiation pattern is omnidirectional. Some calculated radiation patterns for loops of different sizes and shapes are presented in order to illustrate the derived results.

DERIVATION OF THE RADIATION FIELD

Consider an elliptic loop antenna located with its center at the origin of the coordinate system shown in Fig. 1.

The loop is assumed to carry a uniform current of amplitude I_0 . The rationalized m.k.s. system of units is employed and the time variation $e^{i\omega t}$ is understood.

¹Manuscript received February 11, 1958.

Contribution from the Radio and Electrical Engineering Division, National Research Council, Ottawa, Canada.

Issued as N.R.C. No. 4746.

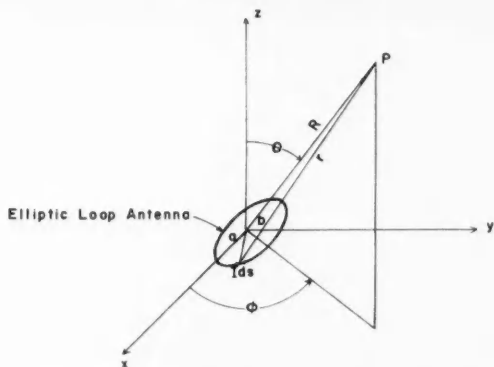


FIG. 1. Elliptic loop antenna placed in center of coordinate system.

The ellipse can be described in rectangular coordinates by the following parametric equations:

$$(1) \quad \begin{aligned} x &= a \cos u, \\ y &= b \sin u, \end{aligned} \quad (-\pi \leq u \leq \pi)$$

where a is the length of the semimajor axis and b is the length of the semiminor axis.

The field components of the loop antenna will be derived from the Hertzian vector potential Π (Kraus 1950), which for a constant current is given by

$$(2) \quad \Pi = \frac{1}{4\pi\epsilon\omega} \frac{e^{-ikR}}{R} \int I_0 e^{ikr\bar{p}} ds,$$

where ϵ is the permittivity of free space,

$k = 2\pi/\lambda$, where λ is the free space wavelength,

I_0 is the current in an elemental length of conductor ds , and \bar{p} is the unit vector in the direction of r .

In terms of the coordinate system in Fig. 1, the x component of Π at point P can be written as follows:

$$(3) \quad \Pi_x = \frac{1}{4\pi\epsilon\omega} \frac{e^{-ikR}}{R} \int_{u=-\pi}^{u=\pi} I_0 \exp[ik(x \cos \phi \sin \theta + y \sin \theta \sin \phi)] dx.$$

Utilizing eq. (1) and substituting in eq. (3) yields

$$(4) \quad \Pi_x = \frac{-I_0 a}{4\pi\epsilon\omega} \frac{e^{-ikR}}{R} \int_{-\pi}^{\pi} \exp[ik(a \cos u \cos \phi \sin \theta + b \sin u \sin \theta \sin \phi)] \sin u \, du.$$

If we introduce

$$(5) \quad \begin{aligned} \xi &= ka \sin \theta \sqrt{\cos^2 \phi + (b/a)^2 \sin^2 \phi}, \\ \gamma &= \tan^{-1}(b/a \cdot \tan \phi), \end{aligned}$$

eq. (4) can be reduced to the following expression:

$$(6) \quad \Pi_x = \frac{-I_0 a e^{-ikR}}{4\pi\epsilon i\omega R} \int_{-\pi}^{\pi} \exp[i\xi \cos(u-\gamma)] \sin u \, du.$$

We may easily obtain a series expansion for eq. (6) since $\exp[i\xi \cos(u-\gamma)]$ may be expanded in the well-known Fourier series with Bessel function coefficients. That is,

$$(7) \quad \exp[i\xi \cos(u-\gamma)] = \sum_{n=-\infty}^{\infty} i^n J_n(\xi) \exp[in(u-\gamma)],$$

$$(8) \quad \Pi_x = \frac{-I_0 a e^{-ikR}}{4\pi\epsilon i\omega R} \sum_{n=-\infty}^{\infty} i^n J_n(\xi) \int_{-\pi}^{\pi} \exp[in(u-\gamma)] \sin u \, du.$$

The integral may be evaluated readily by expressing $\sin u$ in terms of its exponential equivalent. We have then

$$(9) \quad \Pi_x = \frac{-I_0 a e^{-ikR}}{4\pi\epsilon i\omega R} \sum_{n=0}^{\infty} i^n (2-\delta_{0n}) J_n(\xi) \sin n\gamma \left[\frac{\sin(n-1)\pi}{n-1} - \frac{\sin(n+1)\pi}{n+1} \right],$$

where

$$\delta_{0n} = \begin{cases} 0 & \text{for } n \neq 0, \\ 1 & \text{for } n = 0. \end{cases}$$

Since the term in the bracket is always zero except when $n = 1$, eq. (9) reduces to

$$(10) \quad \Pi_x = \frac{-I_0 a e^{-ikR}}{2\epsilon\omega R} J_1(\xi) \sin \gamma.$$

The y component of the Hertzian vector potential can be determined in exactly the same manner as the Π_x component. Hence the expression for Π_y becomes

$$(11) \quad \Pi_y = \frac{I_0 b e^{-ikR}}{2\epsilon\omega R} J_1(\xi) \cos \gamma.$$

To determine the components of Π in spherical coordinates, we employ the following coordinate transformation equations (Schelkunoff 1943):

$$(12) \quad \begin{aligned} \Pi_\theta &= \Pi_x \cos \theta \cos \phi + \Pi_y \cos \theta \sin \phi, \\ \Pi_\phi &= -\Pi_x \sin \phi + \Pi_y \cos \phi. \end{aligned}$$

Substituting the two rectangular components of Π in eq. (12) yields the following results:

$$(13) \quad \begin{aligned} \Pi_\theta &= 0, \\ \Pi_\phi &= \frac{I_0 a e^{-ikR}}{2\epsilon\omega R} J_1(\xi) \sqrt{\sin^2 \gamma + (b/a)^2 \cos^2 \gamma}. \end{aligned}$$

The results given in eq. (13), namely that only a ϕ component of the vector potential exists, could have been inferred at the outset. Since the current in the loop has only a ϕ component, the other components of Π must necessarily be zero.

The electric field components can be derived from the Hertzian vector by applying the following vector relationship (Kraus 1950):

$$(14) \quad E = \omega^2 \mu \epsilon \Pi + \nabla(\nabla \cdot \Pi).$$

In eq. (14) μ is the permeability of free space. In terms of the ϕ component of Π we have

$$(15) \quad E_\phi = \omega^2 \mu \epsilon \Pi_\phi.$$

Therefore the three-dimensional radiation pattern of an elliptic loop antenna with an assumed uniform current distribution of amplitude I_0 is given by the following expression:

$$(16) \quad E_\phi = \frac{ka\eta I_0}{2} \frac{e^{-ikR}}{R} J_1(\xi) \sqrt{\sin^2 \gamma + (b/a)^2 \cos^2 \gamma},$$

where $\eta = \sqrt{\mu/\epsilon}$ = the intrinsic impedance of free space.

The radiation field of a circular loop antenna can be deduced immediately from the general expression by putting $b = a$, yielding the well-known result

$$(17) \quad E_\phi = \frac{ka\eta I_0}{2} \frac{e^{-ikR}}{R} J_1(ka \sin \theta).$$

For a circular loop, the radiation pattern in the plane of the loop is independent of the azimuthal angle ϕ , that is, the pattern is omnidirectional. For an elliptical loop, it can be seen from eq. (16) that the pattern depends on both the size and shape of the antenna and in general the pattern is nonuniform. However, for a small loop, it will be demonstrated that the radiation pattern is independent of shape and is circular.

For small arguments of the first-order Bessel function, the following approximate relation can be used:

$$(18) \quad J_1(x) = \frac{1}{2}x.$$

Consequently eq. (16) may be written as follows:

$$(19) \quad E_\phi = \frac{ka\eta I_0}{2} \frac{e^{-ikR}}{R} \frac{\xi}{2} \sqrt{\sin^2 \gamma + (b/a)^2 \cos^2 \gamma}.$$

Consider the following expression:

$$(20) \quad F = \xi \sqrt{\sin^2 \gamma + (b/a)^2 \cos^2 \gamma}.$$

Substituting in eq. (20) the values of ξ and γ from eq. (5), we have

$$(21) \quad F = \frac{ka \sin \theta \cos \phi}{\cos \gamma} \left(\frac{b \cos \gamma}{a \cos \phi} \right) = kb \sin \theta.$$

Consequently we see that the radiation pattern of a small elliptical loop in the plane $\theta = \frac{1}{2}\pi$ is independent of the angle ϕ and is therefore circular.

Three principal-plane radiation patterns have been computed for loops of different sizes and shapes in order to illustrate the derived result given by eq. (16). The results of these calculations are shown in Fig. 2. All three patterns have been normalized to the same maximum value. It can be seen that for a

loop with $ka = 1$ and $b/a = 0.8$ the pattern is essentially omnidirectional, departing from circularity by about $\pm 2\%$. For larger loops, the pattern is seen to depend on both the size and the shape.

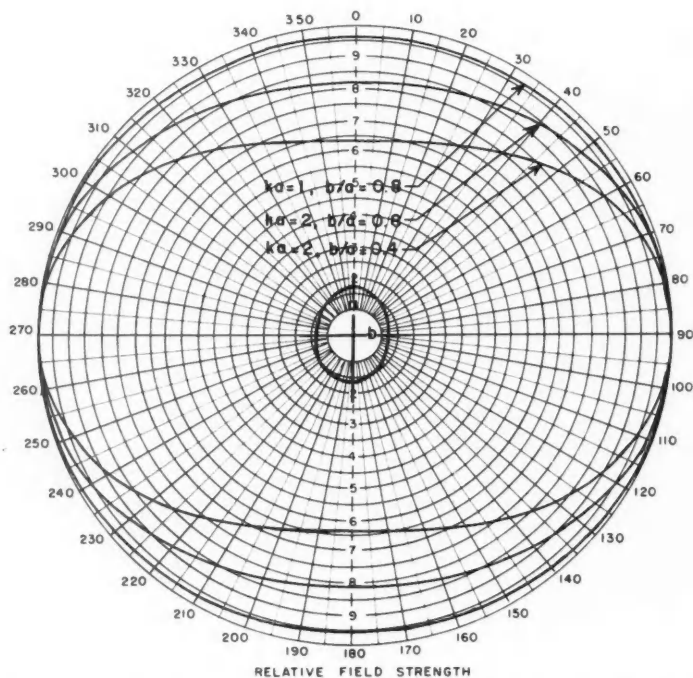


FIG. 2. Calculated radiation patterns in plane $\theta = \frac{1}{2}\pi$ for elliptic loop antennae of different sizes and shapes.

CONCLUSIONS

Expressions for the radiation field have been derived for a loop antenna of elliptical shape assuming a uniform current distribution. It is found that the radiation pattern in the plane of the loop depends on both the size and the shape of the antenna. However, for small loops, the pattern is independent of the shape and is circular. Although the present analysis has been restricted to loops carrying a constant current, the same method of analysis can be extended to loops with a nonuniform current distribution, for example, a sinusoidal distribution.

REFERENCES

- FOSTER, D. 1944. Proc. I.R.E. **32**, 603.
 KRAUS, J. D. 1950. Antennas (McGraw-Hill Book Company Inc., New York).
 SCHELKUNOFF, S. A. 1943. Electromagnetic waves (D. Van Nostrand Co. Inc., New York).

AURORAL RADIATION AT 500 Mc.¹

T. R. HARTZ

ABSTRACT

An observation of radio noise emissions at 500 Mc. from a type A red auroral display which occurred on October 21-22, 1957, is reported. The circumstances surrounding this phenomenon are considered, and the unusual display is linked to a large flare on the sun some 30 hours earlier. It is concluded that an unusually large particle flux for the ejected solar matter would produce sufficient ionization in local regions of the ionosphere so that auroral radio emissions would be possible.

INTRODUCTION

Despite a number of published reports of observations of r.f. noise emanating from the aurora (Covington 1947, 1950; Forsyth, Petrie, and Currie 1949; Hartz, Reid, and Vogan 1956), the measurements have been so infrequent and inconsistent as to leave the results open to doubt. Moreover, a number of observers (Chapman and Currie 1953; Harang and Landmark 1954) have looked for this phenomenon during intense auroral displays, with negative results. In consequence, it now appears that this controversial issue will be resolved only if more observations are obtained and if some justification for the negative results can be found.

Following the suggestion of Chapman and Currie (1953) that auroral noise occurs only at times of high sunspot number, the author has sought to observe the effect at times of great solar activity. On a number of occasions r.f. noise, associated with an intense auroral display at Ottawa, was observed at very high frequencies. These events have been reported by Hartz, Reid, and Vogan (1956). However, the antennas used were not sufficiently directive to establish completely the source of the radiation. The present paper describes an observation made with a more directional antenna at a frequency in the u.h.f. band.

500 MC. AURORAL NOISE

A 500-Mc. receiver with a 20-ft. parabolic antenna, normally used for solar recordings, has been employed on a number of occasions for auroral studies. Whenever an intense display was visible at Ottawa the antenna was directed at the aurora and noise recordings were made. In general, the results indicated that no perceptible noise increase was observed from such auroral forms as homogeneous arcs and bands, rayed structures, and flaming aurora. However, a type A red aurora did produce an increased noise level on the recorder during the night of October 21-22, 1957.

On that occasion the red aurora was observed at Ottawa just after sunset and lasted for about two hours. It appeared in several fairly well defined

¹Manuscript received March 5, 1958.

Contribution from the Radio Physics Laboratory, Defence Research Telecommunications Establishment, Defence Research Board, Ottawa, Canada. This work was performed under project PCC No. D48-28-01-02.

patches in the northern sky with the more usual auroral forms (rayed arcs and rays) present in other parts of the sky at the same time. The receiving antenna was directed at various parts of the display during the evening and the recording shown in Fig. 1 was obtained.

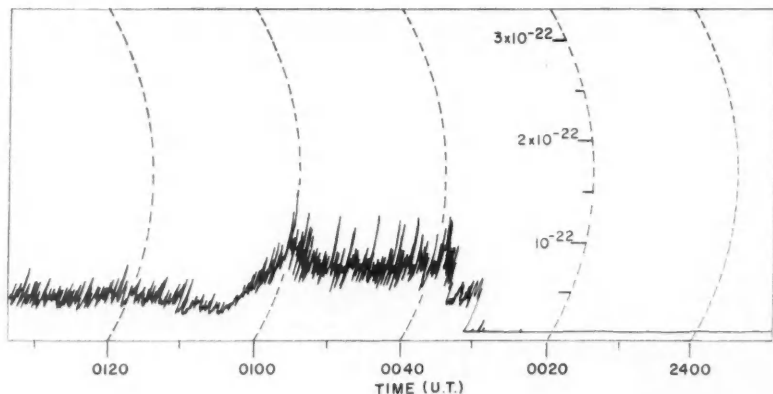


FIG. 1. 500-Mc. radio noise from the aurora during the night of October 21-22, 1957. The intensity levels on the record are in units of watts per square meter per cycle per second.

The display had been in progress for some time when the recording was started at 0032 U.T. At this time the antenna was directed at the southern sky away from the auroral display, and left in that position for a few minutes. At 0037 U.T. the antenna was directed at one patch of red aurora and left pointing in that direction. The increased noise level received at that time is quite evident in the record. The noise level remained high until about 0100 U.T. At this time the red coloring began to fade and the aurora turned into a general diffuse glow that covered most of the northern sky. At 0105 U.T. some slight ray activity was observed which exhibited some red coloring, but this lasted only about five minutes. By 0115 U.T. the aurora had faded leaving only a faint glow in the northern sky. The receiving antenna remained fixed in position during all this time with the exception of one brief period at 0040 U.T. when it was directed at a rayed structure that had no red color. The recording continued for the remainder of the night with the antenna in the same position, but no further noise increase was observed.

While it seemed possible for man-made transmissions to arrive at the receiver after being reflected by the auroral display, this explanation was discounted when order-of-magnitude calculations, based on the recorded signal level, were made, and after all the known radio and radar transmitters in Canada and the northern U.S.A. that operated at frequencies close to 500 Mc. were checked. There was no alternative but to conclude that the noise increase actually originated in the aurora. Moreover, the present measurements, coupled with prior negative results, would indicate that the aurora

on this occasion was quite different from that observed at other times. The red coloring also bears out this contention. Let us then examine the circumstances that surrounded this aurora, and in particular, the possible noise-generation processes in the ionosphere and the conditions on the sun which were responsible for this unusual occurrence.

THE GENERATION OF R.F. RADIATION IN THE IONOSPHERE

It is generally accepted that the aurora results from the influx of solar particles of matter into the ionosphere. Unfortunately, neither the nature of the particles nor their number density can be completely specified at this time. In consequence, the auroral noise-generation process is subject to considerable conjecture. Forsyth, Petrie, and Currie (1950) have examined a number of possible processes and concluded that a plasma oscillation of the ionized volume associated with the display was the most likely source of the 3000-Mc. radiation observed by them. However, they stated that electron densities in at least localized regions would have to be of the order of 10^{11} per cc. By a similar argument, the plasma oscillation process would require electron densities of about 3×10^9 per cc. in localized regions for the generation of 500-Mc. radiation.

Usually, electron densities in the ionosphere are not considered to attain values as high as this, but recent observations of radar reflections from the aurora at u.h.f. (Fricker, Ingalls, Stone, and Wang 1957) would indicate that high electron densities are associated with visual displays. It seems likely that such high densities would depend primarily on the number of particles incident in that region of the ionosphere.

A recent study by Ellis (1957) has shown that low-frequency emission from the aurora is possible. He suggests that the Cerenkov process is operative in the ionosphere, much as Marshall (1956) has suggested for the solar atmosphere. An extension of this argument indicates that Cerenkov radiation at 500 Mc. may be emitted from a region where high electron densities and an appreciable magnetic field exist. These conditions may be found in the ionosphere when a high particle flux is incident, such that local electron densities are of the order of 10^9 or 10^{10} per cc.

On the basis of this argument, it seems that r.f. radiation from the aurora depends on a large particle flux which, incidentally, Vegard (1949) also gave as the requirement for the generation of a red aurora.

THE ORIGIN OF THE INCOMING PARTICLES

The outstanding solar phenomena for the period in question were studied to establish the cause of the ionospheric disturbances. It now appears certain that the large solar flare of October 20, 1957, at approximately 1645 U.T., was the source of the charged particles which entered the earth's atmosphere some 30 hours later and produced the unusual aurora. This flare, of magnitude variously reported as of importance 3 or 3^+ , occurred in an active center on the sun at heliographic coordinates 27 S. 35 W. It was accompanied by the usual short-wave fade-out observed when ultraviolet or X radiation impinges

on the ionosphere and produces short-period absorption conditions. However, its most outstanding characteristic was that it was accompanied by very intense solar radio noise outbursts which were observed throughout the entire v.h.f. and u.h.f. bands. In fact, many v.h.f. communications circuits in Canada were completely jammed by the solar noise during this period.

Because the noise bursts at the different frequencies are known to originate at different levels in the solar corona, it was possible to determine the velocity of the traveling particle cloud that was responsible for the outbursts. The starting time of the respective noise bursts is shown in Fig. 2. The measurements at 500, 53, and 30 Mc. were made at the Radio Physics Laboratory,

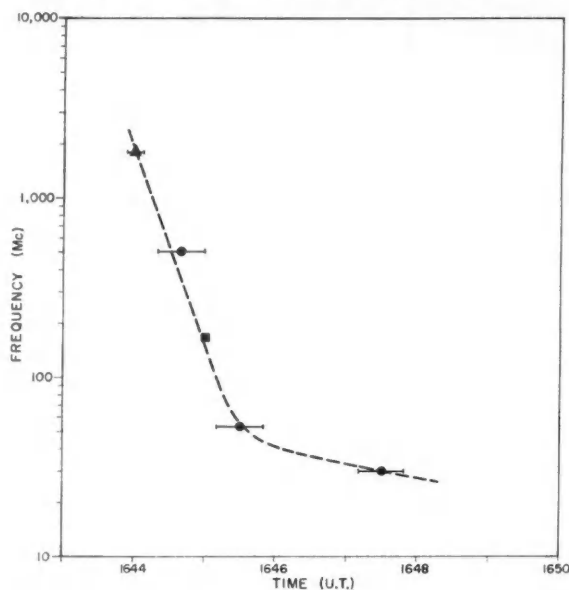


FIG. 2. The starting time of the radio noise outbursts at a number of frequencies for the large flare of October 20, 1957. The value at 167 Mc. was taken from the Preliminary Report of Solar Activity of the High Altitude Observatory, Boulder. A probable error for this point is not known.

while the 2800-Mc. data were obtained from the National Research Council (Ottawa); the 167-Mc. measurement was made at the National Bureau of Standards (Boulder). Using the values for the electron density in the solar corona given by Smerd (1950) and by Jaeger and Westfold (1950), calculations similar to those of Wild, Murray, and Rowe (1954) show that the shape of the curve in Fig. 2 is consistent with accelerated motion of the generating mechanism (in this case the particle cloud) through the corona. A terminal velocity (at a height of 5×10^5 km. above the photosphere) of 2000 km./sec. has been deduced in this case. However, the influence of the magnetic field of the active region on the sun has not been considered in this computation.

If the noise-generation process depends very strongly on the magnetic field, it may not be necessary to postulate accelerated motion in the solar corona, and the same data may yield a uniform velocity of somewhat lower magnitude than that given above for the particle cloud. The Cerenkov process postulated by Marshall (1956) would fit this latter case. Since the details of the solar conditions, such as the strength of the magnetic field and the precise location of the regions of origin in the corona for the various radio frequencies, are not known, velocity estimates for the particle cloud are somewhat hazardous. However, the velocity is not expected to be as great as 2000 km./sec. if the regions of origin for the emissions are relocated in the light of the reduced phase velocity which is an essential feature of Cerenkov radiation.

On the basis of a terminal velocity of 2000 km./sec. for the solar particles, the terrestrial effects should have started some 22 hours after the flare, depending on the actual particle velocity. Direct evidence of the solar particles entering the ionosphere is contained in the auroral observations mentioned above. The unusual display was observed at Ottawa at about 2245 U.T. on October 21. At this same time the magnetometer registered a sudden impulse. This was of short (less than 5 minute) duration, and had a magnitude of some 300 gammas. The planetary indices, K_p , also showed the sudden impulse, indicating that a burst of high-energy particles was entering the earth's ionosphere more or less universally. A smaller disturbance was registered on the magnetometer about an hour earlier, and subsequent disturbances were observed that lasted until 0100 U.T. on October 22.

Therefore, it seems certain that the solar particles spent almost 30 hours in transit, which is somewhat longer than was expected from the solar noise measurements as first considered. However, the accuracy of the velocity determinations as outlined above is not too great and no significance should be given to this apparent discrepancy of 7 or 8 hours. Improved data on the electron densities in the solar corona and a consideration of the local magnetic field may well yield results that are more consistent with the sun-earth delay times.

DISCUSSION

The 30-hour time interval signifies a velocity of approximately 1500 km./sec. for the particle cloud as it left the sun. This means that the solar particles entered the ionosphere with nearly this velocity, barring any acceleration or deceleration process other than the sun's gravitational attraction, which would only reduce this value by about 9%. Under these conditions, and on the assumption that the incoming particles on this occasion were protons, they would have possessed energies of approximately 10 kev. Since this value does not differ significantly from that deduced on other occasions when no auroral noise was observed, it must be concluded that the nature of the particles (and hence their energies) was different on this occasion, or that there was a significant difference in the particle flux. This latter explanation is the more probable in view of the very large solar noise outbursts that were generated in the solar corona by the same cloud of particles.

SUMMARY

The observations of the red aurora on the night of October 21-22, 1957, show clearly that 500-Mc. radiation emanated from it. A study of the circumstances that accompanied this ionospheric disturbance indicate that solar particles with velocities of about 1500 km./sec. were the probable cause. While the process in the ionosphere for the generation of r.f. radiation cannot be specified exactly, several possibilities exist which require only that the number density of the incoming particles be great enough.

REFERENCES

- CHAPMAN, R. P. and CURRIE, B. W. 1953. *J. Geophys. Research*, **58**, 363.
COVINGTON, A. E. 1947. *Terrestrial Magnetism and Atm. Elec.* **52**, 339.
——— 1950. *J. Geophys. Research*, **55**, 33.
ELLIS, G. R. 1957. *J. Atm. and Terrest. Phys.* **10**, 302.
FORSYTH, P. A., PETRIE, W., and CURRIE, B. W. 1949. *Nature*, **164**, 453.
——— 1950. *Can. J. Research, A*, **28**, 324.
FRICKER, S. J., INGALLS, R. P., STONE, M. L., and WANG, S. C. 1957. *J. Geophys. Research*, **62**, 527.
HARANG, L. and LANDMARK, B. 1954. *J. Atm. and Terrest. Phys.* **4**, 333.
HARTZ, T. R., REID, G. C., and VOGAN, E. L. 1956. *Can. J. Phys.* **34**, 728.
JAEGER, J. C. and WESTFOLD, K. C. 1950. *Australian J. Sci. Research, Ser. A*, **3**, 376.
MARSHALL, L. 1956. *Astrophys. J.* **124**, 469.
SMERD, S. F. 1950. *Proc. Inst. Elec. Engrs. (London)*, Pt. III, **97**, 447.
VEGARD, L. 1949. *In Terrestrial magnetism and electricity*, edited by J. A. Fleming (Dover Publications, Inc., New York), p. 634.
WILD, J. P., MURRAY, J. D., and ROWE, W. C. 1954. *Australian J. Phys.* **7**, 439.

KINETICS OF ALLOY SOLIDIFICATION¹

K. A. JACKSON

ABSTRACT

Alloy systems are discussed in terms of the theory of interface kinetics which was developed in a previous paper (Jackson and Chalmers 1956). The non-equilibrium equations which are developed reduce to the thermodynamic expressions if the system is in equilibrium. Several types of phase diagrams are discussed. It is shown that a phase diagram gives a reasonably good estimate of the concentrations at an interface if the system is not in equilibrium.

INTRODUCTION

The rate equations developed in a previous paper (Jackson and Chalmers 1956) can be extended to treat a system having more than one component. The equations that result from the consideration of alloys lead very simply to many standard thermodynamic expressions for the equilibrium of alloys. The description of an alloy system by this method lends itself more readily to physical interpretation than does the corresponding thermodynamic description. There is an additional advantage in the present treatment in that it applies equally well to equilibrium and non-equilibrium situations.

BASIC EQUATIONS

The following equations must be satisfied simultaneously at a phase boundary by any component i :

$$(1) \quad \begin{aligned} R_M^i &= A_M^i G_M^i \nu_S^i N_S^i V^i C^i \exp(-Q_M^i/RT), \\ R_F^i &= A_F^i G_F^i \nu_L^i N_L^i V^i C_L^i \exp(-Q_F^i/RT); \end{aligned}$$

R^i is the rate at which i atoms cross the phase boundary, A^i and G^i are the accommodation coefficient and geometric factors respectively for i atoms crossing the phase boundary, and Q^i is the activation energy for an i atom to traverse the phase boundary. The subscripts M and F refer to the processes of melting and freezing respectively, or, more generally, to the two directions of travel across the phase boundary. ν^i is a frequency factor, N^i is the number of possible sites for i atoms at the phase boundary, V^i is the volume occupied by an i atom in the solid, and the subscripts S and L refer to the two phases in equilibrium at the phase boundary (e.g. solid and liquid) (see Jackson and Chalmers 1956). Equation (1) assumes that the rate of departure of atoms from a phase is proportional to the mole fraction C^i of the species in that phase. A^i , G^i , ν^i , and Q^i may in general be functions of concentration.

For pure i at equilibrium,

$$(2) \quad \frac{A_M^i G_M^i \nu_S^i N_S^i}{A_F^i G_F^i \nu_L^i N_L^i} = \exp(L^i/RT_F^i),$$

since $Q_M^i - Q_F^i = L^i$, the latent heat of fusion for species i .

¹Manuscript received February 7, 1958.

Contribution from the Division of Engineering and Applied Physics, Harvard University, Cambridge 38, Mass.

For any intermediate composition the simultaneous equations

$$(3) \quad \frac{C_S^i N_S^i A_M^i G_M^i \nu_S^i}{C_L^i N_L^i A_F^i G_F^i \nu_S^i} = \exp[(Q_M^i - Q_F^i)/RT]$$

define the equilibrium conditions.

STANDARD THERMODYNAMIC EXPRESSIONS

To examine the usefulness of these equations, let us assume that the Q 's, A 's, G 's, and ν 's are independent of concentration, and compare the resulting equations for equilibrium in a binary alloy system with those obtained thermodynamically. According to this assumption, $Q_M^i - Q_F^i = L^i$. Combining equations (2) and (3) gives

$$(4) \quad \ln \frac{C_S^i}{C_L^i} = \frac{L^i}{R} \left(\frac{1}{T} - \frac{1}{T_E^i} \right),$$

which is a form of the Clausius-Clapeyron equation for Raoultian solutions. T_E^i is the equilibrium melting temperature for pure i . Also, for $C_S^A \rightarrow 1$, $C_L^A \rightarrow 1$ and $T \rightarrow T_E^A$; $\ln C_S^A/C_L^A = -1 + C_S^A + 1 - C_L^A = C_L^B - C_S^B$ and using $\Delta T^i = T_E^i - T$, we obtain

$$(5) \quad \frac{L^A}{R(T_E^A)^2} = \frac{C_L^B}{\Delta T^A} - \frac{C_S^B}{\Delta T^A},$$

which is the van't Hoff relationship (see Wilson 1944) applying to the difference in slope of the liquidus and solidus of a binary alloy for small amounts of an alloying element. (For small amounts of a second component the assumptions made are generally valid.) Moreover, we see that if we regard the part of the rate expression in front of the exponent as related to the entropy, we obtain immediately that the difference in entropy for a component of a phase compared to that component in the pure state is

$$(6) \quad \Delta S^i = -R \ln C^i.$$

This is the thermodynamic expression for the change in entropy in an ideal solution. Our assumption that the A 's, G 's, Q 's, and ν 's are independent of the mole fraction of the species is equivalent to the assumption of an ideal solution.

If we are to consider departures from ideality, the first departure we would anticipate would be a change in energy, i.e. in Q , as a result of the presence of another species. In the thermodynamic treatment this is awkward to do, so that departures from ideality are lumped into the thermodynamic expression (6) in terms of an "effective concentration" or "activity". This turns out to be sufficient mathematically, but physically it results in confusion.

BINARY EQUILIBRIUM DIAGRAMS

Let us now examine these equations (3) in terms of the binary equilibrium diagram. The information so obtained is not new, but the approach affords greater physical insight into the problem.

The simplest case is again the case of ideal solutions. The equations (3) can

be solved explicitly for C_s^B and C_L^B , the solidus and liquidus lines, in terms of T , using the relationship

$$(7) \quad C_s^A + C_s^B = 1 = C_L^A + C_L^B.$$

Using $L^A/RT_E^A = L^B/RT_E^B = 1.15$ (the typical value for f.c.c. metals) and taking, for example, $T_E^A = 1000^\circ \text{K.}$ and $T_E^B = 800^\circ \text{K.}$ the phase diagram (Fig. 1) is obtained.

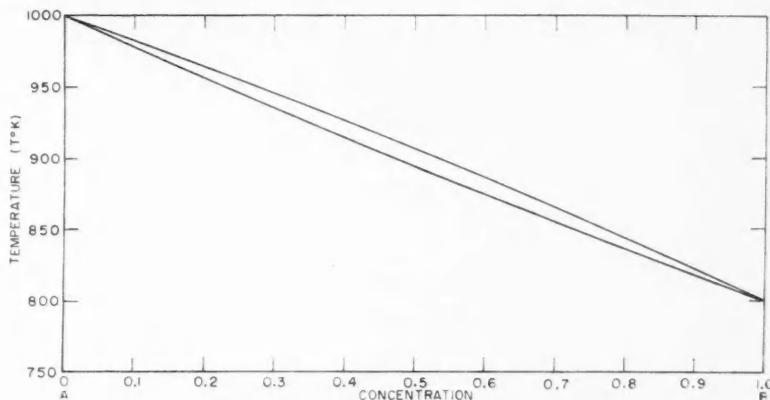


FIG. 1. Phase diagram for ideal alloy; $T_E^A = 1000^\circ \text{K.}$ $T_E^B = 800^\circ \text{K.}$

It is to be noted that this phase diagram is derived on the assumption that there is no interaction between A and B atoms; the only effect is that of dilution as shown in Fig. 2. As A atoms are added to pure B , the average latent heat of the solid increases, i.e., the average energy of the solid with respect to the liquid decreases. This must be the case for the solidus and liquidus to increase with temperature. This is a rare occurrence in cases where a compound is not formed. The solidus and liquidus can rise on both ends in cases where there is a strong A - B attraction.

If the addition of a component tends to increase the average energy of the other component in the solid as shown in Fig. 3 the phase diagram (Fig. 1) will tend to sag in the middle. If the two lines meet at pure B , say, the solidus and liquidus will be horizontal at the pure B end. If the two latent heat curves cross as shown in Fig. 4, we have a situation where A increases the energy of B and vice versa to such an extent that the average energy of each of the pure substances is increased by the addition of the other. Such a system is the Cu-Au system, Fig. 5. These curves have been fitted assuming the latent heat lines of Fig. 4 to be straight. The equations (3) in this case were

$$(8) \quad \begin{aligned} C_s^{\text{Au}}/C_L^{\text{Au}} &= \exp[(1536 - 430C_s^{\text{Cu}})/T - 1.15], \\ C_s^{\text{Cu}}/C_L^{\text{Cu}} &= \exp[(1560 - 478C_s^{\text{Au}})/T - 1.15]. \end{aligned}$$

This was obtained by using $L^{\text{Cu}}/RT_E^{\text{Cu}} = L^{\text{Au}}/RT_E^{\text{Au}} = 1.15$ and $C_L^{\text{Au}} = C_s^{\text{Au}} = C_L^{\text{Cu}} = C_s^{\text{Cu}} = 0.5$ at $T = 1148^\circ \text{K.}$

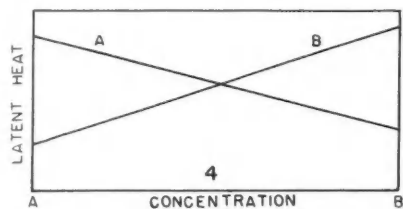
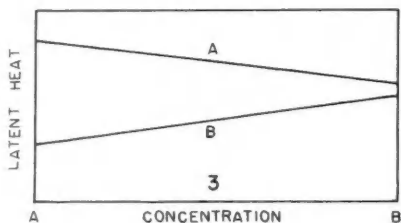
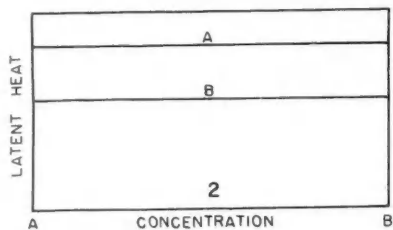


FIG. 2. Latent heat of components *A* and *B* of an ideal alloy as a function of concentration.
 FIG. 3. Variation of the latent heat with concentration for components *A* and *B* of an alloy system that departs slightly from ideality.

FIG. 4. Variation of the latent heat with concentration for components *A* and *B* of an alloy system that departs from ideality. This diagram is typical for an alloy such as the Au-Cu system.

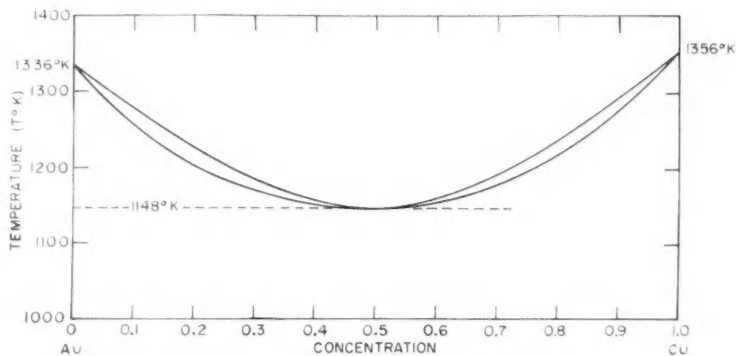


FIG. 5. Phase diagram for the Au-Cu system from equation (8).

The next case to consider is the case in which there is immiscibility in the solid. This case is represented in Fig. 6, for what might be called an ideal eutectic. In this case, adding the other component to the pure substance increases the average energy of the solid. Each pure phase is independent. It is ideal because we have assumed that there is no interaction between the atoms. The effect is merely that of dilution in each phase. In this case we obtain essentially two diagrams like Fig. 1 that cross somewhere. The point where the two liquidus lines cross defines the lowest temperature at which the liquid phase exists in equilibrium with the solid. Below this temperature equilibrium between the two solid phases takes over. This is shown schematically in Fig. 7. The ideal eutectic is seldom met with in practice. A eutectic system usually occurs between two elements which have a mutual interaction

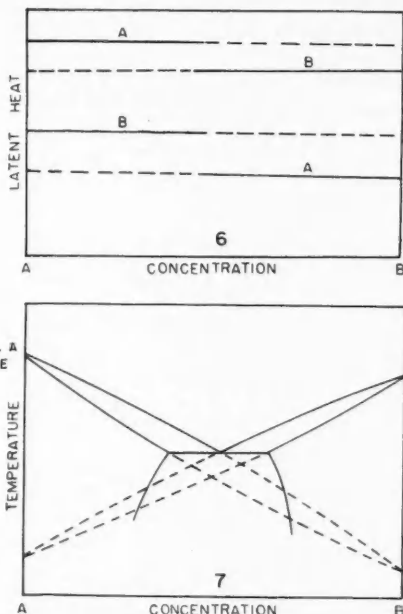


FIG. 6. Variation of the latent heat with concentration for components A and B in the two primary phases of an ideal eutectic alloy.

FIG. 7. Schematic phase diagram for ideal eutectic alloy.

when they are alloyed. The stronger the interaction, the broader will be the gap between the liquidus and solidus, and the smaller will be the "solubility limit" in the primary solid solutions.

THE SILVER-COPPER SYSTEM

The silver-copper system is a simple eutectic system. In considering this system quantitatively, we start by making the simplest possible assumptions

that can describe the phase diagram. The assumption we make is that the energy of the primary component in the primary solid solutions depends linearly on the concentration of the second component. That is, the A 's, G 's, and ν 's are constant. With this assumption, the phase diagram can be derived using only the equilibrium temperatures and latent heats, and the equilibrium concentrations at the eutectic temperature. The resultant equations can not be solved analytically for the solidus and liquidus lines because of the concentration dependence in the exponents. An iterative technique was used, and the resulting phase diagram is quite close to the experimental one, both above and below the eutectic temperature. However, the increase in energy of the solvent atoms in the solid on the addition of the solute atoms was far too large. The assumption made above appears to be too restrictive. If the change in energy of the liquid atoms is also considered, it is possible to obtain more reasonable values for the dependence of the energy of the solid atoms on concentration. However, the method employed (i.e., fixing the two ends of both the solidus and liquidus lines) results in essentially the same phase diagram regardless of how much of the energy change is attributed to the atoms in the liquid. Although it is possible to say that the energy of the atoms in the liquid does depend on the concentration, we can only put broad limits on this dependence using this method.

Another difficulty is that the added complexity of the more general assumption makes the equations difficult to work with. This will be true of any set of equations with which one attempts to describe complicated alloy systems. There are some direct experimental data on the variation, with composition, of the energy and entropy of a given component in a phase (Kubachewski and Evans 1951). This work has been done by two methods: electrolytically and calorimetrically. This type of study, although tedious, is important to the understanding of alloy systems. We have had no success in an initial attempt to use the available data to develop a phase diagram.

NON-EQUILIBRIUM PHASE TRANSFORMATIONS IN ALLOY SYSTEMS

The discussion above has been limited to alloy systems in equilibrium. The equations (1) can be used to describe non-equilibrium systems. It will be shown below that in an ideal alloy, the composition at a phase boundary does not differ appreciably from the equilibrium values for normal transformation rates. It is inferred from this result that the phase diagram is a reasonably good guide to the concentrations at phase boundaries in alloy systems that are not in equilibrium.

VARIATION OF k -VALUE WITH GROWTH RATE

The k -value or distribution coefficient is defined as the ratio of the concentration of a component in the solid to that in the liquid. There are two k -values: one defined in terms of average concentrations in the solid and/or liquid; the other defined in terms of the actual concentrations at the phase boundary. The former is the macroscopic or effective k -value, which we shall denote by \bar{k} ; the latter is the microscopic k -value, which we shall denote by k_0 .

The macroscopic k -value is used by Pfann (1954) to discuss the concentration distribution in a solid as a result of solidification. k depends on the amount of stirring in the liquid, on the conditions of growth, on the rate of growth, as well as on k_0 .

The microscopic k -value (k_0) depends only on the motion of atoms across the phase boundary. It will be shown below that k_0 changes by a very small amount when there is a net flux of atoms across the phase boundary.

IDEAL SOLUTIONS

Let us first consider the case of ideal solutions. For two phases which are not in equilibrium we have the condition that the net rate of growth of one phase is equal to the sum of the net rates of growth of its constituents,

$$(9) \quad \bar{R} = \bar{R}^A + \bar{R}^B + \bar{R}^C + \dots,$$

where \bar{R} is the net rate of growth of the phase and \bar{R}^i is the net rate at which component i crosses the interface. The other condition which we can apply is that the instantaneous composition of the phase being formed depends on the net rate at which atoms of the various species are entering that phase. Thus

$$(10) \quad C_S^A : C_S^B : C_S^C : \dots = \bar{R}_F^A : \bar{R}_F^B : \bar{R}_F^C : \dots$$

We have from equation (1)

$$(11) \quad \bar{R}^i = R_F^i - R_M^i = C_L^i N_L^i V_0^i A_F^i G_F^i \nu_L^i \exp(-Q_F^i/RT) \\ - C_S^i N_S^i V_0^i A_M^i G_M^i \nu_S^i \exp(-Q_M^i/RT).$$

Using the assumption of ideal mixing, this becomes, with the aid of equation (2)

$$(12) \quad \bar{R}^i = C_L^i N_L^i V_0^i A_F^i G_F^i \nu_L^i \exp(-Q_F^i/RT[1 - k_0^i \exp(L^i/RT_E^i - L^i/RT)]),$$

where $k_0^i = C_S^i/C_L^i$.

Let us now take $Q_F^i/RT_E^i = 1.5$, $L^i/RT_E^i = 1.15$, $T_E^A = 1000^\circ \text{K.}$, $T_E^B = 800^\circ \text{K.}$, and use $\Delta T^i = T_E^i - T$. This is the ideal binary alloy plotted in Fig. 1. Combining equations (10) and (12) for this case gives

$$(13) \quad \frac{C_S^A}{C_S^B} = \frac{C_L^A}{C_L^B} \exp(-300/T) \frac{1 - k_0^A \exp(-1.15\Delta T^A/T)}{1 - k_0^B \exp(-1.15\Delta T^B/T)}.$$

This equation was used to calculate the variation of k_0^B with \bar{R} in the following manner. A liquid composition was selected (in this case $C_L^A = C_L^B = 0.5$) and a resultant C_S^A and C_S^B calculated for various temperatures. The corresponding net rate of freezing was then calculated from equation (9). The results of this calculation appear below in Table I.

The equilibrium value was taken from Fig. 1. k_0^B is very close to the equilibrium value even at very large rates of melting or freezing. The limiting value of equation (13) as equilibrium is approached cannot be determined directly. It was hoped that the limiting value of this expression would put limits on the magnitude of the ratio R_F^A/R_F^B . This would have made it possible to estimate the activation energies of melting and freezing. In the Appendix the dependence of k_0 on R_F^A/R_F^B is discussed. Unfortunately, k_0 is virtually independent of

TABLE I

T_i ° K.	k_0^B	\bar{R}_i cm./sec.
950	0.862	-112
925	0.868	-51.2
912	0.874	0.0
900	0.878	20.8
875	0.886	80.0

R_F^A/R_F^B , so that this sort of consideration does not give an estimate of the activation energies.

k_0 IN NON-IDEAL ALLOYS

Examination of non-equilibrium k_0 -values for non-ideal alloys must be done on specific systems. We are not really in a position to do this. We have been unable to treat the equilibrium case exactly for systems that depart radically from ideality. We must, therefore, leave the detailed discussion of the non-equilibrium case until this has been done.

A few general comments can be made. In a non-ideal alloy, k_0 could depend more strongly on growth rate than for an ideal alloy. For some of these alloys it might be possible to obtain information about the ratio R_F^A/R_F^B .

For any alloy system that can be considered ideal, the phase diagram will be approximately correct for all growth rates. If the phase transformation under consideration is melting or freezing, the rate at which atoms are crossing the interface is usually large compared to the net rate of melting or freezing (see Jackson and Chalmers 1956). This implies that normal laboratory growth rates constitute only a slight departure from equilibrium. Moreover, departures from the equilibrium k_0 are predicted only for large growth rates in the ideal alloy case. It is reasonable, therefore, that the phase diagram should be applicable on a microscopic scale to the solidification of many alloy systems at normal growth rates.

SUMMARY

A kinetic theory of freezing has been applied to alloys. The work that is presented here is an outline of the general applicability of this theory. The equations developed above reduce to the thermodynamic equations when appropriate assumptions are made. It is shown that a phase diagram can be applied to non-equilibrium situations if the proper interpretations are made.

ACKNOWLEDGMENTS

The author wishes to thank Professor Bruce Chalmers for his guidance and stimulation during the course of this work. The financial assistance of the U.S. Atomic Energy Commission during the course of this work is also acknowledged.

APPENDIX—VARIATION OF k_0 WITH R_F^A/R_F^B

The general form of equation (13) can be written as:

$$(14) \quad \frac{K^A}{K^B} = \frac{k_1^A}{k_1^B} \frac{C_S^A (C_S^A - 1 + k_1^B C_L^B)}{(C_S^A - 1)(C_S^A - k_1^A C_L^A)}.$$

In this expression

$$K^i = R_F^i / C_L^i, \quad k_1^i = \frac{N_L^i A_F^i \nu_L^i G_F^i}{N_S^i A_M^i G_M^i \nu_S^i} \exp(Q_M^i - Q_F^i) / RT,$$

k_1^i reduces to k_0^i at equilibrium. K^i is proportional to the probability of a given i atom crossing the interface, from liquid to solid, in unit time.

At equilibrium, the right-hand side of equation (14) is of the form 0/0. In this case, k_0^i is independent of K^A/K^B . If the temperature is not the equilibrium temperature, the zero in the numerator and the zero in the denominator of equation (14) do not coincide. The zero in the numerator implies $K^B \gg K^A$; the zero in the denominator implies $K^A \gg K^B$. These two limits correspond to one species of atom or the other dominating the freezing process. As the temperature moves farther from the equilibrium temperature, the zero and the infinity move farther apart. There is only one branch of this equation satisfying the condition $0 \leq C_S^A \leq 1$. The zero and infinity of equation (14) thus define a minimum and maximum k_0^i . Unfortunately, for normal growth rates, the minimum and maximum k_0^i are close together. It would thus be difficult to estimate K^A/K^B from an experimental determination of the non-equilibrium k_0^i .

REFERENCES

- JACKSON, K. A. and CHALMERS, B. 1956. Can. J. Phys. **34**, 473.
 KUBASCHEWSKI, O. and EVANS, E. L. 1951. Metallurgical thermochemistry (Butterworth-Springer Ltd., London).
 PEANN, W. G. 1954. Trans. AIME, **200**, 294.
 WILSON, A. J. C. 1944. J. Inst. Metals, **70**, 543.

OPTIMUM FILTER FUNCTIONS FOR THE DETECTION OF PULSED SIGNALS IN NOISE¹

H. S. HEAPS²

ABSTRACT

This paper is concerned with the optimum method of processing a signal received upon a background of noise. Determination is made of the transfer function of the process that maximizes the ratio of the average power of n successive samples of the output signal to the mean output noise power. For sufficiently large values of n the ratio is a close approximation to the ratio of the signal-to-noise energy contained in a sample of the output over a finite time. The maximum ratio is calculated when the input is a rectangular d.c. pulse upon white noise and when it is a cosine pulse upon non-white noise.

The transfer function to maximize the ratio of signal voltage to noise power was determined in a previous paper. It is found that for the rectangular pulse the two methods of optimization lead to very similar ratios of signal-to-noise energy and that the third-order low-pass Butterworth filter produces a ratio of signal-to-noise energy that lies within a few per cent of the theoretical maximum. Such is not the case for the cosine pulse.

1. INTRODUCTION

In many physical experiments information is converted into electrical signals which are subsequently received upon a background of noise. If the signals are weak in comparison to the noise then the success of the experiment may depend upon the possibility of designing a sufficiently efficient filter for reduction of the noise. Accordingly, for a given signal and noise input, it is of considerable interest to determine the maximum value of signal-to-noise ratio which could be produced by an optimum, but previously unspecified, method of processing the input.

The optimum process may be characterized by a transfer function relating the output to the input. Realization of the transfer function then requires the design of a suitable electrical circuit. The circuit design is feasible provided that the optimum process does not require an electrical circuit to distinguish between positive and negative frequencies and does not require it to have a negative memory. A negative memory would imply that a signal could be processed before it had been received.

For a given input signal and noise background Dwork (1950) has obtained an expression for the transfer function of the electrical network required to produce at its output the greatest possible value of instantaneous peak signal voltage consistent with a fixed value of mean output noise power. Except for the case of white noise the transfer function of Dwork is not always realizable by the use of a physical network. An expression for a physically realizable transfer function was obtained by Zadeh and Ragazzini (1952).

The theories of Dwork and of Zadeh and Ragazzini concern the design of networks to produce a single signal peak that is instantaneously as large as

¹Manuscript received February 11, 1958.

Contribution from the Naval Research Establishment, Dartmouth, Nova Scotia.

²Nova Scotia Technical College, Halifax, Nova Scotia.

possible in comparison to the mean noise. It is often more desirable to produce an output signal that, in comparison to the mean noise, is as large as possible over a finite time interval, or over a succession of sampling times. The transfer function of a network designed to maximize the ratio of the average of n successive samples of the output signal voltage in comparison to the mean output noise was obtained in a previous paper (Heaps and McKay 1958). The transfer function to maximize a continuous average of output signal voltage was also found.

In many instances the processed electrical signal plus noise is observed by means of a device which records power instead of voltage. The present paper concerns the transfer function of a network that is required to produce at its output the greatest value of average signal power in relation to the mean noise power. A method of determining the transfer function and optimum signal-to-noise ratio is described in Section 2. In Section 3 it is shown that the transfer function is realizable by the use of a physical network. Sections 4 and 5 describe the application of the method when the input is a rectangular d.c. pulse upon white noise or a cosine pulse upon non-white noise.

2. OPTIMUM TRANSFER FUNCTION

The signal input $V_i(t)$ and the signal output $V_o(t)$ at time t may be represented in the form

$$(1) \quad V_i(t) = (1/2\pi) \int_{-\infty}^{\infty} F(\omega) \exp(i\omega t) d\omega,$$

$$(2) \quad V_o(t) = (1/2\pi) \int_{-\infty}^{\infty} F(\omega) H(\omega) \exp(i\omega t) d\omega,$$

where

$$(3) \quad F(\omega) = \int_{-\infty}^{\infty} V_i(t) \exp(-i\omega t) dt$$

and $H(\omega)$ is the transfer function of the network.

The convolution theorem for the Fourier transform (Sneddon 1951) shows that

$$(4) \quad \int_{-\infty}^{\infty} |V_o(t)|^2 \exp(-i\omega t) dt = (1/2\pi) \int_{-\infty}^{\infty} F^*(\omega_1) H^*(\omega_1) F(\omega + \omega_1) H(\omega + \omega_1) d\omega_1,$$

where H^* is the complex conjugate of H . Hence the signal output power at time t is given by

$$(5) \quad |V_o(t)|^2 = (1/4\pi^2) \int_{-\infty}^{\infty} \exp(i\omega t) d\omega \int_{-\infty}^{\infty} F^*(\omega_1) H^*(\omega_1) F(\omega + \omega_1) H(\omega + \omega_1) d\omega_1.$$

If the power spectrum of the input noise is $|\sigma(\omega)|^2$, then the mean output noise power is equal to

$$(6) \quad N^2 = (1/2\pi) \int_{-\infty}^{\infty} |\sigma(\omega) H(\omega)|^2 d\omega.$$

For a given function $G(\omega)$, at any time T let $S(T)^2$ denote the expression

$$(7) \quad S(T)^2 = (1/4\pi^2) \int_{-\infty}^{\infty} G(\omega) \exp(i\omega T) d\omega \int_{-\infty}^{\infty} F^*(\omega_1) H^*(\omega_1) F(\omega + \omega_1) H(\omega + \omega_1) d\omega_1.$$

In the special case that

$$(8) \quad G(\omega) = (1/n) \{1 + \exp(-i\omega\tau) + \exp(-2i\omega\tau) + \dots + \exp[-(n-1)i\omega\tau]\} \\ = \frac{1}{n} \frac{\sin(n\omega\tau/2)}{\sin(\omega\tau/2)} \exp[-(n-1)i\omega\tau/2]$$

then $S(T)^2$ denotes the average of the signal output powers at times T , $T - \tau$, $T - 2\tau$, \dots , $T - (n-1)\tau$. These times are chosen to cover the entire sampling period at intervals τ as shown in Fig. 1. If $n\tau$ is denoted by d , and n is allowed

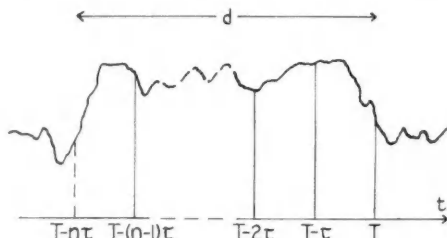


FIG. 1. For a given value of mean output noise power the transfer function is to be chosen to maximize the average of the output signal powers at times T , $T - \tau$, $T - 2\tau$, \dots , $T - (n-1)\tau$.

to tend to infinity subject to the condition that d remain finite, then, after multiplication by d ,

$$(9) \quad G(\omega) = (2/\omega) \sin(\omega d/2) \exp(-i\omega d/2)$$

and $S(T)^2$ denotes the value of the output signal power integrated over the time interval from $T - d$ to T .

If the transfer function $H(\omega)$ is to be chosen so that the value of $S(T)^2$ is as large as possible in comparison to N^2 then $H(\omega)$ must be chosen so that $\partial Q / \partial H(\omega) = 0$, where

$$(10) \quad Q = (1/2\pi) \int_{-\infty}^{\infty} G(\omega) \exp(i\omega T) d\omega \int_{-\infty}^{\infty} F^*(\omega_1) H^*(\omega_1) F(\omega + \omega_1) H(\omega + \omega_1) d\omega_1 \\ - \lambda \int_{-\infty}^{\infty} |H(\omega) \sigma(\omega)|^2 d\omega \\ = (1/2\pi) \int_{-\infty}^{\infty} F(\omega) H(\omega) \exp(i\omega T) d\omega \int_{-\infty}^{\infty} G(\omega - \omega_1) F^*(\omega_1) H^*(\omega_1) \exp(-i\omega_1 T) d\omega_1 \\ - \lambda \int_{-\infty}^{\infty} |H(\omega) \sigma(\omega)|^2 d\omega$$

and λ is a Lagrangian multiplier (Weinstock 1952). The condition $\partial Q/\partial H(\omega) = 0$ is fulfilled provided

$$(11) \quad (1/2\pi)F(\omega)\exp(i\omega T) \int_{-\infty}^{\infty} G(\omega-\omega_1)F^*(\omega_1)H^*(\omega_1)\exp(-i\omega_1 T)d\omega_1 \\ -\lambda H^*(\omega)|\sigma(\omega)|^2 = 0.$$

Thus $H(\omega)$ must satisfy the integral equation

$$(12) \quad H(\omega) = \frac{F^*(\omega)\exp(-i\omega T)}{2\pi\lambda|\sigma(\omega)|^2} \int_{-\infty}^{\infty} G^*(\omega-\omega_1)F(\omega_1)H(\omega_1)\exp(i\omega_1 T)d\omega_1.$$

The maximum value of $S(T)^2/N^2$ is the greatest value of λ for which there is a solution $H(\omega)$ of (12).

If $G(\omega)$ is chosen as in (8) then

$$(13) \quad G^*(\omega-\omega_1) = (1/n)\sum \exp[i\tau(\omega-\omega_1)\tau]$$

in which the summation in τ is from 0 to $n-1$. Thus (12) becomes

$$(14) \quad H(\omega) = \frac{F^*(\omega)\exp(-i\omega T)}{2\pi n\lambda|\sigma(\omega)|^2} \sum I(r\tau)\exp(i\tau\omega\tau),$$

where

$$(15) \quad I(r\tau) = \int_{-\infty}^{\infty} F(\omega_1)H(\omega_1)\exp[i\omega_1(T-r\tau)]d\omega_1.$$

Substitution of $H(\omega)$ from (14) into (12) leads to the identity

$$(16) \quad \sum I(r\tau)\exp(i\tau\omega\tau) - (1/n\lambda)\sum \exp(i\tau\omega\tau)\sum \phi(s\tau-r\tau)I(s\tau),$$

where s is summed from 0 to $n-1$ and

$$(17) \quad \phi(r\tau) = (1/2\pi) \int_{-\infty}^{\infty} \frac{|F(\omega_1)|^2}{|\sigma(\omega_1)|} \exp(i\tau\omega_1\tau)d\omega_1.$$

Since each side of (16) is a complex Fourier series in ω , then for each r

$$(18) \quad I(r\tau) = (1/n\lambda)\sum \phi(s\tau-r\tau)I(s\tau)$$

and hence for each r between 0 and $n-1$, then

$$(19) \quad \sum \phi(s\tau-r\tau)I(s\tau) = n\lambda I(r\tau).$$

For each value of n there are not more than n values of λ for which the n equations (19) have a non-zero solution for the n quantities $I(r\tau)$. The maximum value of $S(T)^2/N^2$ is the greatest value of λ for which (19) has a non-zero solution for the $I(r\tau)$. The transfer function that produces the maximum value of $S(T)^2/N^2$ is then given by (14).

The expression (14) is the transfer function required to maximize the ratio of the average of n successive samples of the output signal power to the mean noise power. The transfer function that maximizes the ratio of the average of n samples of signal voltage to the mean noise power was found in a previous paper (Heaps and McKay 1958) to have the form

$$(20) \quad H(\omega) = \frac{F^*(\omega)G^*(\omega)\exp(-i\omega T)}{\lambda|\sigma(\omega)|^2}.$$

Thus when $G(\omega)$ has the form (8) then $H(\omega)$ has the form (14) in which all the $I(r\tau)$'s are equal. The resulting maximum value of the ratio of the square of the average output signal voltage to the mean output noise power was found to be

$$(21) \quad \lambda_a = (1/2\pi) \int_{-\infty}^{\infty} \frac{|F(\omega)|^2 |G(\omega)|^2}{|\sigma(\omega)|^2} d\omega.$$

When $G(\omega)$ has the form (8) then (21) becomes

$$(22) \quad \lambda_a = (1/n)\phi(0) + (2/n^2)\sum r\phi(n\tau - r\tau).$$

Since the greatest solution λ of (19) is the maximum value of the mean-square output signal voltage in relation to the mean noise power while λ_a of (22) is the maximum value of the square of the mean output signal voltage in relation to the mean noise power, then λ is never less than λ_a .

If $n = 2$ the greatest value of λ for which (19) has a solution is $\lambda = \frac{1}{2}[\phi(0) + \phi(\tau)]$ in which case $I(\tau) = I(0)$ and so (14) coincides with the transfer function that maximizes signal voltage. If $n = 3$ the greatest value of λ for which (19) has a solution is

$$(23) \quad \lambda = \phi(0)/3 + \phi(2\tau)/6 + [\phi(2\tau)^2 + 8\phi(\tau)^2]^{1/2}/6$$

and (14) does not coincide with the function that maximizes signal voltage. For values of n greater than three the transfer function (14) is in general different from that chosen to maximize voltage.

It may be observed that if $r\tau$ is denoted by t_2 , $s\tau$ by t_3 , and $n\tau$ by d , then for fixed d as $\tau \rightarrow 0$ the equation (19) becomes the Fredholm integral equation

$$(24) \quad \int_{-\infty}^{\infty} \phi(t_3 - t_2) I(t_3) dt_3 = d\lambda I(t_2),$$

where

$$(25) \quad \phi(t_2) = (1/2\pi) \int_{-\infty}^{\infty} \frac{|F(\omega_1)|^2}{|\sigma(\omega_1)|^2} \exp(i\omega_1 t_2) d\omega_1.$$

The solution (14) then takes the form

$$(26) \quad H(\omega) = \frac{F^*(\omega) \exp(-i\omega T)}{2\pi d \lambda |\sigma(\omega)|^2} \int_{-\infty}^{\infty} I(t_2) \exp(i\omega t_2) dt_2.$$

3. PHYSICAL REALIZABILITY OF THE TRANSFER FUNCTION

In order that the transfer function $H(\omega)$ of (14) correspond to a physically realizable network it is necessary that the output response $S(t)$ to a unit impulse at time $t = 0$ be zero for $t < 0$. Now with $H(\omega)$ chosen as in (14) the output resulting from a unit impulse is

$$(27) \quad S(t) = (1/2\pi) \int_{-\infty}^{\infty} H(\omega) \exp(i\omega t) d\omega \\ = (1/4\pi^2 n \lambda) \sum I(r\tau) \int_{-\infty}^{\infty} \frac{F^*(\omega)}{|\sigma(\omega)|^2} \exp[i\omega(t - T + r\tau)] d\omega.$$

The condition that $S(t) = 0$ for $t < 0$ is certainly satisfied if for each r between 0 and $n-1$

$$(28) \quad \int_{-\infty}^{\infty} \frac{F^*(\omega)}{|\sigma(\omega)|^2} \exp[i\omega(t-T+r\tau)] d\omega = 0 \quad \text{for } t < 0.$$

But (28) is equivalent to the condition

$$(29) \quad \int_{-\infty}^{\infty} \frac{F(\omega)}{|\sigma(\omega)|^2} \exp[i\omega(T-r\tau-t)] d\omega = 0 \quad \text{for } t < 0,$$

which is certainly satisfied if

$$(30) \quad \int_{-\infty}^{\infty} \frac{F(\omega)}{|\sigma(\omega)|^2} \exp(i\omega t) d\omega = 0 \quad \text{for } t > T-r\tau > T-d.$$

In the case of white noise then $|\sigma(\omega)|^2 = 1$ and (30) reduces by (1) to the condition that $V_i(t) = 0$ for $t > T-d$. This condition implies that the entire pulse must have entered the network prior to the instant at which the first output sample is chosen. The condition is also obvious intuitively since the network cannot make best use of the signal until the entire signal has entered the input.

By a theorem of Paley and Wiener (1934) the condition for the existence of a finite time T for which (30) may be satisfied is equivalent to the condition

$$(31) \quad \int_{-\infty}^{\infty} \frac{1}{1+\omega^2} \log \left[\frac{F(\omega)}{|\sigma(\omega)|^2} \right] d\omega < \infty.$$

The precise formulation (31) of the realizability condition includes the intuitively obvious requirement that there must be no frequency band over which the noise vanishes but the signal does not. The existence of such a frequency band would imply that $S(T)^2/N^2$ could be made infinitely large by the use of an ideal rectangular band-pass filter. The problem discussed in the present paper would then be replaced by the problem of approximating the ideal filter by a realizable one with a finite number of circuit elements. The value of $S(T)^2/N^2$ could be made as large as required by the choice of a sufficiently close approximation to the ideal filter.

To illustrate the meaning of the condition (31) consider the case of an input rectangular pulse of duration a received upon a noise background for which $|\sigma(\omega)|^2 = \omega^2/(\omega^2+b^2)$ where b is a constant. With the origin chosen at the center of the pulse then $F(\omega) = 2A(\sin \frac{1}{2}\omega a)/\omega$ where A is the height of the pulse. The condition (31) is not fulfilled because of the infinite behavior of the integrand at $\omega = 0$. However, the value of $S(T)^2/N^2$ may be made as large as desirable by the use of a sufficiently narrow low-pass filter. Similarly, if a rectangular pulse is received upon a noise background for which $|\sigma(\omega)|^2 = b^2/(\omega^2+b^2)$, then (31) is not true because of the behavior of the integrand at $\omega = \infty$. In this instance $S(T)^2/N^2$ may be made as large as required by the use of a high-pass filter with a sufficiently high low-frequency cutoff. However, if a cosine pulse of shape $V_i(t) = \cos(\pi t/a)$ of duration from $t = -a/2$ to $a/2$ is received upon a noise background for which $|\sigma(\omega)|^2 = b^2/(\omega^2+b^2)$ then

$$(32) \quad F(\omega) = \frac{2\pi}{a} \frac{\cos \frac{1}{2}\omega a}{(\pi/a)^2 - \omega^2}$$

and the condition (31) is fulfilled.

λ exceeds λ_a . The sign / is used in the last part of Table 1 when $n = 3$ to indicate that $\lambda/U = 0.333$ regardless of the value of the $I(s\tau)$.

It is interesting to compare the output signal-to-noise ratios λ and λ_a with the ratio that would be obtained by use of the third-order low-pass Butterworth

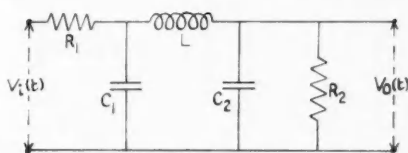


FIG. 2. Third-order low-pass filter. Butterworth response is obtained if equations (36) are satisfied.

filter shown in Fig. 2. The filter has Butterworth response if the circuit components R_1 , R_2 , L , C_1 , and C_2 are chosen in terms of a parameter α as follows:

$$(36a) \quad \frac{R_1 R_2 (C_1 + C_2) + L}{R_1 + R_2} = \alpha,$$

$$(36b) \quad \frac{(R_1 C_1 + R_2 C_2) L}{R_1 + R_2} = \frac{\alpha^2}{2},$$

$$(36c) \quad \frac{R_1 R_2 L C_1 C_2}{R_1 + R_2} = \frac{\alpha^3}{8}.$$

In a previous paper (Heaps and Isaacs 1958) it was shown that if the output is sampled continuously over a time d that lies between $0.4a$ and $2a$ then the maximum ratio λ_b of the signal-to-noise energy in the sample is obtained when the parameter α is chosen according to the equation

$$(37) \quad \alpha = \frac{2a}{3.5 - d/a}.$$

The maximum value of λ_b was plotted in Fig. 5 of the previous paper. Owing to a slightly different representation of the total noise power the values of λ_b must be divided by two before being compared with λ and λ_a .

If $d/a = 1$ then $\frac{1}{2}\lambda_b = 0.657$. If $n = 10$ then $\lambda = 0.679$ and $\lambda_a = 0.670$. Thus, if efficiency of a filter is defined by comparison with the optimum signal-to-noise ratio λ when $n = 10$, then at $d/a = 1$ a Butterworth filter may be designed to be 96.8% efficient in maximizing signal energy. The value of λ_a , the maximum square of the mean signal voltage, is 98.7% of the value λ of the maximum mean-square signal voltage. If $d/a = 2$ then $\frac{1}{2}\lambda_b = 0.437$. If $n = 10$ then $\lambda = 0.438$ and $\lambda_a = 0.420$. Thus a Butterworth three-pole filter may be designed to be practically 100% efficient in maximizing signal energy. The value of λ_a is 95.9% that of λ .

5. COSINE PULSE RECEIVED UPON NON-WHITE NOISE

Although for many purposes it is convenient to use rectangular pulses it is often more realistic to suppose that the discontinuities at the beginning and

end are replaced by gradual increases or decreases. In many instances the shape of the received pulse lies between a rectangular pulse and a pulse of cosine shape given by

$$(38) \quad V_t(t) = \begin{cases} A \cos(\pi t/a) & \text{for } |t| < \frac{1}{2}a, \\ 0 & \text{for } |t| > \frac{1}{2}a. \end{cases}$$

For the cosine pulse then $F(\omega)$ is as in (32). The total energy contained in the pulse is $U = \frac{1}{2}A^2a$.

Let the cosine pulse be received upon a noise background for which $|\sigma(\omega)|^2 = b^2/(b^2 + \omega^2)$. The noise power is then a decreasing function of frequency and the constant b denotes the value of ω at which the mean-square noise power per unit bandwidth of ω is equal to one-half of its value at zero frequency. The case of white noise is obtained by putting b equal to infinity.

According to (17) then

$$(39) \quad \phi(t) = \frac{\pi A^2}{2a^2} \int_{-\infty}^{\infty} \frac{4 \cos^2 \frac{1}{2} \omega a}{[(\pi/a)^2 - \omega^2]^2} \frac{b^2 + \omega^2}{b^2} \cos \omega t d\omega,$$

where t denotes $r\tau$. If $n\tau$ is denoted by d then (see appendix)

$$(40) \quad \phi(r\tau) = \begin{cases} \frac{U(b^2 + \pi^2/a^2)}{b^2} (1 - |rd/na|) \cos(rd\pi/na) & \text{if } |rd/na| < 1, \\ 0 & \text{if } |rd/na| > 1. \end{cases}$$

The maximum value of λ in (19) with $\phi(r\tau)$ according to (40) is plotted in Fig. 3 for $n = 1, 2, 3, 4$, and 5. The corresponding solutions $I(s\tau)/I(0)$ are listed

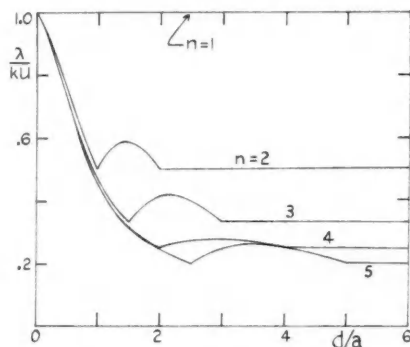


FIG. 3. Maximum signal-to-noise energy ratio λ for a cosine pulse of duration a . The output is sampled over a time d . The noise has power spectrum $|\sigma(\omega)|^2 = b^2/(b^2 + \omega^2)$. k denotes $(b^2 + \pi^2/a^2)/b^2$.

in Table II for $d/a = 1, 2$, and 3 and $n = 1, 2, 3, 4, 5$, and 6. The figures in parentheses are the values of λ_a which arise when $I(s\tau)/I(0) = 1$ and are given by (22).

Comparison of Tables I and II shows that, although there is little difference between λ and λ_a for a rectangular pulse received upon white noise, there may

TABLE II
MAXIMUM SIGNAL-TO-NOISE ENERGY RATIO λ FOR A COSINE
PULSE UPON NOISE OF SPECTRUM $|\sigma(\omega)|^2 = b^2/(b^2 + \omega^2)$ WHEN $d/a = 1, 2, 3$
 k denotes $(b^2 + \pi^2/a^2)/b^2$

$d/a = 1$	$n = 1$	2	3	4	5	6
$\lambda/kU = 1$	0.5	0.465	0.454	0.448	0.446	
$(\lambda_a/kU) = (1)$	(0.5)	(0.444)	(0.188)	(0.419)	(0.415)	
$I(\tau)/I(0) =$	1.	1.687	1.868	1.880	1.839	
$I(2\tau)/I(0) =$		1.	1.868	1.258	2.390	
$I(3\tau)/I(0) =$			1.	1.880	2.390	
$I(4\tau)/I(0) =$				1.	1.839	
$I(5\tau)/I(0) =$					1.	
$d/a = 2$	$n = 1$	2	3	4	5	6
$\lambda/kU = 1$	0.5	0.411	0.250	0.249	0.235	
$(\lambda_a/kU) = (1)$	(0.5)	(0.259)	(0.250)	(0.180)	(0.222)	
$I(\tau)/I(0) =$	1.	-1.409	/	-0.483	-1.	
$I(2\tau)/I(0) =$		1.	/	-0.206	-4.45	
$I(3\tau)/I(0) =$			/	-0.483	-4.45	
$I(4\tau)/I(0) =$				1.	-1.	
$I(5\tau)/I(0) =$					1.	
$d/a = 3$	$n = 1$	2	3	4	5	6
$\lambda/kU = 1$	0.5	0.333	0.277	0.243	0.167	
$(\lambda_a/kU) = (1)$	(0.5)	(0.333)	(0.184)	(0.160)	(0.167)	
$I(\tau)/I(0) =$	1	/	-0.618	-1.731	/	
$I(2\tau)/I(0) =$		/	-0.618	2.	/	
$I(3\tau)/I(0) =$			1.	-1.731	/	
$I(4\tau)/I(0) =$				1.	/	

be appreciable difference between λ and λ_a for a cosine pulse received upon noise of frequency spectrum $b^2/(b^2 + \omega^2)$.

In the case of white noise the optimum signal-to-noise ratio is greater for a rectangular pulse than for a cosine pulse. Thus, if a rectangular transmitted pulse suffers distortion in the form of a smoothing of the discontinuities, then the greatest realizable ratio of received signal-to-noise energy is reduced. This result applies even if the total signal energy and signal duration remain unchanged. If the rectangular pulse is distorted into a cosine shape of the same length then for the various values of n and d/a considered in Tables I and II the signal-to-noise ratio is reduced by approximately 30% to 50% of its original value.

ACKNOWLEDGMENT

The author wishes to express his appreciation to the Defence Research Board of Canada for permission to publish this paper, which has arisen as part of an investigation under N.R.E. Project D12-38-03-03.

APPENDIX

The equation (40) may be proved as follows. Since

$$(41) \quad 4(\cos^2 \frac{1}{2} \omega a) \cos \omega t = 2 \cos \omega t + \cos(a+t)\omega + \cos(a-t)\omega,$$

then for real values of ω the integrand of (39) is the real part of the function

$$(42) \quad z(\omega) = \frac{f(\omega)(b^2 + \omega^2)}{[(\pi/a)^2 - \omega^2]^2 b^2},$$

where

$$(43) \quad f(\omega) = 2\exp(i\omega t) + \exp[i(a+t)\omega] + \exp[\pm i(a-t)\omega].$$

In the term $\exp[\pm i(a-t)\omega]$ the $+$ sign is to be used when $t < a$ and the $-$ sign when $t > a$.

For complex values of ω the function $z(\omega)$ has no singularities inside the contour shown in Fig. 4. The above choice of sign in $\exp[\pm i(a-t)\omega]$ ensures that the integral of $z(\omega)$ around the semicircle tends to zero as the radius of the semicircle tends to infinity.

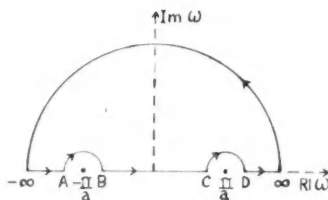


FIG. 4. Path of integration of $z(\omega)$.

For values of ω on the semicircle AB for which $\omega + \pi/a = r\exp(i\theta)$, where $r \ll 1$, then

$$(44) \quad f(\omega) = \begin{cases} -2i\sin(\pi t/a) + 2ir[\exp(i\theta)](t-a)\cos(\pi t/a) & \text{if } t < a, \\ 0 & \text{if } t > a. \end{cases}$$

For values of ω on the semicircle CD for which $\omega - \pi/a = r\exp(i\theta)$, where $r \ll 1$, then

$$(45) \quad f(\omega) = \begin{cases} 2i\sin(\pi t/a) + 2ir[\exp(i\theta)](t-a)\cos(\pi t/a) & \text{if } t < a, \\ 0 & \text{if } t > a. \end{cases}$$

Thus the integral of $(\pi A^2/2a^2)z(\omega)$ around the small semicircles tends to the following value as the radius r tends to zero:

$$(46) \quad (\pi A^2/2a^2) \int_A^B + (\pi I^2/2a^2) \int_C^D = \begin{cases} \frac{U(b^2 + \pi^2/a^2)}{b^2} (1-t/a)\cos(\pi t/a) & \text{if } t < a, \\ 0 & \text{if } t > a. \end{cases}$$

Integration of $(\pi A^2/2a^2)z(\omega)$ around the contour shown in Fig. 3 shows that

$$(47) \quad \phi(t) = -(\pi A^2/2a^2) \int_A^B - (\pi A^2/2a^2) \int_C^D,$$

which by (46) leads to the result (40). In the proof it has been assumed that $t > 0$. The modulus sign appears in (40) since $\phi(t)$ is clearly an even function of t .

REFERENCES

- DWORK, B. M. 1950. *Proc. Inst. Radio Engrs.* **38**, 771.
- HEAPS, H. S. and ISAACS, A. T. 1958. *Electronic and Radio Engr.* (in press).
- HEAPS, H. S. and MCKAY, M. R. 1958. *Proc. Inst. Elec. Engrs. (London)*, Pt. C, Monograph No. 297R, March 1958.
- PALEY, R. E. A. C. and WIENER, N. 1934. *Fourier transforms in the complex domain* (American Mathematical Society Colloquium Publications, Vol. XIX, New York), p. 16.
- SNEDDON, I. N. 1951. *Fourier transforms* (McGraw-Hill Book Co., Inc., New York), p. 24.
- WEINSTOCK, R. 1952. *Calculus of variations* (McGraw-Hill Book Co., Inc., New York), p. 48.
- ZADEH, L. A. and RAGAZZINI, J. R. 1952. *Proc. Inst. Radio Engrs.* **40**, 1223.

THÉORIE DE LA DIFFUSION AU COURS DU DÉVELOPPEMENT DES COUCHES IONOGRAPHIQUES ÉPAISSES¹

PIERRE DEMERS

SOMMAIRE

On démontre que, d'accord avec l'expérience, la durée des diverses étapes du développement (révélateur, arrêt, fixage, lavage, séchage) est proportionnelle au carré de l'épaisseur efficace. L'épaisseur efficace est l'épaisseur vraie de la couche sensible, augmentée d'une constante comprise entre 25 et 100 μ .

En photographie ordinaire, on ne s'est pas beaucoup préoccupé d'analyser les phénomènes de diffusion, et la vitesse des opérations dépend surtout de facteurs chimiques. Au contraire, la diffusion est primordiale dans le traitement des couches épaisses. On a constaté que la durée des diverses étapes est à peu près proportionnelle au carré de l'épaisseur. Nous allons examiner la théorie correspondante, qui justifie ce résultat.

Par unité de surface, la tranche x , dx d'émulsion renferme la quantité cdx d'une substance, c en g/cm^3 . Cette quantité varie avec le temps au taux $\partial c/\partial t$. Par la face x , il pénètre par unité de temps la quantité $-k(\partial c/\partial x)_x$, proportionnelle au gradient des concentrations au point x , et à k constante de diffusion en $\text{cm}^2 \text{sec}^{-1}$. Par la face $x+dx$ il pénètre $k(\partial c/\partial x)_{x+dx}$. En écrivant le bilan on trouve l'équation différentielle fondamentale lorsque les surfaces d'égale concentration sont planes:

$$\partial c/\partial t = k\partial^2 c/\partial x^2$$

qui devient dans le cas à trois dimensions:

$$\partial c/\partial t = k\Delta c.$$

La même équation, avec des significations différentes pour k et pour c , représente la conduction de la chaleur et celle de l'électricité.

Avec plusieurs hypothèses simplificatrices, notamment en négligeant les variations concurrentes de l'épaisseur et du coefficient de diffusion, lesquelles se compensent à peu près, nous allons distinguer et résoudre trois problèmes fondamentaux.

(1) Dans le *fixage*, le thiosulfate doit diffuser de la face d'entrée jusqu'au niveau de la masse de bromure d'argent, à travers une épaisseur x . La concentration est c_0 à la surface ou plutôt à une certaine distance extérieure à celle-ci, ce qui équivaut à accroître de l l'épaisseur L à traverser. La concentration s'annule au contact du bromure d'argent, ou à une distance plus grande si celui-ci est plus difficile à fixer, ce qui équivaut à accroître L (figure 1).

La vitesse avec laquelle le niveau de fixage se rapproche du fond de la couche, verre ou plan de symétrie de la feuille, est

$$[1] \quad dx/dt = bc_0/(x+l).$$

¹Manuscrit reçu le 26 décembre 1957.

Contribution de l'Institut de Physique, Université de Montréal, Montréal, Québec.

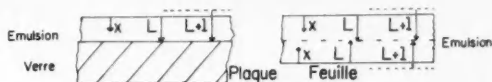


FIG. 1.

Le fixage est terminé quand $x = L$, sa durée est donc $L(L+l)/bc_0$. Pour $L \ll l$, la durée est proportionnelle à l'épaisseur. Pour $L \gg l$, la durée est proportionnelle au carré de l'épaisseur. Les durées observées ou recommandées pour le fixage entre 25 et 1000 μ s'accordent bien avec cette formule si on prend $l = 25$ à 100 μ . Purslow (1946) a trouvé, dans des conditions uniformes d'agitation, avec des coins d'émulsion, une durée proportionnelle au carré de l'épaisseur.

(2) Pour l'imprégnation du révélateur et pour l'arrêt, nous adoptons le critère suivant. L'étape est terminée quand la concentration au fond de la couche, pour $x = L$, est devenue suffisamment voisine de la concentration extérieure c_0 . Cette condition est nécessaire pour assurer l'uniformité du développement. Supposons une couche d'épaisseur L contenant au début une concentration c_1 . Au temps zéro, elle est plongée dans un milieu de composition constante c_0 . En appliquant l'équation générale, on trouve pour la concentration c une expression où apparaissent la profondeur x et le temps t :

$$[2] \quad c = c_1 + (c_0 - c_1) (2/\sqrt{\pi}) \sum (-1)^n \left[\int (\exp - u^2) du + \int (\exp - v^2) dv \right].$$

La première intégrale est prise de $u = (2nL+x)/(4kt)^{1/2}$ à $u = \infty$, la seconde, de $v = (2nL+2L-x)/(4kt)^{1/2}$ à $v = \infty$, et la sommation va de $n = 0$ à $n = \infty$. Pour $x \ll L$ ou pour $L = \infty$, l'expression se simplifie:

$$[3] \quad c = c_1 + (c_1 - c_2) (2/\sqrt{\pi}) \int (\exp - u^2) du, \quad u = x/(4kt)^{1/2} \text{ à } u = \infty.$$

Mais ce n'est pas le cas ici, puisque nous posons $x = L$. Nous trouvons pour ce cas, en étendant la sommation de $n = 0$ à $n = \infty$:

$$[4] \quad c = c_1 + (c_0 - c_2) (4/\sqrt{\pi}) \sum (-1)^n \int (\exp - u^2) du, \quad u = (2n+1)L/(4kt)^{1/2} \text{ à } u = \infty.$$

La concentration pour $x = L$ dépend donc de L et de t uniquement par l'intermédiaire du quotient L^2/t . La durée de l'étape est proportionnelle au carré de l'épaisseur. Accroissons l'épaisseur de la distance extérieure l comme dans (1) et pour la même raison. La durée est proportionnelle à $(L+l)^2$. Ce résultat théorique s'accorde bien avec les mesures de Dainton, Gattiker et Lock (1951) sur la pénétration du révélateur. Ces auteurs ont représenté leurs mesures par la loi $L^{1.4}$, mais leurs mesures s'accordent aussi bien sinon mieux avec la loi $(L+l)^2$, en prenant $l = 25$ à 100 μ .

(3) Pour le lavage et le séchage nous adoptons plutôt le critère suivant. Il faut que la concentration moyenne dans l'épaisseur de la couche, en thiosulfate ou en eau, devienne suffisamment voisine de c_0 . La quantité de substance qui traverse la face $x = 0$ est $dm/dt = k(\partial c/\partial x)_{x=0}$, par unité de surface, c'est-à-dire

$$[5] \quad dm/dt = -[k(c_0 - c_1)/(\pi t)^{1/2}][1 + \sum (-1)^n \exp(-n^2 L^2/kt)].$$

La sommation va de $n = 1$ à $n = \infty$. La concentration moyenne est accrue de $(1/L) \int (dm/dt) dt$:

$$[6] \quad c_{\text{moy}} = c_1 + (c_0 - c_1)(2/\sqrt{\pi}) \int [1 + \sum (-1)^n \exp(-1/w^2)] dw.$$

L'intégrale est prise de $w = 0$ à $w = (kt)^{1/2}/L$.

La concentration moyenne dépend de L et de t uniquement par l'intermédiaire du quotient L^2/t , ou $(L+l)^2/t$ en ajoutant à l'épaisseur la distance extérieure. La durée ici encore est proportionnelle au carré de $L+l$. Les durées recommandées pour le lavage et pour le séchage s'accordent avec cette loi, si on prend $l = 25$ à 100μ . Il est satisfaisant que la même valeur du paramètre l se retrouve dans la solution des trois problèmes. Si la théorie est exacte, l'agitation devrait réduire la valeur de ce paramètre.

Barkas (voir Oliver 1954), à l'aide de telles équations, a représenté les mesures d'Oliver sur le séchage d'une plaque G5 de 884μ , initialement en équilibre à l'humidité relative 50% et contenant $c_1 = 0.0537$ g d'eau par cm^3 d'émulsion, placée dans le vide absolu au temps zéro. Il a déduit $k = 6.58 \times 10^{-6} \text{ cm}^2/\text{jour}$, $L^2/k = 12$ jours. Après 28 jours il reste encore 12% de l'eau initiale. Une couche épaisse placée dans le vide n'atteint l'équilibre qu'après un temps très long, et d'ordinaire ce faisant, elle s'arrache de son support. Dans une couche non en équilibre, la teneur en noyaux d'hydrogène et le pouvoir d'arrêt varient d'un point à l'autre (voir aussi Oliver et Barkas 1952; Oliver 1950).

REMERCIEMENTS

Je remercie pour leur aide financière le Conseil National des Recherches (Canada), et l'Office des Recherches Scientifiques (Québec).

RÉFÉRENCES

- DAINTON, A. D., GATTIKER, A. R. et LOCK, W. O. 1951. *Phil. Mag.* **42**, 396.
 OLIVER, A. J. 1954. *Rev. Sci. Instr.* **25**, 326.
 OLIVER, A. J. et BARKAS, W. H. 1952. *Phys. Rev.* **85**, 756.
 PURSLOW, E. T. 1946. *SELO Phys. Lab.*, File 1479, No 9/46.

LOW-FIELD MOBILITY OF CARRIERS IN NONDEGENERATE SEMICONDUCTORS¹

MAHENDRA SINGH SODHA² AND DESH BANDHU AGRAWAL³

ABSTRACT

Gunn's theory of the low-field variation of carrier mobility has been extended, using Morgan's analysis to include the effect of scattering by a single optical mode of lattice vibrations. Numerical results obtained for *n*-germanium show that there is still a serious disagreement between theory and experiment.

INTRODUCTION

Gunn (1957) has shown that for low electric fields the relationship between mobility μ of carriers in a nondegenerate semiconductor and field E can be expressed as

$$\mu = \mu_0(1 + \beta_0 E^2),$$

where

$$\beta_0 = -(3\pi/64c^2)\mu_0^2,$$

c is the velocity of sound in the crystal,

μ_0 is the zero-field mobility,

and the scattering due to optical modes and ionized impurities is neglected.

Measurements of small quadratic changes in mobility with field have been limited to *n*-type germanium and summarized by Gunn (1957). It is seen that the experimental values of β are 10–100 times lower than that predicted by Gunn. In this communication the authors have derived an expression for β assuming only one optical mode of lattice vibrations of frequency ν to be present. Numerical computations for *n*-type Ge have also been made.

TIME OF RELAXATION

The times of relaxation due to scattering of carriers by acoustic modes, absorption of the optical phonon, and emission of the optical phonon are given by

$$(1A) \quad 1/\tau_1 = W_0 x^{1/2},$$

$$(1B) \quad 1/\tau_2 = BW_0(x + x_0)^{1/2},$$

and

$$(1C) \quad 1/\tau_3 = BW_0 e^{x_0} \text{Re}(x - x_0)^{1/2},$$

where $W_0 \propto T_0^{3/2}$,

T_0 is the temperature of the crystal,

$$x = \epsilon/kT_0,$$

¹Manuscript received February 24, 1958.

Contribution from the Department of Physics, University of British Columbia, Vancouver, British Columbia.

²University of British Columbia.

³25/13 East Patel Nagar, New Delhi 12, India.

ϵ is the energy of the carrier,

k is Boltzmann's constant,

$$B = bx_0/2(e^{x_0} - 1),$$

$$x_0 = h\nu/kT,$$

h is Planck's constant,

b is a constant to be determined by fitting the theoretical variation of zero-field mobility with temperature,

and $\text{Re}(x-x_0)^{1/2}$ denotes the real part of $(x-x_0)^{1/2}$.

The net time of relaxation is given by

$$(1) \quad \tau = \left\{ \frac{1}{\tau_1} + \frac{1}{\tau_2} + \frac{1}{\tau_3} \right\}^{-1} = W_0^{-1} [x^{\frac{1}{2}} + B \{ (x+x_0)^{\frac{1}{2}} + e^{x_0} \text{Re}(x-x_0)^{\frac{1}{2}} \}]^{-1}.$$

ENERGY DISTRIBUTION OF CARRIERS

We may assume with various previous workers that the field in effect raises the carriers to a temperature T , higher than the temperature T_0 of the crystal, the energy distribution being still Maxwellian and given by

$$(2) \quad N(x)dx = Ax^{1/2}e^{-\lambda x}dx,$$

where $N(x)dx$ is the number of carriers in the energy range x to $x+dx$ and $\lambda = T_0/T$.

MOBILITY CONSIDERATIONS

The mobility of carriers for a Maxwellian distribution of energies is given by

$$(3) \quad \mu = \frac{q}{m} \frac{\langle \tau x \rangle}{\langle x \rangle},$$

where q and m are the charge and effective mass of carriers and $\langle \rangle$ denotes average over the whole distribution.

From Eqns. (1A), (2), and (3) the zero-field acoustical mobility is given by

$$\mu_{a,0} = 4qW_0^{-1}/3m\sqrt{\pi}.$$

By using Eqns. (1), (2), and (3) Morgan (1957) has shown that the mobility of carriers at a temperature T is given by

$$(4) \quad \mu = \mu_{a,0}\lambda^{1/2}I(x_0, \lambda) \approx \mu_0\lambda^n \quad (\text{for a large range of } x_0)$$

where $n \sim \frac{1}{2}$,

$$I(x_0, \lambda) = 1 - B \{ 1 + e^{(1-\lambda)x_0} \}^{\frac{1}{2}} \lambda x_0 \cdot e^{\lambda x_0/2} \cdot K_1(\lambda x_0/2) \\ + B^2 [1 + e^{(2-\lambda)x_0} + \lambda x_0 \{ 2e^{x_0} K_1(\lambda x_0) + 1 \}],$$

μ_0 is the zero-field mobility given by

$$(4A) \quad \mu_0 = \mu_{a,0}I(x_0, 1) \\ = \mu_{a,0} [1 - Bx_0e^{x_0/2}K_1(x_0/2) + B^2 \{ 1 + e^{x_0} + x_0(2e^{x_0}K_1(x_0) + 1) \}],$$

and $K_1(x)$ is a Bessel function of the second kind of imaginary argument.

STEADY STATE

In steady state the average power loss in scattering should be balanced by power gain from the field. Thus we obtain

$$(5A) \quad q\mu E^2 = \frac{2}{\pi^{1/2}} W_0 \lambda^{-1/2} 4mc^2 \left(\frac{1}{\lambda} - 1 \right) + \langle h\nu/\tau_3 \rangle - \langle h\nu/\tau_2 \rangle.$$

The first term represents the average power lost to acoustical modes and was evaluated by Shockley (1951). Morgan (1957) has given the complete result as

$$(5) \quad q\mu E^2 = \frac{2}{\pi^{1/2}} W_0 \lambda^{-1/2} \left[4mc^2 \left(\frac{1}{\lambda} - 1 \right) + Bh\nu(\lambda x_0/2) e^{\lambda x_0/2} K_1(\lambda x_0/2) \right. \\ \left. \times \{e^{(1-\lambda)x_0} - 1\} \right].$$

LOW-FIELD MOBILITY

We are now in a position to obtain a simple expression for low-field mobility. This is important because the experimental technique and interpretation of results is much simpler at low fields.

At low electric fields $T \approx T_0$ and $\lambda \approx 1$; hence from Eqn. (4) we obtain

$$(6) \quad \mu = \mu_0 \{1 - n(1 - \lambda)\} = \mu_0(1 + \beta E^2),$$

where $\beta = -n(1 - \lambda)/E^2$.

Putting $\mu = \mu_0$ at low fields and $\lambda \approx 1$ in Eqn. (5) we obtain

$$(7) \quad \frac{1 - \lambda}{E^2} = \frac{3\pi\mu_{a,0}}{32c^2} F(x_0),$$

where

$$F(x_0) = \frac{I(x_0, 1)}{1 + (Bh\nu/8mc^2)x_0^2 e^{x_0/2} K_1(x_0/2)}.$$

From Eqns. (6) and (7) we obtain

$$(8) \quad \beta = 2n\beta_0 F(x_0).$$

When no optical modes are present $B = 0$, $n = \frac{1}{2}$, $F(x_0) = 1$, and $\beta = \beta_0$, the value obtained by Gunn (1957).

Since $\mu_{a,0} \propto x_0^{3/2}$, the temperature variation of β is given by $x_0^3 F(x_0)$.

n-GERMANIUM

By fitting Eqn. (4A) to the observed temperature variation of mobility $\mu_0 \propto x_0^{1.66}$, Morgan (1957) has evaluated $b = 0.34$. Studying the behavior of $I(x_0, \lambda)$ with λ Morgan found that $n = 0.62$ for a large range of x_0 . We may also use the values $h\nu/k = 320^\circ \text{K}$, $c = 5.4 \times 10^8 \text{ cm./sec.}$ and the effective mass m , where

$$\frac{1}{m} = \frac{1}{3} \left\{ \frac{1}{1.58} + \frac{2}{0.082} \right\} \frac{1}{m_0},$$

m_0 being the free electronic mass.

Table I gives the variation of β/β_0 and $x_0^3 F(x_0)$ with temperature.

TABLE I
THEORETICAL VARIATION OF β/β_0 AND $x_0^3 F(x_0)$ WITH
TEMPERATURE FOR *n*-GERMANIUM

T_0 ° K.	$x_0 = \hbar\nu/kT_0$	β/β_0	$x_0^3 F(x_0)$
640	0.5	0.949	0.0956
457	0.7	0.722	0.1998
356	0.9	0.693	0.4076
320	1.0	0.683	0.5505
267	1.2	0.668	0.9303
229	1.4	0.6604	1.4614
213	1.5	0.6596	1.7952

As mentioned in the introduction the experimental values of β are 10 to 100 times lower than β_0 . The consideration of an optical mode does give lower theoretical values for β but still the disagreement between theory and experiment is quite serious.

ACKNOWLEDGMENTS

One of the authors (M.S.S.) is grateful to Dr. G. M. Shrum for kind encouragement and to Professor R. E. Burgess for helpful discussion. He is also grateful to the National Research Council of Canada for the award of a fellowship.

REFERENCES

- GUNN, J. B. 1957. Progress in semiconductors, Vol. 2, *edited by* A. F. Gibson (John Wiley & Sons, Inc., New York).
 MORGAN, T. N. 1957. Final Report on TR Tube Spike Leakage Investigation (1 Oct., 1955 to 31 March, 1957) (Electrical Engineering Laboratory, University of Illinois, Urbana, Ill.).
 SHOCKLEY, W. 1951. Bell System Tech. J. **30**, 990.

ON THE DISPLACEMENT OF AN ION BEAM IMAGE BY MAGNETIC FRINGING FIELDS¹

LARKIN KERWIN

ABSTRACT

Some of the methods proposed for calculating the effect of the magnetic fringing field on the image position of an ion beam are reviewed, and applied to the case of a particular instrument. The differences between the calculated corrections and the observed image suggest an improved method of calculating the image position. Applied to the case under consideration, this method gives essentially the correct image position.

1. INTRODUCTION

One difficulty which presents itself in ion and electron spectrometer design is that the magnetic field extends beyond the limit of the pole piece boundaries, dropping gradually to zero as the distance increases. The trajectory of an ion beam originating outside the pole pieces will therefore curve a certain amount before entering the region between the pole pieces. Theoretical treatments of ion trajectories frequently assume magnetic fields which terminate sharply at the pole boundary, and one effect of the fringing field is to shift the point of image formation from that predicted by such theories. Several methods of correcting for this effect have been proposed, and it is the purpose of this article to assess some of them, apply them to a particular case, and suggest an improved method.

2. ION BEAM TRAJECTORY

The first step in considering the effect of the fringing field is to plot its intensity. This has been done theoretically by Coggeshall (1947) and Reutersward (1952), who obtain essentially the same curve, which is shown in Fig. 1.

This figure gives the magnetic field intensity $h(x)$ (as a fraction of the maximum uniform field measured well within the pole boundaries) as a function of the normal distance from the pole boundary. The function is for the field in the central plane, which the fringing field lines all cross normally. The curve is largely independent of the thickness of the pole pieces (parameter n , Fig. 1). Careful measurements made by Barnard (1956), König and Hintenberger (1955), and others of the fringing field of their magnets confirm this theoretical curve, and it is to be noted that Barnard uses a relatively wide pole gap.

The next step is to consider the precise trajectory of the ion beam in this varying fringe field. Coggeshall's approach, which is the basis for several final corrections, is indicated in Fig. 2.

An ion source at x_0 sends an ion beam into the magnetic field, and in the absence of a fringing field the ion trajectory would be as indicated by the dotted line. The point (0, 0) where the ion beam enters the pole gap is taken as the

¹Manuscript received February 7, 1958.

Contribution from the Département de Physique, Université Laval, Quebec.

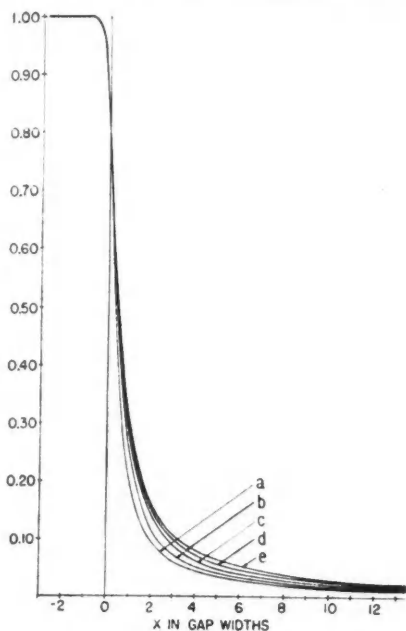


FIG. 11. Magnetic fringing field intensity (after Coggeshall 1947): *a*, $n = 1$; *b*, $n = 2$; *c*, $n = 5$; *d*, $n = 10$; *e*, $n = \infty$ (n = pole thickness/ $(\frac{1}{2}$ gap)).

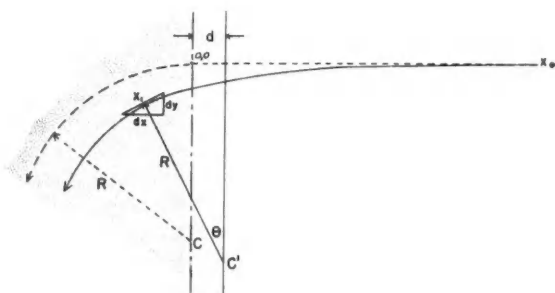


FIG. 2. Deviation of ion beam by fringing field.

center of rectangular coordinates, which are parallel to the initial ion beam direction and pole boundary respectively. We note that the center of curvature *C* of this trajectory in the magnetic field is situated on the pole boundary.

Now in the presence of a fringing field, the ion beam follows the trajectory indicated by the continuous line, which curves increasingly as it approaches the pole boundary. Once within the region of constant field, this trajectory

becomes circular, with the same radius of curvature as the dotted trajectory. However, the center of curvature C' is situated outside the pole boundary, a distance d from it.

To calculate d one may proceed as follows. Coggeshall has shown that the differential equation of the ion trajectory is given by

$$(1) \quad \frac{dy}{dx} = \frac{f}{(R^2 - f^2)^{1/2}},$$

where R is the radius of curvature mentioned and f is given by

$$(2) \quad f = \int_{x_0}^x h(x) dx,$$

where the integration is performed over the distance from the source x_0 to the point x at which dx/dy is measured.

In Fig. 2, d is given by

$$(3) \quad d = R \sin \theta + x_1.$$

From the geometry of the figure we have

$$(4) \quad \frac{dy}{dx} = \tan \theta = \frac{R \sin \theta}{(R^2 - R^2 \sin^2 \theta)^{1/2}}.$$

From (1) and (4), we have

$$R \sin \theta = f = \int_{x_0}^x h(x) dx.$$

If x_1 in eqn. (3) is conveniently chosen 1 gap width inside the pole boundary (where the field has become constant for all practical purposes), then the value of d becomes (in gap widths)

$$(5) \quad d = \int_{x_0}^{x_1} h(x) dx - 1.$$

To calculate d , a numerical integration of the fringing field as given by Fig. 1 must be made between the limits x_0 and x_1 . For this and other purposes (such as the calculation of y_0 , which is to be mentioned) Table I is useful. It gives the value of $\int h(x) dx$ between various limits of x . Bainbridge (1953) gives the equivalent graphical result (Fig. 3).

TABLE I

From		to		$\int h(x) dx =$
-2G		-1G		1.00G
-1G		0		0.98G
0		1G		0.55G
1G		2G		0.21G
2G		3G		0.12G
3G		4G		0.08G
4G		5G		0.06G
5G		6G		0.05G
6G		7G		0.04G
7G		8G		0.04G
8G		12G		0.12G
12G		20G		0.08G

It is important to note that d depends *not only on the magnet but also on the source or detector distance from the magnet.*

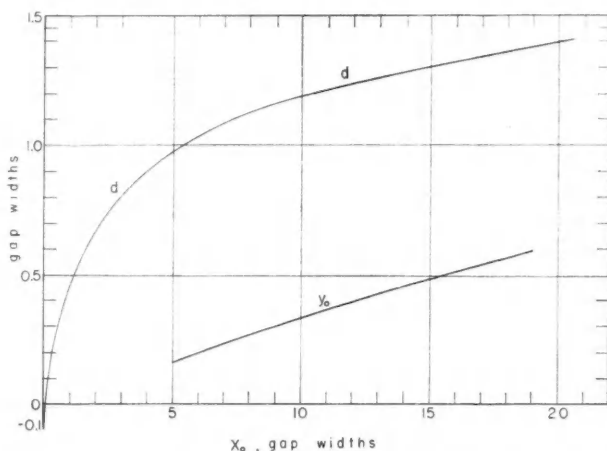


FIG. 3. Fringing field parameters (after Bainbridge 1953). d , separation of the effective field boundary from the actual field boundary; y_0 , sideways displacement of the ion trajectory at $x = 0$ (for $R = 10$ gap widths).

3. SUGGESTED CORRECTIONS

Once d (the distance of the center of curvature C' from the pole boundary) has been calculated, the third step is to decide how to apply it, and unfortunately not enough measurements have been published which give a clear indication of what experimental arrangements correspond to an optimum allowance for this fringing field. Several procedures have been proposed, as indicated in Fig. 4.

Procedure (a) has been followed by Nier (1940)* and many others. The value d is calculated from equation (5), read from Fig. 3, or arbitrarily chosen as 1 gap width (Nier and others). "Effective" boundaries are drawn parallel to the real boundaries at a distance d from them, and the effective field apex, source, and detector are placed in a straight line (for the normal case, here being considered as an example). Analogous procedures are used for inflection or asymmetric magnets. Usually fine adjustment is made for optimum focusing by moving the spectrometer tube relative to the magnet. The precise amount of this final adjustment is never published, and may convert this procedure into one of the others.

At this point, it should be mentioned that a range of corrections by this method is possible. If the magnetic field is considered as being extended a distance d , then a larger radius of curvature for the ion beam may be used.

*Popularized by Nier, this type of correction has been used since the early days of mass spectrometry (e.g. Smyth, W. R., Rumbaugh, L. H., and West, S. S., *Phys. Rev.* **45**, 724 (1934). Professor Bainbridge points out that J. J. Thomson may have been the first to use it. His work on fringing field may be glimpsed in such papers as *Phil. Mag.* **24**, 209 (1912).

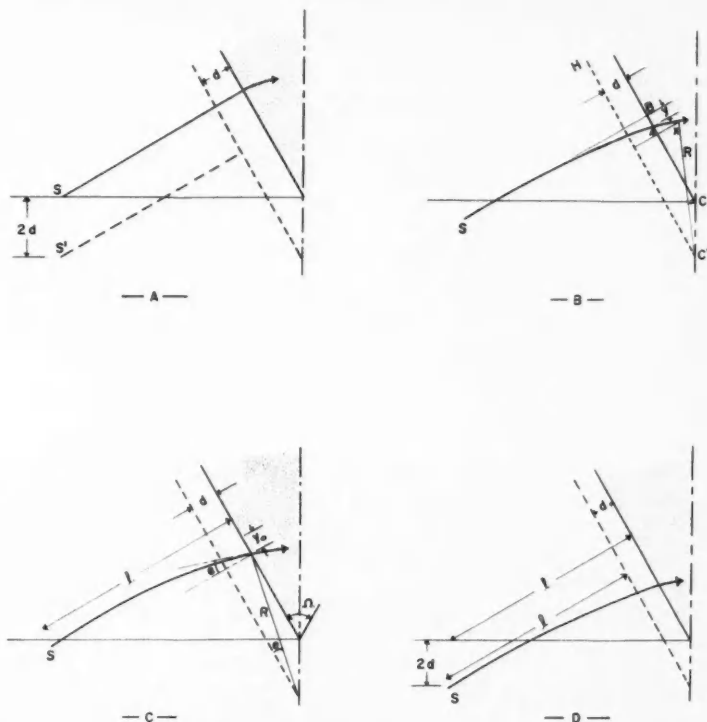


FIG. 4. Various methods of correcting for fringing field: A, Nier; B, Coggeshall; C, Bainbridge; D, Reuterswärd.

On the other hand, the radius of curvature pertinent to the non-extended field may be used, in which case the extended boundaries cause an increased deviation and a changed angle of entry. Between these two extreme cases, intermediate solutions may be chosen. Usually the first type of correction is applied.

Procedure (b) has been suggested by Coggeshall. The source S is placed relative to the pole faces as though no fringe field existed. The ray trajectory from S is then traced into the magnet as previously discussed, and d and the center of curvature C' established. Line $C'C$ at $\Omega/2$ with $C'H$ is then drawn, where Ω is the angle of beam deflection, which is equal to the wedge angle of the magnet in the normal field case. This establishes point C , and distance CB may then be calculated from a knowledge of point S . The advantage of this method is that, as shown by Coggeshall, the angular and spatial separation of the rays is the same in the effective field as in the ideal field, and symmetrical conditions are maintained. The procedure is criticized by Bainbridge and Reuterswärd on the grounds that since the ion beam does not enter the effective

magnetic field normally, the conditions for normal focusing do not apply, and thus the image will not be formed symmetrically. There is no doubt on this score, and anyone applying Coggeshall's procedure would have to make some adjustments.

Procedure (c) is suggested by Bainbridge. d having been calculated by eqn. (5) or otherwise, it is used to calculate e , the angle of entry of the ion beam into the pole boundaries, as indicated in Fig. 4c. e is given by

$$(6) \quad \tan e = d/(R^2 - d^2)^{1/2}.$$

From this value of e and the design angle Ω of the magnet apex, the image distance l may be calculated. There remains to calculate y_0 , the normal displacement from the ideal ion trajectory of the source. y_0 is the sideways displacement of the ion beam as it travels from the source to the pole boundary, and it is given from eqn. (1) as:

$$(7) \quad y_0 = \int_{x_0}^{x_b=0} \frac{h(x)dx}{(R^2 - (\int h(x)dx)^2)^{1/2}} dx$$

and is obtained by numerical integration over the limits x_0 to x_b at the pole boundary. y_0 has been calculated by Bainbridge for the special normal case of $R = 10$ gap widths, and is shown in Fig. 3. To summarize, d and Ω being given, e , l , and y_0 are calculated, which situates the source and detector symmetrically about the magnet.

Procedure (d) has been evolved by Reuterswärd. After deriving graph (1) and an expression for d which is similar to eqn. (5) by somewhat different methods, he places the source and detector at distances from the *effective* field boundary which are the same as those which would be used were no fringing field present. Except for the determination of d , this method produces a similar result to (a). Reuterswärd adopts it because for the normal case he has shown that the total deviation produced by the total field is the same as would be produced for the fringeless field. His correction is shown in Fig. 4d.

Ploch and Walcher (1950) have also considered the fact that the effective field is not only displaced laterally from the real field boundary, but also angularly. They find for the normal case that there would be an effective angular shift of d/R , and thus the deflection would be changed by a similar amount.

Herzog (1955) has extended the consideration of fringing field to the general case of oblique incidence. He sets up first a sharply delineated substitute field which will produce the same deflection of the ion beam as the real field (including its fringe). The initial and final directions of the real beam are thus parallel to the initial and final directions of the substitute ion beam (which coincides with the real one inside the pole gap) drawn for the substitute field. The substitute beam is used to calculate the positions of substitute source and image, and the displacement of the real source and image from these is given.

4. CALCULATED CORRECTIONS

Some of these corrections are now calculated for the precision mass spectrometer described by Barnard. In this instrument the magnet gap width is 1.20 in.

$= G$, the radius of curvature of the ion trajectory in the gap is 4.00 in. $= 3.33G$, and the angle of the normal sector magnet is 60° . These data are indicated in Fig. 5. We see that were no fringing field present, the source would be placed at a distance $R \cot \theta = 6.93$ in. or $5.77G$ from the pole boundary.

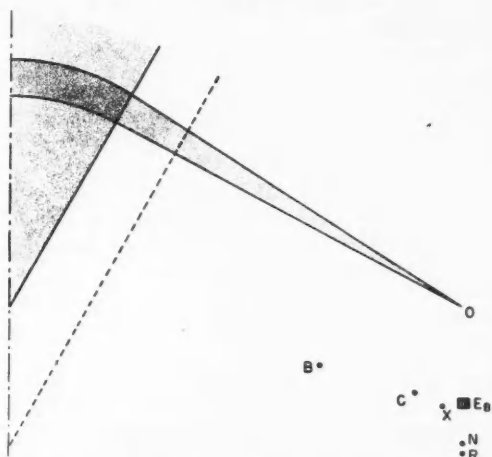


FIG. 5. Various calculated positions of image for Barnard's magnet. O , without fringing field; B , Bainbridge; C , Coggeshall; N , Nier; R , Reutersward; E_B , Barnard (experimental); X , this paper.

(a) *Nier's method*.—It may be calculated from eqn. (5), or read from Fig. 3, that the effective field boundary distance from the pole boundary is $1.02G$. (Note that this is calculated for the source as shown.) Nier has suggested that d be arbitrarily taken as equal to G , and in the case of Barnard's magnet this is an excellent approximation. These effective boundaries lower the apex of the effective field a distance $2d = 2G = 2.4$ in. R and θ are the same, so that the source position according to Nier should be placed at the point indicated by N in Fig. 5.

(b) *Coggeshall's method*.—Here the source is placed at the distance $5.8G = 6.93$ in. from the pole boundary as though no fringing field existed. Integrating the fringing field effect to 1 gap width inside the real boundary (eqn. 2) gives $f = 2.04G$, which is equivalent to d calculated in (a). From eqn. (1) we next obtain $dx/dy = 0.775$, whence the slope of the ion beam at this point is 37.8° and y (the lateral displacement of the ion beam at this point from the initial beam direction) $= 1.14G$ or 1.37 in. Added to $R \cos 37.8^\circ$, this gives us the lateral displacement of the effective center of curvature C' from the initial ion beam direction. This is $3.77G = 4.52$ in. The point C where the real magnet apex must be placed is given as being $1.04G \operatorname{cosec} 30^\circ = 2.50$ in. from C' , in the vertical direction of Fig. 5. From these values and the geometry of Coggeshall's method, we finally obtain that S must be 7.17 in. from the center of the field and 1.37 in. below the vertex of the real magnet. This point, C , is shown in Fig. 5.

(c) *Bainbridge's method*.—A preliminary estimation of d ($= 1G$) applied to eqn. (6) gives an angle of entry $e = 17.5^\circ$. The image distance l may then be calculated as being $4.30G$. This gives a more precise limit over which to integrate the fringing field effect and a better value of d ($= 0.96G$), giving in turn a better $e = 16.6^\circ$ and a better l equal to $4.37G = 5.25$ in. From eqn. (7), y_0 is determined by numerical integration, and is equal to 0.47 in. From the geometry of the figure it may then be established that the source should be placed at the point indicated by B in Fig. 5.

(d) *Reutersward's method*.—The source is placed at the same distance from the effective field as it would be from the real field were no fringing field present. This is $R \cot 30^\circ = 6.93$ in. The source is thus farther from the real field than in the previous cases, and thus d is calculated by successive approximations as being $1.1G = 1.3$ in. His source, effective apex, and detector are in line, and thus the source is placed $2.2G = 2.64$ in. below the real magnet apex, at R as shown in Fig. 5.

5. OBSERVED CORRECTION

Experimental Focus

Barnard has made very careful measurements of the position of best focus for his instrument, and the experimentally determined optimum source location is indicated as E_B in Fig. 5, 8 in. from the central axis, and 1.69 in. below the magnet apex. Although the source-detector separation seems to have been fixed during the experiment, rotation of this line relative to the magnet produced no improvement, as might have been expected if this distance were not indeed optimum.

It is to be noted that of the various corrections considered thus far, those of Nier and Reutersward correspond most closely to the measured position, and so for this particular instrument at least, the rule of thumb that the effective field extends a gap width from the real magnet is as good as any.

Perusal of Fig. 5 permits the following criticisms of the various proposed corrections. Nier's method does not take into account the oblique entry of the beam into his effective field, which results in his calculated point being laterally displaced from the measured focal point. Coggeshall's method, as indicated by Bainbridge and Reutersward, calculates the curvature faithfully, but the source being displaced towards the magnet, the image will not be located symmetrically, but at a greater distance from the magnet than the source distance. This is indicated by his calculated point of best focus being displaced towards the magnet. Bainbridge's method correctly takes into account the oblique entry of the ion beam into the real pole face boundary because of the fringing field effect, but neglects the effective enlargement of the real field by the fringing field. He thus calculates for a smaller field than is actually present, as indicated by the displacement of his calculated point towards the magnet. Reutersward has taken into account both the oblique entry of the beam and the effective extension of the real field by the fringing field, but in his rule for the correction for the normal case he omits the lateral displacement effect of e and so obtains a point close to Nier's.

6. SUGGESTED IMPROVEMENT

Suggested Method (e)

Consideration of the points raised in the last paragraph leads inevitably to a combination of the arguments advanced by the various authors in the following method. Physically the ion beam will have a center of curvature which if symmetrically located below the apex of the real magnet locates two effective boundaries which may be considered as containing the bulk of the effective field. These boundaries may therefore be used to calculate the object and image positions of a beam entering them obliquely, at an angle determined by the bending of the ion beam in the fringing field *outside* of the *effective* boundaries. The calculation of the source position by this method follows closely the procedure outlined by Bainbridge.

Applied to Barnard's magnet this method gives the following results:

(a) d is selected to a first approximation as being equal to $1G$.

(b) l is selected to a first approximation as being equal to $R \cot 30^\circ = 5.77G$ from the effective boundary (i.e. $6.77G$ from the real pole boundaries).

(c) From eqn. (1) the slope of the ion beam as it enters the effective field is calculated, using eqn. (2) with limits $6.77G$ and $1G$, and Fig. 1 or Table I. This gives $dy/dx = \tan e = 0.167$, whence $e = 9.5^\circ$.

(d) Using the design angle of the effective field of 60° and $e = 9.5^\circ$, l may be calculated by Herzog's method, and is found to be equal to $5.06G$.

(e) The result of (d) indicates that the inner limit of calculation (c) is more precisely $1.05G$ (from Fig. 3, or eqn. (5)); this new limit affects the calculation but little while of course the more precise outer limit is $6.11G$. A more accurate e is thus calculated, and is equal to 8.9° .

(f) From (e) a more precise value for l is calculated as in (d), and is equal to $5.12G$ from the effective field, or $6.17G = 7.4$ in. from the real pole boundary.

(g) Finally, y_0 is calculated by numerical integration from eqn. (1), with limits $6.17G$ and the real boundary. This calculation gives the lateral displace-

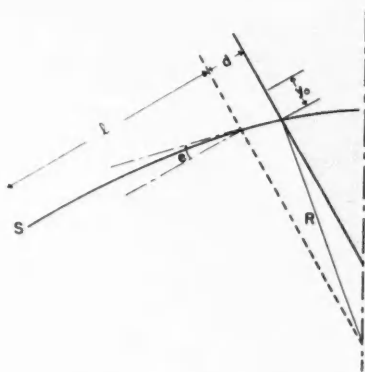


FIG. 6. Suggested construction for fringing field correction.

ment of the source from the line normal to the real field at the point of entry to it, and is 0.60 in.

The construction for this method of correcting for fringing field is indicated in Fig. 6. It has the advantage of taking into account the effective extension of the real field by the fringe field (Nier), the oblique entry of the ion beam into the magnetic field (Bainbridge), the lateral displacement of the ion beam caused by the exterior fringing field (Coggeshall), and provides the same total deflection and initial and final ion beam directions as the ideal field (Reutersward). This would seem to approximate closely the actual behavior of the real ion beam. In Fig. 5, the source position as calculated by this suggested method is shown at *X*. It is seen to coincide very closely with that measured by Barnard. More important, this calculated point is at the correct vertical height, and the slight sideways displacement might not have been detected by Barnard's tube-rocking experiment.

ACKNOWLEDGMENTS

We are pleased to note that this work was done as part of the mass spectrometry program supported by the National Research Council (T-45) and the Defence Research Board (9510-13).

REFERENCES

- BAINBRIDGE, K. T. 1953. In *Experimental nuclear physics*, Vol. I, edited by E. Segré (John Wiley & Sons, Inc., New York), p. 5.
BARNARD, G. P. 1956. *Mass spectrometer researches* (Her Majesty's Stationery Office, London).
COGGESHALL, N. D. 1947. *J. Appl. Phys.* **18**, 855.
HERZOG, R. K. F. 1955. *Z. Naturforsch.* **10a**, 887.
KÖNIG, L. A. and HINTENBERGER, H. 1955. *Z. Naturforsch.* **10a**, 877.
NIER, A. O. C. 1940. *Rev. Sci. Instr.* **11**, 212.
PLOCH, W. and WALCHER, W. 1950. *Z. Physik*, **127**, 274.
REUTERSWARD, C. 1952. *Arkiv Fysik*, **3**, 53.

THE ELECTRIC STRENGTH AND MOLECULAR STRUCTURE OF HYDROCARBON GASES¹

A. E. D. HEYLEN AND T. J. LEWIS

ABSTRACT

Precise measurements of the sparking potentials of a number of hydrocarbon gases over a wide range of pressure and electrode spacing are reported. The range has been extended beyond that reported earlier to include the *n*-paraffins up to *n*-octane and the olefins up to hexene-1. The effect of the triple bond in acetylene and conjugation in butadiene as well as the effects of cyclization are included. Careful experimental control involving the observation of prebreakdown pulses is an important feature of the measurements, and all the gases tested were of the highest purity.

A theoretical argument is given, relating the sparking potentials V_s to the molecular structure of the gases. This assumes a Townsend criterion for breakdown and a particular expression for the Townsend α coefficient. It is then possible to obtain information concerning the relative electron-scattering cross-sections of these hydrocarbons, which are related not to the molecular bonds as has been suggested earlier, but to individual atomic groups. With such a model, CH_3 and CH_2 groups and groups involving double or triple bonds have characteristic cross-sections. The theory then becomes closely allied to that for the ultraviolet spectra of these hydrocarbons. It appears that the present system of description is a more natural one than that involving bond cross-sections.

It is believed that dissociation occurs readily in many hydrocarbons and that photon action is small. This produces a value of γ (the second Townsend coefficient) which is very small ($\sim 10^{-8}$) in comparison with the value ($\sim 10^{-4}$) in more common gases. Such a low value can account for the considerable pulse activity observed in these hydrocarbon gases before breakdown occurs. Few pulses were observed in cyclopentane and cyclohexane, which do not dissociate readily, and it appears that a more usual value of $\gamma = 10^{-4}$ occurs in these particular gases.

1. INTRODUCTION

The relationship between molecular properties and the electric strength of gases has often been considered in the past, but the aim has usually been to obtain gases of high strength for industrial application. Consequently, interest has centered on electronegative gases, which unfortunately have complicated electrical and chemical properties so that results are not easily interpreted (see McCormick and Craggs 1954). The mechanism of electrical breakdown and the role of molecular properties in affecting electron-molecule collisions, which in turn determine the sparking potentials, can best be studied by investigating a series of gases having similar general properties but differing in detail in a known and systematic manner. Hydrocarbon gases, obtainable in a high state of purity, are ideally suited for this since they do not exhibit significant electron attachment, and recently there have been reported (Devins and Crowe 1954, 1956; Heylen and Lewis 1956; Crowe and Devins 1957; Heylen 1957 *a, b*) systematic studies of these. The present contribution extends the measurements of the sparking potential reported earlier (Heylen and Lewis 1956) to certain other important hydrocarbons and attempts an inter-

¹Manuscript received December 3, 1957.

Contribution from the Electrical Engineering Department, Queen Mary College, London, England.

pretation of the results which in many respects is different from the earlier explanation given by Devins and Crowe (1956). It is believed that a more careful control of certain important experimental conditions and an extended range of tests make the present interpretation more reliable.

2. EXPERIMENTAL PROCEDURE

The experimental procedure has been given in the previous communication by the authors and only needs to be outlined here. For each gas, the steady sparking potential V_s was determined over a suitable range of pd (pressure \times electrode spacing) using a uniform field spark gap. The pd range extended from 1 to 150 mm. Hg \times cm., the lower end of the range corresponding approximately to the minimum sparking potentials. Certain of the hydrocarbons are liquid at room temperature so that to obtain a satisfactory pd range for accurate interpretation of these, it was necessary to carry out tests at elevated temperatures by immersing the cell in a heated oil bath. For instance, n -octane was tested over the entire pd range at 113° C. The equilibrium temperature of the vapor in the cell was accurately measured by thermocouples, one of which was placed in one of the electrodes. Measurements of V_s versus pd were then corrected to normal temperature assuming an ideal gas law, which further tests at different temperatures showed to be justified.

When attempting to detect differences between gases of similar molecular structure it is important that traces of other hydrocarbons and impurities such as water vapor should be reduced to a minimum; otherwise anomalous results are obtained, especially at low pd values. For instance, tests on a sample of laboratory grade n -hexane having a boiling range of 60–70° C. produced a V_s versus pd characteristic which coincided with that of neopentane of 99.83% purity. A further example showing the effects of impurity in n -pentane is given in Fig. 1. For the final measurements reported here, hydrocarbons of the highest purity as certified by the Chemical Research Laboratory (D.S.I.R.) or by the National Bureau of Standards were used. These are listed in Table I.

TABLE I
PURITY OF THE HYDROCARBONS TESTED

Hydrocarbon	Purity, %	Most probable impurity
Methane	99.88 \pm 0.06	—
Ethane	100	Ethylene (cannot be detected)
Propane	99.99	—
n -Butane	99.50	—
n -Pentane	99.88 \pm 0.06	—
n -Hexane	99.85 \pm 0.05	3-Methylpentane and Methyl cyclopentane
n -Octane	99.63 \pm 0.18	—
Isobutane	99.88 \pm 0.06	n -Butane
Neopentane	99.83 \pm 0.03	Isobutane
Cyclopentane	99.95 \pm 0.02	2,2-Dimethylbutane
Cyclohexane	99.99 \pm 0.005	—
Ethylene	100	Acetylene (0.2% without detection)
Propylene	99.70 \pm 0.02	Propane and trace of ethane
Butene-1	99.88 \pm 0.20	Iso- and n -butane
Hexene-1	99.22 \pm 0.10	Other hexenes
Butadiene-1,3	99.87 \pm 0.05	Butene-1, butene-2
Acetylene	99.75 \pm 0.15	—

Measurements in some of these gases have been reported already (Heylen and Lewis 1956).

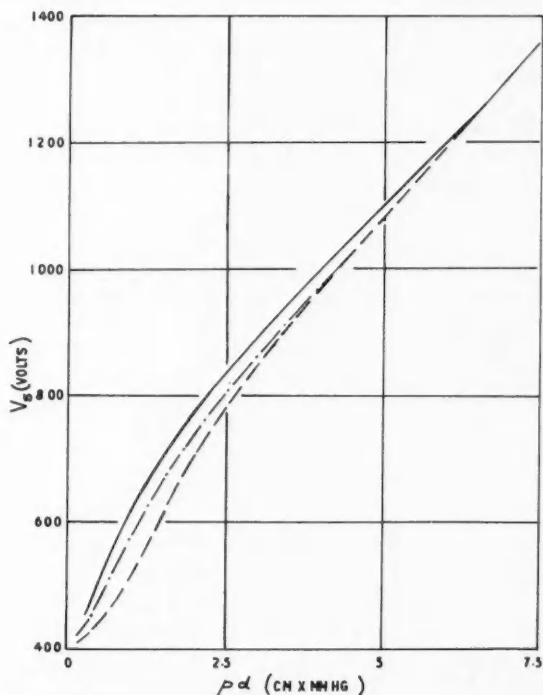


FIG. 1. Effect of impurity on the sparking potential of n -pentane. - - - Analar grade n -pentane, free from aromatics, boiling range $<40^\circ\text{C}$. - · - · - Analar grade pentane dried over sodium for 4 days. — Pure n -pentane, 99.88% purity.

Highly polished aluminum electrodes washed in n -hexane were used throughout because this metal had the most stable surface, giving highly reproducible values of V_s and steady pulse activity at voltages below V_s . Considerable pulse activity at voltages appreciably below V_s occurs in many hydrocarbon gases. This has been attributed to the fact that the second Townsend coefficients γ for these gases are probably 10^5 times smaller than for common gases such as nitrogen (Heylen and Lewis 1956). This permits considerable avalanche formation (large values of α , the first Townsend coefficient) without breakdown and therefore easily detected pulses at voltages below V_s . This pulse activity, which, if observed on an oscillograph, gives clear warning of the imminence of breakdown, needs to be controlled if consistent values of V_s are to be obtained. Fig. 2 illustrates the electrode influence and the effect of controlling the pulses by means of the external illumination. A test gap having one aluminum and one stainless steel electrode prepared in the normal manner was found to give a characteristic for ethane as in (i) of Fig. 2. There was little

distinction between either electrode as a cathode, and the level of gap illumination provided by normal laboratory fluorescent lighting caused considerable

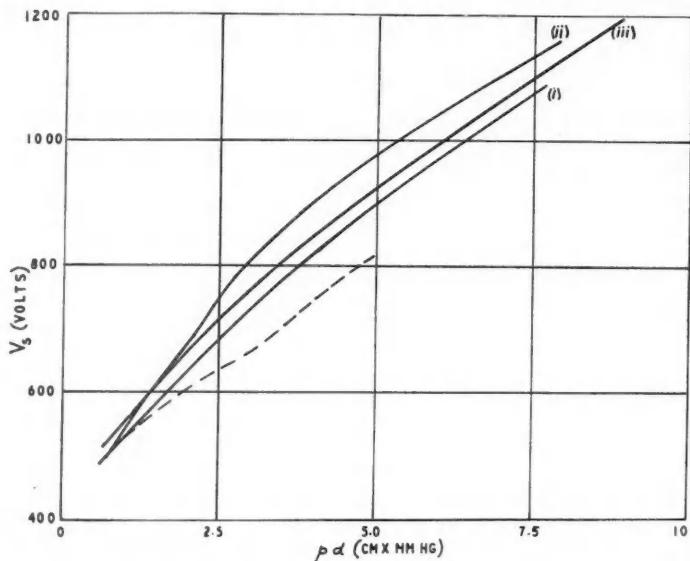


FIG. 2. Effect of cathode material and illumination in ethane.

Curve (i) Laboratory fluorescent lighting, stainless steel or aluminum cathode with normal preparation.

Curve (ii) Stainless steel cathode after glow discharge of 1 ma. for 1 minute in ethane. Aluminum cathode still gave results as in curve (i).

Curve (iii) Both electrodes of aluminum and illumination from a tungsten lamp controlled to give 1000 pulses per second. --- Onset of detectable pulses.

pulse activity and a depression of V_s . A glow discharge of 1 ma. for 1 minute in the gas caused no change with the aluminum cathode, but with stainless steel there was a significant increase in V_s giving curve (ii). Furthermore, in this latter case, both the value of V_s and the pulse activity, which had declined considerably, were erratic. On the other hand curve (iii) shows a controlled result using aluminum electrodes and illumination from an ordinary tungsten lamp so adjusted as to prevent lowering of V_s but at the same time permitting a pulse rate of about 1000 per sec., sufficient to prevent an overvoltage across the gap. Fig. 2 also shows the onset potential of detectable pulses, which coincides with V_s at $p d \approx 1$. Curve (iii) is typical of those reported here for the other pure gases. By careful control and observation of the pulses, the voltage could be raised rapidly to within 99% of V_s and then very slowly at about 0.2% per second until V_s was reached. With this technique only one measurement at any $p d$ value was necessary to establish V_s , and any further measurements were within 0.5% of this value. The values of V_s reported by the present authors both here and in the previous communication are considerably greater ($\sim 20\%$) than values found by Devins and Crowe (1956),

who probably used a much greater degree of illumination. These workers make no comment on the higher values of V_s which they had reported in an earlier communication (Devins and Crowe 1954). High levels of illumination produce excessive pulse activity which, as V_s is approached, results in large conduction currents. In this case, the pulse activity does not grow immediately to its full level when the voltage is raised, and frequently it is possible by immediate reduction of the illumination or the voltage to prevent an instability from which breakdown would ensue. Because of this slow growth to an instability which can occupy several seconds a slow rate of rise of voltage is very important. It is possible that space charge distortion of the applied field occurs when the illumination is excessive and also that dissociation products resulting from illumination of the gas itself upset the sparking conditions (Carr and Stücklen 1936).

Reduction in the number of measurements required for a full V_s versus pd characteristic and efficient spark quenching, such that there was no visible discharge, reduced the damage to both the electrodes and the high-purity gases to negligible proportions. Breakdown was detected only by the collapse of voltage across the gap and was further checked by raising the voltage again to

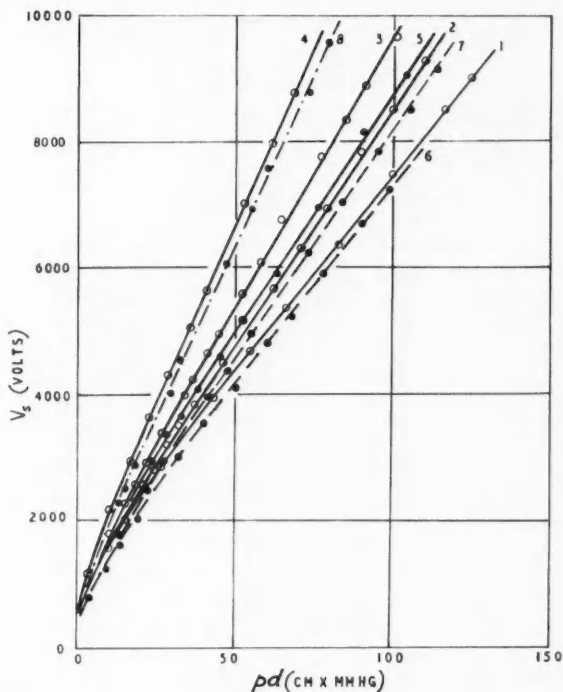


FIG. 3. Breakdown characteristics of some hydrocarbon gases: 1, *n*-butane; 2, *n*-pentane; 3, *n*-hexane; 4, *n*-octane; 5, neopentane; 6, cyclopentane; 7, cyclohexane; 8, hexene-1.

a level near V_s . If a breakdown occurred in the previous voltage application an increase in pulse activity lasting for about one minute was found. This increased activity did not materially affect subsequent measurements of V_s taken immediately after the first when saturated hydrocarbons were being investigated, but a pause of at least 30 sec. was required before further reliable measurements could be made on unsaturated hydrocarbons.

Figure 3 shows V_s versus pd characteristics for a range of hydrocarbons additional to those given earlier (Heylen and Lewis 1956). The range of n -paraffins has been extended to n -octane and the important cyclopentane and cyclohexane results are now given.

3. INTERPRETATION OF THE SPARKING CHARACTERISTICS

Interpretation of V_s in terms of molecular properties involves certain concepts of the breakdown process. As a convenient criterion of breakdown, that postulated by Townsend for current instability is adopted, namely

$$(1) \quad \gamma[\exp(\alpha d) - 1] = 1,$$

where α is the average number of ionizing collisions made by an electron in moving 1 cm. in the field direction and γ is the number of secondary electrons produced at the cathode by a primary electron in the gas. This criterion is one for the onset of an unstable growth of the electron population and does not invoke a particular mode of spark formation. Interpreted in this way it can be related to fundamental collision processes in the gas. The coefficient α is determined by the nature of the gas and was first derived by Townsend and since modified in various ways (Loeb 1955). The general result is

$$(2) \quad \alpha p^{-1} = A_1 \exp(-Bp/E),$$

in which E is the uniform field strength. When equation (1) is also satisfied, then $E = V_s/d$. A recent study (Lewis 1958) has shown that A_1 and B are generally complicated functions of E/p . For the purpose of calculation it is preferable to use $A_1 = AE/p$ (Crowe, Bragg, and Devins 1955), and assuming for the moment that A and B are independent of E/p and combining equations (1) and (2) after neglecting unity on the right-hand side of equation (1), we get

$$(3) \quad \ln V_s = Bpd/V_s - \ln[A/\ln(\gamma^{-1})].$$

Thus provided that A , B , and γ remain sensibly constant a plot of $\ln V_s$ against pd/V_s should yield a straight line of slope B and a negative intercept $\ln[A/\ln(\gamma^{-1})]$ on the ordinate. Typical plots according to equation (3) are given in Figs. 4 and 5. Straight lines have been drawn to fit the experimental points over as wide a range as possible, bearing in mind that certain deviations are to be expected in any case.

Deviations from a linear plot at high pd indicate that B is no longer constant owing to the increased importance of elastic collision losses, which have been neglected in the derivation of equation (2). The term $\ln[A/\ln(\gamma^{-1})]$ does not alter significantly in the higher pressure range although A depends on E/p . When pd is small (E/p large) failure of equation (2) occurs for several reasons

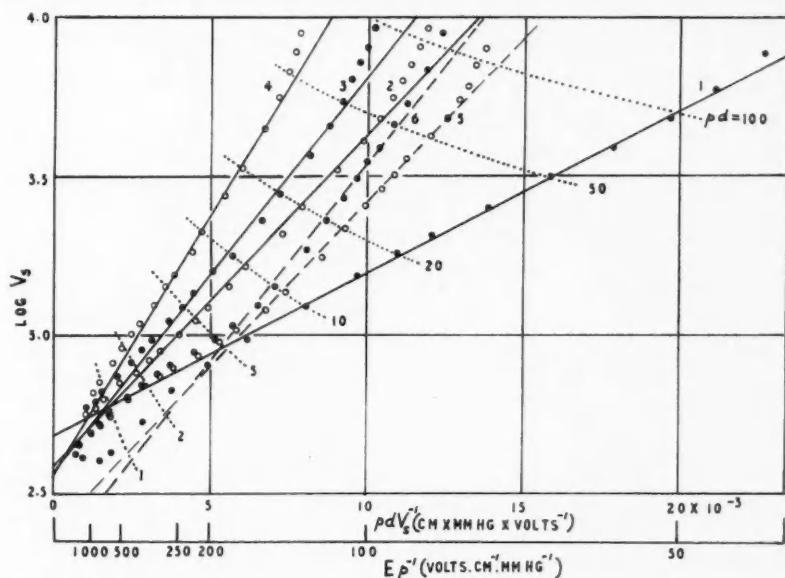


FIG. 4. Plot of $\log V_s$ against pdV_s^{-1} for typical saturated hydrocarbons. According to equation (3), the value of B may be determined from the slope of the characteristics. 1, methane; 2, *n*-pentane; 3, *n*-hexane; 4, *n*-octane; 5, cyclopentane; 6, cyclohexane.

which cannot be discussed fully here. Both A and B vary with E/p in this range and a marked increase of slope can result. At the same time γ also changes (Heylen and Lewis 1956); this will be discussed further in Section 6.

For values of pd in the immediate neighborhood of the $V_s - pd$ minimum marked deviations in the opposite sense occur and equation (2) is not valid. This is well illustrated by the methane characteristic in Fig. 4 for which the minimum occurs at $pd = 0.55$.

The effects discussed above were not found by Devins and Crowe (1956), apparently because those at low pd were beyond their range of measurement and those at high pd were probably masked by 'space-charge' distortion brought about by an uncontrolled high level of external illumination. Their earlier results (Devins and Crowe 1954), obtained with an unspecified level of illumination, lie within 2% of those obtained by the present writers however.

The results obtained for the cyclic hydrocarbons, Fig. 4, are exceptional. Since the observations for both normal and cyclic pentane, and for the two corresponding hexanes, are closely similar, the difficulty of drawing suitable straight lines through the points has been overcome by making them parallel in the two cases. This means that B is assumed to be the same for each pair of gases. The theory developed below supports this procedure as at least a good approximation.

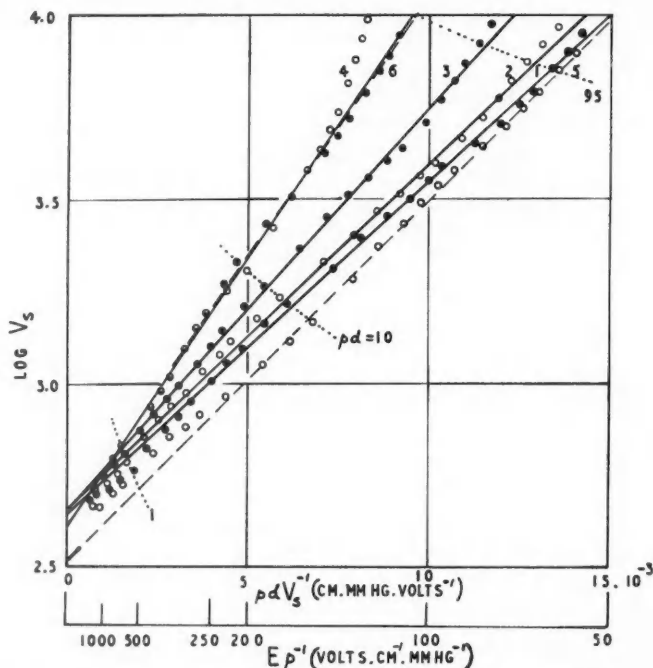


FIG. 5. Plot of $\log V_s$ against pdV_s^{-1} for unsaturated hydrocarbons: 1, ethylene; 2, propylene; 3, butene-1; 4, hexene-1; 5, acetylene; 6, butadiene.

A summary of all the constants found including those reported by Devins and Crowe (1956) and Crowe and Devins (1957) is given in Table II together with the ionization potentials ϵ_i . There is reasonable agreement between the two sets of values of B except for cyclopentane and cyclohexane but there are considerable differences in the values of $\ln[A/\ln(\gamma^{-1})]$ consequent on the original differences in V_s .

4. THE MOLECULAR PARAMETER B

For the range E/p which produces linear plots of $\ln V_s$ versus pd/V_s , it can be shown that (Lewis 1958)

$$(4) \quad B = 6.25 \times 10^{-16} \int_{\epsilon_e}^{\epsilon_i} (\theta Q)^{1/2} d\epsilon,$$

in which θ is the elastic cross-section and Q the inelastic (excitation) cross-section, both in cm^2 , for the electron-molecule collisions and ϵ_e and ϵ_i are excitation and ionization energies of the gas in question. This is at once a simple and easily applied result provided that all the molecular quantities are known. Of these, only ϵ_i (Table II) is available for all the gases tested, the values being of doubtful accuracy for the two cyclic hydrocarbons. The total

TABLE II
CONSTANTS FOR THE DETERMINATION OF THE RELATIONSHIP BETWEEN V_e AND MOLECULAR PROPERTIES

Hydrocarbon	B (v.cm. ⁻¹ mm. ⁻¹) Devins and Crowe	Heylen and Lewis	log $[A/\ln(\gamma^{-1})]$ Devins and Crowe	Heylen and Lewis	Ionization potential ϵ_i (v.)
Methane	114	117	-2.49	-2.68	13.04
Ethane	132	133	-2.39	-2.66	13.16*
Propane	175	171	-2.32	-2.63	11.76
<i>n</i> -Butane	219	210	-2.24	-2.60	11.21
<i>n</i> -Pentane	248	243	-2.33	-2.58	10.80
<i>n</i> -Hexane	272	288	-2.29	-2.57	10.55
					10.43
<i>n</i> -Octane	—	370	—	-2.57	10.54*
Isobutane	217	217	-2.33	-2.62	10.24
Neopentane	254	250	-2.35	-2.61	10.80†
Cyclopentane	216	243	-2.25	-2.37	10.55†
Cyclohexane	239	288	-2.09	-2.29	10.80†
Ethylene	154	209	—	-2.64	10.40†
Propylene	161	216	—	-2.66	10.62
Butene-1	~210	253	—	-2.65	9.84
Hexene-1	—	333	—	-2.62	9.76
Butadiene-1,3	248	333	—	-2.62	9.59
Acetylene	—	224	—	-2.53	9.24*
					11.43

Values of B according to Devins and Crowe have been obtained from their values of $B \epsilon_i^{-3/2}$ (Crowe and Devins 1957) using the values of ϵ_i as listed. All values of ϵ_i are those obtained by Honig (1948) except as follows:

*This result comes from Morrison and Nicholson (1952). Their values for methane and *n*-hexane are also given.

†The values for these isomers are taken to be the same as for the unbranched hydrocarbons.

‡These values are reported by Devins and Crowe (1956).

collision cross-sections up to 25 ev. have been found for the first four paraffins and for ethylene and acetylene by Brüche (1929, 1930) and Schmieder (1930) and will be used to evaluate θ below. Methane has been investigated spectroscopically by Ditchburn (1955) and others, who have given a photon scattering cross-section with a dissociation threshold at 8.13 ev. and ionization beginning at 13.1 ev. These values can be used with reasonable accuracy for ϵ_e and ϵ_i (Morrison and Nicholson 1952). There is a smooth variation in ϵ_i throughout each hydrocarbon series in Table II and we shall assume that a corresponding smooth change occurs in ϵ_e , i.e. that ϵ_e/ϵ_i is constant. Consideration of the data provided by Ditchburn suggests that Q for methane varies linearly between ϵ_e and ϵ_i , and if θ is replaced by its mean θ_m over this same range, then equation (4) becomes

$$(5) \quad B = 4.17 \times 10^{16} (\theta_m Q_0)^{1/2} (\epsilon_i - \epsilon_e)^{3/2}$$

with

$$(6) \quad Q = Q_0(\epsilon - \epsilon_e), \quad \epsilon_e \leq \epsilon \leq \epsilon_i.$$

Equation (5) is the same as that used by Devins and Crowe (1956) following Crowe, Bragg, and Devins (1955). For the saturated hydrocarbons it becomes

$$(7) \quad B \epsilon_i^{-3/2} = \kappa (\theta_m Q_0)^{1/2}$$

in which $\kappa = 4.17 \times 10^{16} (1 - \epsilon_e/\epsilon_i)^{3/2}$. The assumption that ϵ_e/ϵ_i is constant is

probably not strictly correct for the first members of the series, methane and ethane, but the deductions from equation (7) are not strongly dependent on this.

We have to consider next how $(\theta_m Q_0)^{\frac{1}{2}}$ might vary in the n -paraffin series in order to interpret equation (7).

(i) *Application to n -Paraffins*

The total collision cross-sections and the ionization potentials of the n -paraffins vary uniformly throughout the series. These properties arise from the characteristic behavior of individual groups within the molecules, which is retained throughout the series. The invariant behavior of the groups is one of the powerful factors in the spectroscopic analysis of hydrocarbons. We therefore seek to determine θ_m and Q_0 in terms of partial scattering cross-sections arising from specific groups within the molecules. The degree of electron-molecule interaction depends on the energy of the incident electron as well as on the molecular fields. The excitation collisions which determine Q_0 involve both energy transfer and upward changes in the electronic structure of the molecule. A particular limiting case of an electronic change occurs when the molecule is ionized but dissociative processes are also very probable, especially when the molecule is complex.

Otvos and Stevenson (1956) have shown for a wide variety of substances, including the hydrocarbons considered here, that the molecular ionization cross-section may be computed on an additive basis from previously determined atomic cross-sections. It is now suggested as a reasonable hypothesis that the excitation cross-sections will be additive in a similar way. Thus for the n -paraffin C_nH_{2n+2}

$$(8) \quad Q_0 = nQ_C + (2n+2)Q_H,$$

in which Q_C and Q_H are the atomic excitation cross-section quantities defined in the same manner as Q_0 . It will be more convenient in the following to write equation (8) in the form

$$(9) \quad Q_0 = 2(Q_C + 3Q_H) + (n-2)(Q_C + 2Q_H).$$

As Otvos and Stevenson have remarked, the atomic ionization cross-sections of carbon and hydrogen in the n -paraffins are in the same ratio as the atomic volumes determined from measurements in the liquid phase at the boiling point (Moore, Gibbs, and Eyring 1953). Assuming a similar statement for the excitation cross-sections, then the molecular volume V_m is proportional to Q_0 .

For θ_m we cannot develop a straightforward argument in terms of atomic cross-sections. The elastic collision involves the outer fields of the molecule and θ_m must in some way depend on molecular size, which for the n -paraffins involves the chain length n . Brüche (1929, 1930) has discussed the total collision cross-section, of which the main term is θ_m , in terms of a sphero-cylindrical model. The hemispherical ends of the model correspond to the CH_3 groups and the cylindrical portion comprises a chain of CH_2 groups. With this simple model Brüche calculated a mean cross-section from the partial cross-sections

perpendicular to the three major axes of the model and obtained an expression for θ_m which can be written in the form

$$(10) \quad \theta_m = k_1 V_m + k_2.$$

Using equation (9)

$$(11) \quad \theta_m = k_3 Q_0 + k_2 = [2k_3(Q_C + 3Q_H) + k_2] + k_3(n-2)(Q_C + 2Q_H),$$

in which k_1 , k_2 , k_3 are constants; we now have

$$(12) \quad (\theta_m Q_0)^{1/2} = k_3^{1/2} Q_0 [1 + k_2 / (k_3 Q_0)]^{1/2}.$$

The second term on the right of this equation will become less important as Q_0 increases, so that for a first approximation we have

$$(13) \quad (\theta_m Q_0)^{1/2} \simeq k_3^{1/2} Q_0.$$

Combining equations (7), (9), and (13) we get the linear relationship

$$(14) \quad B\epsilon_i^{-3/2} \simeq \kappa k_3^{1/2} [2(Q_C + 3Q_H) + (n-2)(Q_C + 2Q_H)].$$

Using the values in Table II and plotting according to equation (14), the curve shown in Fig. 6(a) results. From the slope and intercept of this line we find $\kappa k_3^{1/2} Q_C = 0.88$, $\kappa k_3^{1/2} Q_H = 0.24$, and the ratio $Q_C/Q_H = 3.7$, which is close to the value 4 found by Otvos and Stevenson (1956) for the atomic ionization cross-sections.

The measurements of the total cross-sections by Brüche and Schmieder

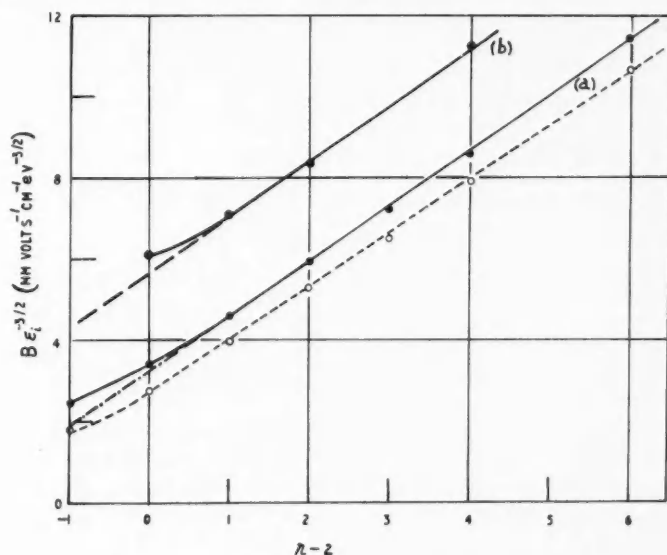


FIG. 6. Dependence of $B\epsilon_i^{-3/2}$ on number of CH_2 groups per molecule, (a) for the n -paraffins according to equation (14), (b) for the monolefins according to equation (16).

enable θ_m to be calculated and the factor $[1 + k_2/(k_3 Q_0)]^{1/2}$ in equation (12) to be found. Plotting the calculated values of θ_m according to equation (11) gives on a 'least squares' basis the linear curve shown in Fig. 7. Using the parameters of this straight line and that of Fig. 6(a) the factor may be evaluated as in Table III. It is seen that the correction is only significant for the first few

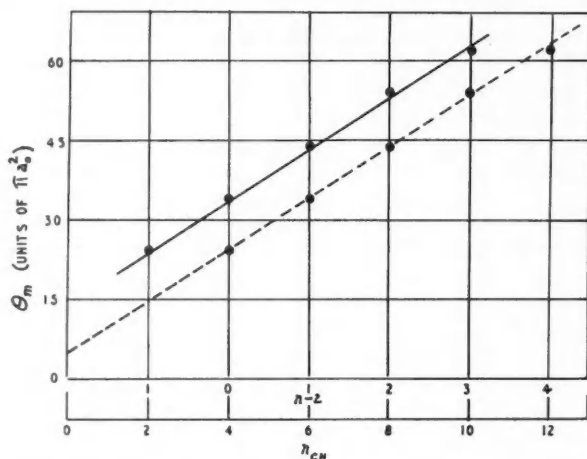


FIG. 7. Plot of θ_m against number of CH_2 groups. Alternative plot against number of C—H bonds n_{CH} shown dotted.

members of the series. Using the reciprocal of this factor, equation (14) has been corrected and the new result given in Fig. 6(b). An improved linear relationship is found and only methane is exceptional. The methane molecule is symmetrical and therefore unlike the higher members of the paraffin series. Its physical properties are in several ways distinct from the rest of the series so that the discrepancy is not surprising. A similar behavior, but to a lesser degree, occurs with ethane.

TABLE III
VALUES OF $[1 + k_2/(k_3 Q_0)]^{1/2}$

n $[1 + k_2/(k_3 Q_0)]^{1/2}$	1	2	3	4	5	6	8
	1.37	1.23	1.16	1.13	1.11	1.09	1.07

It has been noted already that the isomers, isobutane and neopentane, have nearly the same sparking potentials as the corresponding n -paraffins and the derived values of $B\epsilon^{-3/2}$ (from Table II) are only slightly higher. The theory given predicts no change in Q_0 for isomers since the atomic excitation cross-sections have been considered to be additive. Judging from the results of Brüche and Schmieder, branching does not affect θ_m either. The observed differences are small and at the moment our knowledge of the exact nature of Q_0 and θ_m is not detailed enough to account for them.

(ii) *Application to Other Hydrocarbons*

Further support for the theory comes from application to cyclopentane (C_5H_{10}) and cyclohexane (C_6H_{12}), which are saturated but contain no terminating CH_3 groups so that the term arising from this group in equation (14) is zero. The value of the remaining term for the CH_2 groups can be found from Fig. 6(a) and using this, the estimates of $B\epsilon_i^{-3/2}$ are 6.8 and 8.16 for C_5H_{10} and C_6H_{12} respectively. Values based on experiment (Table II) are 6.85 and 8.58. The agreement between experiment and theory is satisfactory, bearing in mind that equations (6) and (7) may be oversimplified in this case. The reported values of ϵ_i for cyclopentane and cyclohexane seem to be somewhat anomalous when compared with the corresponding straight-chain hydrocarbons, especially when the results for normal and cyclic propane, which are 11.21 and 10.14 ev. respectively, (Field and Huckle 1950) are included in the comparison.

We must note that the introduction of a double or triple bond alters the total cross-section considerably for electron energies below about 4 ev. (Brüche 1929, 1930), and corresponding changes must also occur in the other scattering processes. The inelastic collision processes for the saturated hydrocarbons are likely to cause excitation of electrons in the σ or bonding orbitals but the double or triple bond introduces electrons in π antibonding orbitals. These latter orbitals give rise to a new range of excitation levels as the ultraviolet spectra show and therefore cause new electron-scattering processes. We are able to account for the behavior of these unsaturated hydrocarbons by introducing additional scattering centers to be associated with these orbitals having excitation cross-sections Q_{C2} and Q_{C3} for the double and triple bonds respectively. Turning to the elastic collisions we assume that θ_m can be represented approximately in the same form as Q_0 following an argument similar to that for the paraffins. Thus from equations (9), (13), and (14) we have for the monolefin C_nH_{2n}

$$(15) \quad Q_0 = n(Q_C + 2Q_H) + Q_{C2}$$

and

$$(16) \quad B\epsilon_i^{-3/2} = \kappa k_2^{1/2} [Q_{C2} + n(Q_C + 2Q_H)]$$

and for a diolefin C_nH_{2n-2}

$$(17) \quad Q_0 = n(Q_C + 2Q_H) + 2Q_{C2} - 2Q_H$$

and

$$(18) \quad B\epsilon_i^{-3/2} = \kappa k_3^{1/2} [2Q_{C2} - 2Q_H + n(Q_C + 2Q_H)].$$

Figure 6(b) shows a plot according to equation (16) for the monolefins tested. The curve is practically linear and only the first member, ethylene, lies off the curve. The slope gives $\kappa k_2^{1/2} (Q_C + 2Q_H) = 1.36$, which is identical with that found for the paraffins Fig. 6(a), and the intercept gives the value $\kappa k_2^{1/2} Q_{C2} = 3.0$. Using these two values together with the estimate of $\kappa k_3^{1/2} Q_H = 0.24$ from Fig. 6(a) the predicted value of $B\epsilon_i^{-3/2}$ for the diolefin butadiene from equation (18) becomes 10.96, whereas the experimental determination is 11.9. The two double bonds are conjugated in butadiene so that the difference in the two

values is likely to be due to the resonance effect increasing the cross-section of the double bond.

Insufficient data prevent discussion of triple-bond hydrocarbons but from the isolated result for acetylene using the values of Q_C and Q_H already determined from the paraffins we find $\kappa k_2^{1/2} Q_C = 3.56$, which is greater than $\kappa k_2^{1/2} Q_{C_2}$ as might be expected.

5. OTHER INTERPRETATIONS OF B

The ideas given above are different in certain respects from those adopted by the authors in the previous discussion, which followed those developed by Devins and Crowe (1956). In the former treatment, as here, it is assumed that Q_0 and θ_m are proportional but the electron-molecule collision cross-section is constructed differently. It is considered to arise not from atomic centers but from centers associated with the valence bonds. For a saturated hydrocarbon, cross-sections Q_{CC} and Q_{CH} are ascribed to the C—C and C—H bonds. The resultant equation corresponding to equation (14) is

$$(19) \quad B\epsilon_i^{-3/2} = \kappa k_2^{1/2} [n_{CH}(Q_{CH} + \frac{1}{2}Q_{CC}) - 2Q_{CC}]$$

in which n_{CH} is the number of C—H bonds.

The results for the paraffins are interpreted in accordance with equation (19) in Fig. 8. Leaving aside the result for methane, a best straight line gives a negative intercept and relative bond cross-sections as in Table IV. Q_{CC} and Q_{CH} are approximately equal and the C—C bond is not shielded. The values obtained by Devins and Crowe are also shown in Fig. 8 and give a zero value

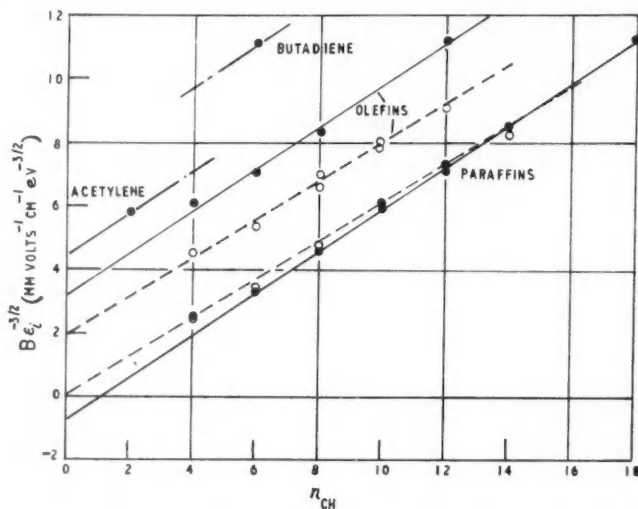


FIG. 8. Dependence of $B\epsilon_i^{-3/2}$ on number of C—H bonds per molecule. Characteristics obtained by Devins and Crowe shown by broken lines.

for Q_{CC} suggesting that the carbon skeleton is screened. These differences will be discussed below. Writing the following modified forms,

$$(20) \quad Q_0 = n_{CH}(Q_{CH} + \frac{1}{2}Q_{CC}) - 2Q_{CC2} + Q_{CC3}$$

and

$$(21) \quad Q_0 = n_{CH}(Q_{CH} + \frac{1}{2}Q_{CC}) - Q_{CC} + Q_{CC3}$$

for the monolefins and acetylene respectively and equation (20) with $2Q_{CC2}$ for the diolefin butadiene, the results for these gases may be added to Fig. 8. Assuming linear characteristics with slopes corresponding to the paraffins then large vertical shifts occur which can be attributed to Q_{CC2} and Q_{CC3} . Their relative magnitudes are given in Table IV and it is clear that the bonds are unshielded. Conjugation effects in butadiene increase Q_{CC2} from 8.5 to 9.4, indicating that the resonance effect has an influence, a conclusion reached also in Section 4.

TABLE IV
RELATIVE BOND CROSS-SECTIONS

Bond	Q_{CH}	Q_{CC}	Q_{CC2}	Q_{CC3}
Relative cross-section	1	0.85 (<i>n</i> -paraffin)	8.5 (monolefins)	10.5
	1	1.0 (cycloparaffin)	9.4 (butadiene)	

Recent results, mainly for the olefins, have been given by Crowe and Devins (1957) and have been added to Fig. 8. Since the paraffins and olefins produce parallel characteristics Devins and Crowe have concluded not only that addition of CH_2 groups causes constant increments in the molecular cross-sections but that Q_{CC} is also zero for both series. Comparison of equations (19) and (20) shows that this latter statement is not necessarily true because characteristics of the same slope can be produced even when Q_{CC} is not zero. The values of the intercepts are quite different in the two series of experiments and some explanation must be given of this.

The values of B reported here have been obtained from an extended range of measurements and must therefore be considered more reliable. Two examples might be quoted. If *n*-hexane had not been tested over a full range up to $pd = 100$ (Fig. 3), a lower value of B would have been deduced. This, used in Fig. 8, could have so modified the best straight line for the paraffins as to lead to the deduction that $Q_{CC} = 0$. Again, the omission of *n*-octane would have had a similar effect, as perusal of the corresponding values provided by Devins and Crowe would show.

The evidence provided by measurements on cyclopentane and cyclohexane is significant. Devins and Crowe find additional evidence from these that $Q_{CC} = 0$ but the present determinations lead to a cross-section comparable with Q_{CH} (Table IV). The curves for determining B (Fig. 4) deviate strongly from straight lines at both high and low pd . Since Devins and Crowe tested cyclohexane over the restricted range of pd , 5 to 35 mm. Hg \times cm., their value of B can be inaccurate, especially as they also find that cyclohexane has a

lower strength than cyclopentane over part of the range, which is an unexpected result for any theory. Their argument for $Q_{CC} = 0$ based on comparison of the values of B with those for n -butane and n -pentane having the same number of CH bonds as the cyclic compounds is not supported by the measurements here (Table II).

The extraordinarily large cross-sections found for the multiple bonds in Table IV are less natural than those arising from the atomic cross-section model (Section 4). It is true, as Crowe and Devins suggest, that the multiple bond will offer a better electron target because of π orbitals but a 10-fold increase over that for the single bond does not seem plausible.

It is appropriate in concluding this section to comment on the use of Brüche's cross-section measurements. These measurements taken together with those of Schmieder do not, in our view, support an argument that θ_m is independent of the C—C cross-section. If Fig. 7 is replotted on the basis of n_{CH} , then a clear intercept is found which represents a contribution to θ_m from the C—C bonds. Alternative evaluations of the total cross-sections either at the ionization potentials ϵ_i or at the cross-section maxima (~ 6.5 ev.) still indicate a non-zero value for the C—C bond cross-section above the limit of any experimental error.

6. THE NATURE OF $\ln[A/\ln(\gamma^{-1})]$

The second term in equation (3) involves both molecular properties of the gas and secondary mechanisms at the cathode, neither of which should change abruptly in a molecular series. Thus $\ln[A/\ln(\gamma^{-1})]$ will not alter appreciably throughout a series when E/p is not too large (< 500) as is shown in Table II. Although there is a significant difference in the two sets of measurements as a whole, the values of this term within either set of measurements remain reasonably constant. In both sets however, the cyclic hydrocarbons are exceptional. A plausible explanation of this which sheds light on the mechanism of breakdown can be given.

Following electronic excitation, dissociation would appear to occur readily for many hydrocarbons (Korff and Present 1944), the absorption spectra showing continuous bands in the energy range of interest. Loss of excitation energy by dissociation will reduce any secondary electron production by photon action in the gas or at the cathode. Thus provided E/p is not too large (< 500) γ can be expected to be smaller than for the common gases in which photon production is normal. It is significant that γ values decreasing from $\sim 10^{-3}$ at $E/p = 3000$ to as low as 10^{-8} – 10^{-9} at $E/p = 500$ have been reported for benzene, toluene, and cyclohexane (Badareu and Constantinescu 1938; Constantinescu 1940; Valeriu-Petrescu 1943). Values in the neighborhood of 10^{-4} would be expected for the common gases in this range. Probable exceptions are the cyclic compounds, which have the unusual sparking behavior mentioned above. γ has not been measured in cyclohexane in the range of $E/p < 500$ but indirect evidence suggests that γ may have a more normal value ($\sim 10^{-4}$) for the cyclic compounds when $E/p < 500$. In the first place the ultraviolet spectrum of cyclopropane, the only cyclic paraffin investigated in the range of interest (600–2200 Å), shows that dissociation does not occur

easily in spite of its olefinic properties, and other cyclic paraffins may behave similarly. If continuous absorption is absent below the ionization potential, more normal photon action with larger values of γ can be expected below $E/p = 500$, i.e. there would be a photoelectric peak at low E/p for the cyclic hydrocarbons but not for the continuously absorbing and dissociating *n*-paraffins. There would then be a pronounced minimum in γ for the cyclic compounds at $E/p \simeq 500$.

Secondly, a marked reduction in prebreakdown pulse activity has been noticed with the cyclic gases. In this respect these gases are comparable with nitrogen, which also showed little activity before breakdown. When γ is $\sim 10^{-8}$, larger values of α can be tolerated without attaining the sparking criterion of equation (1), and these larger avalanche formations produce more easily detected pulses in the gap. For the common gases and apparently for the cyclic hydrocarbons, the attainment of easily detected pulses is prevented by the intervention of a spark.

A third result comes from a comparison of $\ln[A/\ln(\gamma^{-1})]$ for cyclic and normal hexane (Table II). A is the same for both, so that

$$(22) \quad \gamma_n = \gamma_c^{1.9},$$

where γ_n and γ_c refer to the normal and cyclic hydrocarbons respectively. With $\gamma_n \sim 10^{-8}$, γ_c becomes $\sim 10^{-4}$, which is an acceptable value for the range $E/p < 500$.

For higher values of E/p , the minimum suggested for the cycloparaffins should have an effect on the breakdown characteristics. In general, as E/p increases, photon action declines and is replaced as a secondary process by positive-ion bombardment of the cathode, and in the intermediate region in which both processes are inefficient, a minimum in γ occurs. In the range of E/p , above 200, there is considerable deviation from a linear characteristic for the cycloparaffins in Fig. 4 and this coincides with the postulated minimum in γ . No such deviation is observed for the *n*-paraffins for which marked changes in γ are not to be expected because the tendency to dissociate will remain even for positive-ion neutralization at the cathode which is predominant at large E/p . Judging from Fig. 5 the unsaturated hydrocarbons are similar in behavior to the normal paraffins.

In the light of the above discussion the larger values of $\ln[A/\ln(\gamma^{-1})]$ reported by Devins and Crowe (Table II) could arise from larger *effective* values of γ in their experiments, a condition which can in turn be related to the higher level of illumination employed.

7. CONCLUSIONS

Extension of the earlier work of Devins and Crowe to cover a wider range of E/p and careful control of the test conditions as well as the inclusion of more saturated and unsaturated hydrocarbon gases has revealed interesting aspects of the mechanism in breakdown in molecular gases. It is now possible to set up cross-section models which offer consistent explanations of the breakdown strengths and which support the general theory embodied in the criterion of

equation (1). Lack of precise data on sparking potentials for a series of similar molecular gases has hampered the development of a theory relating fundamental molecular parameters to electric strength. For more complex molecules, especially those which are conjugated or involve ring structures, equation (7) may be inaccurate since in these cases the ultraviolet spectra are complex and the electron collision cross-sections may well be the same. For such gases a more realistic evaluation of the integral involved in equation (4) is necessary. Investigations into these matters are continuing (Heylen 1957 *b*).

The uncertainties embodied in a sparking criterion can be avoided by accurate experimental determinations of α from conductivity measurements. Such measurements for a range of hydrocarbons are now being undertaken in this laboratory and should provide a closer check on the influence of molecular collision processes in gaseous breakdown.

In conclusion we should remark that if γ is as small as 10^{-8} in many of these hydrocarbons then the true secondary processes of electron production are very inefficient. Under such conditions the possibility of sparking occurring by mechanisms other than those normally considered in the Townsend theory should be examined. Alternative theories which use a form of space-charge criterion for an individual electron avalanche have been analyzed by Zeleny (1942), who has shown that semiempirical equations of the same form as equation (1) are produced, so that the argument of this paper is not affected. In this connection, these hydrocarbons should offer interesting opportunities for checking some of the controversial matters concerning the mechanism of breakdown in gases.

ACKNOWLEDGMENTS

The authors would like to thank Professors W. J. John and M. W. Humphrey Davies for continued encouragement in the work. One author (A.E.D.H.) acknowledges gratefully a maintenance grant from the Department of Scientific and Industrial Research and lately the award of an I.C.I. Fellowship by the University of London. The other author (T.J.L.) is also grateful to the University of London for a Turner and Newall Fellowship.

Thanks are due to Messrs. G. A. White and J. Frost for valuable assistance in constructing the apparatus.

REFERENCES

- BADAREU, E. and CONSTANTINESCU, L. 1938. *Bull. soc. roumaine phys.* **39**, 45.
BRÜCHE, E. 1929. *Ann. phys.* **2**, 909.
——— 1930. *Ann. phys.* **4**, 387; **5**, 281.
CARR, E. P. and STÜCKLEN, H. 1936. *J. Chem. Phys.* **4**, 760.
CONSTANTINESCU, L. 1940. *Bull. soc. roumaine phys.* **41**, 73.
CROWE, R. W., BRAGG, J. K., and DEVINS, J. C. 1955. *J. Appl. Phys.* **26**, 1121.
CROWE, R. W. and DEVINS, J. C. 1957. *Nature*, **179**, 976.
DEVINS, J. C. and CROWE, R. W. 1954. Annual Report, 1953 Conference on Electrical Insulation, Washington, Academy of Science, National Research Council, 4.
——— 1956. *J. Chem. Phys.* **25**, 1053.
DITCHBURN, R. W. 1955. *Proc. Roy. Soc. (London)*, **A**, **229**, 44.
FIELD, F. H. and HUCKLE, E. A. 1950. *J. Chem. Phys.* **18**, 1122.
HEYLEN, A. E. D. 1957*a*. D.C. breakdown of organic vapours, Ph.D. Thesis, London.
——— 1957*b*. *Nature*, **180**, 703.
HEYLEN, A. E. D. and LEWIS, T. J. 1956. *Brit. J. Appl. Phys.* **7**, 411.

- HONIG, R. E. 1948. *J. Chem. Phys.* **16**, 105.
KORFF, S. A. and PRESENT, R. D. 1944. *Phys. Rev.*, **65**, 274.
LEWIS, T. J. 1958. *Proc. Roy. Soc. (London)*, A, **244**, 166.
LOEB, L. B. 1955. *Basic processes of gaseous electronics* (University of California Press, Berkeley), Chap. VIII.
McCORMICK, N. R. and CRAGGS, J. D. 1954. *Brit. J. Appl. Phys.* **5**, 171.
MOORE, R. J., GIBBS, P., and EYRING, H. 1953. *J. Chem. Phys.* **57**, 172.
MORRISON, J. D. and NICHOLSON, A. J. C. 1952. *J. Chem. Phys.* **20**, 1021.
OTVOS, J. W. and STEVENSON, D. P. 1956. *J. Am. Chem. Soc.* **78**, 546.
SCHMIEDER, F. 1930. *Z. Electrochem.* **36**, 700.
VALERIU-PETRESCU, M. 1943. *Bull. soc. roumaine phys.* **44**, 3.
ZELENY, J. 1942. *J. Appl. Phys.* **13**, 444.

THE REPRODUCIBILITY OF THE STEAM POINT¹

R. J. BERRY

ABSTRACT

A steam-point apparatus and precision manometer have been constructed in connection with the realization of the International Temperature Scale at the National Research Council. By means of this apparatus the steam point may be realized to 0.0002°C . with a reproducibility of 0.0001°C .; the difference is due to uncertainties in the physical constants involved.

The manometer is capable of measuring pressures of from 0 to 85 cm. of Hg with a precision of 1 micron, using electrostatic capacitance detection of the mercury surfaces and end standards to determine the height. The steam boiler gives constant results for a wide variety of operating conditions and has been used to show the increase of temperature with increasing head of water vapor.

The triple-point cells used in these experiments show a similar temperature change with change of immersion. It has been shown that a period of 1 to 3 days is required for them to establish temperature equilibrium, after which they are constant to within 0.0001°C . The resistance thermometer used is extremely stable at the steam and triple points if it is carefully handled.

INTRODUCTION

In 1927 the Seventh Conference of Weights and Measures adopted the International Temperature Scale (B.I.P.M. 1930; Burgess 1928) to provide a practical scale that could be conveniently and accurately reproduced and that would agree as closely as possible with the absolute scale. This international scale and its 1948 edition (C.I.P.M. 1948; Stimson 1949) are based upon six fixed and reproducible equilibrium temperatures (fixed points) to which numerical values are assigned, and upon specified formulae for the relations between temperature and the indications of the instruments calibrated at these fixed points. The size of the degree on this scale is defined by making the interval between two of the fixed points, the ice and steam points, exactly 100 degrees. It was in connection with the establishment of the fixed boiling points required to reproduce the International Temperature Scale of 1948 that the work on the steam point presented in this report was carried out.

Up to the present time there has been very little information published on the reproducibility of the steam point, particularly over long periods of time, and on its constancy under various operating conditions.

In 1937 Beattie and Blaisdell, using a closed hypsometer, found that the steam point could be reproduced with a probable error of $\pm 0.0003^{\circ}\text{C}$. (the number of observations, their values, and the period of time covered are not specified). In addition they reported that changing the distilled water used produced no effect greater than 0.0003°C .; that increasing the heating current from 3 to 3.5 amp. and then to 4 amp. changed the temperature by $+0.0002^{\circ}\text{C}$. and -0.0004°C . respectively; and finally that they felt that rather wide variations from their standard procedure did not change their value of the

¹Manuscript received March 5, 1958.

Contribution from the Division of Applied Physics, National Research Council, Ottawa, Canada.

Issued as N.R.C. No. 4764.

steam point by more than 0.0003°C . In 1953-54 two standard platinum resistance thermometers were sent to a number of national laboratories for the purpose of an international comparison of the ice and steam points. The results of this intercomparison (C.I.P.M. 1955) show that at the National Physical Laboratory and the National Bureau of Standards the steam point can be reproduced to about 0.001°C . over a period of 1 month and that between all the laboratories compared there was no discrepancy exceeding $\pm 0.001^{\circ}\text{C}$.

Using a closed hypsometer we have made measurements at the steam point over a period of 2 years and find that it remains constant to within $\pm 0.0001^{\circ}\text{C}$. In addition we have been able to calibrate a resistance thermometer 27 times at the steam point over a period of 5 months with an average deviation of R_{100}/R_0 equivalent to 0.00004°C . at the steam point. The effect of changing the operating conditions has been investigated by changing the heat input, the thermometer immersion, and the distilled water, and by using different thermometer wells; any variation in the apparent steam point that resulted from these changes was less than 0.0001°C .

In order to obtain this degree of reproducibility a great deal of attention had to be given to the measurement of the resistance of the platinum resistance thermometer and to the maintenance of the triple point of water. However, by far the most difficult problem was the control and measurement of the vapor pressure in the boiler. The steam point is extremely dependent on the water vapor pressure, varying by 0.037°C . per mm. of Hg at 760 mm., and for this reason it was necessary to construct a manometer of the highest possible precision.

PRECISION MANOMETER

The manometer is constructed along the same basic lines as one described by Stimson (1955) but the actual design and equipment used are different in almost every detail. The three major improvements over conventional manometers which increase the precision attainable are:

- (1) Large diameter mercury surfaces avoid the uncertainties of capillary depression.
- (2) One-inch-square end standards support the cells containing the mercury surfaces and determine the height of the mercury column.
- (3) An electrostatic capacitance system locates the surfaces of the mercury.

This manometer allows us to reproduce and measure pressure to within 1 micron of Hg. A schematic diagram is shown in Fig. 1.

Mercury System

The mercury system, which consists of the mercury cells, connecting tubes, valves, and reservoir, is made entirely of stainless steel so that it will not corrode either from the mercury or from the water and solvents used during the initial cleaning. In the mercury cells (B) the pressure on both sides of the insulated capacitance probe (E) is the same so as to eliminate any possible displacement or flexure of the probe when the pressure inside the cell is changed from 0 to 1 atm.; the base of the cell is made about 18 mm. thick

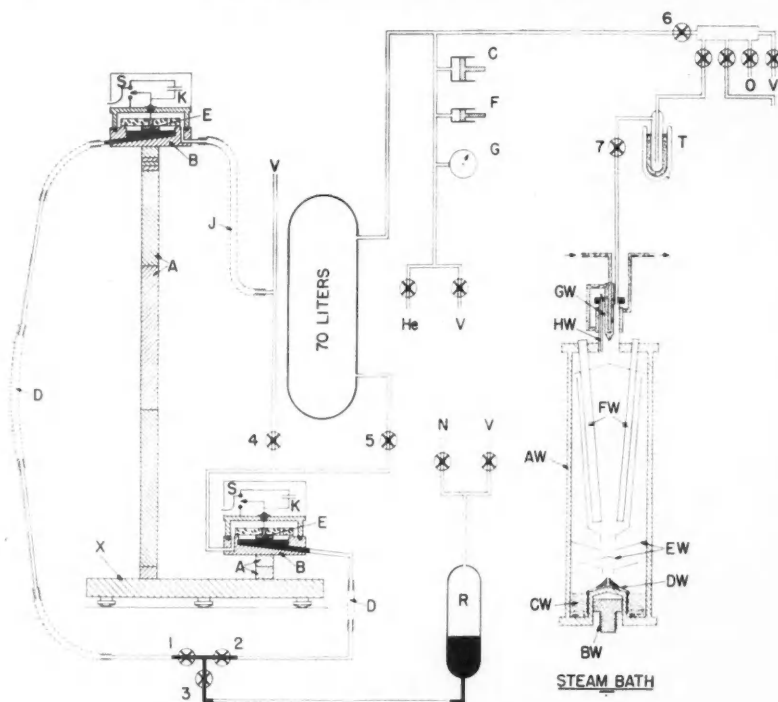


FIG. 1. Schematic diagram of the manometer and steam point boiler.

to reduce flexure to a negligible amount. The probe (E), a 32 mm. diameter stainless steel disk with its sides ground flat and parallel, is screwed to a 12 mm. flat glass plate which in turn is clamped to the ledge around the mercury pool. This ledge and a raised concentric boss on the base of the cell to which the gauge blocks are wrung are also ground flat and parallel. These measures, together with the levelling of the surface plate (X), ensure that the probe is sufficiently parallel to the mercury surface.

The mercury line between the cells is composed of lengths of 5 mm. inside diameter stainless steel tubing welded to short sections of 8 mm. minimum inside diameter flexible stainless steel hose (D). This, and the flexible bronze hose (J) used for the vacuum line connected to the upper cell, permits the level of this cell to be adjusted over a range of 0–85 cm. above the surface plate (X). The mercury is transferred between the 300 ml. reservoir (R) and the cells by adjusting the gas pressure in the reservoir from the nitrogen (N) or vacuum (V) lines and controlling the flow with the three mercury valves marked 1, 2, and 3. For very small mercury volume adjustments the change in the internal volume of the valves as they are opened and closed is utilized. These valves have vacuum jackets around their stems to prevent any possible

gas leak through the teflon packing as this wears with constant use. After the mercury system was cleaned, assembled, and tested for leaks, the mercury was distilled into the reservoir with the system under high vacuum. By means of an applied discontinuous pressure change it can be shown that the mercury system in the manometer is slightly less than critically damped and has a period of about 40 seconds.

In the preliminary tests we found that, when the manometer was not used for several days, the surface tension of the mercury occasionally separated the column in or near a cell that was under vacuum. This troublesome feature was almost completely overcome by making the bore of the mercury line in and near the cell smooth and uniform, and by machining a 6° slope on the inside base of the cell so as to increase the mercury pressure at the outlet from the cell.

Capacitance System

During the operation of the manometer the mercury surfaces must be kept at a fixed distance from the probes (E). To do this the electrostatic capacitance between each mercury surface and probe is kept equal to a reference capacitance (K) which consists of a fixed silver mica capacitor in parallel with a remotely adjustable air capacitor and is mounted directly on top of the mercury cells in a shielding can. A specially constructed low-capacitance relay (S), also located in the can, permits the rapid comparison of these two capacitances. They are brought to equality by means of a Fielden proximity meter which can detect changes in capacitance as small as $5 \times 10^{-4} \mu\text{mf.}$ in a probe fitted to terminate an r.f. coaxial cable and has a zero suppression of up to $40 \mu\text{mf.}$ Because both capacitances are at the end of a single cable, the balance is not affected by any slow capacitance drift in the meter components or the cable; such a drift, however, usually does not exceed the rate of $0.005 \mu\text{mf.}$ per hour. A separate cable is used for each mercury cell, connection to the proximity meter being made by means of a manually operated low-capacitance switch. The proximity meter does not indicate the direction of a capacitance unbalance and so its output is fed into an additional circuit which gives a phase-sensitive response. Either the direct or phase-sensitive output can be placed on a recorder chart.

The mercury surface is 7.6 cm. in diameter and so can be considered, from the point of view of its capacitance to the probe, as flat. With a separation of about 0.7 mm. a change in pressure of 10 microns of Hg will produce a full-scale deflection ($0.05 \mu\text{mf.}$) on the proximity meter. Consequently a change of pressure as small as 0.1 micron of Hg is detectable, and the height of the mercury surface can be reset to this accuracy at any time. By reducing the separation the sensitivity could, if necessary, be increased by at least a factor of four before ground vibrations became troublesome.

End Standards

The two columns of gauge blocks supporting the mercury cells are 18 cm. apart and rest on a 9×14 in. Brown and Sharpe surface plate (X), which is heavily ribbed to reduce distortion. This plate was ground flat in our work-

shops to within 2 microns over the entire surface and is much better than this over smaller areas. The plate stands on three levelling screws and is maintained level with the aid of a level vial having a sensitivity of 2.0 seconds of arc per scale division. Its reading is maintained constant to within one tenth of a scale division, corresponding to a change in the relative height of the bases of the two columns of 0.2 micron.

A set of 1-inch-square Hoke gauge blocks permits the height of the columns to be adjusted within one ten-thousandth of an inch of any desired value. Each block has a hole through its center so that they may be screwed together. The lower cell is screwed down to the surface plate on 1 inch of blocks; in the other column $\frac{1}{2}$ -inch blocks are screwed to the upper cell and to the surface plate. The three long blocks (see Fig. 1) of the second column after being wrung into contact are also lightly screwed together to prevent accidents.

Manometer Operation

To operate the manometer it is first necessary to lower the upper cell into a reference position in which it rests only on the two $\frac{1}{2}$ -inch gauge blocks. Both cells are then evacuated and mercury is injected into them until its separation from the probes gives the required sensitivity; because both cells and columns are practically identical the sensitivity is then the same for both cells if there is a free flow of mercury between them. As soon as the manometer enclosure has reached thermal equilibrium, the reference capacitors (K) are remotely adjusted to equal the mercury-probe capacitance for each cell. Valve 2 is then closed and most of the mercury is withdrawn from the movable cell. This cell is then raised and the required column of end standards is wrung in between the $\frac{1}{2}$ -inch blocks. When the mercury-probe capacitances in both cells have been reset, by reference to capacitors K, the height between the two mercury surfaces is precisely the length of blocks that was inserted.

The raising or lowering of the upper cell is accomplished by placing a carriage under it and sliding carriage and cell together up and down a steel post, the cell being counterweighted while it is moved. Also sliding on the post just above the carriage is a collar to which are attached the two clamps that support the flexible mercury and vacuum lines. These clamps are free to rotate around the post and so permit the top $\frac{1}{2}$ -inch gauge block to be wrung to the rest of the column; they also have a vertical screw adjustment so that any slight tilting action due to the flexible lines can be easily balanced out.

Before a free flow of mercury can be restored between the cells the pressure which will be exerted by the mercury column must be balanced by gas pressure in the lower cell. The vacuum valve (4) is therefore closed and helium gas is allowed to enter the lower cell. The gas pressure is adjusted to within 0.3 mm. of the desired value, using the helium (He) and the vacuum (V) lines to control the gas flow and an altimeter (G) as a coarse pressure gauge. The valve (2) can now be slowly opened and any unbalance in pressure quickly corrected by means of a manually operated piston (C) which changes the gas pressure by 7 microns of Hg per revolution of its control handle.

After a few successive approximations the mercury column is balanced so that both cells have the proper mercury-probe capacitance values; the phase-sensitive meter is particularly useful during these operations. Once the mercury volume and gas pressure have been adjusted, the manometer can be put back in operation in a matter of minutes the next time it is used. For very small pressure adjustments a motor-driven piston (F) is used which changes the pressure at the rate of 5 microns of Hg per minute. This piston is controlled from a portable box which contains a meter showing the phase-sensitive pressure unbalance. This provides an extremely convenient method for controlling the pressure from the resistance bridge table and enables one person to take the measurements on a thermometer.

Temperature-Controlled Enclosure

The density of mercury is highly temperature dependent, changing by 1 p.p.m. for a change in temperature of only 0.006°C . The mercury temperature had to be determined to within a few thousands of a degree and therefore great care was taken in building the isothermal enclosure for the manometer (see Fig. 2). The wooden manometer enclosure, which is about 0.8 by 1.1 meters and 1.8 meters high, has double-walled construction (an air space in between) and is covered with aluminum foil on both the inside and outside

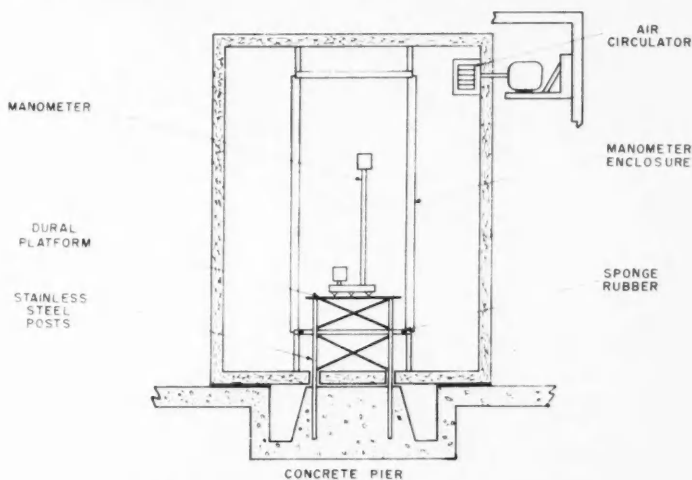


FIG. 2. Schematic diagram of the manometer room layout.

surfaces. One side is hinged for easy access to the manometer and also has a double window, with a shutter, through which the level vial on the surface plate may be checked periodically. This enclosure is situated in a small well-insulated manometer room 1.8 by 2.4 meters and 2.1 meters high and is placed so that clearance is left on all six surfaces between it and the boundaries

of the room. A 20,000 l./min. centrifugal blower continuously circulates the air in the manometer room by sucking it in through ducts at one corner and blowing it out at the diagonally opposite corner. The motor driving the blower is mounted outside the manometer room on the wall of the surrounding main room so as to reduce the vibrations and heat input into the former.

The air in the manometer room is thermostatted at 26.5°C . and cycles about $\pm 0.01^{\circ}\text{C}$. once a minute. Inside the manometer enclosure the temperature does not cycle at all and the gradients are only $\pm 0.01^{\circ}\text{C}$. A fan for circulating the air in the enclosure was found to be unnecessary and also undesirable because of its heating effect. The main room from which the manometer is controlled and in which the remainder of the apparatus is located is thermostatted at 21°C . Valves 1, 2, 3, 4, and 5 (Fig. 1) all have long bakelite shafts to permit their remote operation.

The capacitance between the mercury surface and the probe is affected by some types of ripples on the surface of the mercury. For this reason the manometer is mounted on a duralumin platform which is made vibration-free by supporting it on six stainless steel posts embedded in a concrete pier poured on bedrock. The posts are shock-insulated from the enclosure as well as cross-braced for rigidity. The temperature of the pier is about 21°C . and the heat loss down the posts does not significantly affect the temperature of the platform or that of the enclosure.

Mercury Temperature

To obtain the mercury temperature three sets of three thermocouples in series are mounted along the mercury lines, mainly on the vertical sections. Two sets are distributed on the long line to the upper cell and one set is on the line to the bottom cell. The reference junctions of the thermocouples are screwed down to copper terminals mounted on a large brass block. The e.m.f. from these thermocouples, as well as those from 13 additional ones used to determine the temperature gradients of the manometer enclosure and room, can be measured and recorded with an accuracy equivalent to 0.001°C . or better. A resistance thermometer placed in a hole in the brass block accurately determines the reference temperature. It is sufficient to take the average of the temperatures along the mercury line since the mean temperatures of the three sets of thermocouples seldom have a spread greater than 0.01°C . The average temperature of the mercury usually drifts less than 0.01°C . in a day and so need only be measured occasionally. It is sufficient to assume that the gauge blocks are at the same temperature as the mercury since their length is not nearly so temperature dependent as is the mercury density.

General Stability

It requires about two days to check the reference position, raise the movable cell, and allow the manometer to reach temperature equilibrium. However, once this is done the manometer can be used for several months before it is necessary to reset the pressure. Tests over periods of up to 2 months showed that the drift in the setting of the reference capacitors (K) does not exceed the equivalent of $\frac{1}{2}$ micron of Hg pressure. The surface plate also needs little

attention as it remains perfectly level for weeks. While controlling the pressure during a measurement only one cell need be monitored because the mercury volume remains practically constant once it is set to its proper value. The use of a 70 liter ballast tank located in the manometer enclosure reduces the pressure changes resulting from fluctuations in the height of the vapor column in the boiler and from temperature changes outside the enclosure. At the 1-atm. pressure used in the boiling point determinations these changes are of the order of a few p.p.m. per hour. There is no difficulty in controlling the pressure to within 1 p.p.m. during the temperature measurements.

The Absolute and Relative Accuracy of the Manometer

The pressure p in dynes/cm.² exerted by a column of mercury is given by the relation

$$p = d_t g_m h_t$$

where

d_t = the mean density of mercury in g./cm.³ at temperature t° C.,

g_m = the acceleration due to gravity in cm./sec.² at the manometer,

h_t = the height of the mercury column in cm. (which in this manometer equals the length of a column of gauge blocks at temperature t).

The following discussion concerns the accuracy with which the above three quantities can be determined.

h_t : The gauge blocks were calibrated by our Interferometry Section in May 1956 and again in February 1957 with an accuracy of ± 0.5 p.p.m. By measuring the blocks at 18.5° C. and 23.5° C. the coefficient of linear thermal expansion was found to be $10.85 \times 10^{-6}/^\circ$ C. with an accuracy of better than 1%, giving an additional uncertainty in the length of the blocks at 26.5° C. ($h_{26.5}$) of less than ± 0.3 p.p.m. The two calibrations gave a difference of only 0.5 p.p.m. in $h_{26.5}$ which indicates little if any secular change. Since the calibration of each block includes one wringing film (as little as 0.01 micron thick), the separation between blocks is a negligible source of error. The uncertainty in setting the height of the mercury column equal to the length of the gauge block column, during the operation of the manometer, should not exceed ± 1 p.p.m. A correction of 0.6 micron is made to allow for the compression of the column. The total uncertainty in the determination of $h_{26.5}$ is therefore ± 2 p.p.m.

g_m : The gravitational attraction at the manometer site has been tied in with negligible error to the Ottawa National Reference Station, where the value relative to Potsdam is known with an accuracy of ± 1 p.p.m. However, the internationally accepted value of gravity at Potsdam may be greater than the true value, possibly by as much as 15 p.p.m. This uncertainty should be reduced to 2 or 3 p.p.m. in the near future, but for the present it remains the largest single error in the determination of absolute pressure in dynes.

d_t : The mercury used in this manometer was purified using an oxifier, a gold adhesion filter, and distillation under vacuum.

The density of pure mercury at 20° C. and 1 atm. pressure has recently

been determined by Cook (1957) to within 1 p.p.m. Because mercury is slightly compressible, the above value was corrected to correspond to a mean pressure of 0.5 atmosphere. The close agreement of Cook's results for four different samples supports the belief that the variation in isotopic content between different samples of mercury around the world should not affect the density by more than ± 2 p.p.m. Using the mean coefficient of thermal dilation determined by Beattie *et al.* (1941) the density at temperature $t^\circ \text{C}$. (about 26.5°C .) was calculated from Cook's value at 20°C . with an additional error of not more than ± 0.5 p.p.m. The measurement of the mean temperature of the mercury in the manometer should be accurate to $\pm 0.003^\circ \text{C}$., which results in an additional uncertainty in the density of ± 0.5 p.p.m. The total uncertainty in the absolute density is therefore 4 p.p.m.

p: It appears then that the maximum uncertainty in the absolute pressure is about ± 7 p.p.m. (plus the Potsdam to absolute gravity correction) and is due mainly to the lack of accurate values for a few constants. So far as reproducibility of pressure with this particular manometer is concerned the only sources of error are the determination of the mercury temperature and the setting of the gauge block column; hence we should be able to reproduce pressures here to within $\pm 1\frac{1}{2}$ p.p.m. In fact, if all laboratories calculated their mercury density from the same results and measured their gravity relative to Potsdam, it should be possible to reproduce pressures anywhere in the world to within ± 5 p.p.m. and so reproduce the steam point to about $\pm 0.0001^\circ \text{C}$.

STEAM POINT

On the International Temperature Scale (1948) the steam point is defined as the temperature of equilibrium between liquid water and its vapor under a standard pressure, p_0 , of 1,013,250 dynes/cm.². For pressures different from p_0 by not more than 100 mm. of Hg the equilibrium temperature, t_p , is specified in terms of the actual pressure p by means of the formula

$$(1) \quad t_p = 100 + 28.012 (p/p_0 - 1) - 11.64 (p/p_0 - 1)^2 + 7.1 (p/p_0 - 1)^3.$$

In the range 0° to 630°C . the international temperature, t , is computed from the resistance R_t of a standard platinum resistance thermometer by means of the equation

$$(2) \quad R_t/R_0 = 1 + At + Bt^2,$$

where R_0 is the resistance at the ice point (0°C .) and the constants A and B are determined by calibration at the steam and sulphur points.

The interpolation formula (2) may also be written in the Callendar form

$$(3) \quad t = (1/\alpha)(R_t/R_0 - 1) + \delta(t/100 - 1)(t/100),$$

where

$$(4) \quad \alpha = (1/100)(R_{100}/R_0 - 1).$$

The α coefficient is particularly useful as a measure of the reproducibility of the steam point.

The steam point boiler, manometer, ballast tank, and connecting lines form a closed system in which helium gas transmits the water vapor pressure to the manometer (see Fig. 1). The basic design of the boiler is similar to the latest one used at the National Bureau of Standards (Stimson 1955). It is 9 cm. in diameter and 47 cm. long, and is made of copper tinned on the inside to reduce contamination of the distilled water. The bottom end plate is machined to provide a re-entrant heater dome of 4 mm. wall thickness into which a specially constructed 300 w. electric heater (BW) is screwed to a position slightly below the water surface. Inside the boiler a single layer of closely spaced vertical silver wires (DW) are fastened to the heater dome to reduce pressure fluctuations caused by bumping.

At the top of the boiler the excess vapor flows up a thin-wall german silver tube, 2.5 cm. in diameter, to a water-cooled condenser (GW) the lower end of which is about 2.5 cm. above the top plate. In the condenser the steam and helium form an interface which is very stable as a result of the upward flow of steam opposing the diffusion of helium into the boiler and of the condensing process effectively preventing water vapor from diffusing above the interface. Since a vapor head of 6 cm. corresponds to a change in the steam temperature of 0.0001°C . the position of this interface must be determined, and this is done, to within 0.5 cm., by means of a thermocouple placed in the german silver tube (HW). The position of the interface has been found to remain within 1 cm. of the bottom of the condenser for heater powers of 70 to 250 w. and for wide variations in the rate of flow of water through the condenser.

Six re-entrant thermometer wells (FW), five of which are 8 mm. diameter and one 10 mm. diameter, extend about 35 cm. into the boiler. They are made of thin-wall german silver tubing that is tinned on the outside and are completely surrounded by conical radiation shields (EW) that are sufficiently open at the top and bottom to permit free circulation of the vapor around the wells. The top shield directs the water from the condenser to the outer wall while the bottom set directs the water on to the top of the heater dome to prevent superheating. The boiler is insulated with 5 cm. of Aercor Fiberglas and two coaxial aluminum radiation shields. A wall heater was found to be unnecessary as the bottom heater raises the water from room temperature to the boiling point in less than one hour and continues to boil it on less than 70 w.; a heater power of 125 watts is normally used. Short-term pressure fluctuations observed at the manometer are about one micron of Hg in magnitude. A demountable glass cold trap (T), about one meter from the condenser, prevents the water vapor from diffusing back into the manometer. It is cooled with dry ice and alcohol and seldom needs to be emptied as the boiler can operate for about 2 months before 1 ml. of water is collected.

RESISTANCE MEASUREMENTS

The resistance measurements were made with a Leeds and Northrup high-precision G3 Mueller bridge incorporating the recent improvements described by Stimson in 1955. The detector is a Leeds and Northrup type HS galvano-

meter mounted on a Mueller suspension in a draft-free compartment. Using an effective* optical path of 9 meters and current reversal, it is possible to interpolate between the settings of the 10^{-5} ohm decade to $\pm 2 \mu\Omega$ for a bridge setting of 0 to 40 ohms and a current of 1 ma.

The bridge is completely calibrated every 6 months using a system (Mueller 1916) whereby all the coils are internally compared with the sum of the 10 1-ohm coils. In addition the 10-ohm coils are checked every month, their rate of drift against the sum of the 1-ohm coils being about $2 \mu\Omega$ per month per coil. The average deviation in the calibration of the 10-ohm coils is about $\pm 0.5 \mu\Omega$ and in the smaller coils about $\pm 0.2 \mu\Omega$. Since the calculation of temperature from the formulae (2) or (3) involves a ratio of resistance, the actual value assigned to the sum of the 1-ohm coils is quite arbitrary; for the results reported in this paper a value of exactly 10 was used.†

Each resistance measurement consisted of 12 observations, the commutator and current sequence being 1N 1R 1R 1N, 2N 2R 2R 2N, 1N 1R 1R 1N; zero-current resistances were obtained by extrapolation from the measurements at 1 and 2 ma.‡ The two currents could be set using the bridge milliammeter, which has a mirror scale and was calibrated against a potentiometer, with an uncertainty of $\pm 5 \mu\text{a}$. This gives an uncertainty in the extrapolated zero-current resistance (cf. Table III) of about $\pm 5 \mu\Omega$ for a Barber-type thermometer (Barber 1950) and of less than $\pm 2 \mu\Omega$ for a single-layer helix Meyers-type thermometer (Stimson 1955). A Meyers thermometer (S163) of the above type was used for all but one (specified below) of the experiments described in this paper.

Before and after each measurement the residual resistance of the bridge when the dials are set to zero was determined and its value subtracted from the resistance reading. R_{100} was obtained by correcting the resistance as measured to that corresponding to 1 standard atmosphere of pressure. For both the steam and water triple points at least 20 minutes were allowed between the insertion of the thermometer in the well and the start of the readings. Measurements at the triple point of water indicate that the reproducibility over a period of days of the zero-current resistance determination is of the order of $\pm 1 \mu\Omega$.

TRIPLE POINT OF WATER

In order to determine the reproducibility of the steam point to better than 0.0001°C . from measurements of the α coefficient, R_0 must be determined with an accuracy of a few microhms. Following the recommendations laid down in the International Temperature Scale of 1948, R_0 is computed from the resistance at the triple point of water (R_{TP}), a point to which the temperature of $+0.0100^\circ \text{C}$. has been assigned. This triple point was realized in standard

*A multiple reflection system (Dauphinee 1955) was used in conjunction with a 2.2 meter path distance.

†A calibration of these coils in terms of the ohm as maintained in Canada (September 1957) showed that they were only 1 p.p.m. different from 10 ohms. Hence the bridge unit of resistance is an absolute ohm to a high degree of accuracy.

‡One exception to this sequence of observations is noted later.

pyrex cells (Barber 1954; Stimson 1955) in which the ice mantle was frozen around the thermometer well by rapid cooling from within using dry ice. In this laboratory periodic cell intercomparisons are made to check for cells whose temperature may be subnormal because of a gas leak or because of contamination of the water. Results of these intercomparisons, excluding two subnormal cells and a few recently broken, are presented in Table I.* It will be seen that in 1958 the value of R_{TP} (with one thermometer) found in cells prepared from two sources and of ages ranging from 1 month to 4 years did not differ by more than $12 \mu\Omega$ ($10 \mu\Omega$ is equivalent to 0.0001°C.). The cells made at the same time and place agree to better than $4 \mu\Omega$. Several cells were used for the steam point investigations, appropriate corrections being applied from Table I.

TABLE I

INTERCOMPARISON OF R_{TP} VALUES OBTAINED WITH DIFFERENT TRIPLE POINT CELLS
The figures shown are the differences between R_{TP} of the cell in question and that of cell No. 27

Cell number	Maker	Date cell made	Date of comparison		
			Nov. 1954	April 1956	Feb. 1958
27	N.R.C.*	April 1954	0 $\mu\Omega$	0 $\mu\Omega$	0 $\mu\Omega$
21	"	"	+1	+2	+1
24	"	"	+5	+4	+4
29	"	"	0	+1	+1
32	"	"	+4	+5	
116	J. & J. Co.†	Aug. 1955			-6
117	"	"			-6
201	"	Feb. 1958			+3
202	"	"			+6

*The N.R.C. cells were prepared in this laboratory by Dr. R. S. Turgel.

†The J. and J. Instrument Co., Silver Springs, Md., U.S.A.

At the conclusion of the steam point work a study of the reproducibility and other aspects of the water triple point was carried out. Fig. 3 shows the reproducibility of R_{TP} on thermometer S163 over a period of about 1 month and with several new mantles; one ice mantle on cell 116 gave an average deviation in R_{TP} of about $1 \mu\Omega$ over a period of 4 weeks even though the thermometer was occasionally used at the steam point during this time (see Fig. 8).

Each of the five times a new ice mantle was put on cell 117, R_{TP} rose about 10 to $30 \mu\Omega$ between the 2nd and 48th hours after the mantle was made. By following this type of initial temperature change 23 times using eight different cells and diverse mantle freezing procedures† and by means of other experiments we have been able to show that:

(1) The initial temperature change is not consistently altered by changing in turn the size of the mantle, the rate of freezing, or the past history of the cell or by mixing the water just before freezing.

*The 1954 and 1956 results presented in this table are taken from a previous paper from this laboratory (McLaren 1957a).

†For most of these measurements the usual set of 12 observations was shortened to 6 since the resulting decrease in precision could be tolerated.

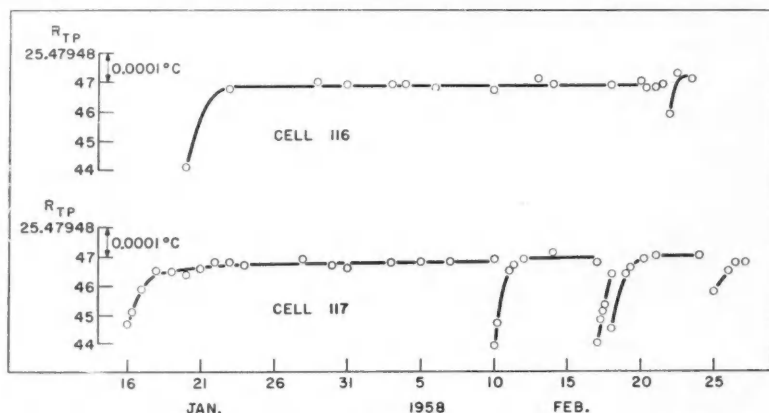


FIG. 3. Variations in R_{TP} for a Meyers thermometer (S163) measured in two triple point cells over a period of about one month.

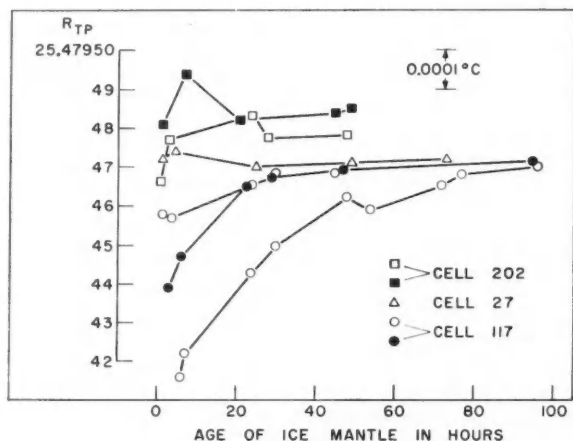


FIG. 4. Initial variations of temperature with time in three triple point cells. Other cells examined had triple point resistances lying inside the range shown in this figure.

(2) To a certain extent the shape and magnitude of the temperature change may depend on the particular cell. Fig. 4 shows the range of curves obtained with three different cells.

(3) Melting the ice mantle away from the thermometer well by as much as 2 mm. does not alter R_{TP} significantly.

(4) While Fig. 3 does show that the equilibrium R_{TP} agrees for each new mantle, we have found that for certain cells R_{TP} may change by up to $8 \mu\Omega$ with a change in mantle. For this reason it is important to use several new mantles for the accurate intercomparison of cells.

These results suggest that it is extremely unlikely that the initial temperature change is due to strains in the ice; because of the comparatively long times involved it seems probable that it is due to the diffusion of impurities. Throughout all the steam point work and all the 1958 intercomparisons at least 2 days were allowed after the preparation of the ice mantle before using the cell.

Fig. 5 shows the effect of changing the depth of immersion of the thermometer coil below the liquid-vapor interface. The first and last measurements were taken at the bottom of the well as a check on over-all stability; the difference of $3 \mu\Omega$ is within the precision of the measurements. The changes of R_{TP} with depth agree exactly with those to be expected as a result of the change in hydrostatic pressure.

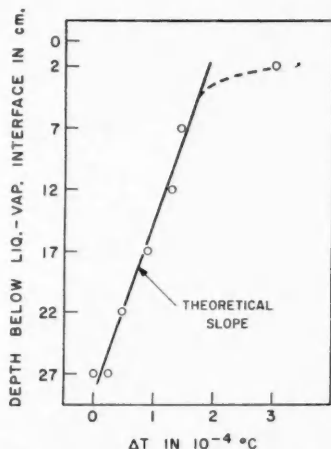


FIG. 5. Change of temperature with change of depth of immersion in a triple point cell. The solid line gives the change computed from the change in hydrostatic pressure. Depths are measured from the center of the platinum resistance coil to the liquid-vapor interface.

RESULTS

The preliminary tests on the steam point reproducibility were carried out from March 14 to April 4, 1956, with the equipment located in a room on the second floor of the building. Because the manometer was affected by local building vibrations and by minute floor movements caused by personnel, wind, etc. it was very tedious taking measurements there. In spite of this difficulty the results shown in Fig. 6 were very promising; 16 determinations of α over a period of 3 weeks had an average deviation equivalent to 0.00004°C . at the steam point. During this time the pressure (756.4 mm. of Hg) was reset 4 times, i.e. the upper cell was lowered, the reference position was checked, and the cell was raised again. The average values of α for each setting of the pressure agree within $\pm 1 \times 10^{-9}$, which corresponds to a pressure reproducibility of ± 1 p.p.m. On March 30 the manometer temperature was raised

from 26.3° to 27.6° C. without producing any significant change in the subsequent (April 4th) values of α . The triple point resistance was determined only occasionally for this preliminary work.

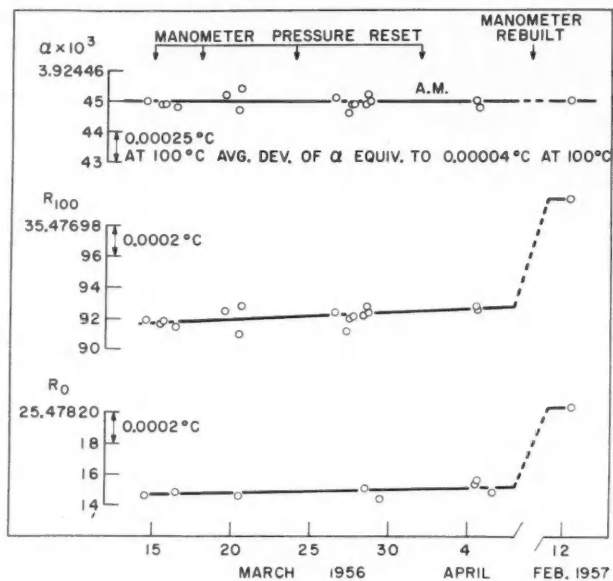


FIG. 6. Determination of R_0 , R_{100} , and α for thermometer S163. Between April 1956 and February 1957 the manometer was moved from the second floor of the laboratory and rebuilt on bedrock. All but one of the measurements were made in one small well; the first measurement on April 4th was in the large well. Both wells were used dry.

During the period June 1956 to January 1957 the manometer was rebuilt on bedrock and has since given extremely stable operation. This time the gauge blocks were selected to give a pressure of almost exactly 760 mm. of Hg. The first steam point measurement in the new location, taken on February 12, is shown in Fig. 6 and gives an α value of precisely the mean of the previous March 14 to April 4 determinations. This excellent agreement of the α values provides a check on a number of possible sources of error, for in addition to the relocation of the manometer, the mercury in the manometer had been changed, the triply distilled water in the boiler had been changed, and the bridge had been recalibrated. The rise in R_0 and R_{100} between April 4 and February 12 is due to changes in the bridge unit of resistance and in the thermometer resistance.

From April 2 to May 14, 1957, thermometer S163 was used at the sulphur point (444.6° C.) for an accumulated time of about 150 hours; in a subsequent determination α was found to have risen by the equivalent of 0.0007° C. (see Fig. 7). To find out if the α value had stabilized at some time less than 150

hours the thermometer was left in an annealing furnace at 435° C. from May 24 to May 28. This resulted in an even greater increase in α , amounting to 0.0011° C., and indicated that it would take an impractical amount of annealing at 435° C. to produce a stable α coefficient. Consequently it was decided to use thermometer S163 only for the steam point investigation. After May 28, as can be seen in Fig. 7, the α value started dropping until by September it had recovered about half the change produced by the high temperature.

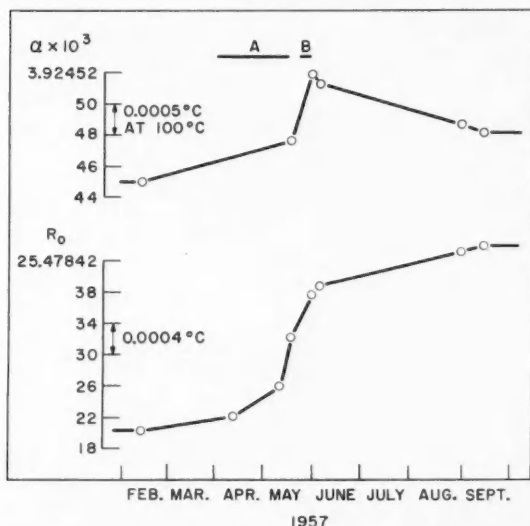


FIG. 7. The effect of heat treatment on R_0 and α for thermometer S163. During period A the thermometer accumulated 150 hours at the sulphur point; in period B it was held at 435° C. for 100 hours. Before April 2nd and after May 28th the thermometer was not used above 100° C.

These apparent changes in the platinum wire are difficult to explain in terms of any single process. Because both R_0 and α were continuously increasing during this heat treatment the changes in the resistances could not have been due solely to removal of strains (lattice defects), to changes in the dimensions of the wire, or to impurities dissolving in the wire. These changes are not peculiar to thermometer S163, for similar increases in α have been found with two other Meyers thermometers after prolonged annealing at 480° C. This shows that at temperatures of 435° to 480° C., as has already been found at temperatures above 660° C. (Waidner and Burgess 1910; Moser 1930), the constants of a platinum resistance thermometer are not stable. Evidence of changes in platinum wire at slightly lower temperatures is given by McLaren (1957b), who attributes an apparent rise of 0.0012° C. in the freezing point of zinc (420° C.) to the hundreds of hours his thermometer was used in the range 420–430° C.

That the variations in the α coefficient of thermometer S163 were not due to steam point changes is shown by the values of α determined for two other Meyers thermometers in March 1956* and in September 1957 (Table II). As can be seen from their average change in α the steam point has not changed by more than 0.0001°C . over the 18 months' interval. These thermometers were not used at high temperatures in the interim period; subsequent annealing did, however, reveal a small amount of cold work in S165 which when annealed out raised the α coefficient to its March 1956 value.

TABLE II
APPARENT CHANGES IN α FOR TWO MEYERS THERMOMETERS OVER AN
18-MONTH PERIOD
 ΔT is the equivalent change of the steam point

Thermometer	$\alpha \times 10^3$		$\Delta\alpha \times 10^3$	$\Delta T \times 10^4, ^\circ\text{C}$.
	March 28, 1956	Sept. 12, 1957		
S165	3.924413	3.924406	-7	-1.8
S178	3.924289	3.924288	-1	-0.2
Average			-4	-1.0

Starting on September 13, 1957, the α coefficient of thermometer S163 was determined about once a week in order to check the reproducibility of the steam point with the manometer on bedrock. The results for 27 determinations of α over a period of 5 months are shown in Fig. 8 and are found to have an average deviation equivalent to 0.00004°C . at the steam point. No significant change in α was produced by the two resettings of the pressure. For these results the triple point of water was usually measured before and after the steam point; the difference was seldom more than $3\ \mu\Omega$ and only the average value is shown in Fig. 8. All but three of these measurements were made in one well using glycerin to improve the thermal contact.

At the first water change indicated in Fig. 8 the triply distilled water originally put in the boiler in January 1957 was drained out and its specific resistance measured. This was found to be about 3000 ohms per cm^3 , which is even lower than the specific resistance of our tap water. The same day fresh triply distilled water testing 10^6 ohms per cm^3 was put in the boiler; as can be seen in Fig. 8, no significant change in the α coefficient resulted. At the second water change the boiler was filled with singly distilled tap water testing close to 10^6 ohms per cm^3 and once again no significant change in α was found. In this latter test we were particularly interested in seeing if volatile organic impurities might be present to affect the steam point. It appears from these results that the design of the boiler very effectively protects the thermometer wells against radiation and splashing from contaminated water and permits the pure water condensing on the wells to give a very stable

*These two determinations of α were made by E. H. McLaren using a modified G2 Leeds and Northrup Mueller Bridge.

temperature. The tinning of the inside of the boiler (except for the wells) may, therefore, have been unnecessary.

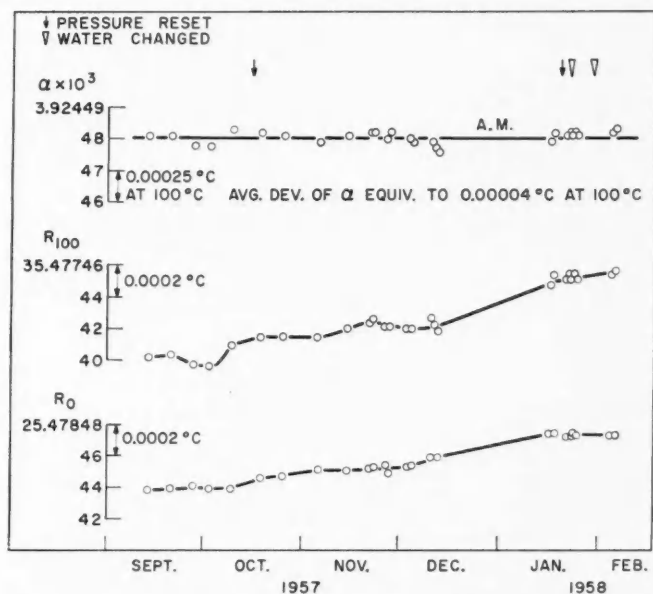


FIG. 8. Determinations of R_0 , R_{100} , and α for thermometer S163 during a period of 5 months. All but three of the measurements were made in a single well. In all measurements glycerin was used to improve the thermal contact.

Fig. 9 shows the results of comparative measurements in the six thermometer wells with and without glycerin in them. On each run the first and last measurements were taken in the same well. The fact that the wells agree within the error of measurement when the thermal contact between thermometer and well is improved by the glycerin layer strongly suggests that no real difference in temperature exists between wells.* The spread of 0.0002° C. between the dry wells may be due to some effect that disturbs the zero current extrapolation.

The effect of thermometer immersion was investigated in the 10 mm. and in an 8 mm. well both with and without glycerin; the results are shown in Fig. 10. The change in temperature with depth is that to be expected from the change in pressure due to the density of the vapor. The actual curve departs from the theoretical line near the top of the well and the point at which this departure occurs may be taken as the minimum depth of immersion.

*The wells should be completely dry or else contain enough glycerin to cover the thermometer coil; a thin film of glycerin left on the well wall often causes instability in the thermometer heating effect.

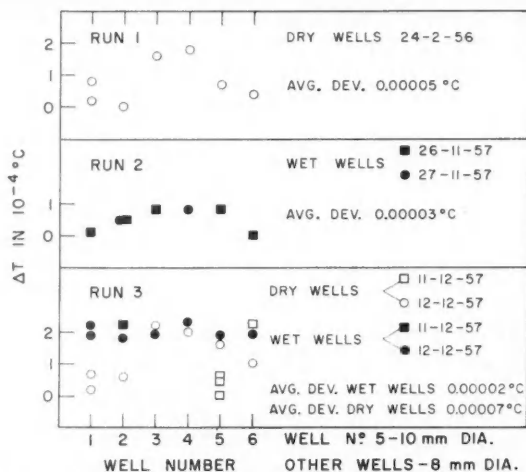


FIG. 9. Comparative measurements in all six thermometer wells of the steam point boiler. Measurements were made both with and without glycerin in the wells. In each set the first and last measurements were made in the same well.

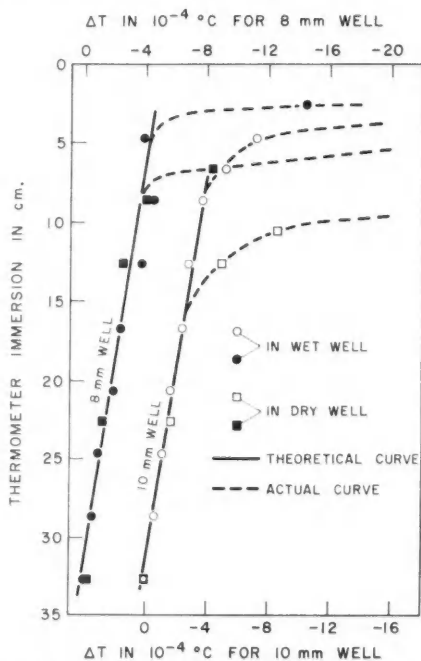


FIG. 10. Change of temperature with change of depth of immersion in two steam point boiler wells. The solid lines give the change computed from the change in pressure due to the density of the vapor. The depths shown are those of the top of the platinum resistance coil below the top of the boiler. Measurements were made both with and without glycerin in the wells.

As can be seen in Fig. 10 the use of glycerin reduced this minimum depth of immersion by about 50%. It also reduces by about 50% the time taken by thermometers to reach temperature equilibrium and, as is shown in Table III, substantially reduces the measuring current heating effect.

TABLE III

THE CHANGES OF RESISTANCE AT THE STEAM POINT (ΔR_{100}) CAUSED BY THE HEATING EFFECT OF A 2 MA. MEASURING CURRENT IN FOUR DIFFERENT TYPES OF RESISTANCE THERMOMETERS

The wet wells contain glycerin

Thermometer coil construction*	Outside diameter of protection tube, mm.	R_0 , Ω	$\Delta R_{100} \times 10^5, \Omega$			
			8 mm. well		10 mm. well	
			Dry	Wet	Dry	Wet
Single-layer bifilar helix (Meyers)	7.3	25	35	17	44	19
Coiled bifilar helix (Meyers)	7.0	25	72	49	103	52
Formerless coil in U-tube (Barber)	8.0	25	—	—	84	49
Formerless coil on twisted quartz ribbon	5.0	10	19	14	—	—

*For a more complete description of all four types of coil construction see Stimson (1955).

The results of measurements at the steam point for boiling powers ranging from 72 to 260 w. are shown in Fig. 11; all variations are within the uncertainty in the measurements. This shows that heat loss through the walls of the boiler and pressure gradients due to viscous flow of the vapor do not introduce significant errors.

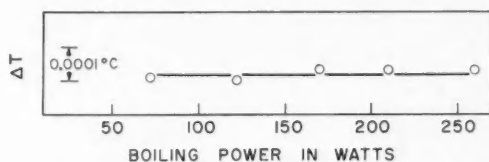


FIG. 11. Temperature plotted against power input to the steam point boiler.

SUMMARY

A steam point apparatus and precision manometer are described which can reproduce the steam point over a period of 2 years to $\pm 10^{-4}^\circ \text{C.}$; over a period of 5 months with an average deviation of $\pm 4 \times 10^{-5}^\circ \text{C.}$; and over a period of 1 or 2 days to $\pm 2 \times 10^{-5}^\circ \text{C.}$ Conversely this shows that the manometer will reproduce 1 atmosphere pressure over a period of 5 months with an average deviation of ± 1 p.p.m.

Glycerin is used to improve the thermal contact between the thermometer and well and substantially reduces the measuring current heating effect. Varying the heat input to the boiler from 72 to 260 w. and the thermometer immersion from 15 to 33 cm. does not affect the steam point by more than $\pm 2 \times 10^{-5}^\circ \text{C.}$ Replacing the distilled water in the boiler with either fresh triply or singly distilled tap water produces no significant change in the steam point, even after the water has been in the boiler for as long as one

year. The design of the boiler very effectively protects the thermometer wells against radiation and splashing from contaminated water and permits the pure water condensing on the wells to give a very stable temperature.

The water triple-point cells have been found to be extremely stable. A group of cells of various ages from two sources have given a maximum spread of $1.2 \times 10^{-4}^\circ \text{C}$. over repeated intercomparisons. Two particular ice mantles in two different cells each gave an average deviation of the equilibrium temperature readings of $\pm 10^{-5}^\circ \text{C}$. over a period of 4 weeks. However, freshly prepared mantles require from 1 to 3 days to reach temperature equilibrium and may change by as much as $6 \times 10^{-4}^\circ \text{C}$. during this period. This suggests that it may be desirable to add an appropriate warning to the recommendations accompanying the definition of the International Temperature Scale.

The resistance thermometer has proved to be extremely stable when it is used only at the steam point and water triple point, and is handled with reasonable care. If, however, the thermometer is used in the range 430°C . to 480°C . the α coefficient rises slowly and periodic recalibration is required.

The reproducibilities of the steam point and of the triple point of water over long periods of time are similar, being of the order of 10^{-4}°C . The fundamental interval of 100°C . between the ice and steam points can, therefore, be realized to a few ten-thousandths of a degree.

The author wishes to thank Mr. N. F. Scardina for his valuable assistance with the resistance measurements.

REFERENCES

- BARBER, C. R. 1950. *J. Sci. Instr.* **27**, 47.
BARBER, C. R., HANDLEY, R., and HERINGTON, E. F. G. 1954. *Brit. J. Appl. Phys.* **5**, 41.
BEATTIE, J. A. and BLAISDELL, B. E. 1937. *Proc. Am. Acad. Arts Sci.* **71**, 361.
BEATTIE, J. A., BLAISDELL, B. E., KAYE, J., GERRY, H. T., and JOHNSON, C. A. 1941. *Proc. Am. Acad. Arts Sci.* **74**, 371.
BUREAU INTERNATIONAL DES POIDS ET MESURES. 1930. *Compt. rend. trav. et mém.* **18**, 94.
BURGESS, G. K. 1928. *Bur. Standards J. Research*, **1**, 635.
COMITÉ INTERNATIONAL DES POIDS ET MESURES. 1948. *Procès-verbaux des séances de 1948*, **21**, T30.
COMITÉ INTERNATIONAL DES POIDS ET MESURES. 1955. *Procès-verbaux des séances de 1954*, **24**, T96.
COOK, A. H. and STONE, N. W. B. 1957. *Phil. Trans. Roy. Soc. A*, **250**, 279.
DAUPHINEE, T. M. 1955. *Rev. Sci. Instr.* **26**, 873.
MCLAREN, E. H. 1957a. *Can. J. Phys.* **35**, 78.
— 1957b. *Can. J. Phys.* **35**, 1086.
MOSE, H. 1930. *Ann. Physik*, **6**, 852.
MUELLER, E. F. 1916. *Natl. Bur. Standards (U.S.) Tech. News Bull.* **13**, 553.
STIMSON, H. F. 1949. *J. Research Natl. Bur. Standards (U.S.)*, **42**, 209.
— 1955. *Temperature, its measurement and control in science and industry*, Vol. 2 (Reinhold Publishing Corporation, New York) p. 141.
WADNER, C. W. and BURGESS, G. K. 1919. *Natl. Bur. Standards (U.S.) Tech. News Bull.* **6**, 149.

THE THEORY OF COLLISION-INDUCED ABSORPTION IN HYDROGEN AND DEUTERIUM¹

F. R. BRITTON² AND M. F. CRAWFORD³

ABSTRACT

Collision-induced absorptions in the 1-0 vibrational band of hydrogen and of deuterium are calculated by considering interactions during binary collisions. The induced dipole moment, μ , of an interacting molecule-pair is derived by combining a moment, μ_a , resulting from overlap forces, with a moment, μ_q , due to the interactions of permanent molecular quadrupole moments. μ_q consists of two additive parts, an indirect part calculated by van Kranendonk and Bird (1951) and a direct part calculated in this paper. μ_q is calculated in two different ways: (a) theoretically and (b) semiempirically. Absorption coefficients are evaluated for temperatures 296° K. and 80° K. For H_2 at 296° K. the total integrated coefficient obtained by using procedure (a) is 8.6% smaller and by using (b) is 8.2% larger than the experimental value. The experimental ratio of the coefficients of the Q and S branches is in much better agreement with (b) than (a). For $T = 80^\circ$ K. the experimental value of the total integrated coefficient is only 61% of that calculated by (b). The good agreement between calculated and experimental values of absorption coefficients at room temperature suggests that at low temperatures the classical distribution function used in this paper must be replaced by the quantal pair distribution function. Experimental data for D_2 are not available.

1. INTRODUCTION

Van Kranendonk and Bird (1951) have published a calculation of the infrared absorption induced in molecular hydrogen by collisions. In their theory the induced dipole moment of a colliding pair arises from two effects: the distortion of the charge distribution produced by electron exchange between the molecules of a colliding pair, and the distortion produced by the quadrupole fields of the two molecules. The exchange, or overlap distortion is formulated generally (van Kranendonk 1952), and can be described as arising from a direct effect due to exchange of electrons between the two molecules and an indirect effect arising from the repulsive distortion of the Rosen wave function of each electron of the two molecules. They computed the indirect effect and neglected the direct effect, but van Kranendonk (1952) remarks that the latter is smaller and might amount to half of the indirect effect. The quadrupole distortion was calculated using an experimental value of the mean polarizability, an estimated value of the mean rate of change of the polarizability, and a quadrupole moment and its derivative derived using the Rosen (1931) function.

Independently the authors of this paper had calculated the induced effect using the Wang single-electron wave function, which is spherically symmetrical. Our calculation gives only the direct effect of the overlap forces and zero for

¹Manuscript received December 23, 1957.

Contribution from the Department of Mathematics, Hamilton College, McMaster University, Hamilton, Ontario, and Department of Physics, University of Toronto, Toronto, Ontario.

²Department of Mathematics, Hamilton College, McMaster University, Hamilton, Ontario.

³Department of Physics, University of Toronto, Toronto, Ontario.

the indirect effect. The quadrupole distortion was evaluated directly using both the perturbation and the variational method without recourse to experimental values of the polarizability and its derivative. Since the paper by van Kranendonk and Bird appeared before the completion of our calculation, we then attempted a more general formulation in which the overlap effect and the quadrupole effect are obtained simultaneously, rather than as additive effects. This formulation leads to extremely complicated integration and as yet has not been completed. However, through personal discussion with van Kranendonk, it appeared that the combination of their calculation of the indirect effect and our calculation of the direct effect would lead to much better agreement between the calculated and the experimental value of the integrated absorption coefficient.

The direct exchange effect is evaluated in this paper using, for consistency, a Rosen instead of a Wang function, and combined with the indirect effect calculated by van Kranendonk and Bird. A variational calculation of the quadrupole effect is also presented and compared with the results obtained using van Kranendonk's formulation with improved experimental values of the polarizability, its derivative, and their anisotropies. The overlap distortion and the quadrupole distortion are then added to evaluate the integrated absorption coefficient. The calculated and experimental values are in good agreement for hydrogen at room temperature and moderate densities

2. ABSORPTION COEFFICIENTS

The measurements of Welsh, Crawford, and Locke (1949) and Crawford, Welsh, MacDonald, and Locke (1950) show that the integrated absorption coefficient of the 0-1 vibrational band of hydrogen at room temperature varies linearly with the square of the density of the gas up to 100 Amagat units of density. The value of the specific integrated absorption coefficient for the low-density range is $10.5 \times 10^{-32} \text{ cm.}^{-1} \text{ sec.}^{-1}$ (per molecule/cm.³)².

The objective of this paper is to calculate theoretically absorption coefficients for this low-density range in which only binary collisions need be considered.

At room temperature, classical statistics give the probability that, in a gas of n molecules per unit volume, one and only one molecule has its mass center in a spherical shell of radius R and thickness dR surrounding another molecule as

$$(1) \quad 4\pi n R^2 \exp(\phi(R)/kT),$$

where $\phi(R)$ in the Boltzmann factor is the interaction energy of a molecule pair averaged over all relative orientations of the molecular axes. Expression (1) is small for $R < 4.0$.*

Van Kranendonk and Bird (1951) and van Kranendonk (1952) used the binary distribution function (1) to calculate absorptions in H₂ gas. Recently van Kranendonk (1957) has given a more general formulation of the problem in which he considers triple and multiple collisions and shows that (1) is a

*Atomic units are used throughout theoretical calculations.

good approximation to the distribution function for low densities and sufficiently high temperatures.

The wave function for a molecule pair is taken to be

$$(2) \quad \Psi = \psi_e \psi_{v_1} \psi_{v_2} \psi_{j_1 m_1} \psi_{j_2 m_2}$$

where $\psi_e(1, 2, 3, 4; R, r_1, r_2, \theta_1, \phi_1, \theta_2, \phi_2)$ is an electronic wave function of electrons 1, 2, 3, 4; R is the intermolecular distance; $r_1 = r_{ab}$ and $r_2 = r_{cd}$; and the internuclear distances and orientation angles are as shown in Fig. 1. ψ_{v_1} and ψ_{v_2} are vibrational functions, $\psi_{j_1 m_1}$ and $\psi_{j_2 m_2}$ rotational functions, and are taken to be normalized harmonic oscillator and rigid rotator eigenfunctions

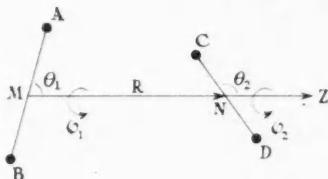


FIG. 1. Coordinates in the two-molecule system.

respectively, the axis of quantization for the latter being \mathbf{R} , taken in direction from molecule AB to molecule CD as the z axis of a Cartesian coordinate system.

The induced dipole moment of the molecule pair,

$$(3) \quad \mu = \mu(r_1, r_2, \theta_1, \phi_1, \theta_2, \phi_2; R),$$

is expanded in a Taylor series in r_1 and r_2 about the equilibrium value $r_1 = r_2 = r_0$, so that

$$(4) \quad \mu = \mu_0 + (\partial\mu/\partial r_1)_0(r_1 - r_0) + (\partial\mu/\partial r_2)_0(r_2 - r_0) + \dots$$

The first term of (4) contributes only to the pure rotational spectrum and need not be considered. The second and third terms give identical contributions to total absorptions in the 0-1 vibration band, so only the second term will be evaluated and absorption coefficients calculated from it will be multiplied by 2. $(\partial\mu/\partial r_1)_0$ will be denoted by μ_0' and primes will be used hereafter to denote differentiation with respect to $r_1 = r_{ab}$. Quadratic terms not given in (4) give rise to 0-2 overtone transitions, and the term with $(r_1 - r_0)(r_2 - r_0)$ to simultaneous 0-1 vibrational transitions in both molecules. These and later terms in (4) do not contribute to the fundamental 0-1 band treated in this paper.

Thus, for the fundamental band, matrix elements of μ are derived solely from μ_0' by expanding in spherical harmonics,

$$(5) \quad \mu_0' = 2\pi \sum D^{(k)}(\lambda_1 \mu_1 \lambda_2 \mu_2) Y_1(\lambda_1 \mu_1) Y_2(\lambda_2 \mu_2),$$

where

$$Y_i(\lambda_i \mu_i) = O_{\lambda_i \mu_i}(\theta_i) \cdot \Phi_{\mu_i}(\phi_i), \quad i = 1, 2,$$

is a normalized spherical harmonic of molecule i and the $D^{(k)}$ are functions of R . The superscript k indicates the component of the dipole moment dealt with, $k = x, y, z$, or $0 = z$, $+1 = 2^{-1/2}(x+iy)$, $-1 = 2^{-1/2}(x-iy)$; but the subscript k will be suppressed for the sake of simplicity when this entails no ambiguity.

Because the H_2 molecule is homonuclear, D coefficients having λ_1 , or λ_2 , odd are zero and the z component of (5) is well represented by the first four coefficients, $D^{(0)}(0000) = D_1$, $D^{(0)}(2000) = D_2$, $D^{(0)}(0020) = D_3$, and $D^{(0)}(2020) = D_4$. For ± 1 components all coefficients D are negligible except $D^{(\pm 1)}(2\pm 100)$, and $D^{(\pm 1)}(002\pm 1)$.

From (3), (4), and (5) the matrix element between an initial state $\rho(0, 0, j_1, m_1, j_2, m_2)$ and a final state $\rho'(1, 0, j_1', m_1', j_2', m_2')$ is

$$(6) \quad \mu_{\rho\rho'} = (m_H \gamma_0 / \hbar)^{-1} \sum 2\pi D(\lambda_1 \mu_1 \lambda_2 \mu_2) (j_1 m_1 | \lambda_1 \mu_1 | j_1' m_1') (j_2 m_2 | \lambda_2 \mu_2 | j_2' m_2'),$$

where m_H is the mass of a hydrogen atom, γ_0 the angular frequency of the fundamental vibration of H_2 , and

$$(jm | \lambda \mu | j'm') = \int Y^*(jm) Y(\lambda \mu) Y(j'm') d \cos \theta d \phi$$

are matrix elements which give the selection rules

$$(7) \quad \Delta j = 0, \pm 2, \pm 4, \dots$$

The contribution of the $\rho \rightarrow \rho'$ transition to absorption coefficients is given by substituting (6) into

$$(8) \quad a_{\rho\rho'}(R) = 2P_\rho \cdot 8\pi^2 \gamma_{\rho\rho'} (3hc)^{-1} |\mu_{\rho\rho'}(R)|^2,$$

where, because almost all molecules are in the ground vibrational state at room temperature or lower, the population factor P_ρ is taken to be $P(j_1 m_1) P(j_2 m_2)$ with $P(jm)$ the Boltzmann distribution over the various rotational states.

From (1) and (8) the absorption coefficient of the gas is that of $\frac{1}{2}n^2$ molecule pairs per unit volume and is given by

$$(9) \quad A_{\rho\rho'} = 2\pi n^2 \int_0^\infty a_{\rho\rho'}(R) \exp(-\phi(R)/kT) R^2 dR.$$

\mathbf{u} is expressed as the sum of two parts, \mathbf{u}_a and \mathbf{u}_q , of which \mathbf{u}_a is the result of the interaction of atom pairs and is calculated in Section 3, and \mathbf{u}_q is the additional moment due to the interaction of the permanent quadrupole moments of the molecules, calculated in Section 4. D coefficients calculated separately from $(\mu_a)_0$ and $(\mu_q)_0$ are denoted by subscripts a and q and are additive:

$$(10) \quad D = D_a + D_q, \quad \mathbf{u} = \mathbf{u}_a + \mathbf{u}_q.$$

3. THE DIPOLE MOMENT \mathbf{u}_a

The dipole moment \mathbf{u}_a is calculated by considering the interaction of pairs

of atoms in the molecular pair system. The electronic ground state of this system is represented by the antisymmetric function*

$$(11) \quad \psi_e(1234) = \psi_1 - \psi_3 - \psi_4 + \psi_5,$$

where

$$\begin{aligned} \psi_1 &= (4!)^{-\frac{1}{2}} \begin{vmatrix} a\alpha & b\beta & c\alpha & d\beta \\ a\alpha & b\beta & c\beta & d\alpha \\ a\beta & b\alpha & c\alpha & d\beta \\ a\beta & b\alpha & c\beta & d\alpha \end{vmatrix}, \\ \psi_3 &= (4!)^{-\frac{1}{2}} \begin{vmatrix} a\alpha & b\beta & c\beta & d\alpha \\ a\alpha & b\beta & c\alpha & d\beta \\ a\beta & b\alpha & c\alpha & d\beta \\ a\beta & b\alpha & c\beta & d\alpha \end{vmatrix}, \\ \psi_4 &= (4!)^{-\frac{1}{2}} \begin{vmatrix} a\beta & b\alpha & c\alpha & d\beta \\ a\beta & b\alpha & c\beta & d\alpha \\ a\alpha & b\beta & c\alpha & d\beta \\ a\alpha & b\beta & c\beta & d\alpha \end{vmatrix}, \\ \psi_5 &= (4!)^{-\frac{1}{2}} \begin{vmatrix} a\beta & b\alpha & c\beta & d\alpha \\ a\beta & b\alpha & c\alpha & d\beta \\ a\alpha & b\beta & c\alpha & d\beta \\ a\alpha & b\beta & c\beta & d\alpha \end{vmatrix} \end{aligned}$$

are determinantal functions with $a\alpha = a(i)\alpha(i)$, etc. Functions of form $a(i)$ are atomic orbitals of electrons $i = 1, 2, 3, 4$ centered on the nuclei and α, β are orthonormal spin functions.

$$(12) \quad \mathbf{u}_a = \mathbf{N}/D$$

where

$$(13) \quad \begin{aligned} \mathbf{N} &= \int \psi_e^2 \left\{ \sum_p \mathbf{r}_{0p} - \sum_i \mathbf{r}_{0i} \right\} d1d2d3d4, \\ D &= \int \psi_e^2 d1d2d3d4, \end{aligned}$$

\mathbf{r}_{0p} is the vector from an origin at the middle point of \mathbf{R} to $P = A, B, C, D$; and \mathbf{r}_{0i} the vector from this origin to electron i .

Writing

$$a(1)b(2)c(3)d(4) \cdot a(1)d(2)c(3)b(4) = adcb,$$

and using similar notations for other permutations, it follows from (11) that, after summing over spin functions,

$$(14) \quad \begin{aligned} \psi_1^2 &= abcd - adcb + cdab - cbad = \psi_5^2, \\ \psi_3^2 &= abcd - acbd + dcba - dbca = \psi_4^2, \\ \psi_1\psi_3 &= -abdc + acdb - dcab + dbac, \\ \psi_1\psi_4 &= -bacd + bdca - cdba + cabd, \\ \psi_1\psi_5 &= badc - bcda + dcba - dabc, \\ \psi_3\psi_4 &= badc - cadb + cdab - bdac, \\ \psi_3\psi_5 &= -bacd + bcad - dcab + dacb, \\ \psi_4\psi_5 &= -abdc + cbda - cdba + adbc. \end{aligned}$$

From (11), (13), and (14)

$$(15) \quad D = 2 \left[S_{aa}S_{bb}S_{cc}S_{dd} + S_{ab}^2S_{cd}^2 + \sum_1^2 \{ S_{aa}S_{bb}S_{cd}^2 - S_{ab}(S_{cc}S_{ad}S_{bd} + S_{dd}S_{ac}S_{bc}) \} - \sum_1^4 S_{aa}S_{cc}S_{bd}^2 - 2S_{ab}S_{cd}(S_{ac}S_{bd} + S_{ad}S_{bc}) + 2(S_{ac}^2S_{bd}^2 + S_{ad}^2S_{bc}^2) + 4S_{ac}S_{ad}S_{bc}S_{bd} \right]$$

*Although expressed differently (11) is identical with the symmetrized function van Kranendonk (1952) used to calculate \mathbf{u}_a .

where

$$\begin{aligned}
 S_{aa} &= \int a^2(i) di, \\
 S_{ab} &= \int a(i)b(i) di, \\
 S_{ac} &= \int a(i)c(i) di.
 \end{aligned}
 \tag{16}$$

S functions of centers in the same molecule and s functions of centers in different molecules are defined similarly, and summations with indices 1, 2 denote two terms, the term analogous to that written being obtained by interchanging a with c and b with d , whilst summations with indices 1, 4 denote four terms analogous to the term given and derived from it by permuting subscripts in all different manners consistent with the definition of S and s functions.

Writing $\mathbf{r}_{ac,i}$ to denote the vector from the middle point of AC to electron i , defining other vectors similarly, and writing

$$\begin{aligned}
 \int a^2(i)\mathbf{r}_{0i} di &= S_{aa}\mathbf{r}_{0a} + \mathbf{m}_{aa}, \\
 \int a(i)c(i)\mathbf{r}_{0i} di &= \frac{1}{2}S_{ac}(\mathbf{r}_{0a} + \mathbf{r}_{0c}) + \mathbf{m}_{ac}, \\
 \mathbf{m}_{aa} &= \int a^2(i)\mathbf{r}_{ai} di, \\
 \mathbf{m}_{ac} &= \int a(i)c(i)\mathbf{r}_{ac,i} di,
 \end{aligned}
 \tag{17}$$

it follows from (11), (13), (14), and (17), that

$$\begin{aligned}
 (18) \quad N &= -2 \sum_1^2 (\mathbf{m}_{aa}S_{bb} + \mathbf{m}_{bb}S_{aa} + 2\mathbf{m}_{ab}S_{ab})(S_{cc}S_{dd} + S_{cd}^2) \\
 &+ \sum_1^4 \mathbf{m}_{aa}(S_{cc}S_{bd}^2 + S_{dd}S_{bc}^2 + 2S_{cd}S_{bc}S_{bd}) \\
 &+ 2 \sum_1^2 \mathbf{m}_{ab}\{S_{cc}S_{ad}S_{bd} + S_{dd}S_{ac}S_{bc} + S_{cd}(S_{ac}S_{bd} + S_{ad}S_{bc})\} \\
 &+ 2 \sum_1^4 \mathbf{m}_a \{s_{ac}(S_{bb}S_{dd} - s_{bd}^2) + S_{ab}S_{dd}S_{bc} \\
 &\quad + S_{bb}S_{cd}S_{ad} + S_{ab}S_{cd}S_{bd} - s_{ac}s_{bd}^2 - 2s_{ad}S_{bc}S_{bd}\},
 \end{aligned}$$

The calculation of \mathbf{y}_a is involved for arbitrary orientations, but is simpler for particular positions of the nuclei. For the four following coplanar positions, for each of which $\phi_1 - \phi_2 = 0$,

$$\begin{aligned}
 (19) \quad \text{Pos. 1: } &\theta_1 = \theta_2 = 0 \text{ or } \pi, \\
 \text{Pos. 2: } &\theta_1 = \theta_2 = \frac{1}{2}\pi, \\
 \text{Pos. 3: } &\theta_1 = 0 \text{ or } \pi, \quad \theta_2 = \frac{1}{2}\pi, \\
 \text{Pos. 4: } &\theta_1 = \frac{1}{2}\pi, \quad \theta_2 = 0 \text{ or } \pi,
 \end{aligned}$$

the symmetry makes the components of \mathbf{y}_a perpendicular to \mathbf{R} and their derivatives zero. These components do not vanish for non-symmetric positions but their contribution to absorptions is negligible. Therefore, only the z component of \mathbf{y}_a need be considered and will be denoted by μ_a .

In (18) \mathbf{N} is replaced by \mathbf{N} and only the components of \mathbf{m} functions are calculated and are denoted by m 's.

The first four D -coefficients in the expansion (5), denoted by

$$D_{a1} = D_c(0000), \quad D_{a2} = D_a(2000), \quad D_{a3} = D_a(0020), \quad D_{a4} = D_a(2020),$$

can be determined from the values of μ_a for the four positions (19). The higher coefficients are neglected since these can be shown to be at most a fraction of 1% of D_{a1} . Denoting the four values of μ_a by μ_{a1} , μ_{a2} , μ_{a3} , and μ_{a4} and solving for the D 's, one gets

$$\begin{aligned} D_{a1} &= 2/9 \cdot \{(\mu'_{a1})_0 + 4(\mu'_{a2})_0 + 2(\mu'_{a3})_0 + 2(\mu'_{a4})_0\}, \\ D_{a2} &= 4/9\sqrt{5} \cdot \{(\mu'_{a1})_0 - 2(\mu'_{a2})_0 + 2(\mu'_{a3})_0 - (\mu'_{a4})_0\}, \\ D_{a3} &= 4/9\sqrt{5} \cdot \{(\mu'_{a1})_0 - 2(\mu'_{a2})_0 - (\mu'_{a3})_0 + 2(\mu'_{a4})_0\}, \\ D_{a4} &= 8/45 \cdot \{(\mu'_{a1})_0 + (\mu'_{a2})_0 - (\mu'_{a3})_0 - (\mu'_{a4})_0\}. \end{aligned} \quad (20)$$

Van Kranendonk and Bird (1951) have calculated an "atomic distortion effect" by using Rosen-like (1931) orbitals.

$$(21) \quad \alpha(i) = (z_{ab}^3/\pi)^{1/2} \exp(-z_{ab}r_{ai}) \{1 + \kappa_{ab}r_{ai} \cos \theta_{abi} + \lambda_{ac}r_{ai} \cos \theta_{aci} + \lambda_{ad}r_{ai} \cos \theta_{adi}\},$$

where $z_{ab} = z(r_{ab})$ is the effective nuclear charge, $\kappa_{ab} = \kappa(r_{ab})$ the attractive distortion parameter for the Rosen H_2 function, $\lambda_{ac} = \lambda(r_{ac})$ the repulsive distortion parameter calculated and tabulated by van Kranendonk and Bird (1951), θ_{abi} the angle at A between \mathbf{r}_{ab} and \mathbf{r}_{ai} , and similar functions are defined for nuclei B , C , and D .

The distortion of spherically symmetric $1s$ orbitals in (21) gives non-zero contributions to N_0 from the first summation term in (18), the contributions from the second and third terms of (18) are negligible, and the fourth term makes a contribution comparable with that of the first term when the orbitals (21) are used. If spherically symmetric $1s$ orbitals are used, the contribution from the fourth term of (18) is of the same order as when the orbitals (21) are used but there is zero contribution from the first term of (18).

Van Kranendonk and Bird (1951) have calculated contributions from the first term of (18) only and their values of the D coefficients are additive with the values calculated separately from the fourth term of (18).

For values of R that give maximum contributions to absorptions the average value of s functions for $r_{ab} = r_{cd} = r_0$ is about 25% of S_{ab} or S_{cd} , but terms that contain squares of s functions give negligible contributions to N_0 .

Using (21) and neglecting λ parameters and squares of κ parameters in comparison with unity,

$$S_{aa} = S_{bb} = S_{cc} = S_{dd} = 1$$

and derivatives of these functions are negligible.

Writing $(S_{ab})_0 = (S_{cd})_0 = S_0$ and using the above approximations in (15) and (18),

$$D_0 = 2(1 + S_0^2)^2,$$

$$(22) \quad N = -2 \sum_1^2 (m_{aa} + m_{bb} + 2m_{ab}S_{ab})(1 + S_{cd}^2) \\ + 2 \sum_1^4 m_{ac}(s_{ac} + s_{bc}S_{ab} + s_{ad}S_{cd} + s_{bd}S_{ab}S_{cd}).$$

A typical function \mathbf{m}_{ac} has components in the plane of the molecular nuclei of positions (19) that will be denoted by $m_{ac;1}$ in direction AC and $m_{ac;2}$ in direction perpendicular to AC . $m_{ac;1}$ is derived from (17) and (21), and is divided for convenience of calculation into two parts,

$$(23) \quad m_{ac;1} = m_{ac;11} + m_{ac;12},$$

where

$$m_{ac;11} = (z_{ab}z_{cd})^{3/2} \pi^{-1} \{1 + \frac{1}{2}r_{ac}(\kappa_{ab} \cos \theta_{abc} + \kappa_{cd} \cos \theta_{cda})\} \\ \times \int \exp\{-(z_{ab}r_{ai} + z_{cd}r_{ci})\} r_{ac,i} \cos \theta_{ac,i} di, \\ m_{ac;12} = (z_{ab}z_{cd})^{3/2} \pi^{-1} (\kappa_{ab} \cos \theta_{abc} - \kappa_{cd} \cos \theta_{cda}) \\ \times \int \exp\{-(z_{ab}r_{ai} + z_{cd}r_{ci})\} (r_{ac,i} \cos \theta_{ac,i})^2 di,$$

and

$$m_{ac;2} = (z_{ab}z_{cd})^{3/2} \pi^{-1} (\kappa_{ab} \sin \theta_{abc} - \kappa_{cd} \sin \theta_{cda}) \\ \times \int \exp\{-(z_{ab}r_{ai} + z_{cd}r_{ci})\} (r_{ac,i} \sin \theta_{ac,i})^2 di,$$

where $\theta_{ac,i}$ is the angle at the middle point of AC between $\mathbf{r}_{ac,e}$ and $\mathbf{r}_{ac,i}$.

Integrated forms of the above and other integrals are given in an appendix.

All functions of type $m_{ac;2}$ and their derivatives are zero for Pos. 1 and their total contributions to $(\mu_a')_0$ are negligible for Pos. 2, 3, and 4. Functions of type $m_{ac;12}$ give zero contributions to $(\mu_a')_0$ for Pos. 2 and give a greatest contribution for Pos. 1. This greatest contribution is not more than 3% of that of functions of type $m_{ac;11}$ for values of R for which the contribution to the absorption coefficients is maximal. Therefore $m_{ac;2}$ and $m_{ac;12}$ functions are neglected and the component of \mathbf{m}_{ac} in direction \mathbf{R} is taken to be

$$m_{ac} = m_{ac;1} \cos \theta_{ac},$$

where θ_{ac} is the angle between \mathbf{r}_{ac} and \mathbf{R} .

The second term in the expression for N in (22) gives the contribution

$$(24) \quad 2 \sum_1^4 [m_{ac;1} \cos \theta_{ac} (s_{ac} + s_{bc}S_{ab} + s_{ad}S_{cd} + s_{bd}S_{ab}S_{cd})].$$

It is shown in the appendix that

$$(25) \quad m_{ac:1} = -1/30 \cdot (z_{ab}z_{cd})^{3/2} r_{ac}^4 \sigma^{-4} e^{-\sigma} \left\{ 1 + \frac{1}{2} r_{ac} (\kappa_{ab} \cos \theta_{abc} + \kappa_{cd} \cos \theta_{cda}) \right\} \\ \times \left\{ (\sigma^3 + 6\sigma^2 + 15\sigma + 15)\tau + \sum_1^{\infty} \tau^{n+1} p_n(\sigma) \right\},$$

where $\sigma = \sigma_{ac} = \frac{1}{2} r_{ac} (z_{ab} + z_{cd})$, $\tau = \tau_{ac} = \frac{1}{2} r_{ac} (z_{ab} - z_{cd})$, and the $p_n(\sigma)$ are polynomials. It follows that

$$(26) \quad (m_{ac:1})_0 = 0,$$

and that

$$(27) \quad (m'_{ac:1})_0 = -1/60 \cdot [z'/z r_{ac} e^{-\sigma} (\sigma^3 + 6\sigma^2 + 15\sigma + 15) \\ \times \{1 + \frac{1}{2} \kappa r_{ac} (\cos \theta_{abc} + \cos \theta_{cda})\}]_0.$$

From (22), (24), (26), and (27) the contribution of the second term of (22) to $(\mu_a')_0$ is

$$(28) \quad (1 + S_0^{-2})^{-2} \sum_1^4 [m'_{ac:1} \cos \theta_{ac} \{s_{ac} + (s_{bc} + s_{ad})S + s_{bd}S^2\}]_0.$$

Contributions to D_{ai} values derived from the second term of (22) are obtained by calculating values of $(\mu_a')_0$ from (28) for a range of R and for each of the four positions $i = 1, 2, 3, 4$ of (19). These values substituted in (20) give the D_{ai} coefficients listed in brackets in Table I, and when added to those derived by van Kranendonk and Bird (1951) from the first term of (22) give the unbracketed values listed in Table I.

TABLE I
THE EXPANSION COEFFICIENTS $D_{ai} \times 10^4$ AS FUNCTIONS OF R

R	D_{a1}	D_{a2}	D_{a3}	D_{a4}
4.0	1098 (490)	102.3 (7.5)	91.6 (7.5)	15.4 (0.2)
4.2	858 (384)	80.2 (5.4)	72.5 (5.4)	11.4 (0.1)
4.4	666 (298)	61.9 (3.8)	55.4 (3.8)	9.8 (0.1)
4.6	517 (229)	49.0 (2.5)	43.6 (2.5)	7.3 (0.0)
4.8	399 (175)	38.2 (1.5)	34.6 (1.5)	5.2 (0.0)
5.0	305 (133)	29.3 (0.9)	26.3 (0.9)	4.0 (-0.1)
5.2	232 (100)	22.7 (0.4)	20.4 (0.4)	3.0 (-0.1)
5.4	177 (75)	17.9 (0.1)	16.1 (0.1)	2.0 (-0.1)
5.6	133 (56)	13.9 (-0.1)	12.5 (-0.1)	1.5 (-0.1)
5.8	100 (41)	10.4 (-0.2)	9.3 (-0.2)	1.3 (-0.1)
6.0	75.8 (30.4)	7.84 (-0.27)	7.06 (-0.27)	1.0 (-0.1)
6.2	56.8 (22.2)	5.92 (-0.28)	5.32 (-0.28)	0.9 (-0.1)
6.4	43.0 (16.2)	4.32 (-0.27)	3.90 (-0.27)	0.8 (-0.1)
6.6	32.8 (11.8)	3.16 (-0.24)	2.80 (-0.24)	0.6 (-0.0)
6.8	25.4 (8.5)	2.06 (-0.21)	1.82 (-0.21)	0.6 (-0.0)
7.0	19.5 (6.1)	1.43 (-0.18)	1.19 (-0.18)	0.6 (-0.0)

4. THE DIPOLE MOMENT μ_a

(a) Theoretical Calculation

The dipole moment μ_a that is added to μ_a to give the dipole moment of a

molecule pair is calculated by applying the method of linear variation functions to a trial function of a form suggested by the following perturbation calculation of Ψ_q .

For a pair of non-interacting H_2 molecules, one with nuclei A, B and electrons 1, 2 and the other with nuclei C, D and electrons 3, 4, the ground-state electronic function is

$$\Psi_{ac} = \psi_a \psi_c,$$

where

$$\psi_a = \psi_{ab}(1, 2),$$

$$\psi_c = \psi_{cd}(3, 4)$$

are normalized ground-state electronic eigenfunctions for H_2 each with energy E_0 . $\Psi_{a'c'} = \psi_{a'} \psi_{c'}$, with energy $E_{a'c'} = E_{a'} + E_{c'}$, is a state of the unperturbed system in which at least one of $\psi_{a'}$, $\psi_{c'}$ is an excited-state H_2 wave function. The perturbing energy is the Coulombic interaction potential

$$(29) \quad V = \sum_{i,j} \frac{e_i e_j}{r_{ij}},$$

where summations are for i and j over the particles of the first and second molecules respectively and the e 's are $+1$ for nuclei and -1 for electrons.

First-order perturbation theory gives the perturbed ground-state electronic function of the molecule pair as

$$(30) \quad \Phi_{ac} = \Psi_{ac} + \sum_{a',c'} \frac{(a'c'|V|ac)}{2E_0 - E_{a'c'}} \Psi_{a'c'}.$$

It is convenient to write

$$\mathbf{p} = \sum_i e_i \mathbf{r}_{ab,i}, \quad \mathbf{q} = \sum_j e_j \mathbf{r}_{cd,j},$$

where summations are for $i = 1, 2$ and $j = 3, 4$ only. Any pair of corresponding components of these vectors is denoted by $p(1, 2)$, $q(3, 4)$. The corresponding component of Ψ_q given by (30) is

$$(31) \quad \mu_q = \int \Phi_{ac}^*(p+q) \Phi_{ac} d1d2d3d4$$

$$= \sum_{a',c'} \frac{(a'c'|V|ac)}{2E_0 - E_{a'c'}} \{ (ac|p+q|a'c') + (a'c'|p+q|ac) \}$$

$$+ \sum_{a',c',a'',c''} \frac{(a'c'|V|ac)(a''c''|V|ac)(a'c'|p+q|a''c'')}{(2E_0 - E_{a'c'})(2E_0 - E_{a''c''})}.$$

Neglecting the second summation term and noting that

$$(ac|p+q|a'c') = (a|p|a')\delta_{cc'} + (c|q|c')\delta_{aa'},$$

$$(a'c'|p+q|ac) = (a'|p|a)\delta_{cc'} + (c'|q|c)\delta_{aa'},$$

$$(a|p|a) = (c|q|c) = 0,$$

(31) gives

$$(32) \quad \mu_q = \mu_{ab} + \mu_{cd},$$

where

$$\mu_{ab} = \sum_{a'} \frac{(a'c|V|ac)}{E_0 - E_{a'}} \{ (a|p|a') + (a'|p|a) \},$$

$$\mu_{cd} = \sum_{c'} \frac{(ac'|V|ac)}{E_0 - E_{c'}} \{ (c|q|c') + (c'|q|c) \}$$

are the separate dipole moments of the two molecules, and primed subscripts refer to excited electronic states of H_2 .

Writing

$$\psi_a^* p = \sum_{a'} (a|p|a') \psi_{a'}^*,$$

multiplying by $(c|V|c)\psi_a$, and integrating gives

$$(33) \quad (ac|pV|ac) = \sum_{a'} (a|p|a')(a'c|V|ac).$$

By using similar expansions, in like manner,

$$(ac|pV|ac) = \sum_{a'} (a'|p|a)(a'c|V|ac),$$

$$(34) \quad (ac|qV|ac) = \sum_{c'} (c|q|c')(ac'|V|ac),$$

$$= \sum_{c'} (c'|q|c)(ac'|V|ac).$$

If each denominator, $E_0 - E_{a'}$ and $E_0 - E_{c'}$, in (32) is replaced by ϵ , where ϵ is the difference between the energies of the ground and the first excited states of H_2 (about 11 ev.), and results (33) and (34) are used, expressions for upper bounds of the absolute values of \mathbf{u}_{ab} and \mathbf{u}_{cd} are given as

$$(35) \quad \mathbf{u}_{ab} = 2\epsilon^{-1} \sum_{i=1,2} \int \{ \psi_{ab}(1,2) \psi_{cd}(3,4) \}^2 \mathbf{r}_{ab,i} V(1234) d1d2d3d4,$$

$$\mathbf{u}_{cd} = 2\epsilon^{-1} \sum_{j=3,4} \int \{ \psi_{ab}(1,2) \psi_{cd}(3,4) \}^2 \mathbf{r}_{cd,j} V(1234) d1d2d3d4.$$

When V is given the Coulombic form (29) and orbitals of the Rosen (1931) form,

$$(36) \quad a(i) = (Z_{ab})^{3/2} \pi^{-1/2} \exp(-Z_{ab}r_{ai}) (1 + \kappa_{ab} r_{ai} \cos \theta_{abi}),$$

are used in (35) with integration over all coordinate space, three- and four-center subintegrals appear that must be approximated, and in addition, some subintegrals are improper because of infinite singularities. It is possible to separate integrals into a part varying exponentially with R and a part varying with R^{-1} , with a leading term varying with R^{-1} . The R^{-1} dependent part dominates the proper exponentially dependent part of \mathbf{u}_q for $R > 5.5$ and gives \mathbf{u}_q for large R , but the exponentially dependent part dominates for the lower part of the collision range.

If V is expanded in powers of R^{-1} , then only terms varying with R^{-1} arise, with a leading term varying with R^{-1} given by the dipole-quadrupole term in the expansion of V that can be identified with the R^{-1} dependent term

obtained when V is not expanded. This R^{-4} dependent term dominates succeeding terms for $R > 5.5$.

Because Section 3 gives short-range terms of exponential character but does not give R^{-1} dependent terms, it is reasonable to approximate the total dipole moment by (10) and to calculate \mathbf{u}_q by expanding V and using only the R^{-4} dependent term so obtained.

Equation (35) is not used with the expanded form of V to evaluate \mathbf{u}_q because of the uncertainty in the value of ϵ even if recourse is made to experimental energy values. However, (35) suggests the use of the following trial function in a variational calculation:

$$(37) \quad \phi = \psi_{ab}(1, 2)\psi_{cd}(3, 4) \left\{ 1 + \sum_{n=2}^{(\infty)} a_n V_n R^{-n} \right\},$$

where the a 's are parameters, ψ_{ab} and ψ_{cd} are normalized Rosen H_2 functions, and, on expansion of (29),

$$(38) \quad V = \sum_{n=2}^{(\infty)} V_n R^{-n},$$

with

$$V_2 = \sum_{i,j} e_i e_j (x_i x_j + y_i y_j - 2z_i z_j),$$

$$V_4 = 3/2 \cdot \sum_{i,j} e_i e_j \{ (r_i^2 - 3z_i^2)z_j - (r_j^2 - 3z_j^2)z_i + 2(z_i - z_j)(x_i x_j + y_i y_j) \}.$$

Origins of i and j coordinates of electrons and nuclei are at the mass centers of the respective molecules and z axes are in direction \mathbf{R} .

Because of axial symmetry of ψ_{ab} and ψ_{cd} ,

$$(39) \quad \begin{aligned} \mathbf{u}_{ab} &= - \sum_{i=1,2} \int \phi^2 \mathbf{r}_{ab,i} d1d2d3d4 \left\{ \int \phi^2 d1d2d3d4 \right\}^{-1} \\ &= -2a_1 R^{-4} \sum_{i=1,2} \int \{ \psi_{ab}(1, 2)\psi_{cd}(3, 4) \}^2 V_4 \mathbf{r}_{ab,i} d1d2d3d4, \\ \mathbf{u}_{cd} &= -2a_1 R^{-4} \sum_{j=3,4} \int \{ \psi_{ab}(1, 2)\psi_{cd}(3, 4) \}^2 V_4 \mathbf{r}_{cd,j} d1d2d3d4, \end{aligned}$$

when R^{-6} and higher powers of R^{-1} are neglected.

Equation (39) has the same form as that given by expanding V in (35) with $-a_1$ replacing ϵ^{-1} .

If a function of electron coordinates is denoted by $f = f(1234)$ it is convenient to write

$$\langle f \rangle_{ab} = \int \{ \psi_{ab}(1, 2) \}^2 f d1d2,$$

$$\langle f \rangle_{cd} = \int \{ \psi_{cd}(3, 4) \}^2 f d3d4,$$

$$\langle \langle f \rangle \rangle = \int \{ \psi_{ab}(1, 2)\psi_{cd}(3, 4) \}^2 f d1d2d3d4.$$

In the appendix the method of linear variation functions is used to show that to the same order in R^{-1} as used in (39)

$$(40) \quad a_4 = -2 \langle \langle V_4^2 \rangle \rangle \cdot \left\langle \left\langle \sum_{i=1,2} (\nabla_i V_4)^2 + \sum_{j=3,4} (\nabla_j V_4)^2 \right\rangle \right\rangle^{-1}.$$

Values of a_4 for the four positions (19) are given in the appendix. The average value of a_4 is about 1.6 compared with the value $\epsilon^{-1} = 2.4$ approximately, which gives an upper bound.

Components of \mathbf{y}_{ab} and \mathbf{y}_{cd} and of their derivatives with respect to r_{ab} perpendicular to \mathbf{R} are zero for each of the four positions (19). From (39) the components of \mathbf{y}_{ab} and \mathbf{y}_{cd} in direction \mathbf{R} are

$$(41) \quad \begin{aligned} \mu_{ab} &= -2a_4 R^{-4} \sum_{i=1,2} \langle \langle V_4 R^{-1} (\mathbf{R} \cdot \mathbf{r}_i) \rangle \rangle, \\ \mu_{cd} &= -2a_4 R^{-4} \sum_{j=3,4} \langle \langle V_4 R^{-1} (\mathbf{R} \cdot \mathbf{r}_j) \rangle \rangle. \end{aligned}$$

The Cartesian coordinate axes, with origins at the mass centers of the two molecules and z axes in direction \mathbf{R} , are rotated to ξ, η, ζ systems with ζ axes along the respective molecular axes.

Ground-state wave functions for H_2 in general, and the Rosen function in particular, are cylindrically symmetric about ζ axes and symmetric with respect to the plane $\zeta = 0$. When V_4 is transformed to the ξ, η, ζ axes and substituted in (41), these symmetry properties can be used to show that many subintegrals are zero. Writing

$$(42) \quad \begin{aligned} \sum_i e_i \langle \zeta_i^2 \rangle_{ab} &= \frac{1}{2} r_{ab}^2 - 2C_1, \\ \sum_i e_i \langle \xi_i^2 \rangle_{ab} &= \sum_i e_i \langle \eta_i^2 \rangle_{ab} = -S_1, \\ \sum_i e_i \langle r_i^2 \rangle_{ab} &= \frac{1}{2} r_{ab}^2 - 2(C_1 + S_1), \\ \langle \zeta_1 \zeta_2 \rangle_{ab} &= X_1, \end{aligned}$$

and using subscripts 2 to denote analogous results for the molecule CD, it can be shown that

$$(43) \quad \begin{aligned} \mu_{ab} &= -3a_4 R^{-4} (2C_2 - S_2 - \frac{1}{2} r_{cd}^2) \times [\{ S_1 \sin^2 \theta_1 + 2(C_1 + X_1) \cos^2 \theta_1 \} \\ &\quad (3 \cos^2 \theta_2 - 1) + 2(S_1 - 2C_1 - 2X_1) \sin \theta_1 \cos \theta_1 \sin \theta_2 \cos \theta_2 \cos(\phi_1 - \phi_2)]. \end{aligned}$$

μ_{cd} can be obtained from (43) by interchanging subscripts 1 and 2, replacing the subscript cd by ab , and changing the sign of the whole expression.

Using the Rosen orbitals (36) in (42) and neglecting κ^2 in comparison with unity it can be shown that*

$$X = \frac{2\kappa r - \frac{1}{4}\sigma^2}{z^2 \{ 1 + (1 + 2\kappa r) \Delta^2 \}},$$

*Exact forms are given by Britton and Bean (1955).

$$\begin{aligned}
 C &= \frac{1 + (1 + 2\kappa r)J\Delta}{z^2 \{1 + (1 + 2\kappa r)\Delta^2\}} - X, \\
 S &= \frac{2 \{1 + (1 + 2\kappa r)I\Delta\}}{z^2 \{1 + (1 + 2\kappa r)\Delta^2\}}, \\
 \Delta &= (1 + \sigma + \frac{1}{3}\sigma^2)e^{-\sigma}, \\
 I &= (1 + \sigma + \frac{2}{3}\sigma^2 + \frac{1}{15}\sigma^3)e^{-\sigma}, \\
 J &= (1 + \sigma + \frac{9}{20}\sigma^2 + \frac{7}{60}\sigma^3 + \frac{1}{60}\sigma^4)e^{-\sigma}, \\
 \sigma &= zr = z_{cd}r_{cd} \text{ for molecule } AB \\
 &= z_{ab}r_{ab} \text{ for molecule } CD.
 \end{aligned}$$

In (43)

$$(44) \quad -(2C - S - \frac{1}{2}r^2) = \frac{2 \{ (1 + 2\kappa r)\sigma^2\Delta^2 + 10\kappa r \}}{5z^2 \{1 + (1 + 2\kappa r)\Delta^2\}} = Q,$$

where Q is the quadrupole moment of H_2 . For the Rosen function $Q_0 = 0.614$,

$$(45) \quad S \sin^2\theta + 2(C + X)\cos^2\theta = \frac{2 \{1 + (1 + 2\kappa r)I\Delta\}}{z^2 \{1 + (1 + 2\kappa r)\Delta^2\}} - (S - 2C - 2X)\cos^2\theta,$$

and

$$S - 2C - 2X = -\frac{(1 + 2\kappa r)\sigma^2\Delta^2}{10z^2 \{1 + (1 + 2\kappa r)\Delta^2\}}.$$

The second term in the square bracket in (43) is zero for each of the four particular orientations (19) and, since it is small for all orientations of molecular axes, it will be neglected.

Using (44) and (45) in (43)

$$\begin{aligned}
 \mu_{ab} &= a_4 R^{-4} Q_2 G_1 (3 \cos^2\theta_2 - 1), \\
 \mu_{cd} &= -a_4 R^{-4} Q_1 G_2 (3 \cos^2\theta_1 - 1),
 \end{aligned}$$

where

$$G = \frac{6 \{1 + (1 + 2\kappa r)(I\Delta + \frac{1}{20}\sigma^2\Delta^2\cos^2\theta)\}}{z^2 \{1 + (1 + 2\kappa r)\Delta^2\}}$$

and subscripts 1 and 2 denote functions of molecule AB and of molecule CD respectively.

The z component of $(\mu_q')_0$ in direction \mathbf{R} is

$$\begin{aligned}
 (\mu_q')_0 &= (\mu'_{ab})_0 + (\mu'_{cd})_0 \\
 (46) \quad &= R^{-4} [a_4 \{Q_2 G' (3 \cos^2\theta_2 - 1) - Q_1 G (3 \cos^2\theta_1 - 1)\}].
 \end{aligned}$$

In (46) $(a_4')_0$ has been neglected because it is small and its contributions to D coefficients show severe cancellation.

From (46), (19), and (20), in a manner the same as for D_a coefficients,

$$\begin{aligned}
 D_{q1} &= D_q^{(0)}(0000) = 0.049R^{-4}, \\
 D_{q2} &= D_q^{(0)}(2000) = 8.428R^{-4}, \\
 D_{q3} &= D_q^{(0)}(0020) = -3.733R^{-4}, \\
 D_{q4} &= D_q^{(0)}(2020) = 0.013R^{-4}.
 \end{aligned}
 \quad (47)$$

Higher $D^{(0)}$ coefficients are negligible.

Because D_{q1} and D_{q4} are relatively very small (46) departs only slightly from the form obtained for point quadrupoles, and therefore

$$(48) \quad \begin{aligned} D^{(\pm 1)}(2 \pm 100) &= 3^{-1/2} D_{q2} = 4.866 R^{-4}, \\ D^{(\pm 1)}(002 \pm 1) &= 3^{-1/2} D_{q3} = -2.155 R^{-4}, \end{aligned}$$

is a good approximation.

From (10) and (47) for $i = 1, 2, 3, 4$,

$$(49) \quad D_i^{(0)} = D_{ai}^{(0)} + D_{qi}^{(0)},$$

and the only $D^{(\pm 1)}$ coefficients are given by (48).

(b) *Semiempirical Calculation*

Van Kranendonk (1952) derived $(\mathbf{y}_q')_0$ from the equation

$$(\mathbf{y}_q')_0 = \alpha \mathbf{E}_0' + \alpha' \mathbf{F}_0,$$

where \mathbf{E} is the electric field at the position of the non-vibrating molecule produced by the quadrupole moment of the vibrating molecule, \mathbf{F} the electric field at the vibrating molecule produced by the quadrupole field of the non-vibrating molecule, α is the polarizability of H_2 , and α' its derivative.

In computing $(\mathbf{y}_q')_0$ he used an experimentally determined mean value of α , an estimated value of α' , and values of Q_0 and Q_0' derived by using the Rosen function for H_2 .

Following his procedure we have re-evaluated $(\mathbf{y}_q')_0$, taking account of the anisotropy in α and α' and using more recently determined experimental values of α' . The Q_0 and Q_0' used are Rosen function values calculated by us and they are in close agreement with those given by van Kranendonk.

The component of $(\mathbf{y}_q')_0$ in direction \mathbf{R} is

$$(50) \quad (\mu_q')_0 = -\frac{3}{2} R^{-4} [Q_0 \alpha' (3 \cos^2 \theta_2 - 1) - Q_0' \alpha (3 \cos^2 \theta_1 - 1)],$$

where values of α and α' are dependent on θ_1 and θ_2 .

$$\begin{aligned} Q_0 &= 0.614, & Q_0' &= 0.633, \\ \alpha_{\parallel} &= 6.302, & \alpha_{\perp} &= 4.845, & \alpha_0 &= 5.331, \\ \alpha_{\parallel}' &= 5.94, & \alpha_{\perp}' &= 2.99, & \alpha_0' &= 3.98, \end{aligned}$$

where α values are as given by Volkmann (1935) and α' values have been recently determined from the field-induced infrared absorption of H_2 (Crawford and McDonald 1957).

For the four positions (19) from (50)

$$(51) \quad \begin{aligned} (\mu_{q1}')_0 &= -\frac{3}{2} R^{-4} [2Q_0 \alpha_{\parallel}' - 2Q_0' \alpha_{\parallel}], \\ (\mu_{q2}')_0 &= -\frac{3}{2} R^{-4} [-Q_0 \alpha_{\perp}' + Q_0' \alpha_{\perp}], \\ (\mu_{q3}')_0 &= -\frac{3}{2} R^{-4} [-Q_0 \alpha_{\parallel}' - 2Q_0' \alpha_{\perp}], \\ (\mu_{q4}')_0 &= -\frac{3}{2} R^{-4} [2Q_0 \alpha_{\perp}' + Q_0' \alpha_{\parallel}]. \end{aligned}$$

From (51) and (20)

$$\begin{aligned}
 (52) \quad D_{q1} &= -0.118R^{-4}, \\
 D_{q2} &= 8.952R^{-4}, \\
 D_{q3} &= -6.657R^{-4}, \\
 D_{q4} &= -0.806R^{-4},
 \end{aligned}$$

and

$$\begin{aligned}
 (53) \quad D^{(\pm 1)}(2 \pm 100) &= -\frac{6}{\sqrt{15}} \alpha_0 Q_0' R^{-4} = -5.226R^{-4}, \\
 D^{(\pm 1)}(002 \pm 1) &= \frac{6}{\sqrt{15}} \alpha_0' Q_0 R^{-4} = 3.781R^{-4}.
 \end{aligned}$$

These values are combined with D_a values as in (49).

A comparison of (47) and (52) shows considerable difference in the values of $D_{q3} = D_q^{(0)}(0020)$ and in consequence in values of $D^{(\pm 1)}(002 \pm 1)$ also. This occurs because the theoretical and the experimentally determined values of the derivative of the polarizability, α' , differ considerably. It is possible to identify α with $-\frac{2}{3}a_4G$ and α' with $-\frac{2}{3}a_4G'$. Theoretical values so given are

$$\alpha_{\parallel} = 5.20, \quad \alpha_{\perp} = 4.81; \quad \alpha'_{\parallel} = 2.48, \quad \alpha'_{\perp} = 2.14.$$

5. INTEGRATED ABSORPTION COEFFICIENTS OF THE 0-1 BAND

Rotational overtones corresponding to $\Delta j = \pm 4, \pm 6$, etc. in (7) and combined transitions corresponding to $\Delta j_1 = \pm 2, \Delta j_2 = \pm 2$, etc. are very weak and give negligible contributions to the total intensity of the fundamental 0-1 band. The Q branch of this band is taken to be formed by lines for which $\Delta j_1 = \Delta j_2 = 0$ with displacements due to molecular interaction neglected. The S branch is composed of lines for which $\Delta j_1 = 2, \Delta j_2 = 0$ and $\Delta j_1 = 0, \Delta j_2 = 2$, with separate lines from initial levels $j = 0, 1, 2$, etc., denoted by $S(0), S(1), S(2)$, etc. The O branch is composed of lines for which $\Delta j_1 = -2, \Delta j_2 = 0$ and $\Delta j_1 = 0, \Delta j_2 = -2$, with separate lines from initial levels $j = 2, 3$, etc. denoted by $O(2), O(3)$, etc.

Absorption coefficients are calculated from (9) with summation over all values of the quantum numbers m_1, m_2, m_1', m_2' in (6) and over all $j_1, j_2, j_1',$ and j_2' for which $\gamma_{\rho\rho'}$ equals the angular frequency of the branch, denoted by γ , as given by

$$(54) \quad \hbar^2/2I[j_1'(j_1'+1) - j_1(j_1+1) + j_2'(j_2'+1) - j_2(j_2+1)] = \hbar(\gamma - \gamma_0),$$

where I is the moment of inertia of a H_2 molecule and γ_0 its fundamental vibrational frequency.

Because

$$(55) \quad \sum_{mm'} (jm|\lambda\mu|j'm')(j'm'|\lambda'\mu'|jm) = \frac{1}{2\pi} L_{\lambda}(jj') \delta_{\lambda\lambda'} \delta_{\mu\mu'}$$

it follows that cross-product terms in $|\mu_{\rho\rho'}|^2$ of form $D_1 D_2$ are all zero and that (55) is independent of μ . All of D_1, D_2, D_3 , and D_4 have $\lambda_i = 0$ or 2 so that only L_0 and L_2 need be evaluated. These are given by

$$\begin{aligned}
 L_0(jj') &= \frac{1}{2}(2j+1)\delta_{jj'}, \\
 (56) \quad L_2(jj') &= \frac{1}{2}j(j+1)(2j+1)(2j-1)(2j+3)\delta_{jj'} \\
 &\quad + \frac{3}{4}j(j-1)(2j-1)\delta_{j-2,j'} + \frac{3}{4}(j+2)(j+1)(2j+1)\delta_{j+2,j'}.
 \end{aligned}$$

From (6), (8), (9), (54), (55), and (56), with summation over quantum numbers as noted above denoted by Σ^* , the integrated absorption coefficient of the branch concerned is

$$(57) \quad A = \frac{4\pi^2 n^2 \gamma}{3m_H c \gamma_0} \sum I^{(k)}(\lambda_1 \mu_1 \lambda_2 \mu_2) \sum P_{j_1 j_2}^* L_{\lambda_1}(j_1 j_1') L_{\lambda_2}(j_2 j_2'),$$

where

$$(58) \quad I^{(k)} = \int_0^\infty \exp\left(-\frac{\phi(R)}{kT}\right) [D^{(k)}(\lambda_1 \mu_1 \lambda_2 \mu_2)]^2 \pi R^2 dR.$$

The first factor in the integrand of (58) is obtained from a paper of Cohen, Offerhaus, van Leeuwen, Roose, and de Boer (1956) and is explicitly

$$(59) \quad \frac{\phi(R)}{kT} = \frac{28690 \times 148.0}{T} \left(\frac{28690}{R^{12}} - \frac{1}{R^6} \right).$$

Two sets of values of D coefficients are used in (58) and are obtained (a) by adding D_a values from Table I to theoretical D_q values given by (47) and (48), and (b) by adding the same D_a values to the semi-empirical values of D_q given by (52) and (53). The two sets of values of $I^{(k)}$ so derived are listed in Table II for two temperatures, 296° K. and 80° K.

TABLE II
THE VALUES OF $I^{(k)}/e^2 a_0^3$ FOR H_2 AND D_2

		$I^{(k)}$	
$\lambda_1 \mu_1$	$\lambda_2 \mu_2$	$T = 296^\circ \text{K.}$	$T = 80^\circ \text{K.}$
(a) Calculated using theoretical values of α, α'			
0 0	0 0	14.12×10^{-2}	8.33×10^{-2}
2 0	0 0	7.77×10^{-2}	6.67×10^{-2}
2 ± 1	0 0	2.00×10^{-2}	1.81×10^{-2}
0 0	2 0	0.660×10^{-2}	0.655×10^{-2}
0 0	2 ± 1	0.392×10^{-2}	0.355×10^{-2}
2 0	2 ± 1	0.275×10^{-3}	0.158×10^{-4}
(b) Calculated using experimental values of α, α'			
0 0	0 0	13.95×10^{-2}	8.22×10^{-2}
2 0	0 0	8.59×10^{-2}	7.31×10^{-2}
2 ± 1	0 0	2.28×10^{-2}	2.13×10^{-2}
0 0	2 0	2.70×10^{-2}	2.85×10^{-2}
0 0	2 ± 1	1.19×10^{-2}	1.11×10^{-2}
2 0	2 ± 1	3.61×10^{-4}	3.49×10^{-4}

Two sets of absorption coefficients, obtained by substituting the $I^{(k)}$ values of Table II (a) and those of Table II (b) in (57), are listed in Table III.

The theoretical values of the absorption coefficients of D^2 are recorded in Table IV. They were calculated in the same manner as those of Table III

for the thermal equilibrium values of the ortho-para ratio, and are expressed in the same units.

TABLE III
THE INTEGRATED ABSORPTION COEFFICIENTS OF THE BRANCHES OF
THE 1-0 BAND OF H_2

Branch	$T = 296^\circ \text{K.}$		$T = 80^\circ \text{K.}$	
	(a)	(b)	(a)	(b)
$O(3)$	0.080	0.112		
$O(2)$	0.093	0.129	0.003	0.004
Q	6.210	6.700	3.611	3.917
$S(0)$	0.647	0.892	2.107	3.008
$S(1)$	2.030	2.800	1.346	1.912
$S(2)$	0.309	0.425	0.009	0.013
$S(3)$	0.213	0.294		
$S(4)$	0.009	0.012		
Tot. theor.	9.59	11.36	7.08	8.85
Tot. exptl.	10.5	10.5	5.43	5.43
Theor. Q/S	1.94	1.51	1.05	0.794
Exptl. Q/S	1.43	1.43	0.961	0.962

Absorption coefficients, multiplied by 10^{32} , are in $\text{cm.}^{-1} \text{sec.}^{-1}$ (per molecule/ cm.^3), and are calculated for the ortho-para ratio corresponding to thermal equilibrium.

TABLE IV
THE INTEGRATED ABSORPTION COEFFICIENTS OF THE BRANCHES OF
THE 1-0 BAND OF D_2

Branch	$T = 296^\circ \text{K.}$		$T = 80^\circ \text{K.}$	
	(a)	(b)	(a)	(b)
$O(6)$	0.006	0.005		
$O(5)$	0.008	0.012		
$O(4)$	0.056	0.075		
$O(3)$	0.066	0.095	0.002	0.002
$O(2)$	0.182	0.251	0.040	0.057
Q	3.044	3.255	1.733	1.846
$S(0)$	0.243	0.335	1.230	1.755
$S(1)$	0.339	0.467	0.392	0.560
$S(2)$	0.561	0.774	0.116	0.193
$S(3)$	0.157	0.217	0.004	0.006
$S(4)$	0.123	0.169		
$S(5)$	0.018	0.025		
$S(6)$	0.008	0.011		
Tot. theor.	4.81	5.69	3.52	4.42

6. DISCUSSION OF RESULTS

Table III shows that at 296°K. the total integrated absorption coefficient obtained by using procedure (a) is 8.6% smaller, and by using (b) is 8.2% larger, than the experimental value.

The theoretical ratios of the coefficients of the Q and S branches, Q/S in Table III, can be compared with the experimental ratio. Although the components of the bands overlap at $T = 296^\circ \text{K.}$ (Crawford, Welsh, MacDonald, and Locke 1950) they can be resolved with considerable certitude. Experi-

mental evidence (Allin, Hare, and McDonald, 1955; Chisholm and Welsh 1954) shows that the Q branch extends to and beyond the $S(0)$ component. Using this information and imposing the theoretical condition that $S(1)/S(0) = 3.15$, a fairly unique analysis can be made and it gives $Q/S = 1.43$. This ratio definitely favors calculation (b); the ratio 1.94 of calculation (a) cannot be attained from any acceptable analysis of the experimental contour. The fact that (b) slightly overestimates both the total integrated coefficient and the Q/S ratio indicates that the 8% discrepancy that exists between theory and experiment arises mainly from an overestimation of the contribution from the overlap forces. Since the same overlap calculation is used in (a), we conclude that (a) appreciably underestimates the quadrupole contribution. This is not unexpected. The main merit of (a) is that it can be extended to the overtone (Welsh, Crawford, MacDonald, and Chisholm 1951).

Experimental data for $T = 80^\circ \text{K.}$ have not been published. Measurements for $T = 78^\circ \text{K.}$ have been made recently by Mr. J. L. Hunt in the Department of Physics, University of Toronto, and are listed in Table III. We greatly appreciate Mr. Hunt's cooperation in permitting us to quote his results. He has also measured at 78°K. the integrated absorption coefficients of a sample with an ortho-para ratio corresponding to 296°K. (unconverted sample) and finds that at 78°K. the coefficient of the unconverted sample is only 1.5% higher than that quoted in Table III for the converted sample. Integrated absorption coefficients for unconverted hydrogen at 80°K. have been calculated, but are not listed. The calculations show that for a given temperature the total integrated absorption coefficient is independent of the ortho-para ratio and that only the relative values of the coefficients of the components change with the ratio. This is in agreement with Hunt's measurements but not with the results quoted by Chisholm and Welsh (1954). Their quotation was based on preliminary results obtained by MacDonald (1951), which gave for the unconverted sample at 80°K. a total integrated absorption 52% larger than Hunt's value. MacDonald's value is unreliable because, in order to reduce the effect of conversion which took place in the steel cell used by him, he reduced the temperature of the refrigerant surrounding the cell quickly and then made the measurements as quickly as possible. Undoubtedly the temperature of the gas in the cell was appreciably above that of the refrigerant.

A comparison of Hunt's results (Table III, $T = 80^\circ \text{K.}$) and the theoretical values obtained by method (b) shows that the experimental value of the total integrated absorption coefficient is only 61% of the theoretical value. This discrepancy cannot be attributed to the cancellation effect discussed by van Kranendonk (1957) since Hunt's measurements permit extrapolation to low density to obtain the values listed in Table III.

The good agreement between the calculated and the observed value of the integrated absorption coefficient at room temperature indicates that our theoretical calculation of μ' is fairly adequate since at room temperatures one expects the classical distribution function (1), with $\phi(R)$ defined by (59), to be a good approximation to the quantal pair distribution function. Thus the

lack of agreement between the calculated and the observed value of the integrated absorption coefficient at 78° K. suggests that the classical distribution function (1) is not adequate for this lower temperature. Qualitatively, replacing (1) by the quantal pair distribution function will give better agreement (de Boer 1949).

Thus a quantitative calculation of the quantal pair distribution function is required and its adequacy can be tested by comparison of the calculated with the observed value of the integrated absorption coefficient of the collision-induced absorptions at low temperatures.

ACKNOWLEDGMENT

The authors wish to thank the Computation Centre, University of Toronto, for facilities placed at their disposal.

APPENDIX

Section 3

In Section 3 integrals involving two nuclei can all be integrated analytically by using prolate spheroidal coordinates, defined for electron i and nuclei a and c by

$$\xi = \frac{r_{ai} + r_{ci}}{r_{ac}}, \quad \eta = \frac{r_{ai} - r_{ci}}{r_{ac}}, \quad \phi = \text{azimuthal angle.}$$

Because derivatives with respect to r_{ab} of integrals are required the screening parameters are given the subscripts of the nucleus to which they refer and results so obtained are particularized for $z_a = z_b = z_{ab}$ and $z_c = z_d = z_{cd}$. It is convenient to write

$$\sigma_{ac} = \frac{1}{2}r_{ac}(z_a + z_c), \quad \tau_{ac} = \frac{1}{2}r_{ac}(z_a - z_c),$$

and to omit the subscripts from σ and τ when these are evident from the context. Zero subscripts denote equilibrium free-molecule values for $r_{ab} = r_{cd} = r_0$ so that $\tau_0 = 0$.

$p_n(\sigma)$ is used to denote polynomials in several integrals, the polynomials not being the same for different integrals but unimportant for final results. Squares of κ parameters are neglected and λ parameters are neglected in comparison with unity in orbitals defined by (21).

Since $r_{ac,i} \cos \theta_{ac,i} = \frac{1}{2}r_{ac}\xi\eta$, it follows that

$$r_{ai} \cos \theta_{ci} = \frac{1}{2}r_{ac}(1 + \xi\eta), \\ r_{ci} \cos \theta_{ai} = \frac{1}{2}r_{ac}(1 - \xi\eta).$$

It can be shown that if exponential functions of τ are expanded after integrating,

$$\begin{aligned} {}_1I_{ac} &= \int \exp\{-(z_a r_{ai} + z_c r_{ci})\} di \\ &= \frac{1}{4} \pi r_{ac}^3 \int_{-1}^1 e^{-\tau\eta} d\eta \int_1^\infty e^{-\sigma\xi} (\xi^2 - \eta^2) d\xi \\ &= \pi r_{ac}^3 \sigma^{-3} e^{-\sigma} \left\{ 1 + \sigma + \frac{1}{3}\sigma^2 + \sum_{n=1}^\infty \tau^{n+1} p_n(\sigma) \right\} \end{aligned}$$

$$\begin{aligned}
{}_2I_{ac} &= \int \exp\{-(z_a r_{ai} + z_c r_{ci})\} r_{ac, i} \cos \theta_{ac, ci} di \\
&= \frac{1}{8} \pi r_{ac}^3 \int_{-1}^1 e^{-\tau \eta} d\eta \int_1^\infty e^{-\sigma \xi} \xi (\xi^2 - \eta^2) d\xi \\
&= -\frac{1}{30} \pi r_{ac}^4 \sigma^{-4} e^{-\sigma} \left\{ \tau (\sigma^3 + 6\sigma^2 + 15\sigma + 15) + \sum_{n=1}^\infty \tau^{n+2} p_n(\sigma) \right\}, \\
{}_3I_{ac} &= \int \exp\{-(z_a r_{ai} + z_c r_{ci})\} (r_{ac, i} \cos \theta_{ac, ci})^2 di \\
&= \frac{1}{60} \pi r_{ac}^5 \sigma^{-5} e^{-\sigma} \left\{ \sigma^4 + 7\sigma^3 + 27\sigma^2 + 60\sigma + 60 + \sum_{n=1}^\infty \tau^{n+1} p_n(\sigma) \right\}, \\
{}_4I_{ac} &= \int \exp\{-(z_a r_{ai} + z_c r_{ci})\} (r_{ac, i} \sin \theta_{ac, ci})^2 di \\
&= \frac{1}{15} \pi r_{ac}^5 \sigma^{-5} e^{-\sigma} \left\{ \sigma^3 + 6\sigma^2 + 15\sigma + 15 + \sum_{n=1}^\infty \tau^{n+1} p_n(\sigma) \right\}.
\end{aligned}$$

Using the above results,

$$\begin{aligned}
S_{ab} &= (z_a z_b)^{3/2} \pi^{-1} (1 + \kappa_{ab} r_{ab}) {}_1I_{ab}, \\
(S_{ab})_0 &= (S_{cd})_0 = S_0 = [(1 + \kappa r) \Delta_{ab}]_0, \\
\Delta_{ab} &= (1 + \sigma + \frac{1}{3} \sigma^2) e^{-\sigma}, \quad \sigma = \sigma_{ab} = r_{ab} \omega_{ab}, \\
s_{ac} &= \frac{(z_a z_c)^{3/2}}{\pi} \int (1 + \kappa_{ab} r_{ai} \cos \theta_{abi} + \kappa_{cd} r_{ci} \cos \theta_{cdi}) \\
&\quad \times \exp\{-(z_a r_{ai} + z_c r_{ci})\} di \\
&= \frac{(z_a z_c)^{3/2}}{\pi} \left[\left\{ 1 + \frac{1}{2} r_{ac} (\kappa_{ab} \cos \theta_{abc} + \kappa_{cd} \cos \theta_{cda}) \right\} {}_1I_{ac} \right. \\
&\quad \left. + (\kappa_{ab} \cos \theta_{abc} - \kappa_{cd} \cos \theta_{cda}) {}_2I_{ac} \right], \\
(s_{ac})_0 &= \left[\left\{ 1 + \frac{1}{2} \kappa r_{ac} (\cos \theta_{abc} + \cos \theta_{cda}) \right\} \Delta_{ac} \right]_0, \\
\mathbf{m}_{ac} &= \frac{(z_a z_c)^{3/2}}{\pi} \int \left\{ (1 + \kappa_{ab} r_{ai} \cos \theta_{abi} + \kappa_{cd} r_{ci} \cos \theta_{cdi}) \mathbf{r}_{ac, i} \right. \\
&\quad \left. \times \exp\{-(z_a r_{ai} + z_c r_{ci})\} di. \right.
\end{aligned}$$

The perpendicular components of \mathbf{m}_{ac} in the plane of the molecular nuclei are $m_{ac;1} = m_{ac;11} + m_{ac;12}$ in the direction AC and $m_{ac;2}$ perpendicular to AC ,

$$\begin{aligned}
m_{ac;11} &= \frac{(z_a z_c)^{3/2}}{\pi} \left\{ 1 + \frac{1}{2} r_{ac} (\kappa_{ab} \cos \theta_{abc} + \kappa_{cd} \cos \theta_{cda}) \right\} {}_2I_{ac}, \\
m_{ac;12} &= \frac{(z_a z_c)^{3/2}}{\pi} (\kappa_{ab} \cos \theta_{abc} - \kappa_{cd} \cos \theta_{cda}) {}_3I_{ac},
\end{aligned}$$

and

$$\begin{aligned}
m_{ac;2} &= \frac{(z_a z_c)^{3/2}}{\pi} (\kappa_{ab} \sin \theta_{abc} - \kappa_{cd} \sin \theta_{cda}) {}_4I_{ac}, \\
(m_{ac;11})_0 &= 0, \\
(m_{ac;12})_0 &= 1/60 \cdot [\kappa z^{-2} e^{-\sigma} (\sigma^4 + 7\sigma^3 + 27\sigma^2 + 60\sigma + 60) (\cos \theta_{abc} - \cos \theta_{cda})]_0,
\end{aligned}$$

and

$$(m_{ac;2})_0 = 1/15 \cdot [\kappa z^{-2} e^{-\sigma} (\sigma^3 + 6\sigma^2 + 15\sigma + 15) (\sin \theta_{abc} - \sin \theta_{cda})]_0.$$

Section 4

The method of linear variation functions is used with the trial function (37) and Hamiltonian $H = H_0 + V$, where H_0 is the Hamiltonian of a non-interacting molecule pair. The energy to be minimized is given by

$$E(a_3, a_4, \dots) = \frac{\left\langle \left(1 + \sum_3^{\infty} a_n V_n R^{-n} \right) H \left(1 + \sum_3^{\infty} a_m V_m R^{-m} \right) \right\rangle}{\left\langle \left(1 + \sum_3^{\infty} a_n V_n R^{-n} \right)^2 \right\rangle}.$$

Since $H_0 \psi_{ab}(1, 2) \psi_{cd}(3, 4) = E_0 \psi_{ab}(1, 2) \psi_{cd}(3, 4)$, where E_0 is twice the ground-state energy of H_2 , this equation together with Hermitian properties of H_0 and Green's Theorem can be used to show that

$$\begin{aligned} \langle \langle H \rangle \rangle &= E_0 \langle \langle 1 \rangle \rangle + \langle \langle V \rangle \rangle, \\ \langle \langle V_n H \rangle \rangle &= \langle \langle H V_n \rangle \rangle = E_0 \langle \langle V_n \rangle \rangle + \langle \langle V V_n \rangle \rangle, \end{aligned}$$

and

$$\begin{aligned} \langle \langle V_n H V_m \rangle \rangle &= E_0 \langle \langle V_n V_m \rangle \rangle + \langle \langle V V_n V_m \rangle \rangle \\ &\quad + \frac{1}{2} \left\langle \left\langle \sum_{i=1,2} \nabla_i V_n \cdot \nabla_i V_m + \sum_{j=3,4} \nabla_j V_n \cdot \nabla_j V_m \right\rangle \right\rangle, \end{aligned}$$

and hence that

$$E - E_0 = \frac{\left\langle \left\langle V + 2 \sum_n a_n V V_n R^{-n} + \sum_{n,m} a_n a_m R^{-(n+m)} \left\{ V V_n V_m + \frac{1}{2} \sum_i \nabla_i V_n \cdot \nabla_i V_m + \frac{1}{2} \sum_j \nabla_j V_n \cdot \nabla_j V_m \right\} \right\rangle \right\rangle}{\left\langle \left\langle 1 + 2 \sum_n a_n V_n R^{-n} + \sum_{n,m} a_n a_m R^{-(n+m)} V_n V_m \right\rangle \right\rangle}.$$

Necessary conditions for an extremum are that $\partial E / \partial a_k = 0$ for $k = 3, 4, 5, \dots$. For $k = 3$, when terms of two higher orders in R^{-1} than those retained are omitted,

$$a_3 = -2 \langle \langle V_3^2 \rangle \rangle \left\langle \left\langle \sum_i (\nabla_i V_3)^2 + \sum_j (\nabla_j V_4^3)^2 \right\rangle \right\rangle^{-1}.$$

a_3 does not contribute to the dipole moment μ_q in (39) but is the coefficient used by Massey and Buckingham (1938) and Britton and Bean (1955) to calculate the dipole-dipole van der Waals energy of a molecule pair.

For $k = 4$ a like neglect of terms of two higher orders in R^{-1} gives

$$a_4 = -2 \langle \langle V_4^2 \rangle \rangle \left\langle \left\langle \sum_i (\nabla_i V_4)^2 + \sum_j (\nabla_j V_4)^2 \right\rangle \right\rangle^{-1}.$$

This latter coefficient, arising from the dipole-quadrupole term in the expansion of V , is used to calculate μ_q .

It is noted that a_3 and a_4 are functions of R and that if terms of high order in R^{-1} are retained, they and other a coefficients are interdependent.

The calculations of

$$\langle\langle V_4^2 \rangle\rangle \text{ and } \langle\langle \sum_i (\nabla_i V_4)^2 + \sum_j (\nabla_j V_4)^2 \rangle\rangle$$

are straightforward but laborious. Additional integrals were evaluated, seven of which are of form similar to Δ , I , and J , and symmetry properties discussed immediately preceding (42) were used. Integrations were made easier by repeated use of the result for m and n integers,

$$\int a(i)b(i)\xi^m\eta^n di = \frac{(1+\kappa r)e^{-\sigma}}{2(n+1)(m+1)\sigma^m} \{ (n+3)F_{m+2} - (n+1)\sigma^2 F_m \},$$

where

$$F_m = \sigma^m + m\sigma^{m-1} + m(m-1)\sigma^{m-2} + \dots + m!\sigma + m!.$$

Values of a_4 were calculated for equilibrium separation of molecular nuclei and for the four positions (20). They are as follows:

$$\text{Pos. 1: } a_4 = -1.610,$$

$$\text{Pos. 2: } a_4 = -1.564,$$

$$\text{Pos. 3 or 4: } a_4 = -1.588.$$

Thus a_4 is slightly dependent on the orientation of the molecular axes, as also is a_3 .

REFERENCES

- ALLIN, E. J., HARE, W. F. J., and McDONALD, R. E. 1955. *Phys. Rev.* **98**, 540.
 BRITTON, F. R. and BEAN, D. W. T. 1955. *Can. J. Phys.* **33**, 668.
 CHISHOLM, D. A. and WELSH, H. L. 1954. *Can. J. Phys.* **32**, 291.
 COHEN, E. G. D., OFFERHAUS, M. J., VAN LEEUWEN, J. M. J., ROOSE, B. W., and DE BOER, J. 1956. *Physica*, **21**, 737.
 CRAWFORD, M. F. and McDONALD, R. E. 1957. *Can. J. Phys.* (in press).
 CRAWFORD, M. F., WELSH, H. L., MACDONALD, J. C. F., and LOCKE, J. L. 1950. *Phys. Rev.* **80**, 469.
 DE BOER, J. 1949. *Repts. Progr. in Phys.* **12**, 305.
 MACDONALD, J. C. F. 1951. Thesis, University of Toronto, Toronto, Ont.
 MASSEY, H. S. W. and BUCKINGHAM, R. A. 1938. *Proc. Roy. Irish Acad.* **45**, 31.
 ROSEN, N. 1931. *Phys. Rev.* **38**, 2099.
 VAN KRANENDONK, J. 1952. On the theory of pressure-broadening and pressure-induced absorption, Thesis, University of Amsterdam, Amsterdam.
 ——— 1957. *Physica*, **23**, 825.
 VAN KRANENDONK, J. and BIRD, R. B. 1951. *Physica*, **17**, 968.
 VOLKMANN, H. 1935. *Ann. Physik*, **24**, 457.
 WANG, S. C. 1931. *Phys. Rev.* **31**, 579.
 WELSH, H. L., CRAWFORD, M. F., and LOCKE, J. L. 1949. *Phys. Rev.* **76**, 580.
 WELSH, H. L., CRAWFORD, M. F., MACDONALD, J. C. F., and CHISHOLM, D. A. 1951. *Phys. Rev.* **83**, 1264.

ON THE RATE OF CONVERGENCE OF THE SPHERICAL-HARMONICS METHOD FOR A SANDWICH REACTOR OF SMALL LATTICE PITCH¹

B. DAVISON

ABSTRACT

There are some cases where the spherical-harmonics-method calculations can be carried out purely algebraically, without specifying numerically the order of approximation used. Such is the problem of determining the spatial distribution of the thermal neutron flux in an infinite sandwich reactor of a small lattice pitch. The spherical-harmonics-method solution of this problem, in an arbitrary order of approximation, is compared with the exact solution. It is shown that if both are expanded in the Fourier series in terms of the optical depth, the n th term of the Fourier series for the spherical-harmonics-method solution differs from the corresponding term for the exact solution by the factor

$$[\tanh(N\epsilon/n\pi) + O(\epsilon)],$$

where N is the order of approximation used in the spherical-harmonics method and ϵ is one-half of the lattice pitch on the optical scale.

This result should provide some guidance in assessing the rate of convergence of the spherical-harmonics method also for the more complex (and realistic) cases.

1. INTRODUCTION

The spherical-harmonics method of dealing with neutron transport problems has the attraction of adaptability to various geometrical arrangements and is known from numerous tests (Mark 1957; Marshak 1947) to converge satisfactorily when the characteristic dimensions are large compared to the mean free paths involved. Less is known, however, about the rate of convergence in small systems or systems with fine structure, though it is clear, from general considerations, that it should be worse. Indeed numerical tests in one system with fine structure failed to give satisfactory convergence even with a quite high order of approximation. The question of the dependence of the rate of convergence on the ratio of the dimensions to the mean free paths has however not been investigated; indeed to do so with any generality would be extremely difficult. A particular problem has, however, been noted in which the spherical-harmonics calculations can be carried out entirely algebraically, so that the dependence of the rate of convergence on the above ratio can be investigated, and it was felt that to do so would provide a useful guide for assessing the rate of convergence in other, more realistic, problems. This particular problem is the calculation of the thermal neutron flux in an infinite slab reactor of small lattice pitch, that is, in a reactor consisting of alternate thin plane parallel layers of uranium and moderator. The thickness of a uranium layer (the same

¹Manuscript received March 19, 1958.

Contribution from the Computation Centre, McLennan Laboratory, University of Toronto, Toronto, Ontario, in association with Atomic Energy of Canada Limited, Chalk River, Ontario. Issued as A.E.C.L. No. 589.

for all) divided by the total mean free path in uranium plus the corresponding ratio for the moderator layers will be called the lattice pitch on the optical scale. This will be supposed small; it will be denoted by 2ϵ .

It turns out that the thermal-neutron flux, as calculated by the spherical-harmonics method in the approximation of order N , can be presented as

$$(1.1) \quad \Phi_N(x, \epsilon) = \Phi_0 + \epsilon F_1(x, N\epsilon) + \epsilon^2 F_2(x, N\epsilon) + \dots,$$

x being distance normal to the layers. Here Φ_0 is a constant and the F_i depend on ϵ and N only through the product $N\epsilon$. The exact solution on the other hand has the form

$$(1.2) \quad \Phi(x, \epsilon) = \Phi_0 + \epsilon \Phi_1(x) + \epsilon^2 \Phi_2(x) + \dots,$$

in which Φ_0, Φ_1 , etc. are readily evaluated. The convergence of the spherical-harmonics method can now be investigated by comparing $F_1(x, N\epsilon)$ and $\Phi_1(x)$ when N is large. It is found, for example, that when the total mean free paths in uranium and moderator are the same, if $\Phi_1(x)$ and $F_1(x, N\epsilon)$ are expanded in Fourier series in x , the non-constant terms ($n \geq 1$) in these two series differ only by a factor $\tanh(N\epsilon/\pi n)$ in the second. The constant terms themselves have the form

$$\sum_{m=1}^{\infty} f_m \quad \text{and} \quad \sum_{m=1}^{\infty} f_m \tanh(N\epsilon/\pi m).$$

Similar results hold when the mean free paths are not equal.

The precise mathematical formulation of the problem of determining the thermal-neutron flux in a sandwich reactor and the determination of the expansion (1.2) for the exact solution of this problem are given in Section 2. In Section 3 we recapitulate, for the reader's convenience, the basic formulae of the spherical-harmonics method and their application to a sandwich reactor. The main part of the analysis is contained in Sections 4 and 5. In Section 4 we apply the formulae of Section 3 to the case of small lattice pitch, and show that, if we work in terms of an expansion in powers of the lattice pitch, much of the numerical work, usually involved in the application of the spherical-harmonics method, can be eliminated. In Section 5 we use the preceding results to examine the asymptotic behavior of various quantities involved as the order of approximation N tends to infinity, derive the expansion (1.1), and evaluate explicitly its first two terms. Finally, in Section 6, we compare these with the corresponding terms of the series (1.2). The further terms in the expansion (1.1) could have been evaluated in the same manner as Φ_0 and $F_1(x, N\epsilon)$. This has not however been done since the calculation of these further terms is rather lengthy and did not seem likely to provide information of much additional value.

*That Φ_0 occurs in both (1.1) and (1.2) is not surprising since, in the limit when $\epsilon = 0$, we deal with an infinite homogeneous medium, in which the spherical-harmonics method gives the correct result.

2. THERMAL FLUX IN A SANDWICH REACTOR— THE EXACT TREATMENT OF THE PROBLEM

2.1 The Statement of the Problem

We calculate below the thermal-neutron flux under the following simplifying assumptions:

A. the deviations of the thermal-neutron spectrum from the Maxwellian can be neglected, so that thermal neutrons can be treated on the basis of the so-called "one-group theory";

B. scattering may be regarded as isotropic in the laboratory system of co-ordinates;

C. the "reactor" contains only two materials, uranium and moderator; production of thermal neutrons occurs only in the moderator and is constant throughout it.

Under assumptions A and B the exact integral equation governing the thermal-neutron flux is (Davison 1957a)

$$(2.1) \quad \Phi(\mathbf{r}) = \frac{1}{4\pi} \iiint \left\{ \frac{c(\mathbf{r}')}{l(\mathbf{r}')} \Phi(\mathbf{r}') + Q(\mathbf{r}') \right\} \exp[-\tau(\mathbf{r}; \mathbf{r}')] \frac{dV'}{|\mathbf{r} - \mathbf{r}'|^2}.$$

Here \mathbf{r} is the position vector; $\Phi(\mathbf{r})$ is the thermal neutron flux; $l(\mathbf{r})$, $c(\mathbf{r})$, and $Q(\mathbf{r})$ are the total thermal mean free path, the mean number of thermal secondaries per collision, and the rate of thermal-neutron production in the material present at the point \mathbf{r} . $\tau(\mathbf{r}; \mathbf{r}')$ is the optical distance between the points \mathbf{r} and \mathbf{r}' defined by

$$(2.2) \quad \tau(\mathbf{r}; \mathbf{r}') = |\mathbf{r} - \mathbf{r}'| \int_0^1 \frac{ds}{l(\mathbf{r} + s[\mathbf{r}' - \mathbf{r}])}.$$

In the case of an infinite sandwich reactor, if x is the Cartesian co-ordinate perpendicular to the layers, all the quantities $\Phi(\mathbf{r})$, $Q(\mathbf{r})$, $l(\mathbf{r})$, and $c(\mathbf{r})$ depend only upon x . Then (2.2) can be rewritten as

$$(2.3) \quad \tau(\mathbf{r}; \mathbf{r}') = |\mathbf{r} - \mathbf{r}'| [\tau(x) - \tau(x')]/(x - x'),$$

where

$$(2.4) \quad \tau(x) = \int_0^x \frac{dx''}{l(x'')}.$$

Integrating now over the planes $x' = \text{const.}$, using (2.3) and taking $\tau(x)$ instead of x for the independent variable, we can rewrite (2.1) as

$$(2.5) \quad \Phi(\tau) = \frac{1}{2} \int_{-\infty}^{\infty} [c(\tau') \Phi(\tau') + l(\tau') Q(\tau')] E(|\tau - \tau'|) d\tau',$$

where

$$(2.6) \quad E(s) = \int_1^{\infty} e^{-st} dt/t.$$

Finally under the assumption C $l(\tau)Q(\tau)$ is zero in uranium and has some constant value in the moderator. This constant value we choose to be unity. Thus

$$(2.7) \quad l(\tau)Q(\tau) = \begin{cases} 1 & \text{for points in the moderator,} \\ 0 & \text{for points in the uranium.} \end{cases}$$

2.2 The Solution of the Integral Equation

We use henceforth the following notations. Let c_U and c_M be the value of $c(\tau)$ in uranium and in the moderator respectively. Let $2\epsilon l_U$ be the optical thickness of uranium layers, i.e. the ratio of the actual thickness to the total thermal mean free path in uranium, and $2\epsilon l_M$ be the optical thickness of moderator layers. Thus, with the definition of ϵ given in the introduction,

$$(2.8) \quad t_U + t_M = 1.$$

Let the origin be situated in the mid-plane of a moderator layer.

Since $c(\tau)$, $l(\tau)$, and $Q(\tau)$ are periodic functions with period 2ϵ the thermal-neutron flux $\Phi(\tau)$ should be a periodic function with the same period. Thus we can expand all these functions into Fourier series. Accordingly we put

$$(2.9) \quad \Phi(\tau) = \sum_{n=-\infty}^{\infty} \phi_n \exp(i\tau\pi n/\epsilon) = \phi_0 + 2 \sum_{n=1}^{\infty} \phi_n \cos(\tau\pi n/\epsilon),$$

while, with our choice of origin,

$$(2.10) \quad \begin{aligned} l(\tau)Q(\tau) &= \sum_{n=-\infty}^{\infty} (1/\pi n) \sin(\pi n t_M) \exp(i\tau\pi n/\epsilon), \\ c(\tau) &= c_U + (c_M - c_U) \sum_{n=-\infty}^{\infty} (1/\pi n) \sin(\pi n t_M) \exp(i\tau\pi n/\epsilon). \end{aligned}$$

Substituting these into (2.6), noting that

$$\frac{1}{2} \int_{-\infty}^{\infty} \exp(i\tau'\pi n/\epsilon) E(|\tau - \tau'|) d\tau' = (\epsilon/n\pi) \tan^{-1}(n\pi/\epsilon) \exp(i\tau\pi n/\epsilon),$$

and equating the coefficients accompanying $\exp(i\tau\pi n/\epsilon)$ for each n separately, we readily obtain

$$(2.11) \quad \begin{aligned} \phi_n &= (\epsilon/n\pi) \tan^{-1}(n\pi/\epsilon) \left\{ \sin(\pi n t_M) / \pi n + c_U \phi_n \right. \\ &\quad \left. + (c_M - c_U) \sum_{n'=-\infty}^{\infty} \phi_{n'} \sin[\pi t_M(n' - n)] / \pi(n' - n) \right\}. \end{aligned}$$

Notice now that for small ϵ

$$(2.12) \quad (\epsilon/n\pi) \tan^{-1}(n\pi/\epsilon) = \begin{cases} 1 & \text{if } n = 0, \\ \frac{\epsilon}{2|n|} + O(\epsilon^2) & \text{if } n \neq 0. \end{cases}$$

Substituting this into (2.11) one can readily see that ϕ_0 will remain finite for ϵ tending to zero and all other ϕ_n will be of order $O(\epsilon)$. Also, insofar as $n \neq 0$ are concerned, in order to determine ϕ_n to the accuracy of ϵ^m we need to know the expression in the braces on the right side of (2.11) only to the accuracy of ϵ^{m-1} . Consequently we obtain

$$(2.13) \quad \begin{aligned} \phi_0 &= \frac{t_M}{1 - c_U t_U - c_M t_M} + \frac{\epsilon}{\pi^2} \frac{(c_M - c_U)(1 - c_U)}{[1 - c_U t_U - c_M t_M]^2} \sum_{n=1}^{\infty} \frac{[\sin(\pi n t_M)]^2}{n^3} + O(\epsilon^2), \\ \phi_n &= \frac{\epsilon}{2\pi n^2} \frac{1 - c_U}{1 - c_U t_U - c_M t_M} \sin(\pi |n| t_M) + O(\epsilon^2) \quad \text{for } n \geq 1. \end{aligned}$$

By substituting these into (2.9) one obtains the final expression for the flux.

Notice that the $O(\epsilon)$ part of the constant term in the series (2.9) is, in its turn, a sum over all $n \neq 0$. Physically the reason for this is as follows. Since we are considering stationary conditions in a leakage-free system, the total absorption of thermal neutrons per lattice period per unit area should be equal to the corresponding total production. But the $n \neq 0$ terms in (2.9) are associated with some (positive or negative) absorption which has to be compensated by some change in the constant term. The $O(\epsilon)$ part of this constant term consists entirely of such compensatory changes.

2.3 An Alternative Form of the Result

For purposes of comparison with results obtained by the spherical-harmonics method we need, in Section 6 below, the expressions for the values of $\Phi(\tau)$ and of all its derivatives in the mid-plane of a uranium layer ($\tau = \epsilon$). Repeated term-by-term differentiation of (2.9), if performed directly, would lead to divergent series. It is known however that at points where the required derivatives exist and are continuous (and such are the mid-planes of uranium and moderator layers) the correct values of the derivative can be obtained as follows: multiply the n th term of (2.9) by r^n , where r is some number less than unity, differentiate term by term the required number of times, then first sum the resulting series and afterwards pass to the limit with r tending to unity. In this manner we obtain for the even-order derivatives at the mid-plane of a uranium layer.

$$(2.14) \quad \left. \frac{d^{2m} \Phi(\tau)}{d(\tau/\epsilon)^{2m}} \right]_{\tau=\epsilon} \\ = \epsilon (-1)^m \pi^{2m-1} \frac{1-c_U}{1-c_U l_U - c_M l_M} \lim_{r \rightarrow 1} \sum_{n=1}^{\infty} (-r)^n n^{2m-2} \sin(\pi n t_M) + O(\epsilon^2) \text{ for } m \geq 1.$$

The odd-order derivatives of course all vanish there.

3. THE SPHERICAL-HARMONICS METHOD—THE BASIC FORMULAE AND THEIR APPLICATION TO THE SANDWICH REACTOR CASE

In the spherical-harmonics method one works in terms of the angular distribution which, in the P_N approximation and the plane case, is presented (Davison 1957a) as

$$(3.1) \quad \psi(x, \mu) = (1/4\pi) \sum_{n=0}^N (2n+1) \psi_n(x) P_n(\mu),$$

in which N is an odd integer, μ is the cosine of the angle between the direction of neutron travel and the x axis, and the $P_n(\mu)$ are Legendre polynomials. Provided scattering and the sources, if any, are isotropic the $\psi_n(x)$ are the solutions of

$$(3.2) \quad (n+1)d\psi_{n+1}/dx + [2n+1-c(x)\delta_{0n}]\psi_n/l(x) + nd\psi_{n-1}/dx = Q(x)\delta_{0n} \\ \text{for } 0 \leq n \leq N,$$

together with

$$(3.3) \quad \psi_{N+1} = 0.$$

Here $c(x)$, $l(x)$, and $Q(x)$ have the same meaning as before while $\psi_0(x)$ is identical with what was previously denoted by $\Phi(x)$.

If, instead of x , we take τ , defined by (2.4), as the independent variable and assume unit source density in the moderator, equations (3.2) become

$$(3.2') \quad (n+1)d\psi_{n+1}/d\tau + (2n+1)\psi_n + nd\psi_{n-1}/d\tau = \begin{cases} (c_M\psi_0 + 1)\delta_{0n} & \text{for } |\tau| \leq \epsilon l_M, \\ c_U\psi_0 \delta_{0n} & \text{for } |\tau - \epsilon| \leq \epsilon l_U. \end{cases}$$

The solutions of these equations are

$$(3.4M) \quad \psi_n(\tau) = \frac{\delta_{0n}}{1 - c_M} + \sum_{j=\pm 1}^{\pm(N+1)/2} A_{j,M} G_n(\nu_{j,M}, c_M) \exp(\nu_{j,M}\tau) \quad \text{for } |\tau| \leq \epsilon l_M,$$

$$(3.4U) \quad \psi_n(\tau) = \sum_{j=\pm 1}^{\pm(N+1)/2} A_{j,U} G_n(\nu_{j,U}, c_U) \exp[\nu_{j,U}(\tau - \epsilon)] \quad \text{for } |\tau - \epsilon| \leq \epsilon l_U,$$

the latter having of course no source term. In these the $G_n(\nu, c)$ are defined by

$$(3.5) \quad (n+1)G_{n+1}(\nu, c) + (2n+1 - c\delta_{0n})G_n(\nu, c) - \nu + nG_{n-1}(\nu, c) = 0$$

and

$$(3.6) \quad G_0(\nu, c) = 1,$$

while the ν_j are the roots of

$$(3.7) \quad G_{N+1}(\nu, c) = 0.$$

These roots, for $c \neq 1$, are all different and in pairs, that is, if $\nu = \nu_j$ is a root so is $\nu = -\nu_j$. We number them so that

$$(3.8) \quad \nu_{-j} = -\nu_j.$$

With this convention symmetry about the mid-planes of uranium and moderator layers requires that the constants of integration, A_j , satisfy

$$(3.9) \quad A_{-j} = A_j.$$

They are to be determined from the $N+1$ boundary conditions at the interfaces

$$(3.10) \quad \psi_n(\tau) \text{ continuous across an interface.}$$

In the completely source-free case it has been shown (Davison 1957b) that this system of equations can be replaced by two systems for the $A_{j,U}$ and the $A_{j,M}$ separately, and more simple in that they do not involve the $G_n(\nu_{j,M}, c_M)$ and $G_n(\nu_{j,U}, c_U)$. The extension to the case when there are sources, as here in the moderator, is straightforward. We obtain

$$(3.11M) \quad \frac{1 - c_U}{(1 - c_M)(c_M - c_U)} \frac{\sinh(\nu_{i,U}\epsilon l_U)}{\nu_{i,U}\epsilon} + \sum_{j=1}^{(N+1)/2} A_{j,M} \left\{ \frac{\sinh(\nu_{i,U}\epsilon l_U + \nu_{j,M}\epsilon l_M)}{(\nu_{i,U} - \nu_{j,M})\epsilon} + \frac{\sinh(\nu_{i,U}\epsilon l_U - \nu_{j,M}\epsilon l_M)}{(\nu_{i,U} + \nu_{j,M})\epsilon} \right\} = 0$$

and

$$(3.11U) \quad \frac{1}{c_M - c_U} \frac{\sinh(\nu_{i,M} \epsilon t_M)}{\nu_{i,M} \epsilon} + \sum_{j=1}^{(N+1)/2} A_{j,U} \left\{ \frac{\sinh(\nu_{i,M} \epsilon t_M + \nu_{j,U} \epsilon t_U)}{(\nu_{i,M} - \nu_{j,U}) \epsilon} + \frac{\sinh(\nu_{i,M} \epsilon t_M - \nu_{j,U} \epsilon t_U)}{(\nu_{i,M} + \nu_{j,U}) \epsilon} \right\} = 0$$

both for $1 \leq i \leq (N+1)/2$.

Recalling now that $\psi_0(\tau)$ is the spherical-harmonics P_N approximation to the flux, which we previously denoted by Φ_N , we have, from (3.4M and U)

$$(3.12M) \quad \Phi_N(\tau, \epsilon) = \frac{1}{1 - c_M} + 2 \sum_{j=1}^{(N+1)/2} A_{j,M} \cosh(\nu_{j,M} \tau) \quad \text{for } |\tau| \leq \epsilon t_M,$$

$$(3.12U) \quad \Phi_N(\tau, \epsilon) = 2 \sum_{j=1}^{(N+1)/2} A_{j,U} \cosh[\nu_{j,U}(\tau - \epsilon)] \quad \text{for } |\tau - \epsilon| \leq \epsilon t_U.$$

4. THE CASE OF A SMALL LATTICE PITCH

4.1 Preliminary Transformations

We concentrate now upon the case when the lattice pitch on the optical scale, 2ϵ , is small and proceed to simplify the formulae (3.11) and (3.12) under this assumption. For the sake of brevity we reproduce the calculations in detail only for points in uranium. The analysis for points in the moderator is quite similar.

Put*

$$(4.1) \quad \tau - \epsilon = \epsilon z,$$

$$(4.2) \quad \Phi_N(\tau; \epsilon) = \sum_{j=0}^{\infty} \Phi_{N,j}(\tau) \epsilon^{2j},$$

$$(4.3) \quad A_{i,U} = \sum_{j=0}^{\infty} A_{i,j} \epsilon^{2j},$$

and expand (3.11U) and (3.12U) into powers of ϵ , equating separately the coefficients involving each particular power of ϵ and introducing also the abbreviation

$$(4.4) \quad \Xi_{k,m} = 2 \sum_{i=1}^{\frac{1}{2}(N+1)} A_{i,m} \nu_{i,U}^{2k}.$$

Then (3.12U) gives

$$(4.5) \quad \Phi_{N,m}(\tau) = \sum_{j=0}^m \Xi_{j,m-j} z^{2j} / (2j)!$$

while the equations (3.11U) give

$$(4.6) \quad \frac{\nu_{j,M}^{2m}}{c_M - c_U} \frac{t_M^{2m+1}}{(2m+1)!} + 2 \sum_{i=1}^{(N+1)/2} \sum_{\alpha=0}^m A_{i,m-\alpha} I_{\alpha}(\nu_{j,M}, \nu_{i,U}) / (2\alpha+1)! = 0,$$

where we have put for brevity

*Since we explicitly confine ourselves to points in uranium, we may omit an otherwise necessary distinguishing subscript U on $A_{i,j}$ and other quantities defined later.

$$(4.7) \quad H_a(\nu_{j,M}, \nu_{i,U}) = \frac{1}{2} \left\{ \frac{(\nu_{j,M} t_M + \nu_{i,U} t_U)^{2\alpha+1}}{\nu_{j,M} - \nu_{i,U}} + \frac{(\nu_{j,M} t_M - \nu_{i,U} t_U)^{2\alpha+1}}{\nu_{j,M} + \nu_{i,U}} \right\}.$$

We notice now that the Φ_N are symmetric functions of the $\nu_{i,U}$ and of the $\nu_{i,M}$, though transcendental symmetric functions of them. The $\Xi_{k,m}$, however, are rational symmetric functions of these same quantities so that, by a well-known theorem in algebra, they are also rational functions of the coefficients of the polynomials $G_{N+1}(\nu, c_U)$ and $G_{N+1}(\nu, c_M)$ of which the $\nu_{i,U}$ and $\nu_{i,M}$ are the zeros. We now proceed to express the $\Xi_{k,m}$ explicitly as functions of these coefficients. To do so we first relate the $\Xi_{k,m}$ to certain other, rather simpler, symmetric functions, $\gamma_{k,s}$, defined by

$$(4.8) \quad \gamma_{k,s} = \sum_{i=1}^{(N+1)/2} B_{i,s} \nu_{i,U}^{2k},$$

where $B_{i,s}$ are the solutions of the equations

$$(4.9) \quad \sum_{i=1}^{(N+1)/2} B_{i,s} \frac{\nu_{i,U}^2 t_U + \nu_{i,M}^2 t_M}{\nu_{i,U}^2 - \nu_{i,M}^2} = \nu_{j,M}^{2s}.$$

To relate the $\Xi_{k,m}$ and the $\gamma_{k,s}$ notice first of all that the quantities (4.7), as can be readily verified (recalling (2.8)), can be alternatively expressed as

$$(4.10) \quad H_a(\nu_{j,M}, \nu_{i,U}) = \nu_{i,U}^{2\alpha} \frac{\nu_{j,M}^2 t_M + \nu_{i,U}^2 t_U}{\nu_{j,M}^2 - \nu_{i,U}^2} + \sum_{\beta=0}^{\alpha} h_{\alpha,\beta} \nu_{j,M}^{2\alpha-2\beta} \nu_{i,U}^{2\beta},$$

where the coefficients $h_{\alpha,\beta}$ depend only upon t_M and t_U . One can also easily verify that $h_{0,0} = 0$, while for $\alpha \geq 1$

$$(4.11) \quad h_{\alpha,0} = t_M^{2\alpha+1}, \quad h_{\alpha,\alpha} = t_U - t_U^{2\alpha+1}.$$

Using (4.10) and (4.4) we can rewrite the equations (4.6) as

$$\begin{aligned} 2 \sum_{i=1}^{(N+1)/2} \frac{\nu_{i,U}^2 t_U + \nu_{i,M}^2 t_M}{\nu_{i,U}^2 - \nu_{i,M}^2} \sum_{\alpha=0}^m \frac{\nu_{i,U}^{2\alpha}}{(2\alpha+1)!} A_{i,m-\alpha} \\ = \frac{\nu_{j,M}^{2m} t_M^{2m+1}}{c_M - c_U (2m+1)!} + \sum_{\alpha=1}^m \frac{1}{(2\alpha+1)!} \sum_{\beta=0}^{\alpha} h_{\alpha,\beta} \nu_{j,M}^{2\alpha-2\beta} \Xi_{\beta,m-\alpha}. \end{aligned}$$

Comparing this with (4.9) we see at once that

$$\begin{aligned} 2 \sum_{\alpha=0}^m \frac{\nu_{i,U}^{2\alpha}}{(2\alpha+1)!} A_{i,m-\alpha} \\ = \frac{1}{c_M - c_U} \frac{t_M^{2m+1}}{(2m+1)!} B_{i,m} + \sum_{\alpha=1}^m \frac{1}{(2\alpha+1)!} \sum_{\beta=0}^{\alpha} h_{\alpha,\beta} \Xi_{\beta,m-\alpha} B_{i,\alpha-\beta}. \end{aligned}$$

Multiplying this by $\nu_{i,U}^{2k}$, summing with respect to i , and recalling (4.4) and (4.8) we finally have

$$\begin{aligned} (4.12) \quad \sum_{\alpha=0}^m \frac{1}{(2\alpha+1)!} \Xi_{k+\alpha,m-\alpha} \\ = \frac{1}{c_M - c_U} \frac{t_M^{2m+1}}{(2m+1)!} \gamma_{k,m} + \sum_{\alpha=1}^m \frac{1}{(2\alpha+1)!} \sum_{\beta=0}^{\alpha} h_{\alpha,\beta} \Xi_{\beta,m-\alpha} \gamma_{k,\alpha-\beta}. \end{aligned}$$

4.2 Evaluation of Auxiliary Symmetric Functions

We proceed now to express the quantities $\gamma_{k,s}$ in terms of the coefficients of the equations (3.7). To avoid the necessity of carrying out the calculations for each s separately we introduce the generating functions $B_i(y)$ and $\gamma_k(y)$ defined by

$$(4.13) \quad B_i(y) = \sum_{s=0}^{\infty} B_{i,s} y^{2s}, \quad \gamma_k(y) = \sum_{s=0}^{\infty} \gamma_{k,s} y^{2s}.$$

Combining (4.13) with (4.8) and (4.9) we get

$$(4.14) \quad \gamma_k(y) = \sum_{i=1}^{(N+1)/2} B_i(y) \nu_{i,U}^{2k}$$

and

$$(4.15) \quad \frac{1}{1-y^2 \nu_{j,M}^2} = \sum_{i=1}^{(N+1)/2} B_i(y) \frac{\nu_{i,U}^2 \nu_{j,M}^2}{\nu_{i,U}^2 - \nu_{j,M}^2}.$$

Starting with (4.15) and recalling (2.8) one can easily show by induction that, for $n \geq 1$,

$$(4.16) \quad y^{2n} / \prod_{k=0}^n (1 - y^2 \nu_{j+k,M}^2) = \sum_{i=1}^{(N+1)/2} B_i(y) \nu_{i,U}^{2n} / \prod_{k=0}^n (\nu_{i,U}^2 - \nu_{j+k,M}^2)$$

for $1 \leq n \leq (N+1)/2 - j$.

On the other hand it is clear, from the definitions (3.5) and (3.6) and the fact that N is odd, that $G_{N+1}(\nu, c_M)$ is a polynomial of order $(N+1)/2$ in ν^{-2} . The fact that the $\nu_{j,M}$ are the roots of (3.7M) then implies that

$$(4.17) \quad G_{N+1}(\nu, c_M) = G_{N+1}(\infty, c_M) \prod_{j=1}^{(N+1)/2} (1 - \nu_{j,M}^2 \nu^{-2}).$$

Using this we can rewrite (4.16) for $j = 1, n = (N-1)/2$, as

$$(4.18.1) \quad \frac{y^{N-1}}{G_{N+1}(1/y, c_M)} = \sum_{i=1}^{(N+1)/2} \frac{B_i(y)}{\nu_{i,U}^{N-1} G_{N+1}(\nu_{i,U}, c_M)}$$

and for $j = 2, n = (N-3)/2$, as

$$\frac{y^{N-3}(1 - y^2 \nu_{1,M}^2)}{G_{N+1}(1/y, c_M)} = \sum_{i=1}^{(N+1)/2} \frac{B_i(y)(\nu_{i,U}^2 - \nu_{1,M}^2)}{\nu_{i,U}^{N-1} G_{N+1}(\nu_{i,U}, c_M)}.$$

Comparing this with (4.18.1) we have

$$(4.18.2) \quad \frac{y^{N-3}}{G_{N+1}(1/y, c_M)} = \sum_{i=1}^{(N+1)/2} \frac{B_i(y)}{\nu_{i,U}^{N-3} G_{N+1}(\nu_{i,U}, c_M)}.$$

Proceeding in this manner one can prove that, for any n in the range $1 \leq n \leq (N-1)/2$,

$$(4.18) \quad \frac{y^{2n}}{G_{N+1}(1/y, c_M)} = \sum_{i=1}^{(N+1)/2} \frac{B_i(y)}{\nu_{i,U}^{2n} G_{N+1}(\nu_{i,U}, c_M)}.$$

For $n = 0$ the calculation is slightly different since we should now use (4.15) instead of (4.16). The difference between the right side of (4.15) and what the

right side of (4.16) would have been if we had put there $n = 0$ is equal, in view of (4.14), to $-t_M \gamma_0(y)$. Bearing in mind this remark and proceeding otherwise much as before we obtain

$$(4.19) \quad \frac{1}{G_{N+1}(1/y, c_M)} + \frac{t_M \gamma_0(y)}{G_{N+1}(\infty, c_M)} = \sum_{i=1}^{(N+1)/2} \frac{B_i(y)}{G_{N+1}(v_{i,U}, c_M)}.$$

The formulae (4.18) and (4.19) show that if $p(y)$ is any even polynomial in y , of an order not exceeding $(N-1)$, then

$$(4.20) \quad \sum_{i=1}^{(N+1)/2} \frac{B_i(y) p(1/v_{i,U})}{G_{N+1}(v_{i,U}, c_M)} = \frac{p(y)}{G_{N+1}(1/y, c_M)} + \frac{t_M \gamma_0(y) p(0)}{G_{N+1}(\infty, c_M)}.$$

To determine $\gamma_0(y)$, let

$$(4.21) \quad p_0(y) = (1 - c_U) G_{N+1}(1/y, c_M) - (1 - c_M) G_{N+1}(1/y, c_U).$$

This is an even polynomial in y and obviously of order not exceeding $(N+1)$. However one can readily see from (3.5) and (3.6) that the coefficient accompanying y^{-N-1} in the expression for $G_{N+1}(y, c)$ is proportional to $(1-c)$. Thus this $p_0(y)$ contains no term in y^{N+1} and so is a polynomial of order not exceeding $N-1$.

Putting now $p_0(y)$ for $p(y)$ in (4.20), recalling (4.14), and bearing in mind firstly that $G_{N+1}(v_{i,U}, c_U)$ is zero in virtue of (3.7) and secondly that $G_{N+1}(\infty, c)$, as one can readily see from (3.5) and (3.6), is in fact independent of c , we obtain

$$(4.22) \quad \gamma_0(y) = \frac{1 - c_U}{1 - c_U t_U - c_M t_M} - \frac{1 - c_M}{1 - c_U t_U - c_M t_M} \frac{G_{N+1}(1/y, c_U)}{G_{N+1}(1/y, c_M)}.$$

To determine the other $\gamma_k(y)$, define $p_k(y)$ for $k \geq 1$ by the equation

$$(4.23) \quad y^{-2k} G_{N+1}(1/y, c_M) = D_k(y) y^{-2} G_{N+1}(1/y, c_U) + p_k(y)$$

together with the stipulations that $p_k(y)$ is an even polynomial in y and $D_k(y)$ is an even polynomial in $1/y$. These stipulations will be met if we put, recalling that $G_{N+1}(\infty, c_U) = G_{N+1}(\infty, c_M)$,

$$(4.24) \quad D_1(y) = 1, \quad p_1(y) = (1/y^2)[G_{N+1}(1/y, c_M) - G_{N+1}(1/y, c_U)],$$

and determine $D_k(y)$ and $p_k(y)$ for $k \geq 2$ from the recurrence relationships

$$(4.25) \quad \begin{aligned} D_k(y) &= \frac{1}{y^2} D_{k-1}(y) + p_{k-1}(0)/G_{N+1}(\infty, c_U), \\ p_k(y) &= \frac{1}{y^2} \left\{ p_{k-1}(y) - p_{k-1}(0) \frac{G_{N+1}(1/y, c_U)}{G_{N+1}(\infty, c_U)} \right\} \quad \text{for } k \geq 2. \end{aligned}$$

Notice that the order of these polynomials $p_k(y)$ does not exceed $N-1$.

Now replacing y by $1/v_{i,U}$ in (4.23), multiplying by $B_i(y)$, summing with respect to i , and recalling (4.8), (3.7), and (4.20) we get

$$(4.26) \quad \gamma_k(y) = \frac{p_k(y)}{G_{N+1}(1/y, c_M)} + \frac{t_M \gamma_0(y) p_k(0)}{G_{N+1}(\infty, c_M)} \quad \text{for } k \geq 1.$$

The formulae (4.13), (4.22), and (4.24) to (4.26) allow us to determine all $\gamma_{k,s}$ once the coefficients in the expression for $G_{N+1}(\nu, c)$ are known.

5. ASYMPTOTIC BEHAVIOR OF THE SPHERICAL-HARMONICS-METHOD SOLUTION AS THE ORDER OF APPROXIMATION INCREASES INDEFINITELY

5.1 Asymptotic Behavior of $G_{N+1}(1/y, c)$ for Large N and Small y

So far the order of approximation, N , has been merely an odd integer. We now investigate the asymptotic behavior of the solution as N tends to infinity. Our objective is to see whether $\Phi_N(\tau; \epsilon)$ can in fact be represented in the form (1.1), and, if so, to evaluate the first few terms of that series. We start by examining the asymptotic behavior of $G_{N+1}(1/y, c)$ for large N and small y .

Comparison of (3.5) and (3.6) with the recurrence relationships for the Legendre polynomials P_n , and the Legendre function of the second kind Q_n , shows that once that

$$(5.1) \quad G_n(1/y, c) = (-1)^n \{ P_n(y) + cy[Q_n(y) - P_n(y)Q_0(y)] \}.$$

On the other hand it is known that for large n the asymptotic behaviors of $P_n(\cos \gamma)$ and $Q_n(\cos \theta)$ are given by

$$(5.2) \quad P_n(\cos \theta) = \frac{2}{\sqrt{\pi}} \frac{\Gamma(n+1)}{\Gamma(n+3/2)} \left\{ \frac{\cos[(n+\frac{1}{2})\theta - \pi/4]}{(2 \sin \theta)^{1/2}} + \frac{1^2}{2(2n+3)} \frac{\cos[(n+3/2)\theta - 3\pi/4]}{(2 \sin \theta)^{3/2}} + \dots \right\}$$

and

$$(5.3) \quad Q_n(\cos \theta) = \sqrt{\pi} \frac{\Gamma(n+1)}{\Gamma(n+3/2)} \left\{ \frac{\cos[(n+\frac{1}{2})\theta + \pi/4]}{(2 \sin \theta)^{1/2}} - \frac{1^2}{2(2n+3)} \frac{\cos[(n+3/2)\theta + 3\pi/4]}{(2 \sin \theta)^{3/2}} + \dots \right\},$$

where Γ is Euler's function (see, e.g., Hobson 1931, p. 295, bearing in mind that Hobson's $\Pi(n)$ is what is more commonly denoted by $\Gamma(n+1)$).

If we take $n = N+1$ and $\theta = \pi/2 - \sin^{-1}(Y/N)$, note that $(N+1)$ is even, express $\Gamma(N+2)/\Gamma(N+5/2)$ in terms of $P_{N+1}(0)$, and then expand the right sides of the resulting expressions in powers of $1/N$, we obtain

$$(5.4) \quad P_{N+1}(Y/N) = P_{N+1}(0) \left\{ \cos Y + \frac{1}{N} \bar{P}_1(Y) + \frac{1}{N^2} \bar{P}_2(Y) + \dots \right\}$$

and

$$(5.5) \quad Q_{N+1}(Y/N) = \frac{\pi}{2} P_{N+1}(0) \left\{ \sin Y + \frac{1}{N} \bar{Q}_1(Y) + \dots \right\},$$

where $\bar{P}_k(Y)$ and $\bar{Q}_k(Y)$ are some functions of Y only.

Combining these results with (5.1), taking $Y = Ny$, and bearing in mind that for small y , $Q_0(y)$ is of the order $O(y)$ we readily get

$$\begin{aligned}
 (5.6) \quad G_{N+1}(1/y, c) &= P_{N+1}(0) \left\{ \cos Ny + O\left(\frac{1}{N} f(Ny)\right) \right\}, \\
 G_{N+1}(1/y, c_M) - G_{N+1}(1/y, c_U) &= P_{N+1}(0) \left\{ (c_M - c_U) \frac{\pi y}{2} \sin Ny + O\left(\frac{1}{N^2} f(Ny)\right) \right\},
 \end{aligned}$$

where $O(N^{-s} f(Ny))$ denotes the collection of terms in which the power of y exceeds that of N by at least s units.

5.2 The Asymptotic Behavior of the $\gamma_{k,s}$ for Large N

We are now in a position to determine the asymptotic behavior of various $\gamma_{k,s}$ and $\Xi_{k,m}$ for large N . We introduce the following abbreviations. Let $p_{k,s}$ be the coefficient of y^{2s} in the expansion of $p_k(y)$, defined by (4.23), i.e.

$$(5.7) \quad p_k(y) = \sum_s y^{2s} p_{k,s},$$

and let $\tilde{p}_{k,s}$, $\tilde{\gamma}_{k,s}$, and $\tilde{\Xi}_{k,m}$ be the leading terms in the expansions of $p_{k,s}$, $\gamma_{k,s}$, and $\Xi_{k,m}$ into descending powers of N . We shall also use the symbols $\tilde{p}_k(y)$ and $\tilde{\gamma}_k(y)$ to denote the expressions arising when we replace $p_{k,s}$ and $\gamma_{k,s}$ by $\tilde{p}_{k,s}$ and $\tilde{\gamma}_{k,s}$ respectively in (5.7) and (4.13).

Now the formula (4.22) shows first of all that

$$(5.8) \quad \gamma_{0,0} = \frac{c_M - c_U}{1 - c_U t_U - c_M t_M}$$

and this is exact, i.e. independent of N , since $G_{N+1}(\infty, c)$ is independent of c . At the same time, substituting (5.6) into (4.22) and using the abbreviations just introduced, we have

$$(5.9) \quad \tilde{\gamma}_0(y) = \frac{c_M - c_U}{1 - c_U t_U - c_M t_M} \left\{ 1 + (1 - c_M) \frac{\pi y}{2} \tan Ny \right\}.$$

The formulae (4.24) and (4.25) give, in a similar manner,

$$(5.10) \quad \tilde{p}_1(y) = P_{N+1}(0) (c_M - c_U) \frac{\pi}{2y} \sin Ny$$

and

$$(5.11) \quad \frac{\tilde{p}_k(y)}{\cos Ny} = \frac{1}{y^2} \left\{ \frac{\tilde{p}_{k-1}(y)}{\cos Ny} - \tilde{p}_{k-1}(0) \right\} \quad \text{for } k \geq 2.$$

Next, (5.9) shows that, insofar as the evaluation of $\tilde{\gamma}_k(y)$ is concerned, we may replace $\gamma_0(y)$ in the second term of (4.26) by $\gamma_0(0)$ so that the presence of this second term affects the constant term in the expression for $\tilde{\gamma}_k(y)$ but not the terms with higher powers of y . Thus combining (4.26) and (5.10) we get

$$(5.12) \quad \tilde{\gamma}_1(y) - \tilde{\gamma}_1(0) = (c_M - c_U) \frac{\pi}{2} \left[\frac{1}{y} \tan Ny - N \right],$$

while combining (4.26) and (5.11) and recalling (4.13) we have, provided $s \geq 1$ and $k \geq 1$,

$$\tilde{\gamma}_{k+1,s} = \tilde{\gamma}_{k,s+1} \quad \text{for } s \geq 1, k \geq 1,$$

and hence finally

$$(5.13) \quad \tilde{\gamma}_{k,s} = (c_M - c_U) \frac{\pi}{2} \frac{1}{(2k+2s-1)!} \frac{d^{2k+2s-1}}{dy^{2k+2s-1}} \tan Ny \Big|_{y=0} \quad \text{for } s \geq 1, k \geq 1.$$

To evaluate $\tilde{\gamma}_{k,0}$ notice that on account of the second term in (4.26) it is increased, as compared to what it would have been in the absence of that second term, by the factor $1 + t_M \gamma_{0,0} = (1 - c_U)/(1 - c_U t_U - c_M t_M)$. Thus

$$(5.14) \quad \tilde{\gamma}_{k,0} = \frac{(c_M - c_U)(1 - c_U)}{1 - c_U t_U - c_M t_M} \frac{\pi}{2} \frac{1}{(2k-1)!} \frac{d^{2k-1}}{dy^{2k-1}} \tan Ny \Big|_{y=0} \quad \text{for } k \geq 1.$$

5.3 The Asymptotic Behavior of $\Xi_{k,m}$ for Large N

We proceed now to evaluate the $\Xi_{k,m}$, i.e. the leading terms in the expansions of $\Xi_{k,m}$ in descending powers of N . We do this in three stages. First we consider these quantities for $m = 0$, any k , next for $m \geq 1$, $k \geq 1$, and finally for $k = 0$, $m \geq 1$.

For $m = 0$ the formula (4.12) reduces to

$$\Xi_{k,0} = \frac{t_M}{c_M - c_U} \gamma_{k,0};$$

from this and (5.8) and (5.14) we get

$$(5.15) \quad \Xi_{0,0} = \frac{t_M}{1 - c_U t_U - c_M t_M},$$

$$(5.16) \quad \tilde{\Xi}_{k,0} = \frac{t_M(1 - c_U)}{1 - c_U t_U - c_M t_M} \frac{\pi}{2} \frac{1}{(2k-1)!} \frac{d^{2k-1}}{dy^{2k-1}} \tan Ny \Big|_{y=0} \quad \text{for } k \geq 1.$$

Notice that, similarly to (5.8), (5.15) is valid for any N .

Turn now to the case $m \geq 1$, $k \geq 1$. The formulae (5.9), (5.13), and (5.14) show that, for $m+k \geq 1$, $\gamma_{k,m}$ is of the order $O(N^{2k+2m-1})$ while using (4.12) one can easily show by induction that, for $m+k \geq 1$, $\Xi_{k,m}$ is also of this order. Now one readily sees by inspection that, for $k \geq 1$ and $m \geq 1$, the only term in the double sum on the right side of (4.12) that is of this order of magnitude is the one corresponding to $\beta = 0$, $\alpha = m$. Thus if $k \geq 1$ and $m \geq 1$ the equation (4.12) reduces to

$$(5.17) \quad \sum_{\alpha=0}^m \frac{1}{(2\alpha+1)!} \tilde{\Xi}_{k+\alpha, m-\alpha} = \frac{1}{(2m+1)!} \tilde{\gamma}_{k,m} \left[\frac{t_M^{2m+1}}{c_M - c_U} + h_{m,0} \Xi_{0,0} \right] \quad \text{for } k \geq 1, m \geq 1$$

and the right side of this, in view of (4.11), (5.15), and (5.13), reduces to

$$\frac{t_M^{2m+1}}{(2m+1)!} \frac{1 - c_U}{1 - c_U t_U - c_M t_M} \frac{\pi}{2} \frac{1}{(2k+2m-1)!} \frac{d^{2k+2m-1}}{dy^{2k+2m-1}} \tan Ny \Big|_{y=0}.$$

Thus if we put, for $k \geq 1$,

$$(5.18) \quad \tilde{\Xi}_{k,m} = \zeta_m \frac{1 - c_U}{1 - c_U t_U - c_M t_M} \frac{\pi}{2} \frac{1}{(2k+2m-1)!} \frac{d^{2k+2m-1}}{dy^{2k+2m-1}} \tan Ny \Big|_{y=0} \quad (k \geq 1),$$

the equations (5.17) give

$$(5.19) \quad \sum_{\alpha=0}^m \frac{1}{(2\alpha+1)!} \zeta_{m-\alpha} = \frac{t_M^{2m+1}}{(2m+1)!}$$

whence one can readily verify that

$$(5.20) \quad \sum_{m=0}^{\infty} \zeta_m y^{2m} = \frac{\sinh(yt_M)}{\sinh y}.$$

If $k = 0$ the calculation differs only in the following respects. Firstly, the value of $\gamma_{0,m}$ should now be taken from (5.9) rather than from (5.13). Secondly, in the double sum on the right side of (4.12), apart from the term with $\beta = 0$ and $\alpha = m$, all the terms with $\beta = \alpha$, for any α , are now also of the order $O(N^{2m-1})$ and consequently should be taken into account. Otherwise the calculation proceeds exactly as for $k \geq 1$, and putting

$$(5.21) \quad \tilde{\zeta}_{0,m} = \eta_m \frac{1 - c_U}{1 - c_U t_U - c_M t_M} \frac{\pi}{2} \frac{1}{(2m-1)!} \frac{d^{2m-1}}{dy^{2m-1}} \tan Ny \Big|_{y=0}$$

one obtains

$$(5.22) \quad \sum_{m=1}^{\infty} \eta_m y^{2m} = \frac{\sinh(yt_M)}{\sinh y} - \frac{c_M - c_U}{1 - c_U t_U - c_M t_M} \frac{\sinh(yt_M) \sinh(yt_U)}{y \sinh y}.$$

6. FINAL RESULTS AND COMPARISON WITH THE EXACT SOLUTION

6.1 Neutron Flux in the Mid-Plane of a Uranium Layer

The results of the preceding sections allow us now to evaluate the flux as given by the spherical-harmonics method and to compare it with the exact expression derived in Section 2. The comparison could be carried out in several ways. The easiest is to evaluate the flux and all its derivatives at the mid-planes of uranium and of moderator, and to compare the expressions given by the two methods. In the present subsection we concentrate on the value of the flux itself in the mid-plane of a uranium layer. For this the formulae (4.2) and (4.5) give

$$(6.1) \quad \Phi_N(\tau; \epsilon) \Big|_{\tau=\epsilon} = \sum_{m=0}^{\infty} \epsilon^{2m} \tilde{\zeta}_{0,m}$$

provided the series on the right side of (6.1) converges. If it does not, we proceed as follows. Notice that the spherical-harmonics calculation involves only analytical operations each of which is permissible for any real ϵ . Thus the value of $\Phi_N(\tau; \epsilon)$ for any given τ/ϵ should be an analytical function of ϵ . Thus, if the series (6.1) converges for sufficiently small ϵ (and we shall see shortly that it does), we can evaluate it for such ϵ values first and then extend the result by means of analytical continuations.

Accordingly we proceed to evaluate (6.1) under the assumption that ϵ is sufficiently small. Recalling that the leading term in the expansion of $\tilde{\zeta}_{0,m}$ into descending powers of N was denoted by $\tilde{\zeta}_{0,m}$, so that $\tilde{\zeta}_{0,m} = \tilde{\zeta}_{0,m} (1 + O(1/N))$, and using (5.15) and (5.21) we can rewrite (6.1) as

$$(6.2) \quad \Phi_N(\tau; \epsilon) \Big|_{\tau=\epsilon} = \frac{t_M}{1 - c_U t_U - c_M t_M} + \frac{\epsilon \pi}{2} \frac{1 - c_U}{1 - c_U t_U - c_M t_M} \sum_{m=1}^{\infty} \eta_m \frac{(\epsilon V)^{2m-1}}{(2m-1)!} \frac{d^{2m-1}}{dy^{2m-1}} \tan y \Big|_{y=0} + O(\epsilon^2 f(N\epsilon)),$$

where $O(\epsilon^2 f(N\epsilon))$ is the assembly of terms in which the power of ϵ exceeds that of N by at least two units. The sum appearing in (6.2) can be alternatively expressed, for $\epsilon N < \pi/2$, as

$$\frac{1}{2\pi} \int_0^{2\pi} d\theta \left\{ \sum_{m=1}^{\infty} \eta_m \exp[(2m-1)i\theta] \right\} \left\{ \sum_{m=1}^{\infty} \frac{[\epsilon V \exp(-i\theta)]^{2m-1}}{(2m-1)!} \frac{d^{2m-1}}{dy^{2m-1}} \tan y \Big|_{y=0} \right\},$$

or else, putting $z = \exp(i\theta)$ and recalling (5.22), as

$$(6.3) \quad \frac{1}{2\pi i} \int \frac{dz}{z^2} \left\{ \frac{\sinh(z t_M)}{\sinh z} - \frac{c_M - c_U}{1 - c_U t_U - c_M t_M} \frac{\sinh(z t_M) \sinh(z t_U)}{z \sinh z} \right\} \tan \frac{N\epsilon}{z},$$

where the integral is taken in the anticlockwise direction on the circle $|z| = 1$.

The singularities of the integrand outside this contour are the poles at the zeros of $\sinh z$, i.e. at the points $z = \pm \pi i n$, $n = 1, 2, \dots$. The deformation of the contour of integration into one consisting of circles embracing each of these poles can easily be justified and the integral can then be evaluated by the method of residues.

Substituting the result into (6.2), and noting that in view of (2.8),

$$\sin(\pi n t_U) = (-1)^{n-1} \sin(\pi n t_M),$$

we finally obtain

$$(6.4) \quad \Phi_N(\tau; \epsilon) \Big|_{\tau=\epsilon} = \frac{t_M}{1 - c_U t_U - c_M t_M} + \frac{\epsilon}{\pi^2} \frac{(c_M - c_U)(1 - c_U)}{(1 - c_U t_U - c_M t_M)^2} \sum_{n=1}^{\infty} \frac{[\sin(\pi n t_M)]^2}{n^3} \tanh(N\epsilon/\pi n) + \frac{\epsilon}{\pi} \frac{1 - c_U}{1 - c_U t_U - c_M t_M} \sum_{n=1}^{\infty} \frac{(-1)^n \sin(\pi n t_M)}{n^2} \tanh(N\epsilon/\pi n) + O(\epsilon^2 f(N\epsilon)).$$

Comparing this with the result of substituting (2.13) into (2.9) for $\tau = \epsilon$, one readily sees that (6.4) differs from the latter expression only by the appearance, in the term corresponding to each particular n , of the factor $\tanh(N\epsilon/\pi n)$.

6.2 The Evaluation and the Comparison of the Derivatives

We turn now to the evaluation of the derivatives of $\Phi_N(\tau; \epsilon)$ at the mid-plane of the uranium layer. All the odd-order derivatives will, of course, vanish there. For the even-order derivatives, proceeding as in the derivation of (6.2) and (6.3), we obtain

$$(6.5) \quad \frac{d^{2m}}{d(\tau/\epsilon)^{2m}} \Phi_N(\tau; \epsilon) \Big|_{\tau=\epsilon} = \sum_{m'=0}^{\infty} \epsilon^{2m+2m'} \Xi_{m, m'} = \frac{\epsilon \pi}{2} \frac{1 - c_U}{1 - c_U t_U - c_M t_M} \frac{1}{2\pi i} \int z^{2m-2} dz \frac{\sinh(z t_M)}{\sinh z} \tan(N\epsilon/z) + O(\epsilon^2 f(N\epsilon)) \quad \text{for } m \geq 1,$$

where the contour of integration is the same as in (6.3). Since the factor $1/z^2$ in the integrand of (6.3) is now replaced by z^{2m-2} , the deformation of the contour of integration used in the previous case can no longer be carried out directly. Notice however that for real z of large absolute value $\sinh(z t_M)/\sinh z$ behaves as $\exp[-(1-t_M)|z|]$ and a similar result holds if z tends to $\pm \infty$ along any line parallel to the real axis. Thus we can in any case deform the contour into one consisting of two straight lines parallel to the real axis, one above the real axis and one below. Suppose now we introduce into the integrand of the integral along the part of the path lying above the real axis the factor $\exp(i\xi z)$ (and $\exp(-i\xi z)$ into the other integral), where ξ is some real positive number. Since the integrals converge, in passing to the limit $\xi = 0$ after the integration we should return to our original expression. But, having introduced these factors, we can deform the contours and apply the method of residues much as in the previous case. Putting $\exp(-\xi\pi) = r$ and passing to the limit with ξ tending to zero we thus obtain

$$(6.6) \quad \left. \frac{d^{2m}}{d(\tau/\epsilon)^{2m}} \Phi_N(\tau, \epsilon) \right]_{\tau=\epsilon} = \epsilon(-1)^m \pi^{2m-1} \frac{1-c_U}{1-c_U t_U - c_M t_M} \lim_{r \rightarrow 1} \sum_{n=1}^{\infty} (-r)^n n^{2m-2} \sin(n\pi t_M) \tanh(N\epsilon/\pi n) + O(\epsilon^2 f(\epsilon N)),$$

which differs from (2.14) again only by the appearance of the factors $\tanh(N\epsilon/\pi n)$.

The comparisons in question imply, in fact, that

$$(6.7) \quad \Phi_N(\tau, \epsilon) = \Phi_0 + \sum_{n=1}^{\infty} [f_n + 2(\phi_n)_{(2.9)} \cos(n\pi\tau/\epsilon)] \tanh(N\epsilon/\pi n) + O(\epsilon^2 f(\epsilon N)),$$

where Φ_0 is the thermal flux for a homogeneous mixture (the first term of (1.2)), $(\phi_n)_{(2.9)}$ are the ϕ_n of (2.9), i.e. are given by the second of (2.13), while f_n is the term corresponding to a particular n in the first of (2.13). The fact that $2(\phi_n)_{(2.9)} \cos(n\pi\tau/\epsilon)$ and f_n would be accompanied in (6.7) by the same factor could have been easily foreseen. For we saw, at the end of subsection 2.2, that f_n is the change in the constant term of the Fourier expansion of the exact expression required to offset the absorption associated with the n th term of that expansion. Thus, the equality of absorption and production being preserved in the spherical-harmonics method and the n th term of the Fourier expansion being reduced, relative to its counterpart in the exact expression, by the factor $\tanh(N\epsilon/\pi n)$, the compensating change in the constant term must be reduced by the same factor.

6.3 Miscellaneous Remarks

It is of interest to notice that the factors by which each term in (6.4) and (6.6) differ from the corresponding terms in the exact expression (2.13) and (2.14) depend only upon ϵ , not upon t_M or t_U . In other words they depend upon the lattice pitch on the optical scale but not upon the optical thicknesses of individual layers separately. However, the rate of convergence of the

complete sum appearing in (6.4) to the correct value will depend also, though indirectly, upon the values of t_M and t_U . For if t_M and t_U are mutually comparable, the terms with $n = 1$ will outweigh the sum of all other terms and for the terms with $n = 1$ the rate of convergence is given by $\tanh(N\epsilon/\pi)$. On the other hand if $t_M \gg t_U$ or $t_U \gg t_M$ the term with $n = 1$, though individually still the most important, will be outweighed by the sum of the other terms; and of these the one that converges fastest is the $n = 2$ term, for which the convergence factor is $\tanh(N\epsilon/2\pi)$, and so on. Thus for a given ϵ significant deviations of t_U/t_M from unity will also decrease the rate of convergence of the spherical-harmonics method. It is obvious, nevertheless, that this effect is comparatively small compared with the dependence of the rate of convergence upon the total lattice pitch.

REFERENCES

- DAVISON, B. 1957*a*. Neutron transport theory (Clarendon Press, Oxford).
——— 1957*b*. Can. J. Phys. **35**, 55.
HOBSON, E. W. 1931. Theory of spherical and ellipsoidal harmonics (University Press, Cambridge).
MARK, J. C. 1957. Spherical harmonics methods CRT-338 (Revised) (A.E.C.L. No. 490).
MARSHAK, R. E. 1947. Phys. Rev. **71**, 443.

LETTERS TO THE EDITOR

Under this heading brief reports of important discoveries in physics may be published. These reports should not exceed 600 words and, for any issue, should be submitted not later than six weeks previous to the first day of the month of issue. No proof will be sent to the authors.

Mu-Meson Scattering from Lead Nuclei*

During recent years several experiments have been carried out to measure the scattering cross section of μ -mesons from heavy nuclei. Most of these investigations have indicated an anomalously high cross section, especially at high energies. These results are summarized by Lloyd, Rössle, and Wolfendale (1957). Other more recent measurements (Fukui, Kitamura, and Watase 1958) have not confirmed the presence of any anomalous interaction, but, on the contrary, agree with the result to be expected for an ordinary coulomb interaction between the muons and the nuclei. The present experiment was undertaken to determine whether any anomaly exists in the scattering cross section of low energy accelerator produced muons.

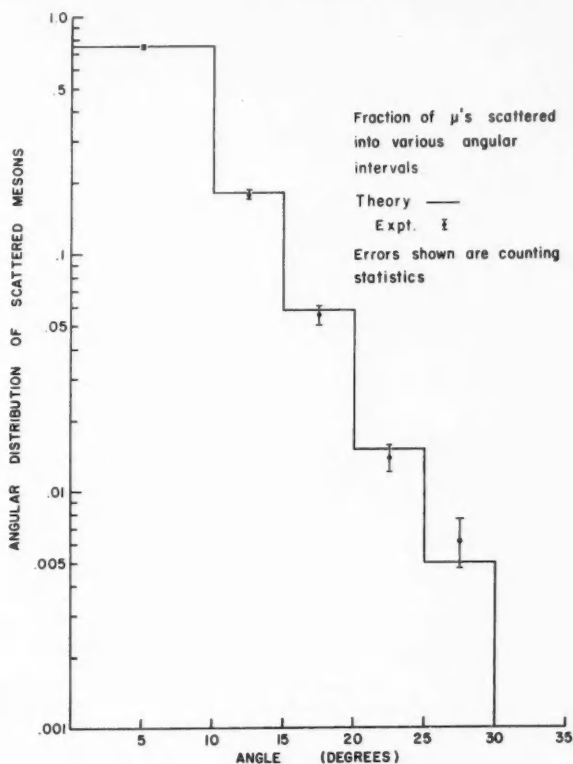


FIG. 1. Angular distribution of scattered μ -mesons.

*This work was supported by the U.S. Atomic Energy Commission.

23-Mev. negative μ -mesons from the C.I.T. synchrocyclotron have been scattered from a 0.022 in. lead plate mounted in a propane bubble chamber. The scattering distribution observed has been compared to an estimate based on Molière's multiple scattering theory (Molière 1948; Bethe 1953) and has been found to be in good agreement.

The μ -meson beam is passed through a bending magnet to select the desired momentum. The μ -meson energies at this point are such that after passing through 1.8 inches of propane and reaching the lead plate their energy has been reduced to 23 Mev. After the mesons pass through the lead plate they stop and decay in the propane in a distance of 2.4 inches. A stereoscopic view of each event is obtained by two cameras which subtend an angle of 28° in air or 22° in propane. In order for an event to be accepted it must be visible in both photographs and have the correct range, and the decay electron must be present. This procedure serves to discriminate against pions and electrons for two reasons. First, the ranges of pions and electrons with the selected momentum lie outside the acceptable limits, and second, the probability that they would produce a track which could be interpreted as a μ -e decay is small. Disregarding μ -mesons which do not decay does not introduce any bias.

All pictures were scanned twice and in cases of disagreement the event in question was measured a third time. Thirteen thousand pictures have been scanned yielding a total of 2428 acceptable events. These events are grouped according to scattering angle in 0° - 10° , 10° - 15° , 15° - 20° , 20° - 25° , 25° - 30° , and greater than 30° bins. This distribution was weighted to account for muons scattered out of the field of view, a factor which is a function of scattering angle.

The theoretical angular distribution was calculated using the Molière theory for multiple scattering in lead and taking into account multiple scattering effects in the propane near the lead plate. The contributions to the different bins were evaluated from this distribution with effects due to scanner accuracy being taken into consideration. The Molière theory assumes point nuclei, but the effect of finite nuclear size should be small at this energy.

The calculated and observed values are shown in Table I and Fig. 1 and are seen to be in good agreement for the entire angular range up to 30° . The errors shown in the experimental points are statistical errors only. Further data in the interval 25° - 30° are being analyzed to improve the accuracy of this point.

TABLE I
COMPARISON OF THEORETICAL AND EXPERIMENTAL ANGULAR DISTRIBUTION

Bin	Theoretical	Experimental	Statistical error, %
1: 0 - 10°	0.740	0.747	1.1
2: 10 - 15	0.181	0.177	4.5
3: 15 - 20	0.058	0.055	8.3
4: 20 - 25	0.015	0.0137	13.8
5: 25 - 30	0.0052	0.0061	23.8

- BETHE, H. A. 1953. Phys. Rev. **89**, 1256.
 FUKUI, S., KITAMURA, T., and WATASE, Y. 1958. Private communication.
 LLOYD, J. L., RÜSSLE, E., and WOLFENDALE, A. W. 1957. Proc. Phys. Soc. A, **70**, 421.
 MOLIÈRE, G. 1948. Z. Naturforsch. **3a**, 78.

RECEIVED APRIL 23, 1958.
 PHYSICS DEPARTMENT,
 CARNEGIE INSTITUTE OF TECHNOLOGY,
 PITTSBURGH, PENNSYLVANIA.

B. CHIDLEY
 G. HINMAN
 P. GOLDSTEIN
 R. SUMMERS
 R. ADLER

Measurements of Fluctuations of Atmospheric Temperature

Much information about the structure of atmospheric turbulence can be obtained through measurements of fluctuations of temperature. This has been investigated recently for the lowest few hundred feet of the atmosphere by Krechner (1952) and MacCready (1953). However, in these and most other cases the scope of the work was more or less restricted by one or more of the following equipment characteristics: sensitivity and time constant, the physical size of the sensing elements and, in those studies which involved the measurement of the spectrum of the fluctuations, the frequency range of the spectrum analyzer.

In the study initiated at this laboratory it is felt that all of these restrictions have been relaxed to some extent.

The sensing elements are platinum resistance thermometers, of wire $2.5\ \mu$ in diameter, mounted on tapered Inconel rods. The elements are either single-looped, of approximately 100 ohms, or multi-looped, of approximately 600 ohms. The elements have dimensions (loop diameter and winding length) of the order of 3-4 millimeters and a measured time constant of 1 millisecond. For expected values of mean wind speed this combination of element characteristics permits the study of turbulent structure of dimensions down to the order of 5 millimeters.

Two types of measurement are in progress: (a) temperature fluctuations at one point and (b) temperature difference at two points whose separation (either horizontal or vertical) is continuously variable in the range 3 millimeters to 3 meters. The atmosphere is sampled from platforms located at several levels on a 64-meter tower. The sensing element is located approximately ten feet from the tower and no measurements are taken when the wind blows from the tower to the element. In this initial note only results for temperature fluctuations at a point are presented.

Two inherently different statistical methods of analysis of the experimental results are being used. One method involves a statistical description of the results, in particular the determination of various moments of the probability distributions. The second approach involves a description of the fluctuations in terms of spectra and correlation functions. The latter approach is covered briefly in this note.

Figure 1 indicates the equipment arrangement, as used for a spectrum determination. The bridge, of which the elements form either one or two arms (depending on the type of

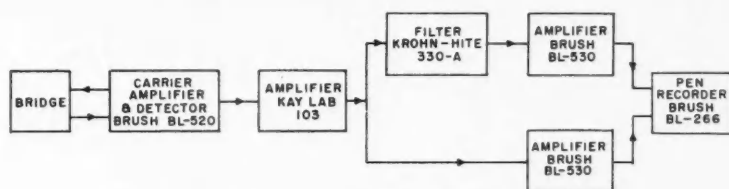


FIG. 1. Block diagram of equipment for spectrum measurements.

measurement being made), is associated with the Brush Model BL-520 carrier amplifier and its associated phase sensitive detector. The bridge excitation frequency is 2000 cycles per second. The output of the phase sensitive detector, after further amplification in a Kay Lab. Model 103 d-c. amplifier, can be fed directly to an oscillograph, or alternatively to a bank of Krohn-Hite Model 330A band-pass filters, arranged in parallel. These filters are used with one-octave bandwidths and have their center frequencies in the range 0.03-1500 cycles per second. The signals are passed finally to a Brush Model BL-266 6-channel oscillograph.

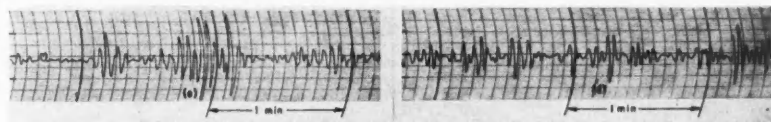


FIG. 2. Sample temperature records: (a) and (b) temperature fluctuations at a point; (c) and (d) outputs of filter with center frequency of 0.31 cycle per second.

Some examples of the records obtained are given in Fig. 2. The details of the runs are shown in Table I, which also indicates the full-scale sensitivities of the records of Fig. 2.

TABLE I

	(a)	(b)	(c)	(d)
Date (1957)	Sept. 9	Oct. 10	Sept. 17	Oct. 10
Time (E.D.T.)	1605	1325	1430	1325
Temperature (deg. C.)	20	10.5	18	10.5
Wind speed (m./sec.)	4.5	10	5	10
Sky conditions	Sunny	Cloudy	Sunny	Cloudy
Sensitivity (C. deg. full scale)	4	0.8	0.51	0.19
Sample length (min.)	2.75	2.75	2.75	2.75
Height (m.)	11	44	11	44

Records (a) and (b) were obtained without any filtering. Record (a) illustrates the type of fluctuation characteristic of a clear, sunny day. The temperature variation is seen to be highly skew, or one-sided, suggesting as a model the convection of warm air bubbles from near the ground due to solar heating.

Record (b) is typical of the conditions obtaining during cloudy periods. The trace is more symmetrical about the mean temperature than is that of (a). It is suggestive of dynamic, rather than convective, turbulence.

Records (c) and (d) are samples from the filter with center frequency of 0.31 cycle per second. They illustrate another temperature fluctuation characteristic, which we have termed "burstiness". During sunny periods the records show periods of up to a minute when the amplitude of the fluctuations is very small. These quiet periods alternate with bursts of large amplitude. Record (c), obtained during sunny conditions, indicates a high degree of burstiness. Record (d), by contrast, is typical of a predominantly cloudy period.

A measured spectrum of the temperature fluctuations at a point is shown in Fig. 3. The square root of the mean square temperature fluctuation per unit bandwidth has been plotted as a function of frequency on a log-log scale. The experimental curve is seen to approximate

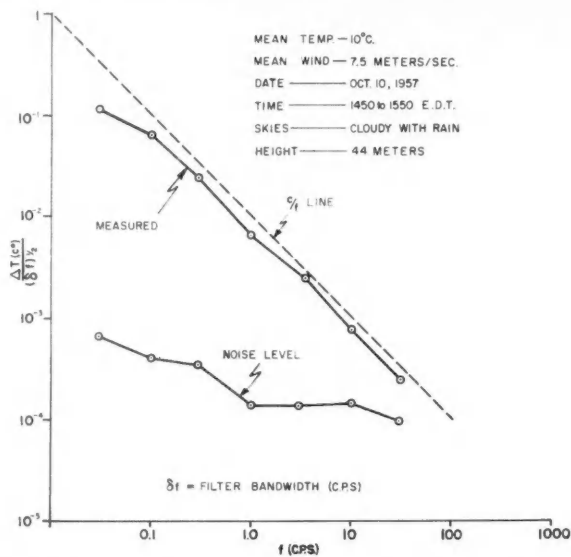


FIG. 3. Sample spectrum of the r.m.s. temperature fluctuations per unit bandwidth at a point.

to a c/f line, where c is a constant. Also shown for reference is the noise level of the equipment. This spectrum is typical of those obtained so far, but whether or not it is a general characteristic of the atmosphere remains to be determined.

The assistance of Mr. D. Wills, who obtained and analyzed the data, is gratefully acknowledged.

KRECHNER, S. I. 1952. Doklady Akad. Nauk, S.S.S.R. **84** (1), 55.
MACCREADY, P. B. 1953. J. Meteorol. **10**, 325.

RECEIVED FEBRUARY 5, 1958.
RADIO PHYSICS LABORATORY,
DEFENCE RESEARCH TELECOMMUNICATIONS ESTABLISHMENT,
DEFENCE RESEARCH BOARD,
OTTAWA, ONTARIO.

A. W. ADEY
W. J. HEIKKILA

Ultrasonic Attenuation in Superconducting Aluminum

A number of experimental investigations (Bömmel 1954; MacKinnon 1955, 1957; Mason and Bömmel 1956; Morse, Tamarkin, and Bohm 1956) have been reported concerning ultrasonic attenuation in superconducting lead, tin, and indium. Except for a solitary observation (Morse and Bohm 1957) on the fall of attenuation in superconducting aluminum, work on the latter has not been reported. The present paper reports measurements of the attenuation of 20 Mc. longitudinal waves in normal, superconducting, and intermediate states of polycrystalline aluminum.

The aluminum was of 99.99% purity. It was recrystallized from the cold-rolled condition by annealing at 500° C. for 5 hours. The grain size was then ≈ 2 mm. Measurements of attenuation were made by the conventional ultrasonic pulse technique. A pulse of 20-Mc. ultrasonic waves was applied to one end of the cylindrical 20-Mc. quartz crystal (diameter 22 mm., length 0.5 in.) which was also used to receive the reflected pulses. After amplification the pulse and its echoes were displayed on an oscilloscope and photographed. The absolute attenuation was calculated from the magnitudes of the exponentially decaying echo pulses. A pair of Helmholtz coils around the helium Dewar gave a variable magnetic field. Temperatures down to 0.84° K. were obtained in a booster cryostat (Atkins, Edwards, and Pullan 1955).

The attenuation as a function of temperature is shown in Fig. 1. The lowest T/T_c ratio obtainable is unfortunately too high to differentiate with certainty between a power relation connecting attenuation and temperature and the relation given by the recent theory of superconductivity (Bardeen, Cooper, and Schrieffer 1957).

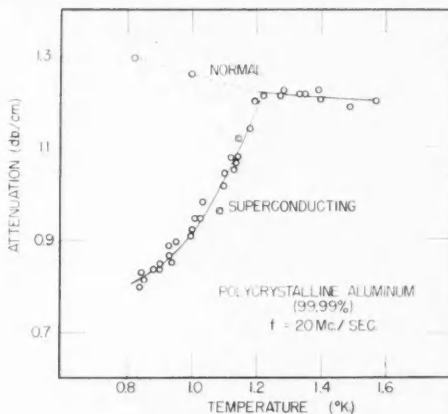


Fig. 1. Attenuation of 20 Mc./second longitudinal waves in superconducting aluminum.

When an increasing magnetic field was applied to the superconducting metal, the attenuation remained essentially unchanged until a particular field was reached, when a sharp rise in attenuation occurred. As the field was decreased to zero and then reversed in direction the attenuation followed a "hysteresis" loop as shown in Fig. 2. Such loops have been observed in lead (Bömmel 1954) and tin (MacKinnon 1957). However, Fig. 2 has some distinctive features. It shows little residual attenuation at zero field in contrast to the 30-60% observed by Bömmel and MacKinnon. This may be due to higher purity or less strain in our specimens, giving rise to less trapped flux.

The attenuation reached a constant value in about 9 seconds after a magnetic field change. This relaxation time of flux ejection has interesting features and is being given further study.

The area of the hysteresis loop is a function of temperature and increases as the temperature is decreased. The lack of symmetry apparent in Fig. 2 and the observation of lower attenuation value on reversal of field, as indicated by (a) in Fig. 2, requires further clarification.

This work was supported by the Defence Research Board of Canada, Grant No. 7510-14, Project No. D44-75-10-14, whose assistance is gratefully acknowledged. We are also grateful to Dr. M. H. Edwards, who designed the booster cryostat.

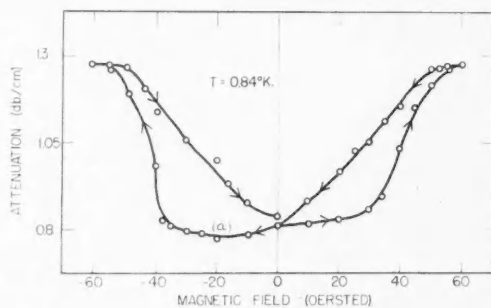


FIG. 2. "Hysteresis" of ultrasonic attenuation with magnetic field applied on superconducting aluminum.

- AIKINS, K. R., EDWARDS, M. H., and PULLAN, G. T. 1955. *Rev. Sci. Instr.* **26**, 49.
 BARDEEN, J., COOPER, L. N., and SCHRIEFFER, J. R. 1957. *Phys. Rev.* **108**, 1175.
 BÖMMEL, H. E. 1954. *Phys. Rev.* **96**, 220.
 MAC KINNON, L. 1955. *Phys. Rev.* **100**, 955; 1957. *Phys. Rev.* **106**, 70.
 MASON, W. P. and BÖMMEL, H. E. 1956. *J. Acoust. Soc. Am.* **28**, 930.
 MORSE, R. W., TAMARKIN, P., and BOHM, H. V. 1955. *Phys. Rev.* **101**, 1610.
 MORSE, R. W. and BOHM, H. V. 1957. *The Fifth International Conference on Low Temperature Physics and Chemistry*, Madison, Wis.

RECEIVED MARCH 3, 1958.
 DEPARTMENT OF PHYSICS,
 ROYAL MILITARY COLLEGE OF CANADA,
 KINGSTON, ONTARIO.

K. L. CHOPRA
 T. S. HUTCHISON

CANADIAN JOURNAL OF PHYSICS

Notes to Contributors

Manuscripts

(i) **General.** Manuscripts, in English or French, should be typewritten, double spaced, on paper $8\frac{1}{2} \times 11$ in. **The original and one copy are to be submitted.** Tables and captions for the figures should be placed at the end of the manuscript. Every sheet of the manuscript should be numbered.

Style, arrangement, spelling, and abbreviations should conform to the usage of recent numbers of this journal. Names of all simple compounds, rather than their formulas, should be used in the text. Greek letters or unusual signs should be written plainly or explained by marginal notes. Superscripts and subscripts must be legible and carefully placed.

Manuscripts and illustrations should be carefully checked before they are submitted. Authors will be charged for unnecessary deviations from the usual format and for changes made in the proof that are considered excessive or unnecessary.

(ii) **Abstract.** An abstract of not more than about 200 words, indicating the scope of the work and the principal findings, is required, except in Notes.

(iii) **References.** References should be listed **alphabetically by authors' names**, unnumbered, and typed after the text. The form of the citations should be that used in current issues of this journal; in references to papers in periodicals, titles should not be given and only initial page numbers are required. The names of periodicals should be abbreviated in the form given in the most recent *List of Periodicals Abstracted by Chemical Abstracts*. All citations should be checked with the original articles and each one referred to in the text by the authors' names and the year.

(iv) **Tables.** Tables should be numbered in roman numerals and each table referred to in the text. Titles should always be given but should be brief; column headings should be brief and descriptive matter in the tables confined to a minimum. Vertical rules should not be used. Numerous small tables should be avoided.

Illustrations

(i) **General.** All figures (including each figure of the plates) should be numbered consecutively from 1 up, in arabic numerals, and each figure referred to in the text. The author's name, title of the paper, and figure number should be written in the lower left corner of the sheets on which the illustrations appear. Captions should not be written on the illustrations (see Manuscripts (i)).

(ii) **Line Drawings.** Drawings should be carefully made with India ink on white drawing paper, blue tracing linen, or co-ordinate paper ruled in blue only; any co-ordinate lines that are to appear in the reproduction should be ruled in black ink. Paper ruled in green, yellow, or red should not be used. All lines should be of sufficient thickness to reproduce well. Decimal points, periods, and stippled dots should be solid black circles large enough to be reduced if necessary. Letters and numerals should be neatly made, preferably with a stencil (**do NOT use typewriting**) and be of such size that the smallest lettering will be not less than 1 mm. high when reproduced in a cut 3 in. wide.

Many drawings are made too large; originals should not be more than 2 or 3 times the size of the desired reproduction. Whenever possible two or more drawings should be grouped to reduce the number of cuts required. In such groups of drawings, or in large drawings, full use of the space available should be made; the ratio of height to width should conform to that of a journal page ($4\frac{1}{2} \times 7\frac{1}{2}$ in.), but allowance must be made for the captions.

The original drawings and one set of clear copies (e.g. small photographs) are to be submitted.

(iii) **Photographs.** Prints should be made on glossy paper, with strong contrasts. They should be trimmed so that essential features only are shown and mounted carefully, with rubber cement, on white cardboard, with no space between them. In mounting, full use of the space available should be made to reduce the number of cuts required (see Illustrations (ii)). Photographs or groups of photographs should not be more than 2 or 3 times the size of the desired reproduction.

Photographs are to be submitted in duplicate; if they are to be reproduced in groups one set should be mounted, the duplicate set unmounted.

Reprints

A total of 50 reprints of each paper, without covers, are supplied free. Additional reprints, with or without covers, may be purchased at the time of publication.

Charges for reprints are based on the number of printed pages, which may be calculated approximately by multiplying by 0.6 the number of manuscript pages (double-spaced type-written sheets, $8\frac{1}{2} \times 11$ in.) and including the space occupied by illustrations. An additional charge is made for illustrations that appear as coated inserts. Prices and instructions for ordinary reprints are sent out with the galley proof.

Any reprints required in addition to those requested on the author's reprint requisition form must be ordered officially as soon as the paper has been accepted for publication.

Contents

<i>W. N. Abbott</i> —Displacements of the radiant point during the auroral disturbance of September 22, 1957 - - - - -	643
<i>A. E. Scheidegger</i> —The random-walk model with autocorrelation of flow through porous media - - - - -	649
<i>B. W. Schumacher and E. O. Gadamer</i> —Electron beam fluorescence probe for measuring the local gas density in a wide field of observation - -	659
<i>S. C. Loh and J. Y. Wong</i> —Radiation field of an elliptic loop antenna with a constant current - - - - -	672
<i>T. R. Hartz</i> —Auroral radiation at 500 Mc. - - - - -	677
<i>K. A. Jackson</i> —Kinetics of alloy solidification - - - - -	683
<i>H. S. Heaps</i> —Optimum filter functions for the detection of pulsed signals in noise - - - - -	692
<i>Pierre Demers</i> —Théorie de la diffusion au cours du développement des couches ionographiques épaisses - - - - -	704
<i>Mahendra Singh Sodha and Desh Bandhu Agrawal</i> —Low-field mobility of carriers in nondegenerate semiconductors - - - - -	707
<i>Larkin Kerwin</i> —On the displacement of an ion beam image by magnetic fringing fields - - - - -	711
<i>A. E. D. Heylen and T. J. Lewis</i> —The electric strength and molecular structure of hydrocarbon gases - - - - -	721
<i>R. J. Berry</i> —The reproducibility of the steam point - - - - -	740
<i>F. R. Britton and M. F. Crawford</i> —The theory of collision-induced absorption in hydrogen and deuterium - - - - -	761
<i>B. Davison</i> —On the rate of convergence of the spherical-harmonics method for a sandwich reactor of small lattice pitch - - - - -	784
Letters to the Editor:	
<i>B. Chidley, G. Hinman, P. Goldstein, R. Summers, and R. Adler</i> —Mu-meson scattering from lead nuclei - - - - -	801
<i>A. W. Adey and W. J. Heikkilä</i> —Measurements of fluctuations of atmospheric temperature - - - - -	802
<i>K. L. Chopra and T. S. Hutchison</i> —Ultrasonic attenuation in superconducting aluminum - - - - -	805

